Design, Development and Experimental Investigation of Hydrogen Production Using Modified Solar Reactor from Two – Step Water Splitting CeO_2 based Thermochemical Cycle

Thesis Submitted for the Award of the Degree of

Doctor of Philosophy

in

Mechanical Engineering

By

Jeet Prakash Sharma

(Reg. no. - 11720108)

Supervised by

Prof. Dr. Ravindra D. Jilte
UID: 20336

Co-Supervised by

Dr. Ravinder Kumar
UID: 22218

LOVELY PROFESSIONAL UNIVERSITY
PUNJAB
April 2022

Declaration

I do hereby acknowledge that,

The thesis entitled "DESIGN, DEVELOPMENT AND EXPERIMENTAL INVESTIGATIONOF HYDROGEN PRODUCTION USING MODIFIED SOLAR REACTOR FROM TWO – STEP WATER SPLITTING CeO_2 BASED THERMOCHEMICAL CYCLE" is a presentation ofmy original research work done under the guidance of my thesis supervisor(s). Wherever contributions of others are involved, every effort is made to indicate this clearly, with due reference to the literature, and acknowledgement of collaborative research and discussions.

I hereby confirm that the thesis is free from any plagiarized material and does not infringe any rights of others. I also confirm that if any third party owned material is included in my thesiswhich required a written permission from the copyright owners, I have obtained all such permissions from respective copyright owners.

I carefully checked the Final Version of Printed and Softcopy of the Thesis for thecompleteness and for incorporation of all suggestions of Doctoral Committee.

I hereby submit the FINAL VERSION of the printed copy of my thesis as per the guidelinesand the exact same content in CD as a separate PDF file to be uploaded in Shodhganga.

DATE: 23-DEC-21 SIGNATURE OF CANDIDATE

Place: Phagwara Reg. No.: 11720108

Certificate by advisor/co-advisor

I hereby affirm as under that:

1. The thesis presented by Jeet Prakash Sharma is worthy of consideration for theaward of the degree of Doctor of Philosophy.
2. He has pursued the prescribed course of research.
3. The work is original contribution of the candidate.
4. The candidate has incorporated all the suggestions made by the DepartmentDoctoral Board during Pre -Submission Seminar held on 30 Oct 2021.

Advisor Name & Signature	Co-Advisor Name & Signature
Prof. Dr. Ravindra D. Jilte	Dr. Ravinder Kumar
Date: 23 Dec 2021	Date: 23 Dec 2021

Abstract

The solar driven two-step water or CO_2 splitting thermochemical cycles are the best possible way to produce hydrogen and syngas. In this work, a hybrid design of closed cavity solar thermochemical has been proposed and numerically analyzed with the geometrical, optical and thermal aspects. The study was carried out in a sequential and systematical way. In the first step, the optical analysis was performed with the help of SolTrace software. The optical analysis provided with the Gaussian solar flux profile capable of generating the temperature distribution to carry out the high-temperature reduction reaction. The optical analysis aspect was also further bifurcated in two parts: (1) the influence of focal point displacement on the flux and temperature distribution, (2) the geometrical and optical effect on two different STCR cavity shapes on the solar flux and temperature distribution.

In the next part, a transport and chemical kinetics model in the proposed solar thermochemical reactor was simulated with steady state as well as the transient conditions to achieve the reduction temperature. This aspect of the study was carried to investigate the effect of varying RPC thickness on the temperature distribution in porous media as well as in the whole reactor cavity. Further, the effect of varying gas flow gap and increasing fluid velocity on the temperature distribution in the porous region along with entire reactor cavity was also studied. The solar-to-fuel conversion efficiency was also estimated for the cerium oxide based solar thermochemical cycle using the reaction rate model. Ceria based solar thermochemical cycle is a high-temperature based redox chemical reactions to split H_2O or $CO_2$to produce hydrogen and/or syngas. The redox reactions are carried out in a reactor cavity thus the analysis and optimization of design as well as thermal analysis is a crucial factor to improve the solar-to-fuel conversion efficiency.

This study proposed the hybrid design of cylindrical and hemispherical cavity and its effects of geometrical parameters such as reticulated porous ceria (RPC)

thickness (*15 mm, 20 mm,* and *25 mm*) and gas flow gap (*5 mm*&*10 mm*) on temperature and flux distribution and solar-to-fuel efficiency for both steady-state and transient condition. A numerical computational fluid dynamics (CFD) analysis is carried out to study heat and mass transfer as well as geometrical design consideration of the STCR cavity under SolTrace generated Gaussian distributed concentrated solar flux. Two-step water-splitting reaction in the Solar Thermochemical cavity reactor (STCR) using ceria (CeO_2) has been modeled to explore the oxygen evolution/reaction rate and to estimate solar-to-fuel efficiency and its relationship with geometrical factors. The RPC of *25 mm* thickness yields the highest oxygen evolution rate of *0.34 mL/min/gCeO*$_2$ and solar-to-fuel efficiencies are *7.82%, 12.07%* and *16.18%* for *15 mm, 20 mm* and *25 mm* of RPC thickness, respectively without heat recovery.

The effect of thermal performance on the solar thermochemical reactor associated with the geometrical parameters such as inlet positioning and orientation was also investigated. The study was carried out with five inlet positions (5, 8, 10, 12 and 15 mm from the front quartz glass window) and three inlet orientations (65^0, 75^0 and 90^0 from the horizontal plane). The main objective of the study to find out the optimum position and orientation to place the inlets to avoid the swirling phenomenon caused by the directly faced inlet at the high velocity of sweep gas. The nitrogen gas flows through the solar thermochemical reactor for cooling the quartz window and also it sweeps the oxygen gas from the reactor-receiver cavity after the end of the reduction step of redox thermochemical cycle of hydrogen production.

The uniform distribution of nitrogen gas throughout the reactor-receiver cavity necessitates during its operation. This study is carried out to investigate the effects of gas flow inlet positioning from the quartz window and its orientation on the vertical axis. It is observed that the inlet position at 10 mm combined with the orientation of 75^0 inclination from the horizontal plane was seen to achieve the highest avg. temperature of 1587 K in the radial direction in the porous media. While, the avg. temperature in the axial direction in the porous media reached highest value of 1666 K for the inlet position of 10 mm with the orientation of 900 and the highest avg. temperature of 1353 K was achieved by the inlet position of 12 mm at the orientation of 75^0 along the centerline of the STCR cavity.

The thermodynamic analysis was performed to investigate the effect of non-stoichiometry on the solar-to-fuel conversion efficiency of the two-step water splitting solar thermochemical cycle. The cerium oxide (CeO_2) undergoes the reduction reaction when subjected the high temperature. The high-temperature destabilizes the ceria stoichiometry and converts it into CeO_{2-x} and produces the $\frac{x}{2}O_2$ in thermal reduction step. Therefore, two sets of non-stoichiometric cerium oxides as $CeO_{1.72}$ and $CeO_{1.83}$ were formulated and thermodynamically compared in terms of solar-to-fuel conversion efficiency.

The thermal reduction (TH) and re-oxidation temperatures (TL) were determined by the equilibrium analysis. The Equilibrium composition of CeO_2, $CeO_{1.72/1.83}$ and O_2 show that the thermal reduction of CeO_2 starts at 1400 K and it reaches the full extent at 2734 K. The change in Gibbs free energy (ΔG) suggest that the re-oxidation was feasible at 1050 K and 1200 K for $CeO_{1.83}$ and $CeO_{1.72}$, respectively. The efficiency analysis show that the solar-to-fuel conversion efficiency ($\eta_{solar-to-fuel}$) reached the maximum value of 7.45% ($CeO_{1.72}$) and 7.69% ($CeO_{1.83}$) at the %TR of CeO_2 of 61.72% without heat recuperation and it attained the maximum value of 14.92% and 13.54% for $CeO_{1.83}$ and $CeO_{1.72}$, respectively at the %TR of CeO_2 of 80% with the 50% heat recuperation.

Another thermodynamic analysis was carried out to evaluate the solar-to-fuel conversion efficiency of the solar driven cerium (III) sulfate ($Ce_2(SO_4)_3$)-cerium (IV) oxide (CeO_2) water splitting cycle for hydrogen production to evaluate the solar-to-fuel conversion efficiency of the cycle with and without consideration of the heat recuperation technique. The thermal equilibrium analysis was performed to identify the thermal reduction (TH) and re-oxidation temperatures (TL). The equilibrium composition of $Ce_2(SO_4)_3$, CeO_2, SO_2 and O_2show that the thermal reduction of $Ce_2(SO_4)_3$ starts at 900 K and the full extent of reduction is achieved at 1200 K. The change in Gibbs free energy (ΔG) imply that the re-oxidation reaction was feasible at the temperature of 550 K. The efficiency analysis show that the $\eta_{solar-to-fuel}$ attained the maximum value of 22.35 without employing the heat recuperation technique.

However, the $\eta_{solar-to-fuel}$ improved to 25.42%, 32.15%, 39.12%, 50.16% and 58.51% with 20%, 50%, 70%, 90% and 100% heat recuperation, respectively.

In the final part of the work, the zirconia porous honeycomb structure was stabilized with the cerium oxide and thermally treated. The SEM analysis was also performed to estimate the pore and strut size of the material. The porosity of the doped material was analyzed with the one-dimensional analysis which could be used in the numerical analysis of a solar thermochemical reactor.

Acknowledgement

This PhD thesis work would not have been possible without the generous support and help of many individuals and organization. I would like to extend my sincere thanks to all of them.

First and foremost, I am exceedingly grateful and eternally indebted to my supervisor ***Prof. Dr. Ravindra D. Jilte, Department of Mechanical Engineering, Lovely Professional University*** for his invaluable guidance, unparalleled brilliance and constant supervision which helped me successfully complete my thesis work. Prof. Jilte took a risk to accept me as his advisee to explore a relatively new and amazingly interesting field of research, for which I will always be thankful. He corrected me on my smallest mistakes, motivated me through rough times, and provided me with the freedom to explore my own ideas. He paved a path for me to tread on and never let me stop until a better researcher was furnished. In reality, mere words cannot suffice to express my sincere gratitude towards him for making me a confident researcher. I wish him the best in his future endeavors and I believe he will continue his academic journey to inspire the upcoming generations of students.

I would like to thank my co-supervisor ***Dr. Ravinder Kumar (Associate Professor), Department of Mechanical Engineering, Lovely Professional University*** for giving me opportunity to work with him in the area of solar energy research.

I would like to thank ***Dr. Ajit Sharma (Associate Professor), Department of Chemical Engineering and Physical Science, Lovely Professional University*** who provided his finest counsel, under no obligation, at the most critical time of my research. He helped me to better understand the essential chemical aspect and its integration with the solar thermal energy in this research work.

I would like to thank ***Dr. Aashish Sharma (Assistant Professor), Department of Mechanical Engineering, Lovely Professional University*** for his invaluable insights and support. He was always ready to resolve my problems and always provided me with meticulous advice during this research period.

I want to thank the ***Center Instrumentation Facility (CIF)***, ***Lovely Professional University*** and their personnel for providing me with the instruments and their academic excellence to test my samples to help better my research.

I also would like to express my gratitude towards my mother ***Mrs. Mithlesh Sharma*** and my father ***Mr. Yogendra Kumar Sharma,*** who have always put my happiness above everything else and allowed me to take my own decisions in life.

I also want to thank my grandmother ***Mrs. Dropdi Sharma*** and my grandfather ***Mr. Narayan Dutt Sharma,*** also the rest of my family, my uncle and aunts, Mr. Maheshwari Prasad Sharma & Mrs. Sudha Sharma and Mr. Purendra kumar Sharma & Mrs. Neetu Sharma and my siblings, Sheetal, Anjali and Deshbandhu & cousins, Manju, Navneet, Piyush, Palak and Saksham, for standing by my side through thick and thin and pushing me to pursue my higher education to achieve my dreams.

Finally, I also would like offer my sincere gratitude to one person who, more than anyone else, made the past few years wonderful. She encouraged me to continue my work with passion and focus at times when I was unable to find the answers. She worked out all the secondary things for me so I could lead a successful research work uninterrupted. She celebrated small leaps and bounds with me and never let me down. ***Rasleena Thakur***, I just hope that would be able to do justice with your kindness, support and patience to bear with me.

I dedicate this thesis work, and all of the extended work of my career, to the loving memory of my beloved father, Mr. Yogendra Kumar Sharma.

Dear father, I started this work as per you wish but you weren't here to see it get finished. I was always a day late and a dollar short, so to speak, but I promised to be a better person whom you could be proud of, I will always keep that promise.

Table of Contents

List of Tables

List of Figures

List of Appendices

Chapter – 1

1 Introduction and background

1.1 Solar concentrated energy systems

Solar energy an eternal and most abundant source of power on this planet and a number of technologies have been developed to utilize for the various purpose at small, medium and large scale for industrial as well as house hold application. The solar radiation strikes the earth in the wavelength of 0.1 to 10 μm. Therefore, it is necessary to convert the solar radiation in to directly usable energy such as electric energy via PV panels or solar concentrating technology.

It's been nearly 30 years since the development of solar concentrating energy systems and these systems have been categorized in 4 parts such as 1) parabolic trough, 2) solar tower, 3) solar dish system, and 4) double concentrating system as shown in Fig. 1.

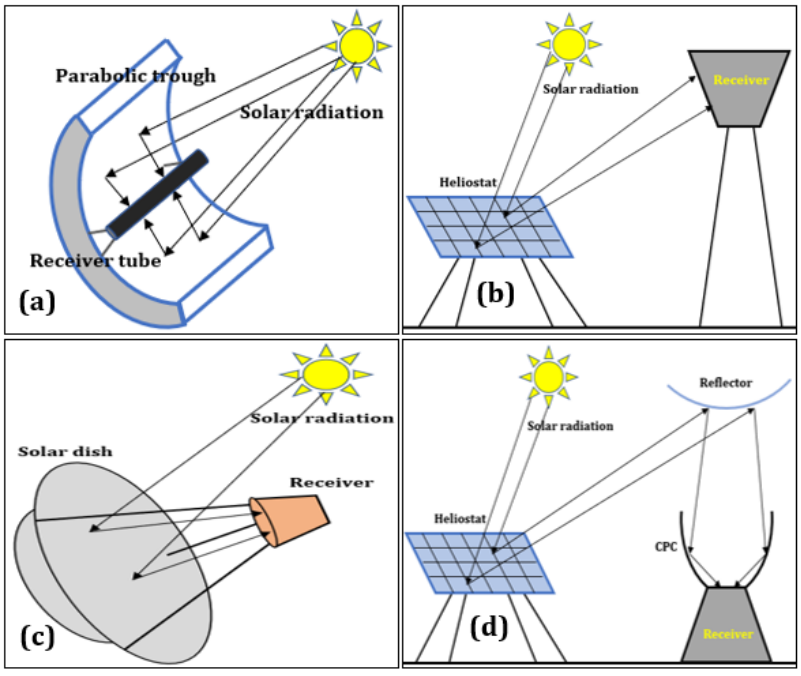

Fig. 1: Solar concentrating technologies (a) Parabolic trough; (b) Solar tower; (c) Solar dish system and (4) Double concentrating system [1]

The systematic development of solar concentrating technologies has increased the capability of harnessing solar power to be converted into electricity via. solar thermal energy system and solar chemical fuels [1]. Each concentrating system has been developed for its own specific purpose and with different concentration ratio (C) to meet the required input power. The output solar thermal power or the achievable temperature of a solar concentrating system is typically the function of concentrating ratio (C) [2].

$$C = \frac{Q_{input\ solar\ power}}{I \cdot A_s} \tag{1}$$

Therefore, the capability of an optical – thermal system to concentrate the solar energy is measured in terms of concentration ratio of the mean solar flux striking over the targeted surface area (A_s) at the focal plane, perpendicular to the incident normal beam insolation (I).

Parabolic trough shown in Fig. 1(a) uses the linear parabolic reflectors to concentrate the sunlight on the receiver tube to raise the temperature of the circulating fluid. Solar tower system shown in Fig. 1(b) uses the highly reflective surfaced heliostats to re-direct the incident solar rays to receiver in order to generate the electricity. Solar towers typically can achieve the concentration ratio from 300 to 1500 and reach the operational temperature up to 1500 K. Solar dish systems as shown in Fig. 1(c) are the combination of a parabolic dish which concentrates the incidents solar rays and focuses on to the receiver cavity. Solar dish systems can achieve the concentration ratio in the range of 1000 to 5000 and operate at the temperature of 1800 K to 2000 K. The double concentration system operates with two optical systems i.e. heliostat and reflective tower. The heliostat re-directs the solar rays towards the reflective tower which diverts them into CPC or compound parabolic concentrator. CPC concentrates the solar radiation and directs it in to the receiver as shown in Fig. 1(d).

1.2 Optical – thermal system design

1.2.1 High flux solar simulator

The solar simulators are commonly known as the source of the artificial light which is used to carry out the solar thermochemical processes instead of using real concentrated sunlight. Concentrated solar technologies use the optics systems to focus solar radiation into a very small area (aperture). Solar concentrated technology (CST) is the source of a clean, green and reliable source of energy which is further used as heat, electricity and fuel development [3]. Low-density solar energy is collected by the solar collector and concentrated by the concentrators. Mainly glass mirrors are used concentrators due to their extraordinary reflectivity quality.

1.2.2 Solar simulator design consideration

Simplest solar simulator design is ellipsoidal as shown in Fig. 2 in which the lamp is mounted inside the reflector in the middle. Most often the arc lamps and metal halide lamps are used in simulators to generate the concentrated radiation at the other focus. The other reflectors such as the paraboloid dish and the parabolic trough are used in the industrial applications. The solar simulator is ellipsoidal shape therefore, the general equation for the ellipse is given as;

$$\frac{x^2}{a^2}+\frac{y^2}{b^2}=1; \quad \text{a > b} \tag{2}$$

where a is known as the semi-major axis and b is known as a semi-minor axis. Foci are the half distance from one focus to another and it's related to the major and minor axis as in Eqs. (3) and (4);

$$c=\sqrt{a^2+b^2} \tag{3}$$

$$c=ea \tag{4}$$

where e is known as eccentricity.

The designing parameters can be given as below;

The length of the reflector can be given as given in Eq. (5);

$$l_{refl}=a-\left(c-l_{trunc}\right)-l_{ap} \tag{5}$$

l_{ap} is known as the aperture length and it is calculated as given in Eq. (6);

$$l_{ap} = a\left[1-\sqrt{1-\left(\frac{r_{ap}}{b}\right)^2}\right] \tag{6}$$

The truncation length is given by Eq. (7) and (8);

$$l_{trunc} = 2c - d_{center} \tag{7}$$

$$\frac{r_{in}^{\ 2}}{b^2} + \frac{(l_{trunc}-c)^2}{a^2} = 1 \tag{8}$$

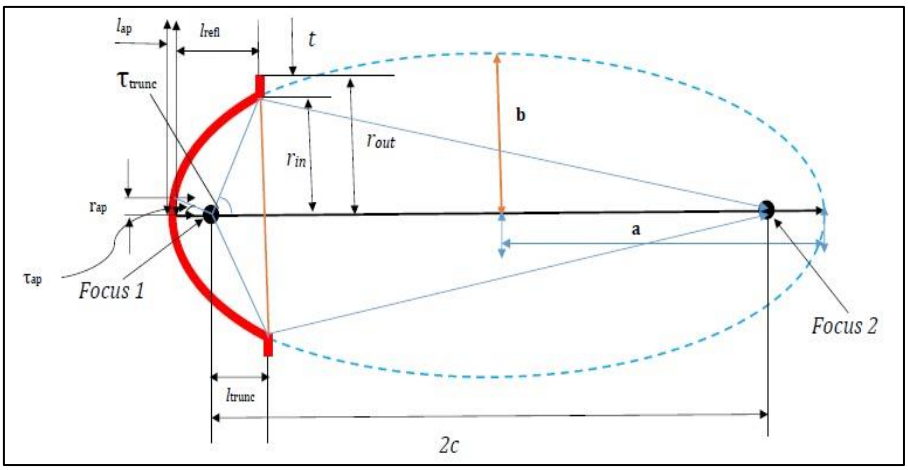

Fig. 2: Schematic of ellipsoidal solar reflector [4]

The equation for half distance between focus-1 and focus-2 can be written as Eq. (9);

$$c = \frac{d_{center}}{2} + \frac{1}{e^2-1}\left(\frac{d_{center}}{2}\left(1+e^2\right) - e\sqrt{d_{center}^{\ 2} + r_{in}^{\ 2}}\right) \tag{9}$$

And the truncation angle can be found from of Eq. (10);

$$t_{trunc} = \tan^{-1}\left(\frac{r_{in}}{l_{trunc}}\right) \tag{10}$$

1.2.3 Paraboloid reflector design

The parabolic reflector has been shown in Fig. 3(a) and (b). The parameters and the design criteria for the paraboloid reflector design are being presented below;

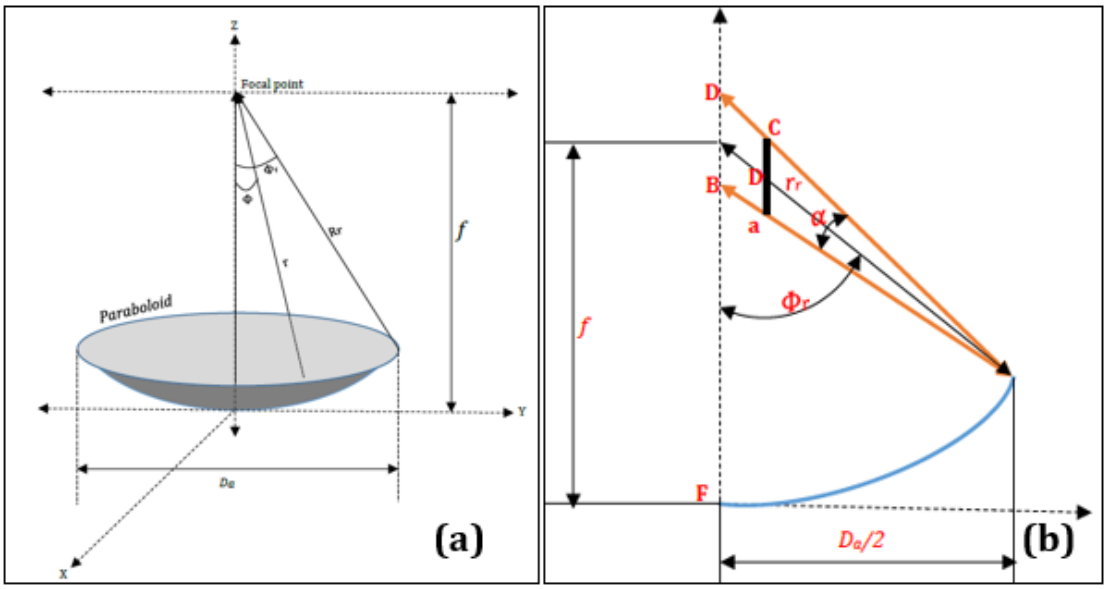

Fig. 3: The design parameters of the paraboloid dish [5]

The relation for the aperture diameter and the maximum angle to define it, can be given as Eq. (11);

$$\varnothing = 2arctg\frac{D_a}{4f} \tag{11}$$

The edge radius (r_r) or the maximum distance from the focal point to the extreme of paraboloid can be given as Eq. (12);

$$r_r = \frac{2f}{1+cos\varnothing} \tag{12}$$

The solar reflectors are designed on the basis of concentration ratio as in higher the concentration ratio, higher the temperature of the solar system will reach. The concentration ratio relation can be defined as the ratio of the area of aperture to the area of the receiver as given in Eq. (13);

$$C = \frac{A_a}{A_r} \tag{13}$$

and the area of aperture is given as in Eq. (14);

$$A_a = \frac{\pi D_a^{\,2}}{4} \tag{14}$$

1.2.4 Parabolic trough design

The parabolic trough as shown in Fig. 4 is a collector which has its cross-section in the shape of a parabola. Its section is symmetrical around its vertex.

Parabola trough possesses the focal lines and the focal points on the parabolic cross-section. The solar irradiation enters in the parabolic trough parallel to the vertically arranged optical plane, then it reflects from the surface to strike on the focal point [6].

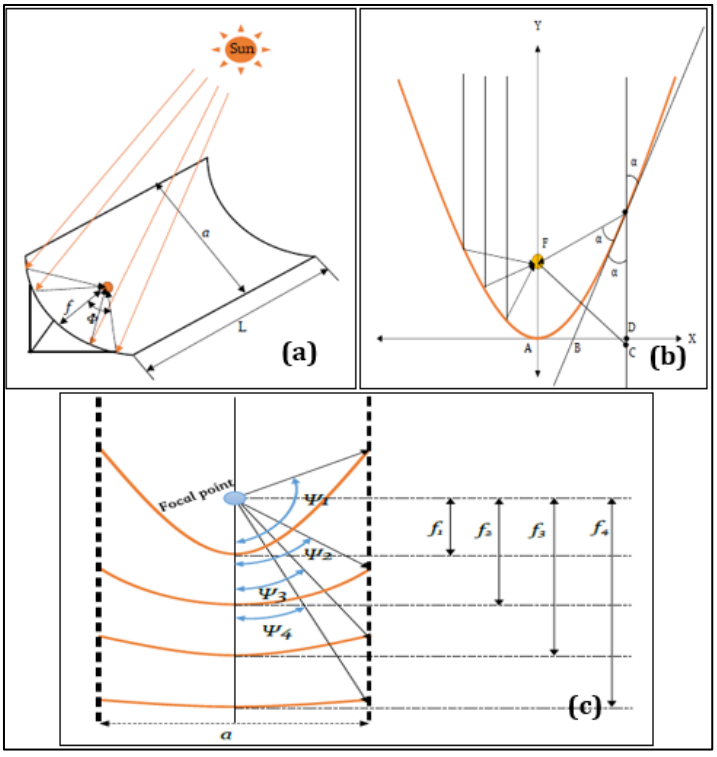

Fig. 4: (a) Geometrical parameter of parabolic trough; (b) Parallel rays path at parabolic mirror; (c) Focal length and rim angle relation [6]

The mathematical representation of parabola can be given as Eq. (15),

$$y = \frac{1}{4f} x^2 \tag{15}$$

Where *f* is focal distance, a distance between the focal point and the vertex.

The given Fig. 4(a) describes the geometrical parameters of a parabolic trough such as length, focal length, aperture width and rim angle. Fig. 4(b) shows the path of parallel rays striking on the parabolic mirror and then concentrating on the focal point. The radiation travels from the parallel plane to the optical plane and gets reflected to pass through the focal point. In Fig. 4(c), the relation between focal length and rim angle has been shown. The rim angle affects the concentration ratio and total absorbed radiation. The design characterization of the parabolic trough is based on basically four parameters: (i) rim angle, (ii) aperture width, (iii) focal length and (iv) trough length.

(i) ***Aperture width:*** It is the distance between one rim and another.

(ii) ***Rim angle:*** It is the angle between the line between the focal point and the mirror rim and the optical axis. The function of focal length to aperture width ratio is denoted by Ψ and can be expressed as Eq. (16):

$$\tan\Psi = \frac{a/f}{2 - \frac{1}{8}\left[\frac{a}{f}\right]^2} \tag{16}$$

also, the ratio of the focal length to the aperture width can be expressed as Eq. (17):

$$\frac{a}{f} = -\frac{4}{tan\Psi} + \sqrt{\frac{16}{tan^2\Psi} + 16} \tag{17}$$

The area of aperture (A_{ap}) is the result of the product of collector length and aperture width as given in Eq. (18);

$$A_{ap} = a * l \tag{18}$$

The surface area of the parabolic trough is calculated as Eq. (19),

$$A = \left[\frac{a}{2}\sqrt{1 + \frac{a^2}{16f^2}} + 2f * ln\left(\frac{a}{4f} + \sqrt{1 + \frac{a^2}{16f^2}}\right)\right] * l \tag{19}$$

1.3 Solar thermochemical two – step cerium oxide (CeO_2) water splitting cycle

The production of solar fuels from the solar thermochemical cycles is one of the most ambitious long-term goal of the researchers working in the renewable energy area. The direct splitting of water molecules by providing a huge amount of energy have been already investigated by many researchers around the world [7]. Nakamura investigated the direct dissociation of water molecules or solar thermolysis [8]. It was understood that the solar thermolysis poses a great problem of hydrogen and oxygen separation at extremely high-temperature. The direct solar thermal water splitting was investigated by Kogan [9]. This process is currently under development at WIS-Israel. In this process, the temperature of the solar reactor approaches up to 2500 K and the hydrogen gas is synthesized by the stream of superheated steam diffused through porous media. It was stated that even though the process seems technically feasible but the sintering process poses a great challenge.

Since, the direct splitting of the water molecules requires an extremely high operating temperature, it is required to develop other methods and processes for the easier production of solar fuels. The need of low reduction temperature to achieve high solar-to-fuel conversion efficiency is the need of the future. Therefore, the solar driven two-step water/CO_2 splitting thermochemical cycles have presented a great option. To this end, various metal oxide and redox pair thermochemical cycles have been tested for the feasibility and solar-to-fuel conversion efficiency on the laboratory scale [10]. The two-step metal-oxide thermochemical cycles involve a reduction and a re-oxidation step as given follows;

First step: Thermal reduction

$$M_xO_y \rightarrow M_xO_{y-1} + \frac{1}{2}O_2 \tag{20}$$

Second step: Re-oxidation step

$$M_xO_{y-1} + H_2O \rightarrow M_xO_y + H_2 \tag{21}$$

The two-step thermochemical cycles have been divided as volatile and non-volatile materials categories. The non-volatile materials based thermochemical cycles use the metal oxide which does not undergo the phase change process, meanwhile the

volatile materials based thermochemical cycles undergo the solid-to-gas phase transition. It has been established that the volatile materials produce higher amount of oxygen as compared to the non-volatile materials. However, the sintering phenomenon remains a great problem in the volatile materials based solar thermochemical reactors to this date.

The non-volatile metal oxide based solar thermochemical cycles have been further divided in to two types generally known as stoichiometric and non-stoichiometric cycles. The stoichiometric reactions undergo the reduction reaction and form solid solutions (Fe_3O_4(s)/FeO(s) and Fe_3O_4(s)). However, non-stoichiometric metal oxides persevere the crystallographically stability and the change occurs in the charge vacancies in the lattice (CeO_2/CeO_{2-x}). It was also seen that the doping mechanism radially affects the thermodynamics and chemical kinetics of the redox reaction and the overall performance of the solar thermochemical cycle. The cerium oxide doped zirconia results in the increased oxygen storage capacity [10]. The stoichiometric reactions have the superior oxygen storage capacity as compared to the non-stoichiometric reactions. However, the stoichiometric reactions tend to have sluggish reaction rate and deprived stability.

In the recent times, cerium oxide has considered as the most favorable redox pair material for two-step water splitting thermochemical cycle for hydrogen production. Cerium oxide based solar thermochemical cycle of the hydrogen production was first proposed in the year 2006 by S. Abanades [11]. The redox reactions of non-stoichiometric cerium oxide can be written as follows;

First step: Thermal reduction step

$$CeO_2 \rightarrow CeO_{2-x} + \frac{1}{2}O_2 \tag{22}$$

Second step: Re-oxidation step

$$CeO_{2-x} + xH_2O \rightarrow CeO_2 + xH_2 \tag{23}$$

The first step or the thermal reduction step of the redox cycle is endothermic which means that this step requires high heat supply which can raise the temperature

such as over 1600 K to carry out the reduction reaction. In this step, stoichiometric form of cerium oxide is thermally reduced to non-stoichiometric form of cerium oxide. In the second step, non-stoichiometric cerium oxide reacts with water and produces the hydrogen gas at the temperature close to 1200 K and a huge amount of energy is released [12]. Many studies have approved cerium oxide as one of the most promising material for the solar fuel production. Researchers around the globe have used ceria pellets, cerium oxide powder and reticulated cerium oxide structure to produce hydrogen and syngas [13-14]. Most of the studies have only been performed at only lab scale and they are currently being prepared for the pilot scale demonstration.

This thesis work has been structured into nine sections i.e. chapters.

In the section – 1, the background of the solar thermochemical cycles has been presented. In the section – 2, the literature review has been resented to identify the research gaps to carry out the research. In the section – 3, the solar thermochemical reactor has been analyzed from the optical and thermal aspects. In the section – 4, the chemical kinetics has been modelled in the high-temperature based solar thermochemical reactor to carry out the reduction reaction of cerium oxide to split the water and to production the hydrogen. In the section – 5, the discussion about the effects of inlet position and its orientations on the thermal performance of solar thermochemical reactor. In the section – 6, the thermodynamic analysis on the non-stoichiometric ceria was discussed and the efficiency analysis was performed. In the section – 7, the thermodynamic analysis on the cerium sulfate – cerium oxide was discussed and the efficiency analysis was performed. In the section – 8, the experimental and morphological characterization was carried out on the ceria stabilized zirconia. In the section – 9, the summary of the thesis has been presented and the conclusion have been drawn.

Chapter – 2

2 Literature review

Solar energy is a prominent and sustainable source of renewable energy used in household to industrial applications [15]. Solar technology is used to produce electricity using PV cells as well as used to generate heat using solar thermal collectors [16]. Concentrating solar systems use solar energy to generate heat at different temperature levels i.e. low, medium, or high [17]. Parabolic trough, solar tower, solar dish, and linear Fresnel reflector are the most promising solar technologies [18]. The application of these solar technologies is different according to their operating temperature range. Parabolic trough and linear Fresnel reflector are linear solar concentrators having an operating temperature of 500 °C. While the solar tower and dish systems have a very high concentration ratio and can operate at very high temperatures [19-20].

The wide range of applications of the solar tower in power generation and solar dishes in high temperature-based applications makes it the most promising renewable energy technology [21]. Solar dish systems are used to generate power used in cooling, heating, and chemical processes [22–26]. Reduction of fuel consumption using solar dish concentrator was studied by Wang et al. [27]. Meas and Bello-Ochende [28] investigated solar-powered gas turbines and concluded that the inter-cooling process is highly efficient as compared to reheating process.

A study carried out on absorption chiller integrated with solar dish collector for cooling and electricity production showed the maximum efficiency to be 27% [19]. The solar dish systems are designed to produce heat to be used in high-temperature-based applications. A solar dish system consists of a parabolic dish concentrator and a receiver. This dish system also has a tracking device that tracks the sun position to obtain proper reflection from parabolic dish to receiver [21]. Unlike the parabolic trough collector, there is no specific design for solar dish systems. Over the years many designs have been investigated numerically and experimentally. Thus, there are gaps in research in solar dish system design.

The concentrating solar thermal collectors (compound parabolic concentrator, parabolic trough collector, linear Fresnel reflector, and solar dish concentrator) with and without nanofluids were studied by Bellos and Tzivanidis [29]. The concentrating direct absorption in solar collector using nanofluids was investigated by Rasih et al. [30] and results showed that the nanofluids can improve the thermal efficiency of solar collectors. A numerical investigation was carried out to investigate the effects of Cu–H_2O nanofluid on parabolic-trough solar collector. The results showed that the Nusselt number (Nu) depends on the Cu nanoparticle concentration and the decrease in Reynolds number increases the heat transfer while the Cu concentration decreases [31]. Methods to increase the thermal efficiency of LFR with evacuated tube receiver were investigated and found that the maximum thermal efficiency increases by 1%. Additionally, it was seen that the fins are a better option to increase the thermal efficiency as compared to the nanofluids [32]. The thermal performance of the parabolic trough was enhanced using the conical strips and the results showed that the Nusselt number increased up to 91.95% and the thermal performance is at its best at Re=8000. Solar energy is available in abundance, inexhaustible, and has usage flexibility in household and in industries. The solar thermochemical process is based on the concept of conversion of solar energy into fuels (hydrogen and syngas) via. Water or carbon dioxide splitting process.

This is the period where the world is going through the energy and environmental crisis. At these times solar thermochemical hydrogen production provides with the alternative as well as an efficient option of clean and green fuel production [33-34]. The solar thermochemical processes are operational at a high-temperature. Therefore, the advancement of solar concentrated technology has been a matter of significant concern [35–38]. The design, development and the thermal performance of various types of solar thermochemical reactors have been thoroughly researched. The porous medium was also introduced to improve its thermal performance and obtain an uniform flux distribution in the reactive zone [39–42].

The non-stoichiometric ceria-based thermochemical cycles have been largely investigated [43-44]. The first ceria-based solar thermochemical reactor was used for hydrogen production in the year 2006. This study provided some valuable insights and

predicted that the ceria is the prime candidate for the hydrogen production cycles. Many studies have investigated the reduction capacity and fuel production capability of ceria. Researchers have focused to reduce the gap between the reduction and re-oxidation step of ceria based redox cycle to lower the required operational temperature

Researchers have carried out numerical studies to investigate the fluid flow and heat transfer characteristics of the solar thermochemical reactor. Most of the numerical studies have been performed on the volumetric porous media solar thermochemical reactor. A three-dimensional numerical study was performed by PitzPaal et al. [45] to understanding the solar incident radiation distribution and fluid flow effect. It was evident from the results that in a volumetric porous media reactor, the temperature distribution depends on the solar incident irradiation distribution inside the porous media. The investigation carried out by Alazmi and Vafai [46] indicated that the velocity field is rather strongly affected by the variances as compared to the temperature distribution. In another numerical investigation carried out by Wu et al. studied the flow field and pressure drop in the ceramic porous media and proposed a model to predict the pressure drop [47]. Wu et al. also studied the effects of thermal conductivity on the temperature in a solid phase [48-49].

A numerical model to simulate the fluid flow, heat, and species transfer and to solve the chemical reactions in a volumetric porous media reactor was developed by Villafán-Vidales et al. [50]. Wang et al. [51] also developed a numerical model to generate the heat flux distribution on the porous surface by incorporating the ANSYS Fluent solver and Monte Carlo Ray Tracing (MCRT) [52-53]. Researchers have also explored the axisymmetric numerical approach for the investigation of coupled heat transfer in porous media reactor [54-55]. Some other transport models have also been investigated to understand the thermal performance of the porous media reactor [56], [57]. In the model developed by Chen et al. [58], solar radiation was coupled with internal heat transfer to analyze the thermal performance of a porous media reactor. To investigate the solar thermochemical reactor numerically, CFD (computational fluid dynamics) presents itself as a tool to simulate the operating conditions [59]. One dimensional heat transfer model (steady and unsteady) was developed to investigate the thermal decomposition of ZnO at the operating temperature range of 1950–2400 K [60].

They also developed a cylindrical solar thermochemical reactor and studied the effects of inert gas flow [61].

The radiative properties of an indirectly irradiated solar reactor having a quartz glass window was studied by Yong et al. by using the MCRT method [62]. The geometrical effect of solar thermochemical reactor on temperature distribution including the heat loss was studied by Costandy et al. [63]. A multi-chamber porous media reactor was developed by Thomey et al. [64] for the sulphuric acid (H_2SO_4) decomposition. Konstandopoulos and Agrofiotis [65] developed 'Conti-reactor' model to tackle the intermittent problem in hydrogen production. Primarily, solar thermochemical cycles used metal oxides for the hydrogen production in two-steps metal oxide redox reactions. First step is reduction step (endothermic) in which metal oxide gets decomposed into metal and releases oxygen at high temperature. Second step is oxidation step (exothermic) in which metal oxide reacts with H_2O/CO_2 to produces H_2/CO as product. Further, hydrogen and syngas can be converted in to hydrocarbon fuels via. Fischer-Tropsch process. Since year 2006, Non-stoichiometric cerium oxide or ceria (CeO_2) has emerged as one of the best-suited redox material [66–69] for solar thermochemical cycle due to its high oxygen solid-state conductivity, fast redox kinetics [70] and crystallographic stability.

High-performance cork-templated ceria was used to produce hydrogen via a two-step H_2O splitting cycle. The study pointed out that the major challenge is to develop such materials which can withstand the extremely high temperature as well as ensure the high redox chemical kinetics and activity at relatively low temperatures. The study also revealed that cork-templated ceria enhances the performance significantly. The increasing reduction temperature by 50 ^{0}C results in the highest H_2 production rate (1.6 mL/min-g) [71]. Jia Zeng et al. [72] carried out a study on direct solar thermochemical conversion to produces hydrogen from methanol at low temperatures. The result of the study shows that the direct solar thermochemical conversion performance significantly increasing by using the nano-sized catalyst ($CuO/ZnO/Al_2O_3$). Ezbiri et al. [73] studied the redox performance of $Y_{0.5}Ba_{0.5}CoO_{3-\delta}$ in oxygen production and separation. It was pointed out that $Y_{0.5}Ba_{0.5}CoO_{3-\delta}$ has better performance than Cu_2O. Results of the study show that this compound has the fastest

reaction rate, highest O_2 exchange capacity, and lowest reaction temperature. Tou et al. [74] investigated the first-ever experimental demonstration of solar-based co-thermolysis of CO_2 and H_2O. Gaseous mixtures of CO_2/H_2O at molar ratios from 3:4 to 2:1 were passed through conducting non-stoichiometric ceria ($CeO_{2-\delta}$) membrane incorporated with 4200 suns solar concentrated radiation. Isothermal (1723-1873 K) and isobaric (0.2-1.7 Pa O_2) conditions were used to enhance the hydrogen production rate of 2.3 µmol/cm-min at 1873 K. Binlin Dou et al. [75] studied the issues and challenges in hydrogen production via thermochemical biomass conversion. The study pointed out that Ni-based catalysts are important for economically viable hydrogen production.

Shane Ardo et al. [76] presented a broad view on the implementation of solar-based hydrogen production technologies. It was pointed out that in the long run solar hydrogen technologies will have to compete against the fossil fuel market in various aspects and the main challenge will be to keep the fuel cost to a minimum. Marxer et al. [36] experimentally investigated the solar thermochemical-based CO_2 splitting into different streams of CO and O_2. This study was carried out using a 4 kW solar reactor consisting of an RPC catalyst structure under the exposer of 3000x flux irradiation. The result of the study showed the highest ever measured solar-to-fuel energy efficiency of 5.25%. Qibin Zhu and Yimin Xuan [77] numerically investigated the heat transfer and fluid flow characteristic in porous volumetric solar receivers. They studied the effects of porosity, incident angle and receiver absorptivity, reflection loss, and radiation propagation. Results show that the small incident angle increases the radiation propagation and also the pore diameter shows a strong impact on the pressure drop.

Shaner et al. [78] compared the techno-economic analysis of renewable solar-based hydrogen production. They pointed out that the electricity prices from CO_2-neutral nuclear and low-CO_2 fossil fuel with CCS technologies are lower than electricity prices from solar or wind systems. Further, the direct reduction of CO_2 into hydrocarbon fuel will require new and innovative ideas in transportation and storage. Herron et al. [79] presented the general framework to assess solar fuel technologies. They discussed the catalytic conversion and direct reduction of CO_2. Bork et al. [80] investigated the Perovskite $La_{0.6}Sr_{0.4}Cr_{1-x}Co_xO_{3-\delta}$ for solar thermochemical fuel

production. Results showed that the perovskite splits 25 times more CO_2 as compared to ceria. Scheff et al. [81] investigated the oxidation of a cobalt ferrite–zirconia composite. Results show that the second-order reaction and diffusion-limited mechanisms occur takes place simultaneously but at a different rate of oxidation. Furler et al. [82] investigated the H_2O and CO_2 splitting for syngas production using ceria. They directly exposed ceria felt to the concentrated radiation of 2865 suns. Result show the fuel production 5.88 ±0.43 mL/g CeO_2 in ten consecutive cycles. Roeb et al. [83] presented an overview in solar fuel technologies and trends. It was pointed out that the application of CSP technology as primary energy source can help in reducing the carbon foot print while increasing the electricity generation.

Over the years, researchers have thoroughly investigated the thermal performance and the geometrical influence of cavity receivers. Jilte et al. investigated the thermal performance of different shapes (conical, reverse conical, cylindrical, spherical, and hetro-conical) of cavity receivers and the results show that the conical cavity has minimum convective losses as compared to the other shapes [84–86]. A study on the volumetric receiver showed the loss of 12% of the input energy through convective and radiative losses from the aperture window of the solar reactor-receiver cavity [87]. The Monto Carlo Ray Tracing (MCRT) method was used to perform an optical analysis on the CSP system [88]. Li et al. [89] performed an investigation on parabolic dish systems and results showed that the optical efficiency is a function of focal length and aperture diameter [89]. Daabo et al. [90-91] carried out a study on three-receiver geometries using MCRT which showed that the solar flux value depends on the cavity geometry.

Another study by Daabo et al. investigated as well as compared the optical efficiencies of three cavity shapes (cylindrical, spherical, and conical) [90, 92–94]. It has been proved that cavity orientation has a significant effect on convective losses, radiative losses, and optical losses [95]. The surface and geometrical properties of the cavity such as height to diameter ratio, and wall absorptivity affect the dish system performance [96]. Barreto et al. [97] investigated the volumetric porous media-based receiver and results showed the effects of optical thickness of porous media and inclination angle. The aspect ratio, incident radiation, and system error also affect the

flux on the cavity receiver walls [98]. The study performed by W. Huang et al. [99] confirmed that the concentration ratio above 3000 can be achieved if the optical error kept less than 4 mrad. G. Xiao et al. [100] stated that the optimization of dish system can increase the intercept factor and concentration ratio from 0.66 to 0.9 and 500 to 1500, respectively. Garrido et al. [101] reported the analyses of a dish-Stirling system for four shapes of receiver cavities using MCRT method.

2.1 Research gaps

1. Ceria based thermochemical cycle for hydrogen/syngas production have not been thoroughly explored on lab scale.
2. Design and development of solar thermochemical reactor is in development phase.
3. Solar-to-fuel conversion efficiency improvement process is in initial stage.

2.2 Research objectives

1. Investigation of flux distribution in the solar cavity receiver for analyzing CeO_2-based reactions
2. Thermal characterization and Porosity analysis of Nano-structured ceria stabilized zirconia
3. Investigation on CeO_2-based solar cavity receiver with oxy-fuel radiant heat source
4. Performance evaluation of a CeO_2-based cavity reactor for hydrogen production

The tabulated summary of literature review has been given below:

Ref	Year	Parameters	Main findings
[15]	2019	Dish dia. = 7.5m	• MCRT method was used to predict the Stirling engine performance. • Global conversion efficiency varies from 19% to 26%
[16]	2019	Max. temp. = 600 ^{0}C	• Optical efficiency = 64% and thermal efficiency = 52% at 600 °C was reported.
[18]	2009	Cavity shapes	• Heat loss minimization can be effectively achieved through aspect ratio, cavity opening ratio, and tilt angle. • Apart from the radiation losses, all other heat losses are negligible due to high operating temperature.

[20]	2017	Comparison of tools: Tonatiuh, SolTrace, TracePro and CRS4-2.	• SolTrace can be a suitable tool for the simulation of small scale CRS plants • Tonatiuh or CRS4-2 are best suited for large scale plant simulations
[21]	2016	Solar dish design	• The optimal system performance is strongly dependent on the rim angle, diameter of the receiver, and the concentration ratio of the dish • Net conversion efficiency of solar dish was reported to be more than 30%
[22]	2016	Cost analysis of small scale CSP design	• 27.3% and 40.4% potential cost savings can be achieved if the production rate is increased to 104 and 106 units/year
[23]	2017	hybrid solid oxide fuel cell and solar parabolic dish	• Electrical efficiency = 48.73 % and overall thermal efficiency = 79.49 % • Optimum solar fraction = 0.242
[24]	2018	Thermal power = 21030 kW	• The overall exergy efficiency = 66.05%, net overall thermal efficiency = 80.70%
[25]	2018	CO_2 emission reduction	• 39.40 million tons of coal equivalent and 98.22 million tons of CO_2 emission can be reduced in china with SHIP
[26]	2018	Solar dish dia. = 4.4 m Aperture dia. = 60 mm	• Peak solar concentration ratio = 5010 suns • Average concentration ratio = 2710 suns
[28]	2017	Entropy generation minimization	• Geometric constraints essential to keep the receiver shape. • Design flexibility is greater for rectangular section absorber tubes than for absorber tubes of circular section
[31]	2020	Cu–water nanofluid Re = 10^4, 10^5 & 10^6	• Increase in DNI from 900 to 1100 W/m2 leads to increase in Nu by 8.6%, 9.78% and 11.43% which in turn is responsible for the increase in thermal efficiency by 3.87%, 3.82% and 2.04%, respectively.
[32]	2018	primary reflectors area = 27 m^2 Working fluid = Syltherm 800 Operating temp. = 650 K	• Thermal efficiency improvement with 4% nanofluid and finned absorber = 0.82% • With finned absorber and pure oil = 0.61% • With 4% nanofluid and smooth absorber = 0.28%
[36]	2017	Solar reactor = 4 kW_{th}	• Solar-to-fuel energy efficiency = 5.25%

[37]	2010	Total power = 40 MW_{th}	• A hybrid natural gas/solar plant design can reduce H_2 production cost to 5.8 ¢/kW-h
[39]	2011	LTNE model	• Nu number is affected by : (i) fluid conduction, (ii) heat exchange in porous medium, (iii) channeling effect
[47]	2010	mean cell size = 1.35 to 1.55 mm, porosity = 0.55 to 0.85	• The penetrability properties of ceramic foams increase with increase in porosity.
[48]	2010	LTNE model with P1 approximation Pore size = 0.5–3 mm	• Temperature distribution is dependent on the material properties as well as the working conditions.
[49]	2010	Mean cell dia. = 4 mm Tetrakaidecahedral model	• Heat transfer coefficient increases with the Reynolds number and decreases with the mean cell
[50]	2011	Solar reactor = 1 kW_{th} Mean concentration ratio = 1040 suns	• Maximum temp. of the foam reached upto 1400 K • Incident solar power of 500-700 W is essential to reach reaction temperatures of about 1200K
[54]	2015	$NiFe_2O_4$	• Temperature is strongly affected by the absorption factor • Aperture velocity and reactant diameter were found to have inverse effects on the reaction extent of $NiFe_2O_4$
[55]	2012	MCRT with FVM	• The effects of optical properties are essential to determine the porosity • Geometric concentration ratio increases with the increasing first concentrator diameter.
[56]	2014	LTNE with MCRT Rosseland approximation and modified P1 approximation	• The maximum temperature difference between the modified P1 approximation and Rosseland approximation is 4.97%. • The maximum solid phase and fluid phase temperature for the modified P1 approximation condition is higher than that for the Rosseland approximation condition.
[57]	2014	Feeding gas = CH_4/H_2O mixture	• Momentum source term has significant impact on pressure drop as well as on pressure distribution.

			• Radiation heat transfer cannot be omitted during thermal performance analysis.
[58]	2016	LTNE model with P1 approximation	• The deviations of inlet solid and outlet air temperatures are up to 76.4% and 13.2%, respectively
[62]	2011	MCRT	• The decreased efficiency of the reactor is caused by the re-radiation losses.
[63]	2012	Reactor design	• Losses from spherical cavity = 22% and cylindrical cavity = 32% • Hydrogen production amount fluctuates from 1.27 g/s to 8.95 g/s for spherical cavity, and 0.94 g/s to 8.94 g/s for cylindrical cavity.
[72]	2020	$CuO/ZnO/Al_2O_3$ nanocatalyst	• The catalyst particles at nanoscale have higher temperature intensification rate and enhanced catalytic performance than the particles at macroscale

Chapter – 3

3 Optical and thermal analysis of solar thermochemical reactor

3.1 Introduction

Solar energy is converted into thermal energy and in turn into electrical energy using concentrated solar power systems (CSP) [102-103]. A Concentrated Solar Power system can be classified into 4 types known as the solar tower, parabolic trough, linear Fresnel, and parabolic dish. The conversion of solar energy occurs in the receiver. Some high-temperature based systems use concentrated solar energy which requires the capture of a huge amount of solar irradiation. Thus, these systems require the combination of heliostat field and parabolic dish. Heliostat field tracks the sun position and captures the solar irradiation which is directed towards the parabolic dish. When solar irradiation falls onto parabolic dish, it gets concentrated and directed into the solar thermochemical reactor-receiver cavity aperture. The parabolic dish system delivers higher concentration ratios for high temperature based solar thermochemical cycles [104]. The chemical reactions to yield hydrogen take place in the solar reactor-receiver cavity thus its design becomes crucial to limit the thermal and optical losses to attain maximum temperature at given thermal heat flux.

Many studies have been carried out to investigate the thermal performance of cavity receivers of different shapes and sizes. Jilte et al. carried out studies on different shapes (conical, reverse conical, cylindrical, spherical, and hetro-conical) of cavity receivers and compared their thermal performance [84–86]. The results of their study revealed that the conical cavity has the lowest thermal (convective) losses among all other cavity shapes. The tabular cylindrical shaped cavity receiver was also analyzed for understanding the effects of operational and structural parameters on thermal performance [105]. A review on the volumetric receiver revealed that 12% of the input energy is lost as convective and radiative losses at the aperture window of the solar reactor-receiver cavity [87].

The optical analysis for the CSP system is performed using the Monto Carlo Ray Tracing (MCRT) method [88]. A study carried out by Li et al. proved that for a parabolic dish system, optical efficiency is a function of focal length and aperture diameter [89]. Daabo et al. performed an investigation on three-receiver geometries using MCRT and results showed that the value of solar flux depends on the type of cavity geometry [90-91]. Daabo et al. carried out another study to investigate and compare the optical efficiencies of three cavity shapes (cylindrical, spherical, and conical) [90, 92–94]. It has been proven that the orientation of the cavity receiver affects the heat losses and these heat losses can be in terms of convective losses, radiative losses, and optical losses [95]. The surface and geometrical properties such as height ratio, diameter ratio, and wall absorptivity affect the dish system performance [96]. A study carried out by Barreto et al. [97] on porous media based volumetric receiver showed that the effects of optical thickness of porous media and inclination angle. The flux on the cavity receiver walls is affected by the aspect ratio, incident radiation, and system error [98]. W. Huang et al. proved that if the optical error is kept below 4 mrad, in that case, the concentration ratio above 3000 can be achieved [99]. A study carried out by G. Xiao et al. pointed out that by optimization of dish system, the intercept factor and concentration ratio can be increased from 0.66 to 0.9 and 500 to 1500, respectively [100]. J. Garrido et al. [101] reported the analyses of a dish-Stirling system for four shapes of receiver cavities using MCRT method.

3.2 Mathematical modelling

The governing equations used in the present simulations are given as follows [106-107];

[i] Continuity equation

$$\frac{\partial \rho}{\partial t} + \nabla.\left(\rho \vec{v}\right) = 0 \tag{24}$$

Where ρ is fluid density and $\vec{v}$ is superficial fluid velocity.

[ii] Momentum equation

The momentum conservation equation in the porous media based STCR is solved as

$$\frac{\partial}{\partial t}\left(\rho \overset{\mathrm{r}}{v}\right)+\nabla.\left(\rho \overset{\mathrm{rr}}{vv}\right)=-\nabla p+\nabla.\left(\mu \nabla \overset{\mathrm{r}}{v}\right)+S_p \tag{25}$$

In the above given Eq. (25), the Sp is denotes the fluid pressure drop source term and P and μ designates the fluid pressure drop and dynamic viscosity, respectively. The pressure drop source term is calculated as [48];

$$S_p=-\left(\frac{1039-1002\phi}{{d_s}^2}\right)\mu u-\left(\frac{0.5138\phi^{-5.739}}{{d_s}^2}\right)\rho_f u^2;\quad 0.66\le\phi\le 0.93 \tag{26}$$

In the above given Eq. (26), ϕ and d_s denote material porosity and mean cell size, respectively. The flow is given at fluid inlet in the porous media, the gradient is set 0 at the fluid outlet.

Inlet: $u = u_0$, $v = 0$

Outlet: $\frac{\partial u}{\partial x}=\frac{\partial u}{\partial y}=\frac{\partial v}{\partial x}=\frac{\partial v}{\partial y}=0$

[iii] Energy equation

$$\frac{\partial}{\partial t}(\rho h-p)+\nabla.\left[\overset{\mathrm{r}}{v}(\rho h)\right]=\nabla.(\lambda_{eff,f}\nabla T)+S_h \tag{27}$$

In the above equation, S_h is known as the source term which allows the convective heat transfer between solid and fluid phase.

$$S_h=h_v(T_s-T_f) \tag{28}$$

where h_v (W/m^3k) is known as volumetric convection heat transfer coefficient and it can be calculated using the correlation given by Wu et al. [48]

$$h_v=\frac{\lambda_f\left(32.504\phi^{0.38}-109.94\phi^{1.38}+166.65\phi^{2.38}-86.98\phi^{3.38}\right)\mathrm{Re}^{0.438}}{{d_s}^2};\quad \left(0.66\le\phi\le 0.93\ and\ 70\le\mathrm{Re}\le 800\right) \tag{29}$$

For solid zones, the Eq. (27) becomes,

$$\frac{\partial}{\partial t}(\rho h)=\nabla.(\lambda_{eff,s}\nabla T)+S_s \tag{30}$$

$\lambda_{eff,f}$ and $\lambda_{eff,s}$ denote the effective thermal conductivity of the fluid and solid phase, respectively and Ss known as volumetric heat source term. These entities can be calculated using the following given correlations [108];

$$\lambda_{eff,f} = \phi\lambda_f \tag{31}$$

$$\lambda_{eff,s} = \lambda_s(1-\phi) \tag{32}$$

The source term includes the radiative (S_{rad}), convective ($S_{conv,s}$) as well as heat dissipation (S_w).

$$S_s = S_{conv,s} + S_{rad} + S_w \tag{33}$$

Convective heat transfer source term

The convective heat transfer source term calculates the heat transfer between solid and fluid phase.

$$S_{conv,s} = -S_{conv,f} = -h_v(T_s - T_f) \tag{34}$$

Wall heat dissipation source term

Solar thermochemical reactor operates at high temperature thus the heat dissipation consideration becomes crucial and it can be calculated by following equation,

$$S_w = -\varepsilon_w\sigma(T_s^4 - T_0^4) \tag{35}$$

[iv] Discrete Ordinates irradiative transfer model

The energy and radiative transfer equation for fluid flow through the porous media can be written as follow [109];

Fluid energy equation

$$-\varphi\rho_f u_f c_f \frac{\partial T_f}{\partial x} - (1-\varphi)hA(T_f - T_s) + \varphi Q(y)\delta(x) + \varphi k_f\left(\frac{\partial^2 T_f}{\partial x^2} + \frac{\partial^2 T_f}{\partial y^2}\right) = 0 \tag{36}$$

Solid energy equation

$$\nabla.q + (1-\varphi)hA(T_s - T_f) - (1-\varphi)k_s\left(\frac{\partial^2 T_s}{\partial x^2} + \frac{\partial^2 T_s}{\partial y^2}\right) = 0 \tag{37}$$

In the above given equations, h is the heat transfer coefficient and A is the surface area of the porous medium. The thermal conduction via. gas can be easily neglected due to the poor thermal conductivity of the inert gas.

[v] Radiation transport equation

$$\frac{dI_\lambda(\vec{r},\vec{s})}{ds} + (k_\lambda + \sigma_\lambda)I_\lambda(\vec{r},\vec{s}) = \varepsilon_\lambda I_{b,\lambda} + \frac{\sigma_\lambda}{4\pi}\int_0^{4\pi} I_\lambda(\vec{r},\vec{s}')\phi_\lambda(\vec{s}\to\vec{s}')d\Omega' \tag{38}$$

The radiative transfer equation is solved in the wavelength of 0 to 1.5 μm and 1.5 to ∞ μm.

The radiative heat flux (q) in the solid region of porous media can be calculated by the following equation;

$$q = \int_{4\pi} I(r,\hat{s})\hat{s}d\Omega \tag{39}$$

In the discrete ordinates (DO) radiation model, the radiative transfer equation (RTE) is solved for a finite number of discrete solid angles. Each angle is in association with the directional vector ($\vec{s}$). The number of transport equations solved by the DO model is equal to the directions ($\vec{s}$). The RTE equation considered in the DO model for an absorbing, emitting, and scattering medium at position $\vec{r}$ in the direction $\vec{s}$ is given in Eq. (38).

Table 1: Thermophysical properties of RPC-CeO_2

Material	Property	Expression /value	T (K)
RPC-CeO_2	Density (kg/m^3)	7220	298
	Specific heat (J/kg-K)	$-(0.0001271)\times T^2 + (0.2697656)\times T + 299.8695684$	280-1100
		444.27	>1100
	Thermal conductivity (W/m-K)	$-(1.7234232)\times10^{-9}\times T^3 + (1.1203174)\times10^{-5}\times T^2 - (0.024019964)\times T + 17.800409$	280-2000
	Absorption coefficient (m^{-1})	$(1-(-6\times10^{-5}\times T + 0.411))\times497.8$	300-2500
	Scattering coefficient (m^{-1})	$(-6\times10^{-5}\times T + 0.411)\times497.8$	300-2500
Quartz glass	Density (kg/m^3)	2500	298
	Specific heat (Jkg^{-1}-K^{-1})	$-0.0001\times T^2 + 0.1791\times T - 0.173$	273–847
		$0.0072\times T + 61.717$	847–2000
	Thermal Conductivity (Wm^{-1} -K^{-1})	$1.18 + (3.14)\times10^{-3}\times T + 17966/T^2$	273–2000

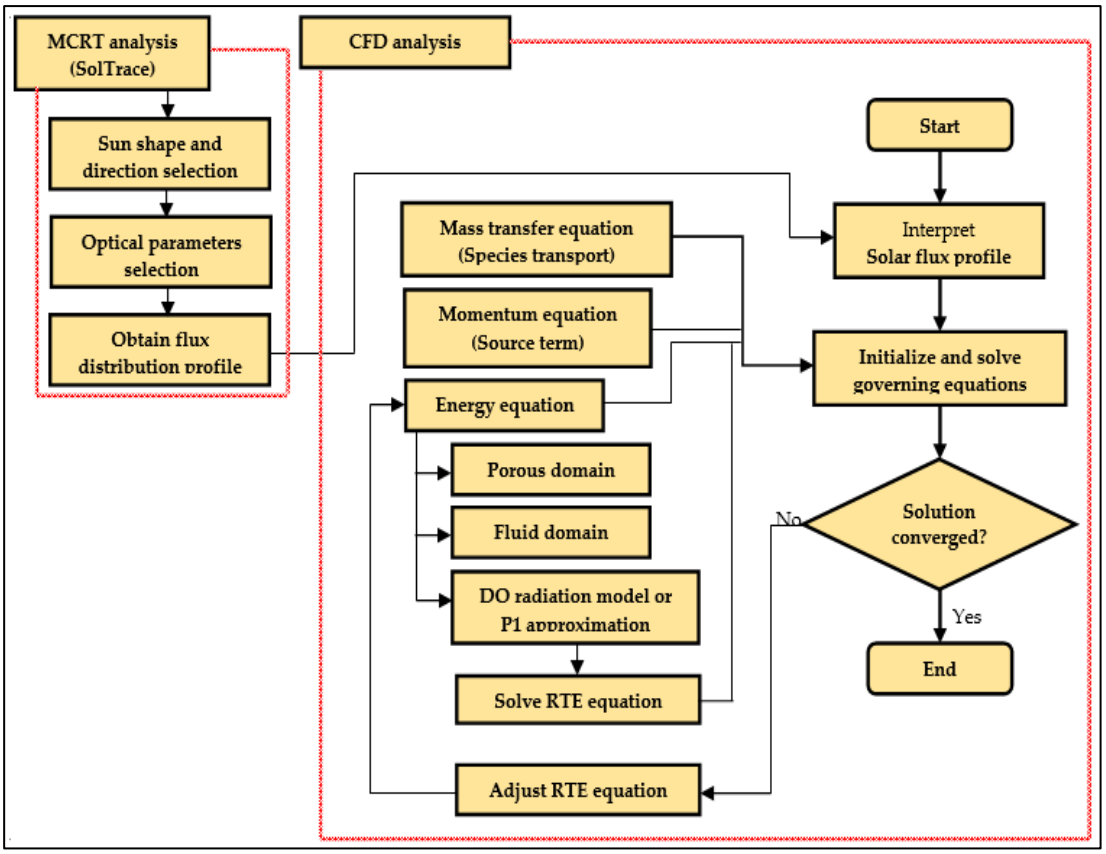

Fig. 5: Solution algorithm to obtain solar flux and temperature distribution in STCR cavity

The optical – thermal aspect of the solar thermochemical reactor was explored using the solution algorithm give in Fig. 5. In the first part of the solution, the Monte Carlo Ray Tracing (MCRT) technique was executed using the SolTrace software. The ray tracing allows the generation of solar flux profile at the cavity aperture. In the second part of the study, the obtained solar flux profile is used as the Gaussian distribution solar flux profile subjected at the quartz glass window to obtain the temperature distribution at the STCR cavity walls.

3.3 Solar flux-temperature distribution in the RPC based STCR cavity - A SolTrace-CFD approach

3.3.1 Motivation and objective

After the careful analysis of available literature on the optical analysis of solar thermochemical reactor cavities, it was found that there are some research gaps in the field of optical *vis-à-vis* thermal analysis of indirectly irradiated solar thermochemical cavities. The main three objectives of this study are given below:

1. The optical analysis of STCR and understanding the effects on flux distribution caused by the shift in focal point from cavity aperture to 20 mm inside the cavity using MCRT method.
2. To study the effect of slope error and its direct influence on flux magnitude and profile.
3. Integration of 2-D computational fluid dynamics (CFD) numerical simulation to generate the temperature distribution inside the STCR using the flux profile obtained from the SolTrace.

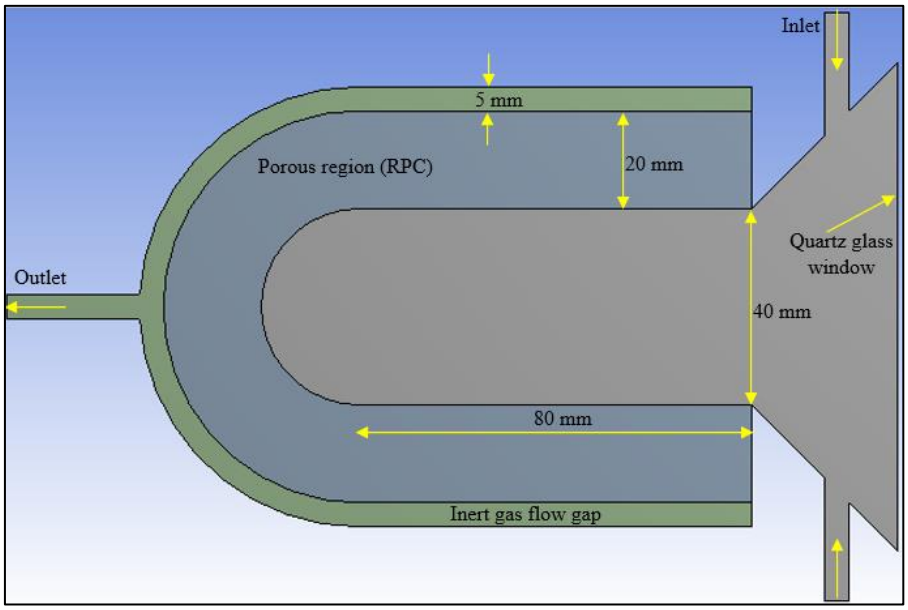

Fig. 6: STCR cavity configuration

3.3.2 Conceptual design of the solar thermochemical reactor

In this analysis, a solar thermochemical reactor cavity is designed for the geometrical and optical analysis as shown in Fig. 6. The solar thermochemical reactor cavity has a quartz glass window for incoming solar flux. The RPC catalyst thickness is kept 20 mm with 5 mm gas flow gap. To carry out this analysis the study has divided into two cases. In case-1, the focal point is kept at the cavity aperture, and in case-2 the focal point is kept 20 mm inside the reactor cavity as shown in Fig. 7. For both cases, the slope error is varied from 2 mrad to 4 mrad to obtain the flux profile using SolTrace. This flux profile is used to obtain the flux and temperature distribution on the reactor cavity walls using the CFD software Fluent 16.0. The DO radiation model is used for numerical analysis. Table 1 contains the Thermophysical properties of RPC.

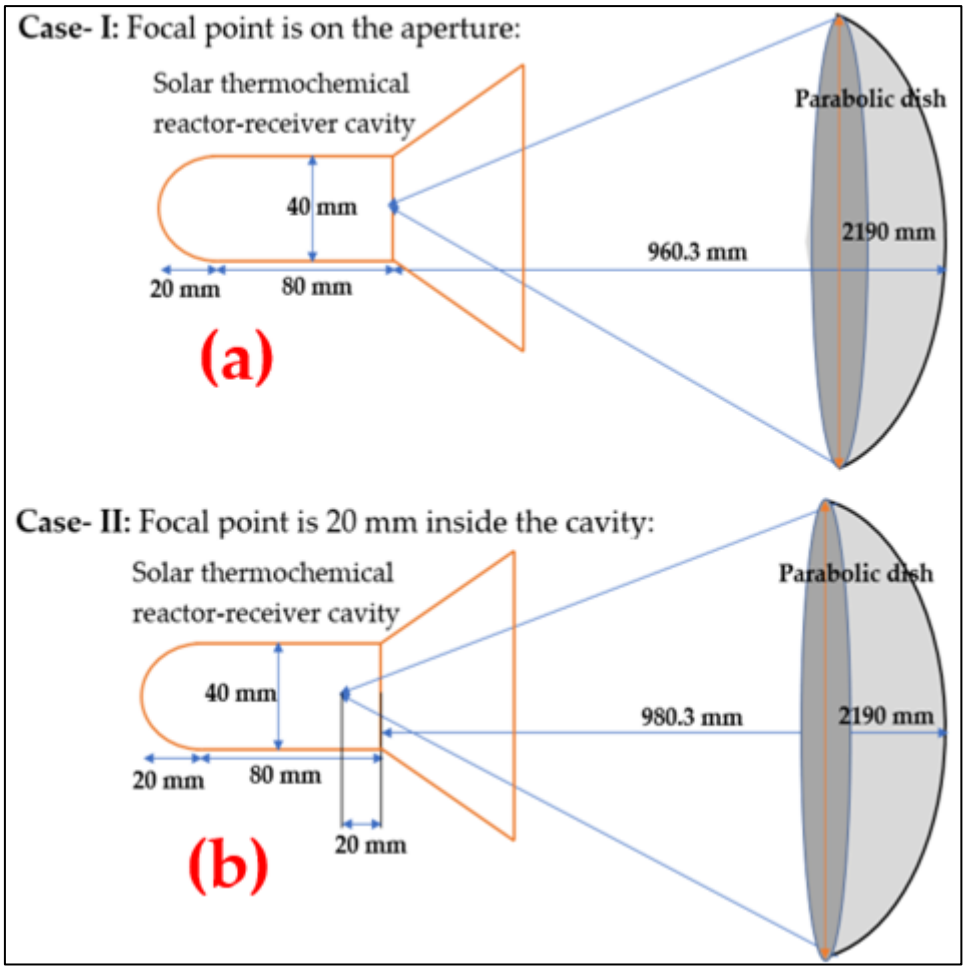

Fig. 7: Optical modelling schematic of STCR cavity and parabolic dish arrangement with two cases; (a) case – 1: focal point is at x = 0 and case – 2: (b) focal point is at x = -20 mm

The results of the present study have been validated against the results of the MCRT code from a study carried out by Hyunjin Lee [110]. The parameters considered for the result validation are as follows;

The focal length (f) = 5 m

Rim angle (Ø) = 45^0

Slope error = 2 mrad

3.3.3 SolTrace modelling and results validation

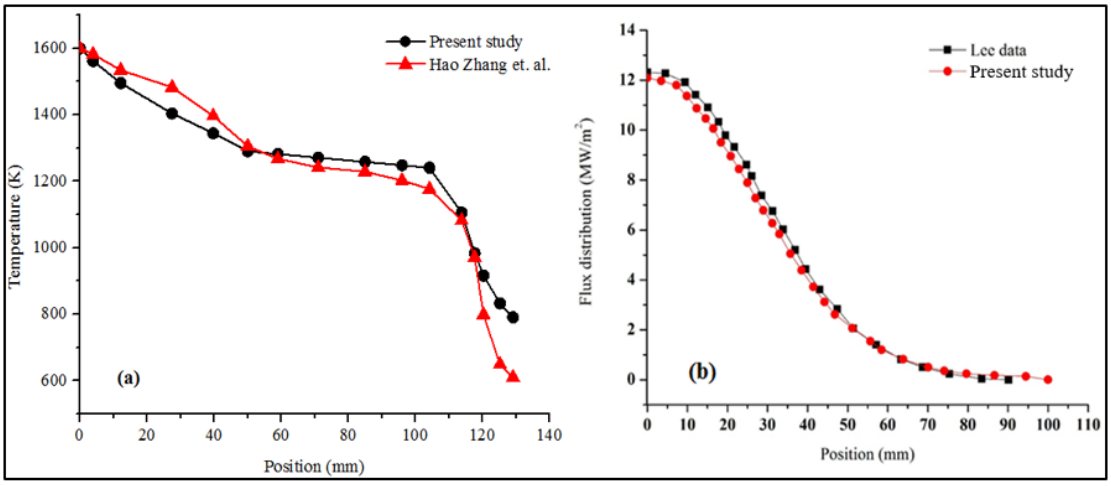

Fig. 8: (a) Fluid phase temperature validation against Zhang et al. [111] and (b) Flux distribution comparison for SolTrace validation with Lee's study [110]

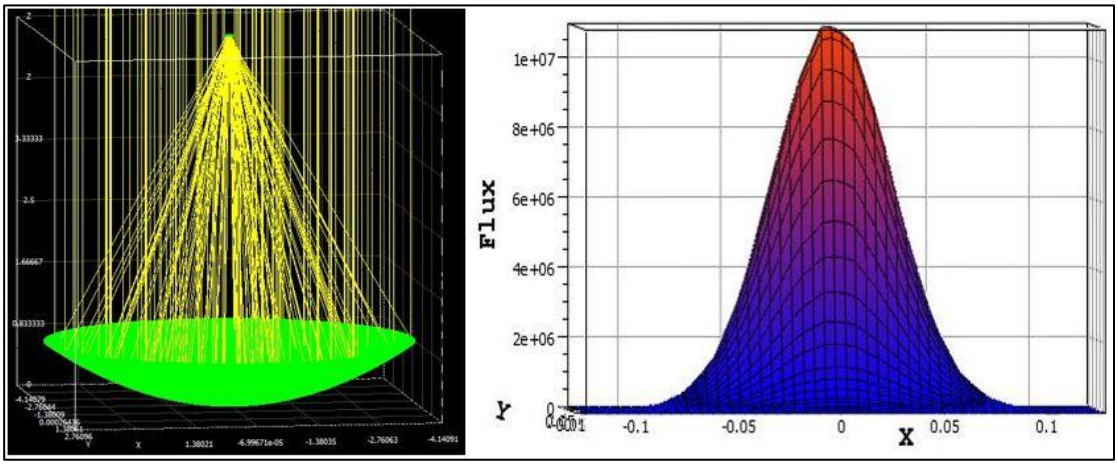

Fig. 9: (a) The SolTrace modelling of parabolic dish and the target receiver, (b) The solar flux profile generated by the SolTrace

In SolTrace, a parabolic concentrator of 8.284 m diameter was formulated in the first stage and a target having the diameter of 40 mm was formulated in the second stage. The fluid phase temperature along the centerline of the STCR cavity has been validated against Zhang et al. and solar flux distribution at the focal plane is compared and the results are plotted against Lee's data as shown in Fig. 8(a) and (b), respectively. The comparison reported that the results are in very good agreement with the referenced study. It was also seen that the obtained results are a good match with other studies reported in the literature. The results of the present study can be validated against some other studies such as [105, 112–114]. A grid independence analysis performed to obtain accurate and precise results. The grid independence analysis was carried out by using

the tetrahedral element type. The residual values were adopted to be $1x10^{-6}$ for all the simulations as solution convergence criteria. The parameters for the grid independence analysis has been mentioned in Table 2. The solar flux distribution profile has been shown in Fig. 710 (a) and the grid independence plot has been presented in Fig. 710 (b).

Table 2: Grid independence analysis parameters

Grid Independence Analysis		
Wall Temp. (K)	**Element Size (mm)**	**Number of Elements (10x-04)**
2083.61	2	0.18
2081.35	1.5	0.34
2078.51	1	0.76
2076.96	0.8	1.15
2075.53	0.6	2.06
2074.74	0.5	3
2073.91	0.4	4.6
2073.04	0.3	8.3
2072.99	0.2	18.51

3.3.4 Results and discussion

3.3.4.1 Sensitivity flux distribution in the reactor cavity walls

The design of the solar thermochemical reactor cavity for optical analysis has been shown in Fig. 7. The reactor cavity has a quartz glass window for solar irradiation to come in and porous or catalyst region loaded of RPC where redox reactions take place. The reactor cavity design is a combination of cylindrical and hemispherical shape to improve the radiation distribution and achieve a uniform and maximum temperature to carry out the chemical reactions. The cylindrical part is 80 mm long and hemispherical part has a radius of 20 mm. the porous media designed to have a thickness of 20 mm with 5 mm additional gas flow gap. Thus, the total length of the reactor cavity is 135 mm. the main focus of the analysis is kept on the geometric influence of the focal length variation. The optical analysis on the solar thermochemical reactor cavity is performed using the SolTrace software and focus is kept on the convergence criteria. It can be seen from Fig. 10 (a) that in case-1, when the slope error is 4 mrad, the flux value is higher than case-2 for both slope errors.

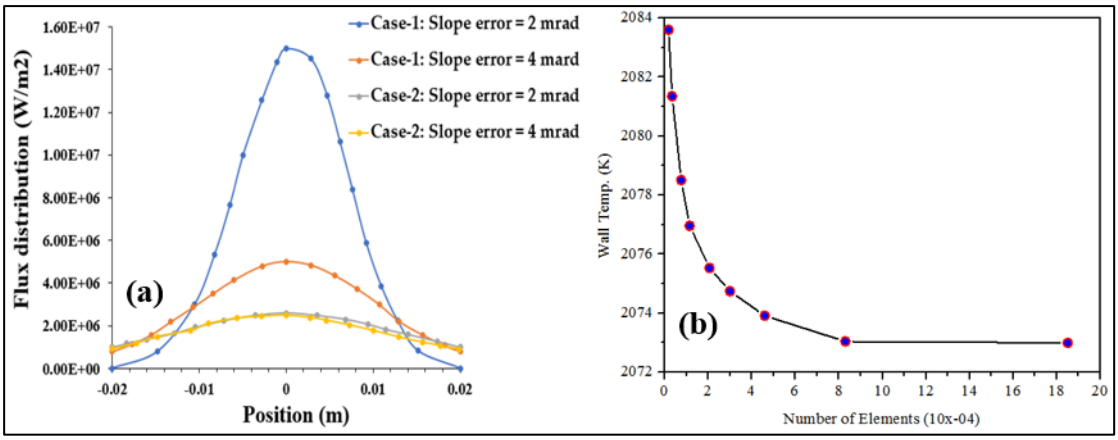

Fig. 10: (a) Flux distribution for case-1 and case-2; (b) Grid independence analysis

3.3.4.2 Radial temperature distribution in the porous media

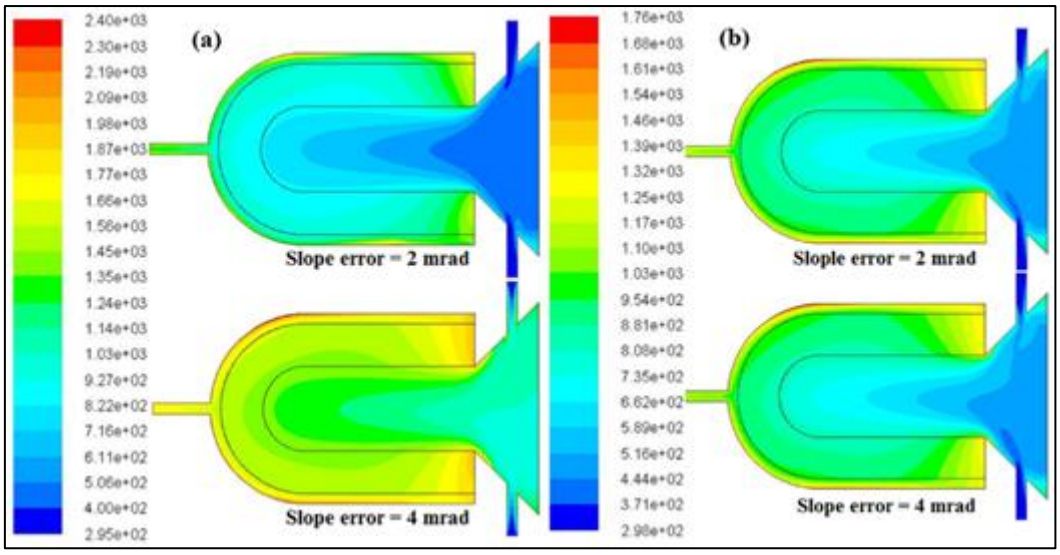

Fig. 11: Temperature contours for slope error 2 mrad and 4 mrad for each case; (a) Case-1: When the focal point is on the cavity aperture, (b) Case-2: When the focal point is 20 mm inside the cavity

To attain the uniform temperature distribution inside the reactor cavity is the main point of concern. Fig. 11(a) and (b) show the temperature contours for case-1 and case-2. In Fig. 11(a), it can be seen that the temperature distribution inside the solar thermochemical reactor cavity for slope error 4 mrad is comparatively more uniform and higher as compared to the slope error 2 mrad. Even though the 2 mrad slope error in case-1 yields the higher value of flux as compared to 4 mrad slope error yet the temperature in the reactor doesn't reach as high as for 4 mrad slope error. This particular phenomenon occurs because the focal point of the dish in case-1 is located at the cavity aperture but the flux doesn't quite get distributed and cover the cavity walls enough to

generate the higher temperature. However, in the case of 4 mrad error, the flux profile allows the flux to reach inside the cavity and get uniformly distributed on the cavity wall so the cavity generates higher temperatures than 2 mrad slope error flux profile as can be seen in Fig. 11(b).

The temperature distribution in the radial direction in porous media is an important factor as it provides information regarding the optimum catalyst (RPC) thickness. As it can be observed in Fig. 12(a), for case-1, the temperature distribution along the radial direction in porous media is much higher for slope error 2 mrad as compared to the 4 mrad slope error. This happens because of the same reason as described above that the 4 mrad slope error generates a uniform flux which allows the temperature to reach a higher value. However, it doesn't happen in case-2 because the flux profile obtained from both slope errors (2 and 4 mrad) is much alike in shape and uniformly distributed as can be seen in Fig. 12(b). Hence, 2 mrad slope error flux yields a higher value as compared to the 4 mrad slope error. Thus, the 2 mrad flux profile yields a higher temperature in the radial direction in porous media.

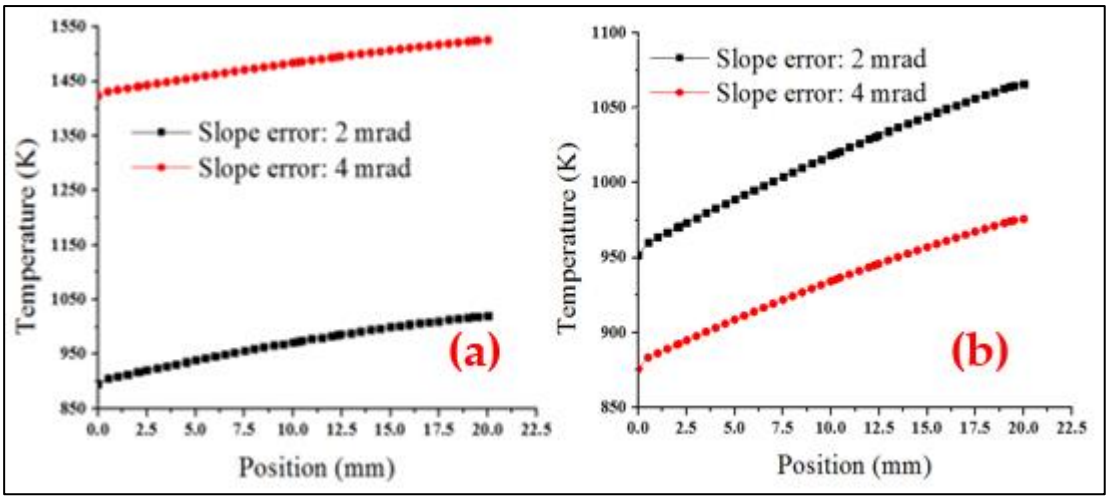

Fig. 12: Temperature distribution in the porous media for (a) Case-1; (b) Case-2

3.3.4.3 Temperature distribution in the axial direction in the porous media

Another important parameter of reactor cavity design analysis is the length of the porous medium thus it becomes necessary to analyze the temperature distribution along the axial direction in the porous media. Since the cylindrical part of the cavity has a length of 80 mm. Thus, the temperature distribution in the axial direction is evaluated for this portion only and the dome part of the cavity is covered in the full

reactor temperature analysis along the centerline. It can be observed in Fig. 13(a) that at (x=0) cavity aperture, the temperature is considerably high and it drop from x=0 to x=80 mm. The slope error 4 mrad for case-1 yields the highest temperature and from x=50 mm to x= 80 mm and it doesn't show any further drop in temperature and the temperature of porous media remains above 1500 K from x=50 to x=80. Thus, it gives the uniformly distributed temperature along the axial direction in porous media. Even though case-2 with slope errors 2 and 4 mrad show the temperature difference about 180 K at x=0 but this temperature difference gets reduced at x=50 and also temperature doesn't drop further and stabilizes and keeps the porous media above 900 K. Considering all the above scenarios, case-1 with 4 mrad flux profile becomes the obvious and most suitable choice for achieving the high and uniformly distributed temperature for carrying out redox reactions. To analyze the optimum temperature to carry out a redox reaction, it is necessary to evaluate the reactor temperature. Fig. 13(b) shows the temperature distribution in the reactor cavity along the centerline. It can be seen in the plot that the case-1 with slope error 4 mrad yields the highest reactor temperature. At x=0 (cavity aperture), the temperature is at over 1000 K and it goes up to 1500 K at x=125 mm. Case-2 with 2 mrad and 4 mrad slope error yield the temperature up to 1000 K however, the temperature at cavity aperture temperature remains at little above 500 K.

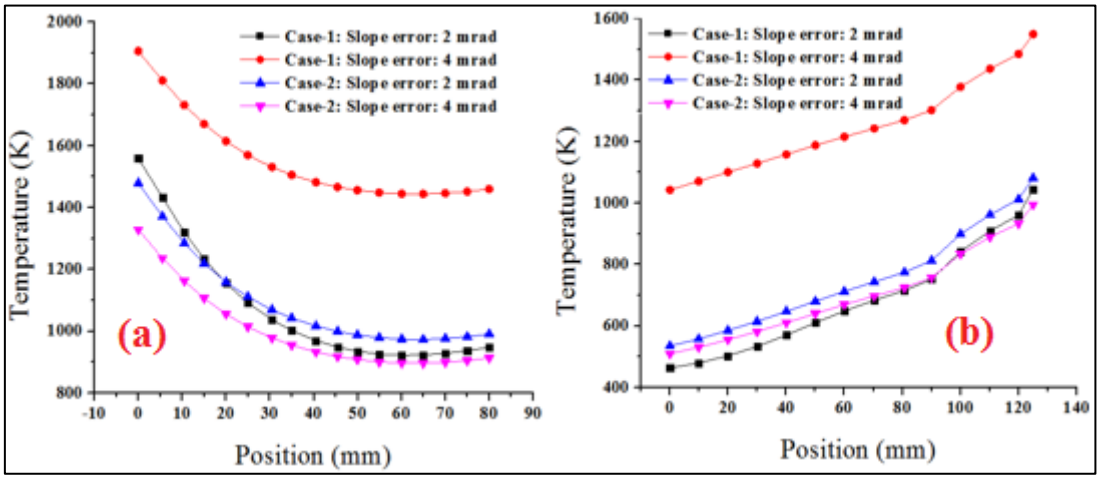

Fig. 13: Temperature distribution along the (a) axial direction in porous media; (b) in the reactor cavity along the centerline

3.3.4.4 Flux distribution

The flux distribution contours are shown in Fig. 14(a) and (b). It can be seen in Fig. 14(a) that flux is uniformly distributed with 4 mrad slope error but with slope error 2 mrad the flux doesn't quite cover the porous (RPC) region. In turn, it doesn't allow to rise the cavity temperature to the desired value despite having the higher peak flux value as compared to the 4 mrad slope error. Fig. 14(b) shows the flux distribution for case-2. It shows that with both slope errors (2 mrad and 4 mrad), the flux distribution is uniformly distributed.

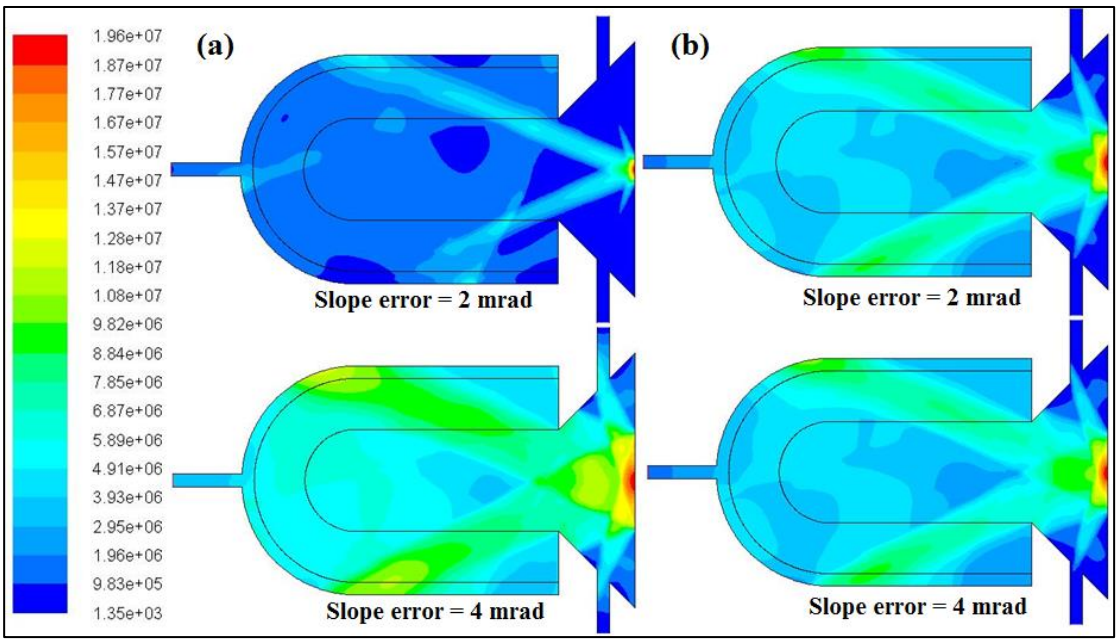

Fig. 14: Flux distribution contours for slope error 2 mrad and 4 mrad for each case; (a) Case-1: When the focal point is on the cavity aperture, (b) Case-2: When the focal point is 20 mm inside the cavity

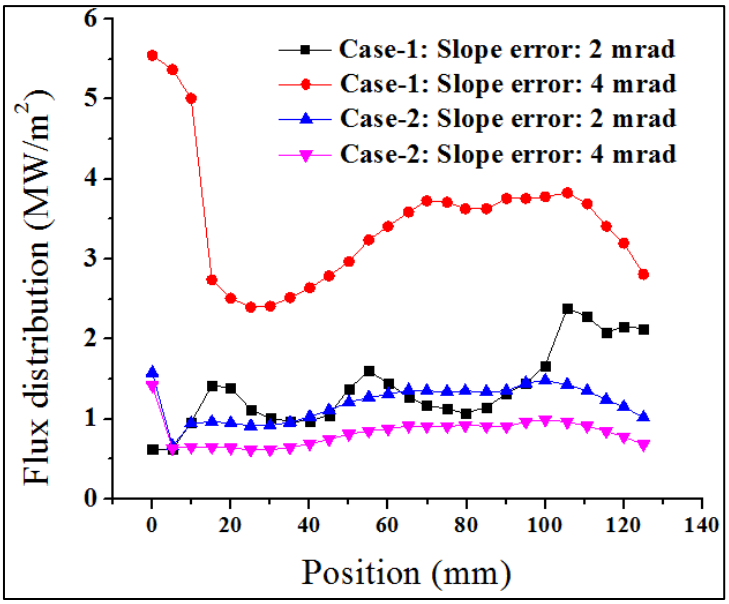

Fig. 15: Flux distribution (incoming) in the reactor cavity

Uniform flux distribution inside the reactor cavity allows achieving a higher temperature. Fig. 15 shows the flux distribution in the reactor cavity. It can be observed from the plot that case-1 with 4 mrad slope error has the highest flux as expected among all four cases.

3.3.4.5 Influence of optical error

The flux profile is affected by the optical errors of the concentrator. The optical error is mainly due to slope error which typically varies from 2 mrad to 4 mrad. The variations in the solar flux profile due to slope errors can be seen in Fig. 10. It can be observed from the figure that the magnitude of the flux profile decreases as the slope error increases. The maximum value of flux obtained 15 MW/m^2 for case-1 with 2 mrad slope error. Whereas, in case-2 the maximum value of flux was 5 MW/m^2 with slope error 2 mrad was obtained.

3.3.4.6 Conclusions

Considering the aforementioned results, the following conclusions are drawn;

1. The distribution of solar flux inside the solar thermochemical reactor cavity is seen to be uniform for case-1 with slope error 4 mrad and in case-2 for both slope errors (2 and 4 mrad). Even though the solar flux attends the highest value

for case-1 with 2 mrad slope error but the flux distribution inside the cavity is non-symmetrical.

2. It was observed that the high value of flux doesn't necessarily yield high temperature unless the heat flux gets uniformly distributed inside the cavity. Case-1 with slope error 2 mrad yields 33% higher solar flux value as compared to the 4 mrad slope error and yet 4 mrad slope error yield the higher temperature inside the reactor cavity.
3. The location of the focal point affects the magnitude of solar flux and also the distribution inside the solar thermochemical reactor cavity gets affected significantly.
4. When the focal point is at cavity aperture, it allows the incoming solar flux to uniformly distribute on the cavity walls and raise the temperature of the catalyst region. However, when the focal point is inside the reactor cavity, the flux gets uniformly distributed but the magnitude of flux gets significantly reduced thus it doesn't attain the high temperature in the reactor cavity as compared to case-1.
5. The magnitude solar flux for case-2 with slope error 2 mrad is 50% less than case-1 with slope error 4 mrad and 16.67% less than case-1 with slope error 2 mrad.

3.4 Thermal modeling of RPC based STCR cavity Shapes for solar flux and temperature distribution - A SolTrace-CFD approach

3.4.1 Methodology and STCR modelling

In the presented study, two models of solar thermochemical reactor cavities as shown in Fig. 16 have been proposed to investigate the influences of geometrical and optical parameters on the temperature and solar flux distribution in the STCR cavities. This study has been structured in three distinct cases of focal point variation as shown in Fig. 17.

(a) Case-1: The focal point is at $x = 0$ (at cavity aperture)

(b) Case-2: The focal point is at $x = -10\ mm$ (10 mm inside the cavity)

(c) Case-3: The focal point is at $x = -20\ mm$ (20 mm inside the cavity)

In front of the cavity aperture, a transparent quartz glass window is placed which allows the solar radiation to enter the cavity. The solar heat flux on the quartz glass window is applied using a user define functions: UDF solar flux profile. Inlets and outlet are provided in the cavity for the circulation of flowing fluids (argon). As the solar flux radiates the cavity and increases its temperature, the flowing fluid are injected from the inlet, pass through the porous media and exit from the outlet. Flowing fluid allows the temperature to be distributed uniformly in the porous region.

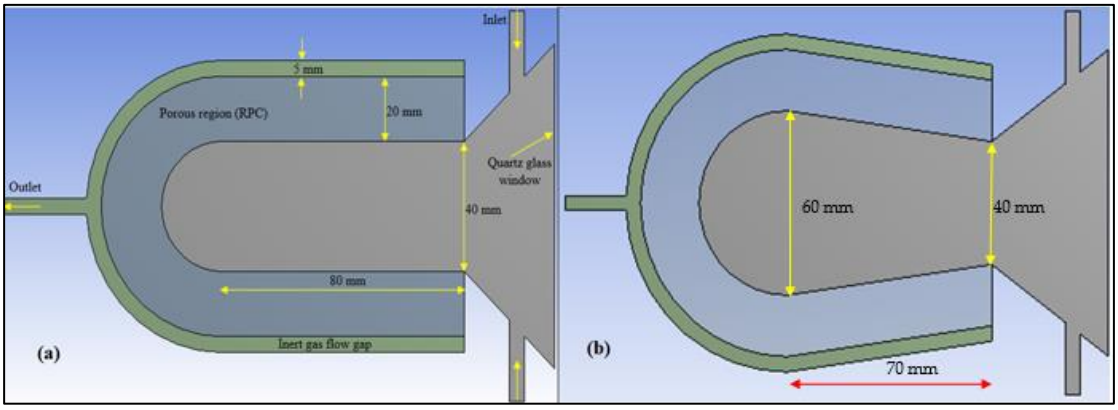

Fig. 16: Schematic of solar thermochemical reactor cavity; (a) STCR-1 and (b) STCR-2

The outer region of the cavity is packed in a stainless-steel shell and outer layers are made fully insulated to reduce thermal loss. In this paper, the effect of displacement of focal point and cavity geometry on the thermal performance of reactor cavity has been investigated. The main focus of the study is maintained on the radial and axial heat transfer, as well as the distribution of heat flux in the solar thermochemical cavity in all three, considered cases for both STCR models.

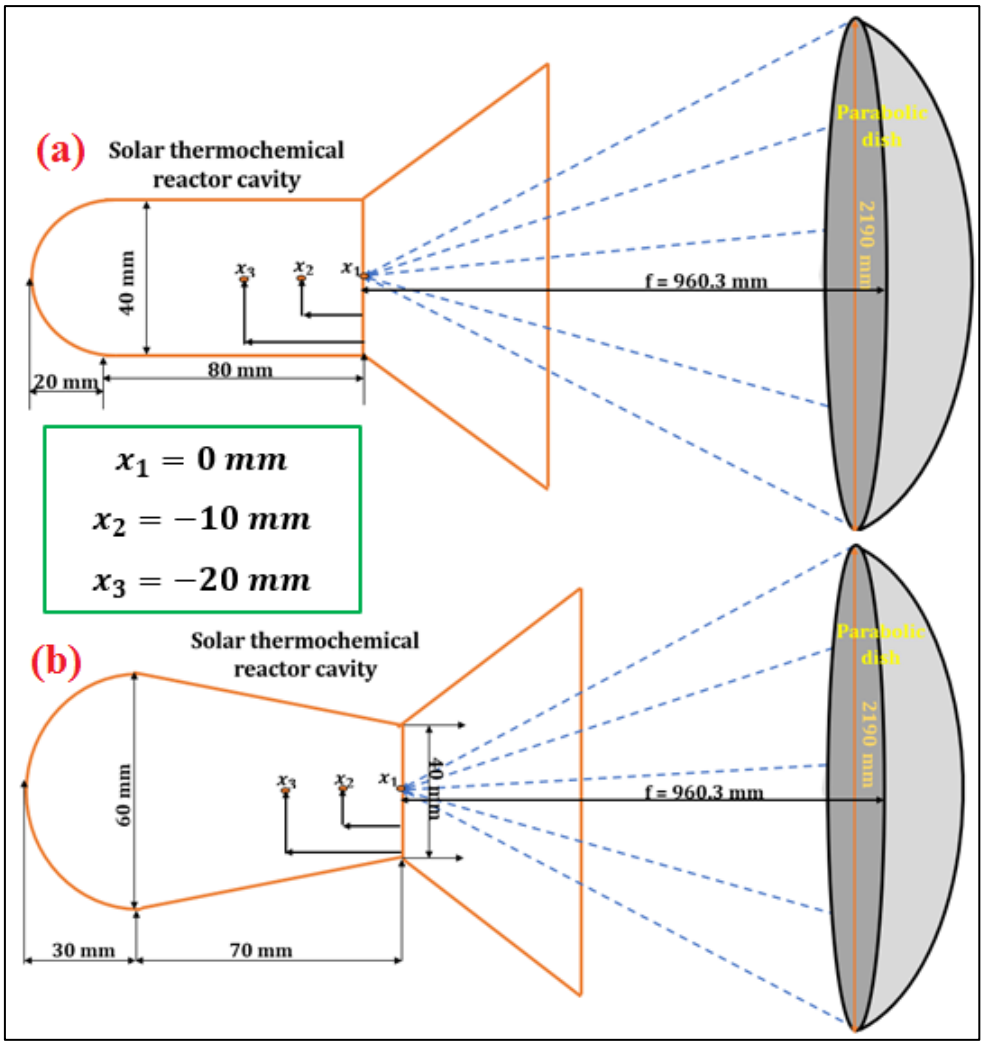

Fig. 17: Schematic of two STCR cavity shapes and three cases considered for each model

The slope error for all three cases has been varied from 2 mrad to 4 mrad and the numerical analysis was carried out by following the algorithm given in Fig. 5. The solar flux profile is generated by the MCRT method using SolTrace software. The temperature and flux distribution on the reactor cavity walls were generated using the CFD software ANSYS Fluent v16.0. The discrete ordinates (DO) radiation model is used to solve the radiative transfer equation for the numerical analysis. Table 1 contains the Thermophysical properties.

3.4.2 Numerical implementation

The numerical simulation was carried out using SolTrace which traces solar ray path using the Monte Carlo Ray Tracing (MCRT) technique. MCRT uniformly distributes solar power by dividing it into larger number of rays determined by the sun

shape and slope error [97]. The interaction between the rays and the reactor cavity is influenced by the transmissivity, reflectivity and absorptivity. The SolTrace results were validated against Lee's study and further used as radiative flux boundary condition on the quartz glass window. ANSYS Fluent v16.2 solver was used to solve the conservation equations by the finite volume method with a tetragonal/hexagonal unstructured mesh having 0.5 mm element size. The DO radiation model was applied to calculate the radiation heat transfer (RTE equation) in the solar thermochemical reactor cavity. Steady-state simulation with COUPLED first-order upwind for discrete ordinates and second order for energy calculation was implemented. The boundary conditions used in the numerical simulation have been given in the Table 3.

Table 3: Boundary conditions [115]

Surface	Boundary conditions
Inlets	$v_{inlet} = \frac{\overset{*}{v}}{Ac_{inlet}};\ T_{inlet} = T_{initial}$
Outlet	$P_{out} = P_{atm}$
Inner surface	$k_q \frac{\partial T}{\partial n} = S_{E,rad} + h_q \Delta T\ ;\ \varepsilon = 0.08,\ \tau = 0.86$
Insulation wall	$k_s \frac{\partial T}{\partial n} = \Delta q_r + h_s \Delta T\ ;\quad \varepsilon = 0.28,\ \tau = 0$
Quartz window	$T_{aperture} = T_{initial}\ ; \varepsilon = 0.08,\ \tau = 0.86$
Other surfaces	$\frac{\partial T}{\partial n} = 0$

3.4.3 Results and discussion

3.4.3.1 The sensitivity of flux distribution at the STCR cavity aperture

Two STCR cavity models shown in Fig. 16 were considered for the thermal analysis. The solar irradiation enters the cavity through the semi-transparent quartz glass window. The cavity also consists of RPC-ceria based porous region which acts as a reactant in the chemical redox reactions to produce hydrogen gas. The first STCR cavity model is the combination of cylindrical and hemispherical shape and the second model consist of the conical frustum and hemispherical shape. The variation in shape is done to evaluate the improvement in the radiation distribution and to achieve a

uniform and maximum temperature at low solar flux magnitude in the porous RPC region. The length of the cylindrical section is kept at 80 mm while the hemispherical section has a radius of 20 mm for the first model. In the second model, the length of the conical frustum section is 70 mm and the radius of the hemispherical section is 30 mm. The aperture diameter of both models is 40 mm with a porous catalyst region is 20 mm. The analysis is mainly focused on the influence of shift in focal point on the flux and temperature distribution in the STCR cavity. The optical analysis of the STCR cavity was facilitated by using SolTrace software.

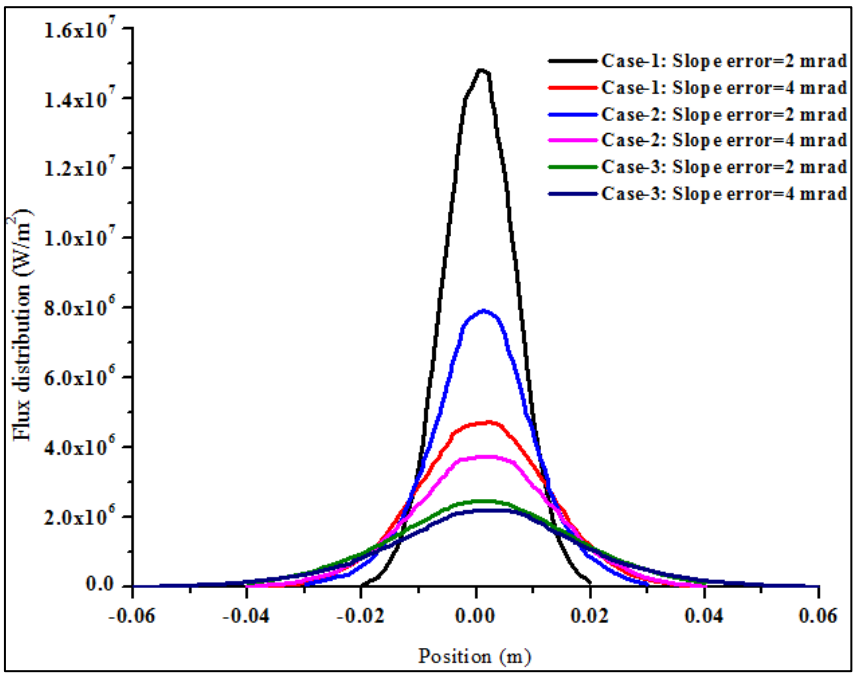

Fig. 18: Concentrated solar flux distribution for all three cases

The flux distribution for all three cases obtained using SolTrace software has been shown in Fig. 18. The focal distance (f) for 1st, 2^{nd,} and 3rd was kept at 0.9803 m, 0.9703 m, and 0.9603 m, respectively. It was evident from the plot that case-1 with slope error 2 mrad yields the highest value of solar flux at cavity aperture. However, the value of flux for case-2, where the focal point is kept 20 mm inside the cavity with slope error 2 mrad, yields a relatively and considerably low value. It also can be seen that the value of flux for case-1 with slope error 4 mrad is higher than case-2 with both slope error values. Obtaining the solar flux profile was the primary step for performing the thermal analysis on the STCR cavity. These flux profiles were later used as a user-defined function (UDF) to generate the solar flux inside the STCR cavity on the porous

walls to generate the required temperature for carrying the water/CO_2 splitting redox reactions.

3.4.3.2 Temperature distribution

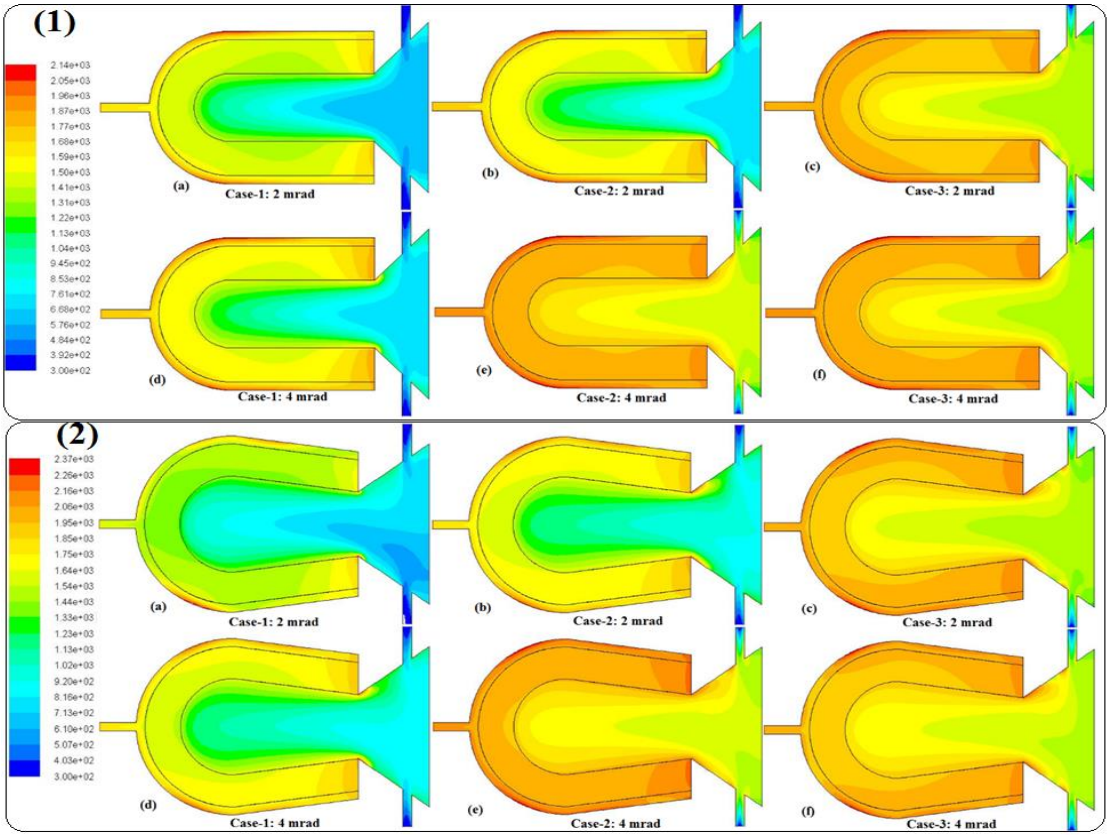

Fig. 19: (1) Fluid phase temperature contours for model-1 for all three cases with both slope errors, (2) Fluid phase temperature contours for model-2 for all three cases with both slope errors

Achieving uniform temperature and flux distribution in the STCR cavity is a major concern for the smooth operation of water/CO_2 splitting reaction and it was done through optical and geometrical optimization. The temperature contours for model-1 and model-2 has been shown in Fig. 19(1) & (2), respectively. The temperature distribution inside the first model of the STCR cavity for slope error 4 mrad is relatively more uniform and higher as compared to the slope error 2 mrad. Even though the case-1, 2, and 3 with 2 mrad slope error yield the higher flux compared to the 4 mrad slope error but the temperature distribution is higher for 4 mrad slope error compared to 2 mrad slope error. Since, the focal point is located at the cavity aperture in case-1, the incoming flux doesn't quite get uniformly distributed in the porous region and on the cavity walls resulting in generating a lower temperature than expected. However, with a 4 mrad slope error, the solar flux reaches inside the STCR cavity and generates

uniform flux distribution which leads to higher temperature distribution compared to 2 mrad slope error. The geometrical aspect of STCR cavity design plays a significant role in uniform flux and temperature distribution as well as can be seen in the temperature contours. The second model poses the advantage of having conical frustum at the entrance which allows the more uniform distribution of collimated rays resulting in yielding the higher temperature at the porous region as compared to the first model.

3.4.3.3 Temperature distribution in radial direction in the porous media

The RPC zone is the region where the redox reactions take place for the generation of hydrogen gas. It is necessary to optimize the thickness of the RPC zone for the loading of the appropriate amount of reactant ceria (CeO_2). Thus, the investigation of temperature distribution in the radial direction in the catalyst region is a crucial factor to optimize the RPC thickness in the STCR cavity. The radial temperature distribution in the porous media for the 1st, 2nd and 3rd case in which the focal point was considered at (x=0, -10 and -20 mm) has been shown in Fig. 20(a) and (b) for model-1 and 2, respectively. It was seen that the case-2 combined with 4 mrad slope error presents the best suited scenario to achieve the highest temperature through 20 mm porous media thickness. It is evident from graphs that even though both models offer the uniform temperature distribution in the radial direction but model-2 reached the 50.0 K higher than model-1.

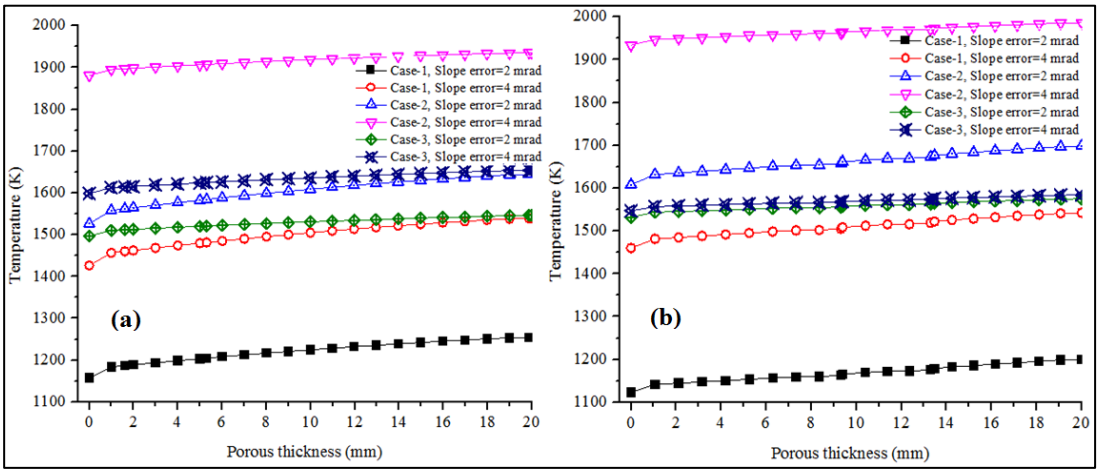

Fig. 20: Fluid phase temperature distribution in radial direction in the porous media for (a) model-1 and (b) model-2

If the flux gets uniformly distributed in the porous region, a higher and more uniform temperature can be achieved even at an increased value of inert gas velocity. The reported data also reveals that the cavity geometry has an apparent effect on the radial temperature distribution. The radial temperature distribution in model-2 is more uniform and comparatively higher as compared to model-1. The frustum section allows the flux to get uniformly distributed on the cavity walls resulting in achieving the higher radial temperature in the porous region. The effect of slope error on radial temperature becomes less significant resulting in the minimal temperature difference for both slope errors. Given that the focal point is situated 20 mm inside the STCR cavity thus allowing the solar flux to enter into the cavity with lower scattering which results in uniform flux distribution *vis. a vis.* uniform and high-temperature distribution in the catalyst region as compared to the first and second cases.

3.4.3.4 Temperature distribution in the axial direction in porous media

The temperature distribution in the axial direction in the catalyst region is a crucial factor to investigate the optimum catalyst (RPC) thickness in the STCR cavity. Thus, it becomes necessary to analyze the temperature distribution along the axial direction in the catalyst region. Since the cylindrical and conical frustum part of the cavity has the length of 80 mm and 70 mm, respectively. Thus, the temperature distribution in the axial direction was evaluated for this portion only and the dome part of the cavity is covered in the full reactor temperature analysis along the centerline. The fluid phase temperature of the porous media in the axial direction has been plotted in Fig. 21(a) for model-1 and (b) for model-2. It is reported that the case-2 (x= -10 mm) exhibit the higher temperature trends among all three cases in both models. However, a comparative analysis of the both models reveal that model-2 for case-2 with 4 mrad slope error yield 328.8 K higher mean temperature as compared to model-1 while subjected under same conditions. It was also seen that in terms of uniformity of the temperature distribution in the axial direction in the porous media, from x=0 to x= -80 mm, model-2 offers significant advantage over model-1. The uniformity in the temperature distribution throughout the length is resulted due to the geometric effects.

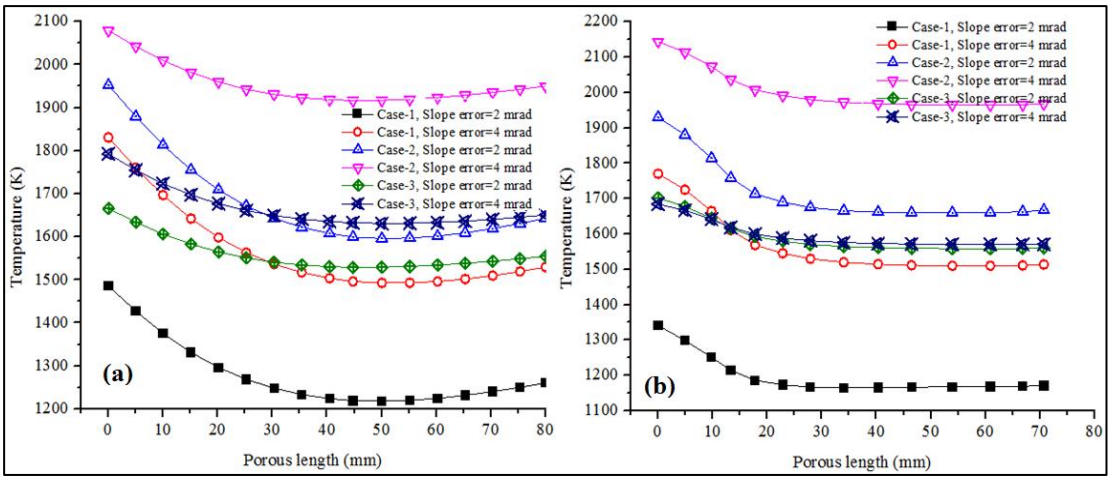

Fig. 21: Fluid phase temperature distribution in axial direction in the porous media for (a) model-1 and (b) model-2

3.4.3.5 Temperature distribution in Reactor cavity along the centerline

The analysis of reactor temperature is necessary to optimize the fluid phase temperature in the solar thermochemical reactor to carry out redox reaction and for the better control of the thermal conditions when it is required to switch between both steps of the ongoing reaction.

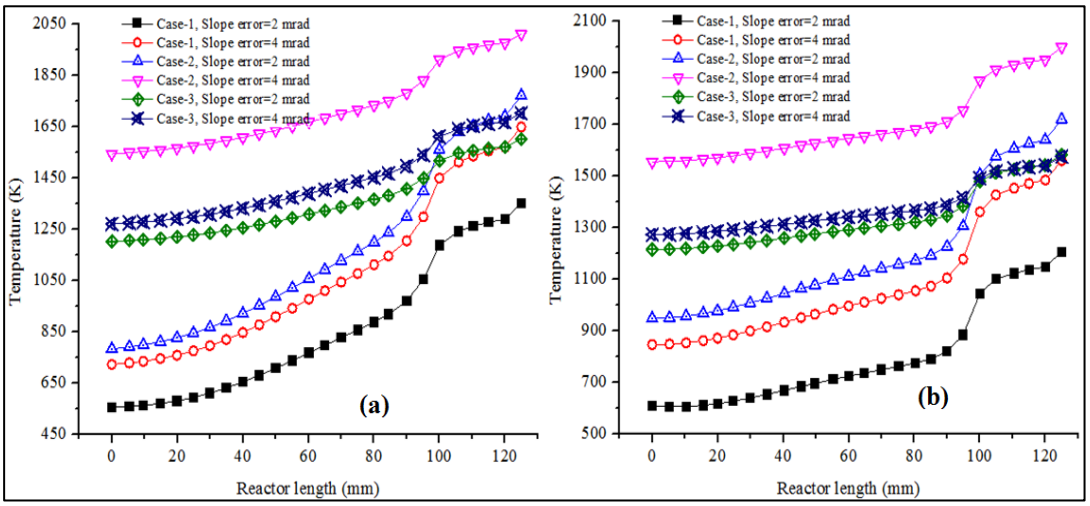

Fig. 22: Fluid phase temperature distribution along the centerline in the STCR cavity for (a) model-1 and (b) model-2

Fig. 22(a) and (b) presents the fluid phase temperature distribution along the centerline in the reactor cavity for model-1 and 2, respectively. The concentrated solar flux enters the cavity from the quartz glass window and passes through the aperture x=0 and at this point temperature of STCR cavity started to rise by means convection (heated inert gas) and radiation. Given the stipulation that the focal point is at the x=0

which means the scattering of the collimated rays starts at this point. It is observed in Fig. 22(a) & (b) that the case-2 with slope error 4 mrad yields the highest reactor temperature for both models. However, model-1 reached 21.28 K higher mean temperature as compared to model-2. In terms of uniformity throughout the entire length of the solar thermochemical reactor, both models perform equally well.

3.4.4 Flux distribution in the porous region

The flux distribution inside the STCR cavity is the crucial part of the optical analysis. The flux distribution contours for both models and all three cases has been shown in Fig. 23(1) and (2) for model-1 and model-2, respectively. The flux distribution contours show that the focal distance is a main factor for obtaining the uniformity of solar concentrated flux distribution in the porous region.

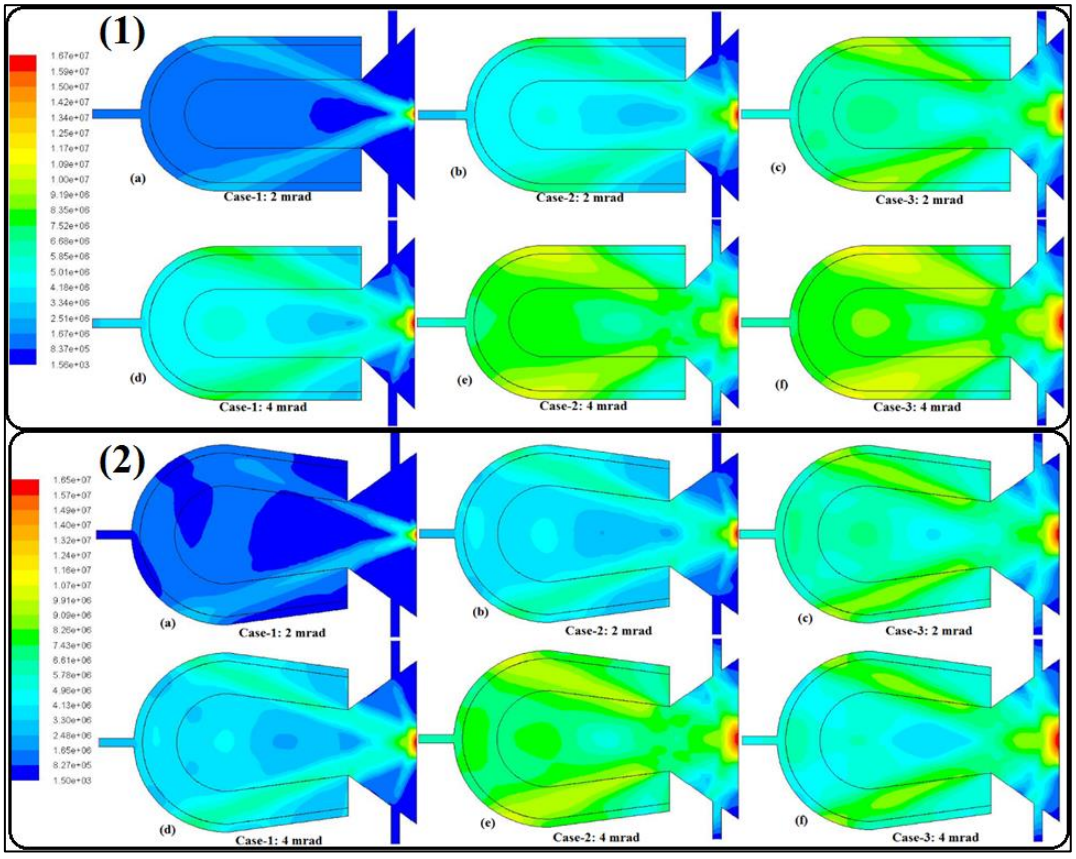

Fig. 23: Flux distribution contours for model-1 for all three cases with both slope errors

When the focal point is situated inside the cavity, it provides with better scattering of rays thus achieving a uniform distribution of flux as well as temperature

for both models. Slope error is another factor that certainly can't be overlooked as it shows a promising importance and dependence on cavity shape.

In both Fig. 23(1) and (2), it can be observed that the flux distribution is more uniform and higher in magnitude for slope error 4 mrad. However, the effect is only apparent when the focal point s inside the cavity *i.e.* in case-2 and case-3. Another important observation was that when the focal point was at cavity aperture the model-1 achieved the higher flux magnitude and better uniformity but as the focal point slides deeper inside in cavity, model-2 becomes better choices for achieving the uniform flux as compared to model-1.

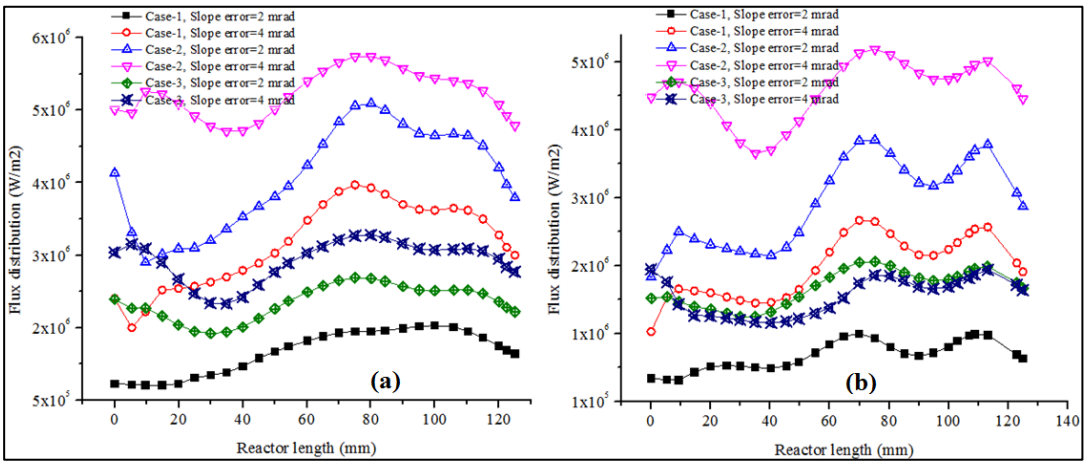

Fig. 24: Flux distribution in the STCR cavity for (a) model-1 and (b) model-2

Fig. 24(a) and (b) shows that the flux distribution inside the cavity depends on the focal point shift and the cavity shape. It is evident that the flux distribution in STCR cavity also depends on the slope error. The flux distribution in model-1 and model-2 was seen to be higher for 4 mrad slope error compared to 2 mrad for the case-1. However, the flux distribution in mode-1 is comparatively higher than model-2. It can be also seen in both figures that the model-1 STCR cavity shape provides more uniform flux distribution as compared to model-2. As the focal point moves 10 mm inside the STCR cavity in second case, the flux distribution for both models and for both slope error increase significantly. It is also seen that the model-1 with slope error 4 mrad offers more uniform flux distribution as compared to model-2. In the third case, as the focal point was located at 20 mm inside the STCR cavity, the flux distribution in the cavity reduces drastically as compared to the second case but remains higher than the

first case. The magnitude of flux in model-1 is higher for slope error 4 mrad while in in model-2, the impact of slope error doesn't show much significance.

3.4.5 Influence of optical error

Optical errors of the concentrators affect the solar flux distribution profile. The optical errors are mainly caused by the slope errors and its value varies between 2 to 4 mrad. The variation in solar flux profile caused by slope errors can be seen in Fig. 18. It is clearly seen that the magnitude of the solar flux decreases with the increase in solar error value. However, the distribution of flux distribution for 4 mrad slope error is higher than 2 mrad slope error. The maximum value of solar flux 15, 7 and 2 MW/m^2 is obtained for case-1, 2 and 3 with 2 mrad slope error, respectively. The statistical influence of slope errors on average fluid phase temperature in the porous media for both models by taking the effects of inert gas velocity into account have been discussed in Fig. 25 fluid temperature in radial direction, Fig. 26 fluid temperature in axial direction and Fig. 27 for fluid temperature in reactor along the centerline.

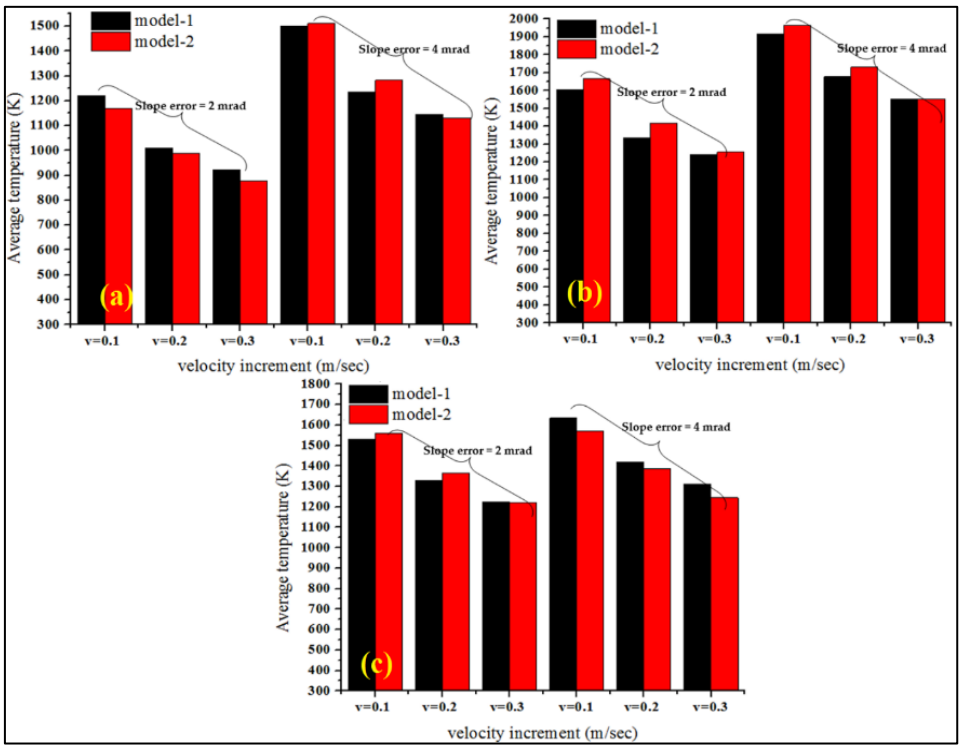

Fig. 25: Average fluid phase temperature in radial direction wrt. Inert gas velocity for slope error 2 and 4 mrad (a) case-1, (b) case-2 and (c) case-3

The average fluid phase temperature in the porous region for all three cases has been plotted in Fig. 25(a), (b) and (c). When the inert gas velocity was 0.1 m/sec at inlet

and the slope error 2 mrad, the avg. fluid temperature in the RPC region reached 1220 K and 1168 K for model-1 and model-2 respectively. However, the avg. temperature reached the value of 1500 K and 1510 K for 4 mrad slope error at same velocity as shown in Fig. 25(a) for case-1. This rise of 280 K and 342 K in avg. temperature for model-1 and model-2, respectively signifies the importance of slope error. It also should be noted that the increment in inert gas velocity from 0.1 m/sec to 0.3 m/sec causes in decrease of avg. temperature by 296 K & 354 K for model-1 and 291 K & 378 K for model-2 for 2 mrad and 4 mrad slope error, respectively.

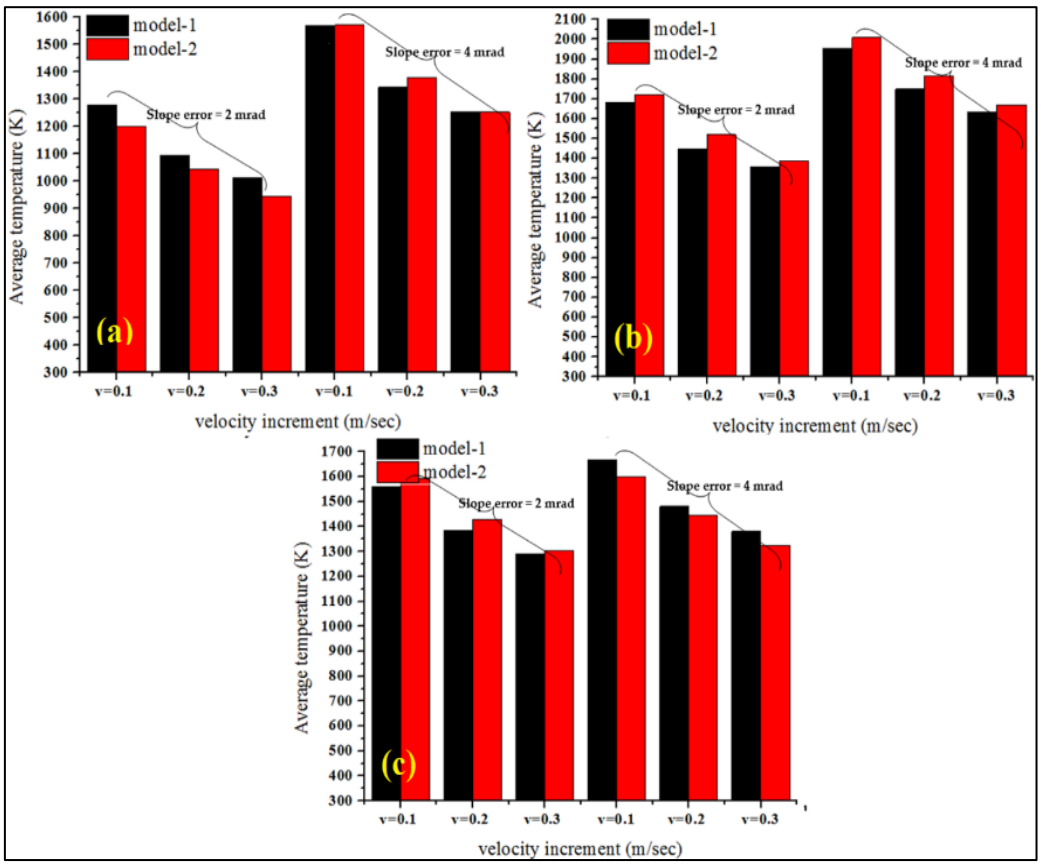

Fig. 26: Average fluid phase temperature in axial direction wrt. Inert gas velocity for slope error 2 and 4 mrad (a) case-1, (b) case-2 and (c) case-3

In case-2 where the focal point is 10 mm (x=-10 mm) inside the cavity, the avg. fluid temperatures for both models have been shown in Fig. 25(b). It was observed that the avg. temperature reached much higher than case-1. Statistically, for inert gas velocity of 0.1 m/sec, the avg. temperature for model-1 goes up to 1604 K and for model-2 goes up to 1664 K for 2 mrad slope error. However, if slope error is set to be

4 mrad, the avg. temperature goes up to 1917 K and 1966 K for model-1 and model-2, respectively. Whereas shifting of focal point 20 mm inside the cavity (x=-20 mm) reduces the avg. temperature for both models with both slope errors is shown in Fig. 25(c). The model-1 and model-2 with slope error 2 mrad yield 1528 K and 1560 K and with slope error 4 mrad yield 1634 K and 1571 K of avg. temperature, respectively. Thus, it is statistically stipulated that model-2 provides with the best-case scenario to achieve the highest avg. fluid temperature with 4 mrad slope error and case-2 when the focal point is 10 mm inside the cavity is the best choice among all three cases.

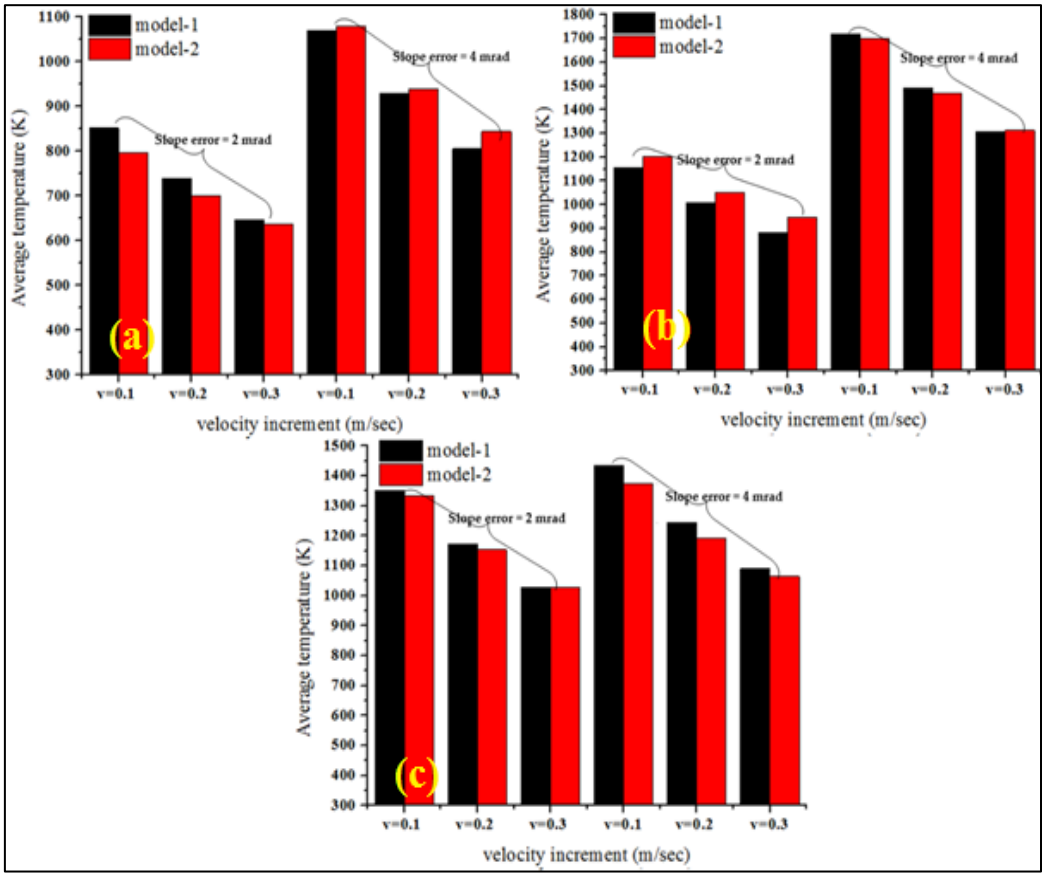

Fig. 27: Average fluid phase temperature along the centerline in STCR cavity wrt. Inert gas velocity for slope error 2 and 4 mrad (a) case-1, (b) case-2 and (c) case-3

The avg. fluid temperature distribution in axial direction has been shown in Fig. 26(a), (b) and (c) for case-1, 2 and 3. In the first case as shown in Fig. 26(a), the avg. temperature goes up to 1280 K for model-1 and 1200 K for model-2 at 2 mard and 1570 K for model-1 and 1572 K for model-2 at 4 mrad slope error at 0.1 m/sec inert gas velocity. By shifting the focal point 10 mm inside the cavity (case-2) as shown in Fig.

26(b), the avg. temperature gets higher and reached up to 1670 K and 1722 K for model-1 and model-2, respectively at 2 mrad and 1955 K and 2008 K for model-1 and model-2, respectively at 4 mrad slope error. While in case-3 as shown in Fig. 26(c), the avg. temperature for model-1 and model-2 reached up to 1561 K and 1594 K, respectively at 2 mrad and 1667 K and 1599 K, respectively at 4 mrad. It is clear that the distribution of avg. fluid temperature in axial direction highest for case-2 at 4 mrad and model-2 is best suitable choice in this scenario.

The avg. temperature of the reactor along the centerline for all three cases have been plotted in Fig. 27(a), (b) & (c). In the first case as shown in Fig. 27(a) the avg. reactor temperature goes up to 852 K and 798 K for model-1 and model-2, respectively for 2 mrad and 1070 K and 1079 K for model-1 and model-2, respectively at 4 mrad slope error for 0.1 m/sec fluid velocity. However, for case-2 the avg. reactor temperature for model-1 and model-2 reached up to 1156 K and 1201 K, respectively at 2 mrad and 1720 K and 1700 K for model-1 and model-2, respectively at 4 mrad as shown in Fig. 27(b). However, in the 3rd case as shown in Fig. 27(c), the avg. reactor temperature goes up to 1353 K and 1335 K for model-1 and model-2 at 2 mrad and 1434 and 1374 for model-1 and model-2 for 4 mrad. Thus, the model-1 reached the highest temperature at 4 mrad slope error in case-2 at 0.1 m/sec fluid velocity.

3.4.6 Summary and conclusion

This study presented the effects of geometrical and optical parameters on incident solar flux distribution in the solar thermochemical reactor cavity. Based on the result obtained from the numerical investigation the following conclusions are drawn:

1. The flux distribution inside the STCR cavity is more uniform in model-1 for case-1 with 4 mrad slope error compared to model-2. In the case-2 with 4 mrad slope error, the distribution of flux becomes comparatively more uniform and achieve greater magnitude than the case-1. However, magnitude and the uniformity of the flux distribution reduces in comparison to case-1 and case-2. Even though the solar flux attends the highest value for case-1 with 2 mrad slope error but the flux distribution inside the cavity is non-symmetrical.
2. It was observed that the high value of flux does not necessarily yield high temperature unless the heat flux gets uniformly distributed inside the cavity.

Case-1 with slope error 2 mrad yields almost 27% higher solar flux value as compared to the 4 mrad slope error and yet 4 mrad slope error yield the higher temperature inside the reactor cavity.

3. The incident solar flux gets uniformly distributed on the cavity walls for case-1 and case-2 and yields the highest temperature in the catalyst region. However, the flux distribution losses its uniformity for case-3 and its magnitude also reduces significantly, thus it doesn't attain the high temperature in the reactor cavity as compared to case-1.
4. It was seen that model-2 for case-2 with 4 mrad slope error yields the highest average temperature 1966 K and 2008 K in the STCR cavity in radial direction and axial direction, respectively. However, the fluid temperature along the centerline reached the highest value (1720 K) for model-1 in case-2 with 2 mrad slope error. The fluid velocity seen to play an important role in as controlling parameter for the temperature rise.
5. It was also seen that the model-2 yields the better uniformity and higher magnitude of temperature in the catalyst region in radial direction as compared to model-1 in case-1 and case-2. However, in case-3, model-1 and model-2 both yield the same radial temperature in the porous catalyst region.
6. The study revealed that even though the both models yield almost same catalyst temperature in the axial direction but the distribution of temperature in axial direction was comparatively more uniform in model-2 for all three cases.

Chapter – 4

4 Model of transport and chemical kinetics in a solar thermochemical reactor for H_2O splitting

4.1 Introduction

In the present era, solar energy is the best suited renewable and eternal source of green energy for domestic as well as commercial use. Research and advancement in solar energy over the years have brought solutions to complex problems such as the production of solar fuel i.e. hydrogen and syngas. The solar collector technology has advanced solar energy applications in terms of performance by improving their efficiencies [115-116]. Solar thermochemical cycles present one of the best possible way for the production of solar fuels using solar concentrated power. Moreover, this approach also can be integrated with electricity production on the pilot scale. Solar thermochemical processes are used in two major areas: hydrocarbon fuel production and for the production of industrial commodities such as lime and ammonia [118]. Solar thermochemical processes have the major application in hydrocarbon fuel production (from hydrogen and syngas).

Solar thermolysis is the single-step process where H_2O is decomposed into hydrogen and oxygen at the temperature of 2500 K [119]. In this process, the hydrogen and oxygen separation is difficult. Thus, it's a highly dangerous process with complicated reaction conditions. Due to the complicacy of the solar thermolysis process, solar thermochemical cycles provide the best-suited alternative of fuel production in a multiple-step reaction system which reduces the temperature requirement. Solar thermochemical cycles were introduced based on the difficulties faced in the solar thermolysis process which requires extremely high temperature and product separation [120]. Primarily, solar thermochemical cycles used metal oxides for hydrogen production in two-steps metal oxide redox reactions. The first step is the reduction step (endothermic) in which metal oxide gets decomposed into metal and releases oxygen at high temperatures. The second step is the oxidation step

(exothermic) in which metal oxide reacts with H_2O/CO_2 to produces H_2/CO as a product. Further, hydrogen and syngas can be converted into hydrocarbon fuels via. Fischer-Tropsch process. Since the year 2006, Non-stoichiometric cerium oxide or ceria (CeO_2) has emerged as one of the best-suited redox material [67,121] for the solar thermochemical cycle due to its high oxygen solid-state conductivity, fast redox kinetics [70] and crystallographic stability. The redox reactions for two-step H_2O/CO_2-splitting solar thermochemical cycle based on non-stoichiometric ceria has been given as:

High-temperature reduction

$$CeO_2 \xrightarrow{+\Delta H} CeO_{(2-\delta)} + \frac{\delta}{2} O_2 \tag{40}$$

Low-temperature oxidation (with H_2O)

$$CeO_{(2-\delta)} + \delta H_2O \xrightarrow{-\Delta H} CeO_2 + \delta H_2 \tag{41}$$

Low-temperature oxidation (with CO_2)

$$CeO_{(2-\delta)} + \delta CO_2 \xrightarrow{-\Delta H} CeO_2 + \delta CO \tag{42}$$

The first step is known as the reduction step which takes place at high temperature. In this step, ceria gets reduced to a non-stoichiometric state by solar concentrated energy. After the reduction step, the low-temperature oxidation step takes place. In this step, ceria is re-oxidized by reacting with water and/or CO_2 and produces H_2 and/or CO. These redox reactions take place in the solar reactor cavity receiver. These cavity receivers can be designed in various ways according to the requirement such as stationary or rotating [122–124], aerosol flow reactors [125], glass dome reactors [126] and moving and fluidized bed reactors [126-127]. Water slitting process was demonstrated using monolithic reactors of 50 kW power and yearly performance of solar thermochemical plant was investigated. It was concluded that with advanced strategies the overall performance can be improved up to 46% [129]. A transient heat transfer model of solar thermochemical reactor of reticulated porous ceramic was investigated. Results of the numerical study show that the RPC reduction time reduces when the input radiative power is increased and solar-to-fuel conversion efficiency about 6% at input power of 50 kW [130].

The reduced level of non-stoichiometry of ceria is represented by δ. According to the studies of Panlener et al.[131] and Zinkevich et al.[132], the lowest deviation is about *0.35* in the temperature range of *1000–1500 °C*. Lapp et al. [133] performed a thermodynamic analysis to study the value of non-stoichiometry (δ) at the temperature range of *1000–1500 °C* keeping partial pressure of oxygen from 10^{-2} to 10^{-24} atm. The study of Scheffe and Steinfeld [134] showed that the ceria (CeO_2) requires temperature greater than *1000 °C* to initiate the reduction step. However, the oxygen partial pressure should be less than 10^{-2} bar Bulfin et al.[135]. The high temperature (energy input) can be achieved by concentrated solar power (for pilot scale) and by other means such as oxy-fuel radiant heating (for lab scale). The oxygen partial pressure can be controlled by either using a vacuum condition or using an inert gas [136]. The theoretical solar-to-fuel efficiency can be expressed as (Li et al. [137]);

$$\eta_{th} = \frac{n_{fuel} HHV_{fuel}}{Q_{solar}} \tag{43}$$

where n_{fuel} is product amount, HHV is higher heating value and Q_{solar} is input concentrated solar energy.

Solar thermochemical reactors are the most crucial part where the reactions take place and can be categorized as directly and indirectly irradiated reactors. The concentrated solar energy doesn't directly come in contact with reactive materials in indirectly irradiated reactors instead the solar irradiation gets absorbed by opaque wall and gets further transferred through convection and conduction. However, in directly irradiated reactors the concentrated solar energy directly irradiates the reactive materials. The indirectly irradiated reactors are mostly used in solar methane reforming [138–140] as well as in solar thermochemical cycles [141-142]. They are designed as tubular reactors (single or multi-tube) using alumina material. However, the reactor body material concern cannot be neglected in solar thermochemical cycles as the reduction step takes place at the temperature higher than *2000* K. Thus, the materials having high melting points such as silicon carbide (SiC) and alumina are used in the reactor body. The directly heated reactor possesses the advantage of comparatively efficient heat transfer than an indirectly irradiated reactor because it transfers the energy through radiative heat transfer. The directly-irradiated reactors can be majorly

classified into three categories: moving front reactor, packed bed reactor and rotary type reactor.

The moving front type reactor has a moving shaft mounted at the reactor center which allows the reaction catalysts to be exposed to the solar radiation directly. They are mostly used with volatile catalysts such as *ZnO/Zn* and *SnO_2/SnO* thus after the vaporization of some amount of catalysts, freshly coming catalysts remain fully exposed to the solar radiation [143-144]. The packed bed reactor was firstly used in the year *2012* by Chueh et al. [145] with reticulated porous ceria (*RPC*) foam. In this reactor, the reduction and oxidization reaction can take place continuously alternatively. This cavity-receiver reactor design provides porous surface for effective radiation exposure and can be operated under temperature-swing as well as isothermal condition. In rotary type reactors, the continuous reduction and oxidation take place in two separate regions divided by placing a rotary monolith catalyst axis perpendicular to the reactor axis [124, 146-147].

Lougou et al. [148] experimentally and numerically investigated the reactor design and thermochemical energy conversion. Study reported that the targeted radiation receiver surface and the volume of reactor are the main factors which affect the thermochemical energy storage efficiency. Result showed that the reactor efficiency during thermal charging and discharging was reported to be 85.27% at 1787.73 K and 76.9% at 1315. 16 K, respectively. In a study carried out by Safari and Dincer [149], two step, three step, four step and hybrid thermochemical water splitting cycles were comparatively evaluated. These thermochemical cycles were evaluated in terms of energy-exergy efficiency and global warming potential (GWP). It was found that the vanadium chlorine yields the highest exergy efficiency of 77%. Sulfur-Iodine and hybrid sulfur cycles are the most promising candidate having the GWP of 0.48 and 0.50 kg CO_2·eq/kg H_2, respectively. Bhosale et al. [150] performed thermodynamic analysis on SnO_2/SnO water splitting cycle. Results of the study indicated that if the thermal reduction temperature is maintained at 1780 K, the cycle efficiency of 41.17% and solar-to-fuel energy conversion efficiency of 49.61% can be achieved. Chen et al. [151] numerically investigated the thermochemical methane dry reforming using foam reactor.

The results of the study showed with increasing the velocity and CH_4/CO_2 reduces the methane conversion. However, as the thermal conductivity of solid phase is increased, the methane conversion increases. Study also revealed that the maximum efficiency and conversion is obtained at the porosity and pore diameter of *0.9* and *1.5 mm*, respectively. Wang et al. [152] investigated numerically methane reforming process in porous thermochemical reactor using LTNE model coupled with P1-radiation model. The results of the study indicated that the radiative heat loss poses a strong influence on solid phase temperature, thus it reduces the hydrogen production. Further, as the thermal conductivity of porous media increases, it decreases the temperature of solid phase however, it improves the chemical reaction rate. Wang et al. [153] performed a numerical analysis on methane reforming using LTNE model in a porous media based reactor. The results of the study showed that the fluid phase temperature is affected by the concentrated solar irradiation and forms a big temperature gradient of solid phase.

Charvin et al. [154] presented the process analysis of three thermochemical cycles, ZnO/Zn, Fe_3O_4/FeO and Fe_2O_3/Fe_3O_4. Study indicated the cost of hydrogen production estimated to be 7.98$/kg and 14.75$/kg for 55 MWth and 11 MWth solar power plant, respectively. Results also showed that efficiency for Fe_3O_4/FeO, Fe_2O_3/Fe_3O_4 and ZnO/Zn reached to 17.4%, 18.6% and 20.8%, respectively. Bhosale et al has performed thermodynamic analysis on different cycles to calculate the cycle and solar-to-fuel conversion efficiency on samarium oxide ($\acute{\eta}_{cycle}$=24.4% and $\acute{\eta}_{solar\text{-}to\text{-}fuel}$ = 29.5%) [155], erbium oxide ($\acute{\eta}_{cycle}$ = 9.96% and $\acute{\eta}_{solar\text{-}to\text{-}fuel}$ = 12.01%) [156], Terbium oxide($\acute{\eta}_{cycle}$ = 39% and $\acute{\eta}_{solar\text{-}to\text{-}fuel}$ = 47.1%) [157], Zinc oxide-zinc sulfate ($\acute{\eta}_{cycle}$ = 40.6% and $\acute{\eta}_{solar\text{-}to\text{-}fuel}$ = 48.9%) [158], Cr_2O_3/Cr ($\acute{\eta}_{cycle}$ = 71.1% and $\acute{\eta}_{solar\text{-}to\text{-}fuel}$ = 54%) [159], $MnSO_4/MnO$ ($\acute{\eta}_{solar\text{-}to\text{-}fuel}$ = 47.6%, 53.1% and 60% with 10, 30 and 50% of heat recovery) using HSC chemistry [160]. The doping effect of metal cations on thermal reduction was analyzed using TGA and results show that at 1400 ^{0}C, CeZn and CeFe release higher amount of O_2 than other $Ce_{0.9}M_{0.1}O_{2-\delta}$ materials [161].

Sarwar et al. [162] experimented and numerically studied the effect of aperture size on efficiency of solar energy harvesting 7 kW xenon short arc lamp solar simulator. Results indicated that the optimum aperture size is related to irradiance intensity. They

also concluded that the power consumption reduces to half with variable aperture size as compared to the fixed temperature. While, variable aperture can maintain the steady temperature of 1000 K, 1100 K and 1200 K with 26.8 kW, 33.2 kW and 26.9 kW, respectively. Siddiqui et al. [163] proposed a novel solar and geothermal integrated trigeneration system in *CuCl* cycle to generate the electricity, hydrogen and cooling. Results showed the energy and exergy efficiency to be *19.6%* and *19.1%*, respectively. Further, the energy efficiency and exergy efficiency to be *35.3%* and *35.9%*, respectively for hydrogen production in *CuCl* cycle. Jiang et al. [164] investigated the hydrogen production via methane reforming using perovskite ($La_{1-y}CayNi_{0.9}Cu_{0.1}O_3$). Study showed that the increasing calcium substitute increases the perovskite reactivity and methane conversion reaches up to *52%*. It was found that $La_{0.1}Ca_{0.9}Ni_{0.9}Cu_{0.1}O_3$ has the highest reactivity. Sedighi et al. [165] studied the point focus gas phase receiver operated on high temperature. Study concluded that the trend is moving towards the reach of high thermodynamic efficiency thus, the high temperature at outlet will be required in the future. It was also pointed out that the reactor design needs to be improved.

Lee et al. [166] carried but a numerical investigation on hydrogen production via methane reforming using a packed bed reactor, sorption reactor and membrane reactor. Results of the numerical investigation showed that H_2 yield rate of *0.00143, 0.00145, 0.00127, 0.00121*, and *0.00852 mol/s* were found with the SEMR with counter-current flow, SEMR with co-current flow, MR with counter-current flow, MR with co-current flow, and a packed-bed reactor, respectively. Wang et al. [167] proposed a new structure for solar receiver/reactor for hydrogen production. They investigated the changing the aperture diameter, width and receiver length. Results showed that the MCR increases when the aperture width is decreased and the maximum porous bed temperature decreases by *17.9* ^0C. It was also found that the reactor performance is improved as the aperture and diameter changes along the flow direction harmoniously.

The solar thermochemical energy storage is high temperature based reversible chemical reactions. It is a two-step process known as charging step and discharging step. In the charging step, the redox material is heated up to *1600* K and in discharging

step, H_2O/CO_2 are converted into fuels at comparatively low temperature [168–171]. Solar thermochemical process is still under development at lab scale and researcher are finding new ways to convert solar thermal energy into clean fuels. The performance of High-temperature thermochemical energy storage system depends upon thermal and chemical characteristics of redox material. Studies have shown that the solar thermochemical process have much potential to become high temperature based energy storage system as compared to other storage technologies [172–177]. Porous media structure has been adopted to increase the thermal performance of the reactor due to the larger area of heat transfer. Banerjee et al. [178] stated that the heat transfer in reactor can be increased by *9* fold by using the RPC rather than bare tubes. A RPC based heat exchanger model was developed and integrated with solar reactor. Study reported the *85-90%* porosity yielded the higher heat transfer and improved solar-to-fuel conversion efficiency [179-180]. Distribution of solar power density and thermal chemical reaction performance increases with the increasing porosity and cell size also the higher thermal performance leads to higher solar-to-fuel conversion efficiency [181–184].

In another study, it was shown that the use of porous media in thermochemical reactor increases the thermal performance as well as helps in the amalgamation of various redox materials [185-186]. The coupled conduction-radiation heat transfer in solar reactor to evaluate thermal performance have been explored extensively [77,186–188]. Many studies have pointed out that the thermal performance of heat storage medium is affected by temperature gradient in porous media in solid phase [190–192]. In past few years, researchers have developed potential candidate redox material to increase the thermal stability and chemical reactivity to increase the solar-to-fuel conversion efficiency [193–197]. Regarding the literature, the reticulated porous ceria (RPC) based solar thermochemical reactors have been considered as better alternative among perspective of industrial applications.

Based on abovementioned studies, as of authors' best of knowledge, effects of RPC thickness and gas flow gap in STCR cavity has not been yet investigated. The present study aim to investigate following objectives:

1. To investigate the effect of varying RPC thickness on the temperature distribution in porous media as well as in the whole reactor cavity.

2. To study the effect of varying gas flow gap and increasing fluid velocity on the temperature distribution in the porous region along with entire reactor cavity.
3. To explore the geometrical parameters variation effects on flux distribution in the solar thermochemical reactor cavity.

In this work, a numerical analysis (steady-state and transient) has been performed on six hybrids, cylindrical-hemispherical cavity shape models to study the effects of RPC thickness and geometrical parameters of the cavity receiver.

4.2 Reactor conceptualization and configuration

The solar thermochemical production of hydrogen via a two-step water splitting process requires two inputs known as, material input and energy input. In this process, water is used as material input and solar heat is used as the energy input. The solar concentrated energy splits the water into hydrogen and oxygen in a thermochemical reactor at high temperature. The schematic diagram of the solar reactor cavity is shown in Fig. 28. This reactor cavity consists of a hybrid, cylindrical and hemispherical reactive chambers. In the solar thermochemical reactor cavity, the RPC region is the core section having the RPC thickness as 15 mm, 20 mm and 25 mm with 5 mm and 10 mm gas flow gap.

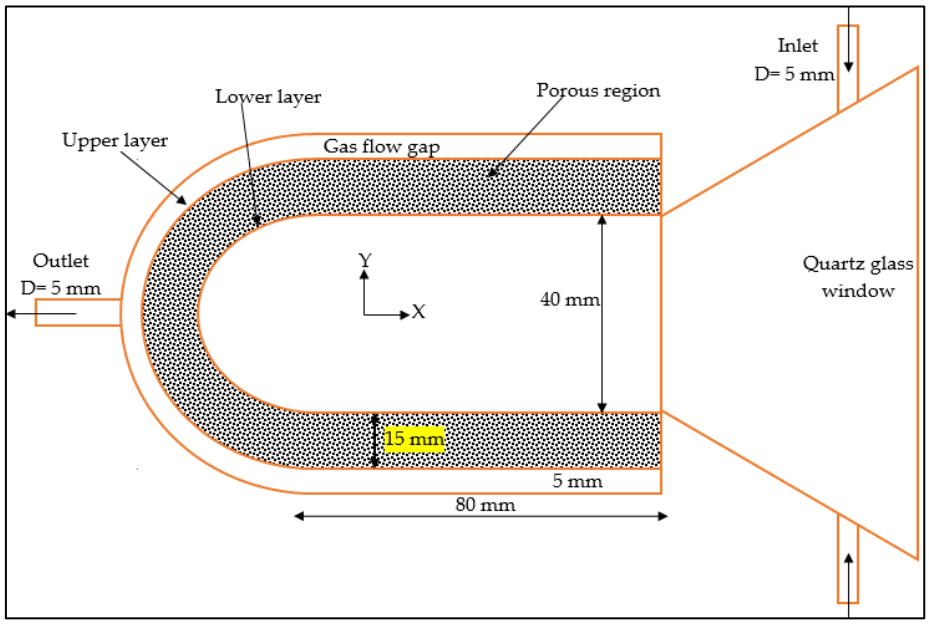

Fig. 28: Schematic displaying dimensions of the solar thermochemical reactor-receiver cavity

In front of the cavity aperture, a transparent quartz glass window is placed which allows the solar radiation to enter the cavity. The solar heat flux on the quartz glass window is applied using a user define functions: UDF heat flux profile in ANSYS fluent version *16.2*. Inlets and outlet are provided in the cavity for the circulation of flowing fluids (nitrogen and argon). As the solar flux radiates the cavity and increases its temperature, the flowing fluid are injected from the inlet, pass through the porous media and exit from the outlet. Flowing fluid allows the temperature to be distributed uniformly in the porous region. The outer region of the cavity is packed in stainless-steel shell and outer layers are made fully insulated to reduce the thermal loss. As some geometric factor affect the thermal performance of the solar thermochemical cavity. In this paper, the effect of RPC thickness and gas flow gap on the thermal performance of reactor cavity has been investigated. The main focus of the study is maintained on the radial and axial heat transfer as well as the distribution of heat flux in the solar thermochemical cavity. In this investigation, entire cavity has been simulated using CFD technique. ANSYS fluent v.*16.2* was used to carry out the simulation.

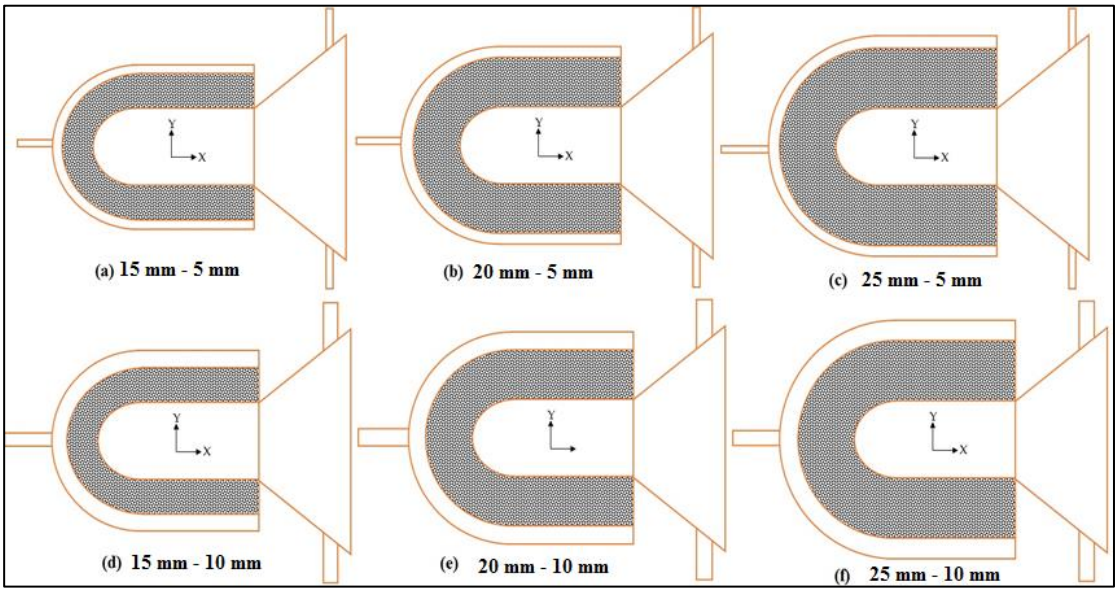

Fig. 29: Cases considered in numerical simulation

RPC based solar thermochemical reactor as shown in Fig. 28 used for numerical simulation. Solar concentrated radiation enters into the reactor cavity through the transparent quartz glass window and heats the RPC region to enable the redox reactions. The nitrogen gas is fed into the reactor cavity through the inlets to sweep the remains

of hydrogen or oxygen from the cavity. Six different reactor cavity models as shown in Fig. 29 were considered for the numerical simulation. Fig. 29(a), (b), and (c) show the reactor cavities having the RPC thickness as 15 mm, 20 mm, and 25 mm, respectively with 5 mm gas flow gap. Whereas, Fig. 29(d), (e), and (f) show the reactor cavities having RPC thickness as 15 mm, 20 mm, and 25 mm, respectively but the gas flow gap is increased to 10 mm.

4.3 Mathematical and numerical approach

The governing equations used in the present simulations are given as follows [106][198]:

(i) Conservation of mass

Steady state: $\frac{\partial \rho}{\partial t} + \nabla.\left(\rho_f v\right) = 0$ (44)

ρ_f and v represents the fluid density and superficial velocity of fluid, respectively.

However, when the mass transfer occurs in the RPC domain the mass conservation equation of non-reactive RPC zone is given below;

Mass transfer

$$\frac{\partial(\rho_f Y_i)}{\partial t} + \nabla.(\rho_f v Y_i) = 0 \quad (45)$$

$$\frac{\partial(\chi\rho_f Y_{O_2})}{\partial t} + \nabla.(\chi\rho_f v Y_{O_2}) = S_{m,O_2} \quad (46)$$

$$\frac{dm_p}{dt} = \dot{m}_p \quad (47)$$

In the above given equations, component concentration, particle mass transfer rate and mass source term are denoted by *Yi*, $\dot{m}_p$ and S_{m,O_2}, respectively. The absolute value of particle mass transfer rate equals the rate of oxygen evolution. The particle mass changed fraction defines the reaction rate as shown [199];

$$\frac{dx}{dt} = k_{red}(1-x) \quad (48)$$

$$x = \frac{m - m_i}{m_f - m_i} \tag{49}$$

In the above given equations, k_{red} is the reduction rate co-efficient and *m, mi* and $m_f$denote the time-dependent, initial and final mass of the particle and the value of m can be calculated by the Eq. (50)

$$m = m_i - \delta n_{CeO_2} \frac{M_{O_2}}{2} \tag{50}$$

Thus, the reaction rate can be given as Eq. (51)

$$\frac{dm_p}{dt} = (m_f - m_i) k_{red} \left(1 + \frac{\delta \frac{m_i}{M_{CeO_2}} M_{O_2}}{2(m_f - m_i)} \right) \tag{51}$$

$$\frac{\delta}{(0.35 - \delta)} = 8700 \left(P_{O_2} bar \right)^{-0.217} \exp\left(-195.6\ kJ - mol^{-1} / RT \right) \tag{52}$$

In the above given equation, δ denotes the non-stoichiometric coefficient and it depends on the reaction temperature as well as the oxygen partial pressure [200]. The oxygen partial pressure can be calculated from the Eq. (53);

$$P_{O_2} = (M_{O_2} \times P_{tot}) \tag{53}$$

(ii) Conservation of momentum

The momentum conservation equation in the porous media based STCR is solved as;

$$\frac{\partial}{\partial t}\left(\rho \overset{\mathrm{r}}{v} \right) + \nabla . \left(\rho \overset{\mathrm{rr}}{v v} \right) = -\nabla p + \nabla . \left(\mu \nabla \overset{\mathrm{r}}{v} \right) + S_p \tag{54}$$

In the above given Eq. (54), the S_p is denotes the fluid pressure drop source term and *P* and μ designates the fluid pressure drop and dynamic viscosity, respectively. The pressure drop source term is calculated as [48]:

$$S_p = -\left(\frac{1039-1002\phi}{{d_s}^2}\right)\mu u - \left(\frac{0.5138\phi^{-5.739}}{{d_s}^2}\right)\rho_f u^2; \quad 0.66 \le \phi \le 0.93 \qquad (55)$$

In the above given Eq. (55), ϕ and d_s denote material porosity and mean cell size, respectively. The flow is given at fluid inlet in the porous media, the gradient is set *0* at the fluid outlet.

Inlet: $u = u_0$, $v = 0$

Outlet: $\frac{\partial u}{\partial x} = \frac{\partial u}{\partial y} = \frac{\partial v}{\partial x} = \frac{\partial u}{\partial y} = 0$

(iii) Conservation of energy

$$\frac{\partial}{\partial t}(\rho h - p) + \nabla.\left[\overset{\mathrm{r}}{v}(\rho h)\right] = \nabla.(\lambda_{eff,f}\nabla T) + S_h \qquad (56)$$

In the above equation, S_h is known as the source term which allows the convective heat transfer between solid and fluid phase.

$$S_h = h_v(T_s - T_f) \qquad (57)$$

where h_v (W/m^3k) is known as volumetric convection heat transfer coefficient and it can be calculated using the correlation given by Wu et al. [48]

$$h_v = \frac{\lambda_f\left(32.504\phi^{0.38} - 109.94\phi^{1.38} + 166.65\phi^{2.38} - 86.98\phi^{3.38}\right)\mathrm{Re}^{0.438}}{{d_s}^2}; \quad \left(0.66 \le \phi \le 0.93 \; and \; 70 \le \mathrm{Re} \le 800\right) \qquad (58)$$

For solid zones, the Eq. (19) becomes,

$$\frac{\partial}{\partial t}(\rho h) = \nabla.(\lambda_{eff,s}\nabla T) + S_s \qquad (59)$$

$\lambda_{eff,f}$ and $\lambda_{eff,s}$ denote the effective thermal conductivity of the fluid and solid phase, respectively and Ss known as volumetric heat source term. These entities can be calculated using the following given correlations [108];

$$\lambda_{eff,f} = \phi\lambda_f \tag{60}$$

$$\lambda_{eff,s} = \lambda_s(1-\phi) \tag{61}$$

The source term includes the radiative (S_{rad}), convective ($S_{conv,s}$) as well as heat dissipation (S_w).

$$S_s = S_{conv,s} + S_{rad} + S_w \tag{62}$$

- Convective heat transfer source term:

The convective heat transfer source term calculates the heat transfer between solid and fluid phase.

$$S_{conv,s} = -S_{conv,f} = -h_v(T_s - T_f) \tag{63}$$

- Wall heat dissipation source term:

Solar thermochemical reactor operates at high temperature thus the heat dissipation consideration becomes crucial and it can be calculated by following equation,

$$S_w = -\varepsilon_w\sigma(T_s^4 - T_0^4) \tag{64}$$

(iv) Radiative transfer equation

The solution of radiative transfer equation (RTE) [201] gives the irradiative source term mentioned in Eq. (65)

$$\frac{dI(s)}{ds} = -k_e I(s) + k_a I_b(s) + \frac{k_s}{4\pi}\int_{4\pi} I(s,\vec{\Omega}')\phi(\vec{\Omega}',\vec{\Omega})d\Omega' \tag{65}$$

In the equation given above, I denotes the local radiation intensity in the porous medium and ke is known as the extinction coefficient [202]. The absorption and scattering coefficient can be calculated using correlations given below [108];

$$k_a = \frac{3\varepsilon(1-\phi)}{2d_s} \tag{66}$$

$$k_s = \frac{3(2-\varepsilon)(1-\phi)}{2d_s} \tag{67}$$

$$k_e = k_a + k_s = \frac{3(1-\phi)}{d_s} \tag{68}$$

Discrete Ordinates irradiative transfer model

The energy and radiative transfer equation for fluid flow through the porous media can be written as follow [109];

Fluid energy equation:

$$-\varphi\rho_f u_f c_f \frac{\partial T_f}{\partial x} - (1-\varphi)hA(T_f - T_s) + \varphi Q(y)\delta(x) + \varphi k_f \left(\frac{\partial^2 T_f}{\partial x^2} + \frac{\partial^2 T_f}{\partial y^2} \right) = 0 \tag{69}$$

Solid energy equation:

$$\nabla . q + (1-\varphi)hA(T_s - T_f) - (1-\varphi)k_s \left(\frac{\partial^2 T_s}{\partial x^2} + \frac{\partial^2 T_s}{\partial y^2} \right) = 0 \tag{70}$$

In the above given equations, h is the heat transfer coefficient and A is the surface area of the porous medium. The thermal conduction via. gas can be easily neglected due to the poor thermal conductivity of the inert gas. In discrete ordinates (DO) radiation model, the radiative transfer equation (RTE) are solved for finite number of discrete solid angles. Each angle is in association with directional vector ($\vec{s}$). The number of transport equation solved by *DO* model are equal to the directions ($\vec{s}$).

4.3.1 Reactor model configurations

The effects of RPC thickness and gas flow gap variation on the thermal and fluid flow characteristics in the solar thermochemical reactor cavity were studied. The configurations for six STCR cavity models have been presented in Table 3. The initial and boundary conditions adopted in the simulation are listed in Table 4 and Table 5. The RPC zone consists of RPC with varying thickness (15-25 mm) as well as the gas flow gap (5-10 mm). The inlet velocities were calculated in Reynolds number range of 100-300. The non-uniform flux profile was applied to the quartz glass window to generate the uniform temperature in the porous region of the reactor cavity. The

outermost surface of the reactor cavity was made fully insulated to reduce the thermal loss.

Table 4: Reactor cavity model configurations

Part name	***Case-1 Dimensions (mm)***	***Case -2 Dimensions (mm)***	***Case -3 Dimensions (mm)***	***Case -4 Dimensions (mm)***	***Case -5 Dimensions (mm)***	***Case -6 Dimensions (mm)***
Cylindrical Length	*80*	*80*	*80*	*80*	*80*	*80*
Hemispherical inner radius	*20*	*20*	*20*	*20*	*20*	*20*
RPC thickness	*15*	*20*	*25*	*15*	*20*	*25*
H_2/O_2 flow gap	*5*	*5*	*5*	*10*	*10*	*10*
Inlet diameter	*5*	*5*	*5*	*10*	*10*	*10*
Outlet diameter	*5*	*5*	*5*	*10*	*10*	*10*
Total length of cavity	*120*	*125*	*130*	*125*	*130*	*135*

Table 5: Initial conditions

Preheating stage	
$T_{initial}$	*300 K*
Pressure	*1 atm*
Species mole ratio	$N_2:O_2::1:0$
Ceria reduction stage	
$T_{initial}$	*1300 K*
Species mole ratio	$N_2:O_2::1:1e\text{-}5$
Rate of reaction	*0*

Table 6: Boundary conditions

Surface	*Boundary conditions*
Inlets	$v_{inlet} = \frac{\overset{*}{v}}{Ac_{inlet}};\ T_{inlet} = T_{initial};\ n_{N_2} : n_{O_2} = 1:10^{-5}$
Outlet	$P_{out} = P_{atm}$
Inner surface	$k_q \frac{\partial T}{\partial n} = S_{E,rad} + h_q \Delta T;\ \varepsilon = 0.08,\ \tau = 0.86$
Insulation wall	$k_s \frac{\partial T}{\partial n} = \Delta q_r + h_s \Delta T;\quad \varepsilon = 0.28,\ \tau = 0$
Quartz window	$T_{aperture} = T_{initial};\ \varepsilon = 0.08,\ \tau = 0.86$
Other surfaces	$\frac{\partial T}{\partial n} = 0$

4.3.2 Reaction Kinetics

The empirical co-relations for reaction kinetics for cerium oxide at the high-temperature thermal reduction temperature (T_H) such as 1600 K or above have not been mentioned in the literature. Therefore, in this study, a modified expression for the kinetic reaction, initially presented by Bulfin et al. [203], for the re-oxidation of cerium oxide have been used. The oxygen generation vacancy rate has been presented as a function of re-oxidation rate (k_{ox}) as mentioned in the Eq. (71).

$$\frac{d\delta}{dt} = k_{ox}\delta\left[\left(\frac{p_{o_2,eq}}{p_{ref}}\right)^n - \left(\frac{p_{o_2}}{p_{ref}}\right)^n\right] \tag{71}$$

where,

$$k_{ox} = A_{ox}\exp\left(-\frac{E_{ox}}{R_u T}\right) \tag{72}$$

The mass source term for the oxygen evolution from the re-oxidation of cerium oxide have been given below;

$$\dot{r}_{o_2,CeO_2} = \frac{M_{O_2}}{2M_{CeO_2}}(1-\phi_{eff})\rho_{CeO_2}k_{ox}\delta\left[\left(\frac{p_{o_2,eq}}{p_{ref}}\right)^n - \left(\frac{p_{o_2}}{p_{ref}}\right)^n\right] \quad (73)$$

4.4 Numerical implementation and study validation

To carry out the numerical simulation, the solar collector was simulated using an open source software, SolTrace, which traces the solar ray path by MCRT technique. MCRT uniformly distributes solar power by dividing it into larger number of rays determined by the sun shape and slope error [204], [205]. The interaction between the rays and the reactor cavity is influenced by the transmissivity, reflectivity and absorptivity. The flux profile obtained from the SolTrace shown in Fig. 9 (b) was validated against Lee's study as shown in Fig. 8 (b) and further used as radiative flux boundary condition on the quartz glass window.

ANSYS Fluent v.16.2 solver was used to solve the conservation equations by the finite volume method with a tetragonal/hexagonal unstructured mesh having 0.5 mm element size. The DO radiation model was applied to calculate the radiation heat transfer (RTE equation) in the solar thermochemical reactor cavity. Steady-state simulation with SIMPLE first-order upwind for discrete ordinates and second order for energy calculation was implemented. The transient simulation for cavity preheating as well as CeO_2 reduction was carried out using first order implicit unsteady scheme having a time step of 0.2 second. The non-stoichiometric CeO_2 reduction was modelled by species transfer at porous wall surface to solve the mass transfer equations.

The quality of the mesh is one of the crucial factors which affects the numerical results. Thus, it becomes necessary to adopt adequate mesh for the numerical simulations to obtain precise results. To carry out mesh independence analysis, nine mesh sizes were compared. The plot in the Fig. 30(a) shows that as the number of elements increases, the temperature of the reactor cavity reduces and provides results with accuracy. Finally, the temperature deviation reduces to a minimum between element sizes 0.3 mm to 0.2 mm. Thus, 0.3 mm mesh element size with 83102 elements was adopted in this numerical study.

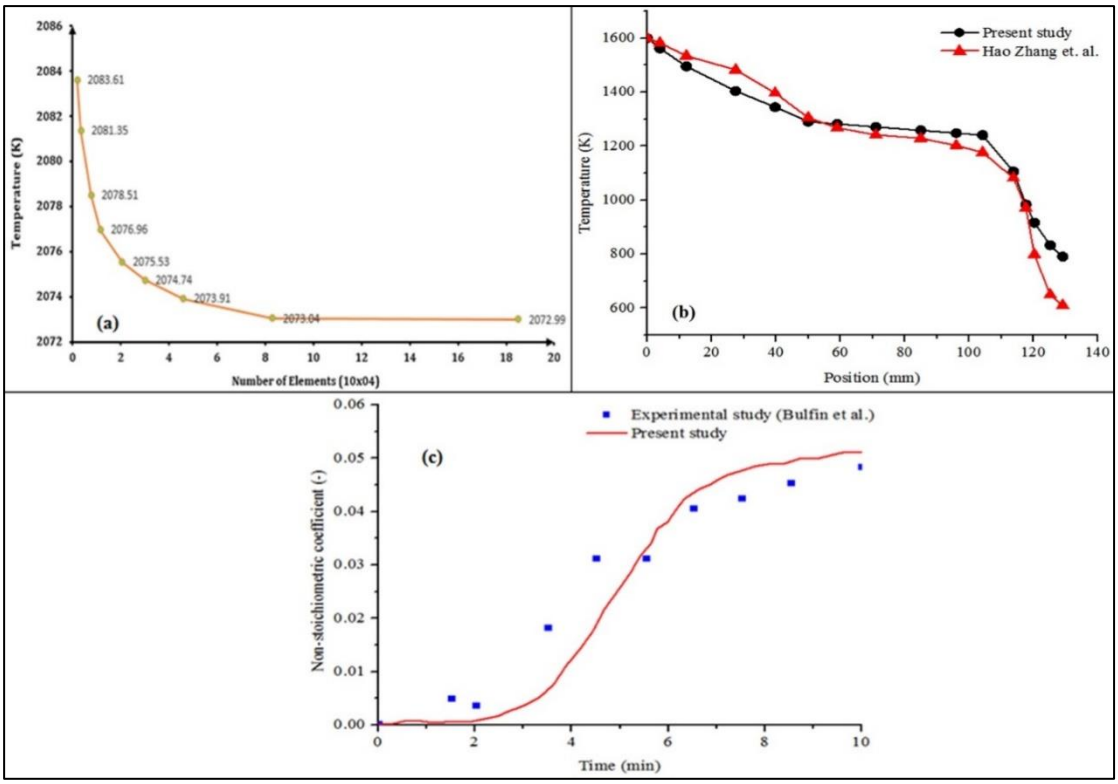

Fig. 30: (a) Grid (mesh) independence analysis, (b) Fluid phase temperature distribution along the centerline of solar thermochemical reactor compared with Zhang et. al. [111], (c) Non-stoichiometric coefficient (δ) against time validated with Bulfin et al.[203]

The study carried out by Zhang et al. [111] is used to validate the numerical model adopted in this study. P1 approximation radiation model with similar operating and boundary conditions were used in a SiC porous-media based reactor cavity with porosity of 0.8, the emissivity of 0.92, and mean cell size 1.5 mm. The density, thermal conductivity, and heat capacity of porous SiC were considered as 3200 kg/m^3, 80 W/(m^2-K), and 750 J/(kg-K), respectively. The total depth of the cavity and the porous medium was taken as 130 mm and 60 mm, respectively. Air was considered as flowing fluid inside the cavity. The velocity of flowing fluid was taken as 0.005m/s and the inlet temperature were considered to be 300 K. The fluid phase temperature distribution along the centerline of the solar thermochemical reactor was compared with the referred study. Fig. 30(b) shows good agreement between the fluid phase temperatures of both simulations. Hence present numerical scheme is used for analysis.

The thermodynamic and Ceria reduction models were simulated and validated against the experimental results of non-stoichiometric coefficient with bulfin et

al.[203]. The reduction reaction of ceria pellet with 65% void fraction subjected to 100W radiative power was modelled. The results of CeO_2 non-stoichiometric coefficient between the present numerical study and the experimental data as shown in the Fig. 30(c). The minor differences in the comparable results are caused by the operating conditions and simulation assumptions.

4.5 Results and discussion

4.5.1 RPC thickness

The RPC thickness of the reactor cavity was varied to study its effects on solar flux distribution and temperature distribution in porous media. Fig. 31 shows the temperature contours for RPC thickness of 15 to 25 mm with 5 mm gas flow gap. It can be seen for 15 mm RPC thickness, argon and nitrogen gases generate uniform temperature distribution for Reynolds number 100. However, as the value of Reynolds number increases to 300, the cavity temperature reduces.

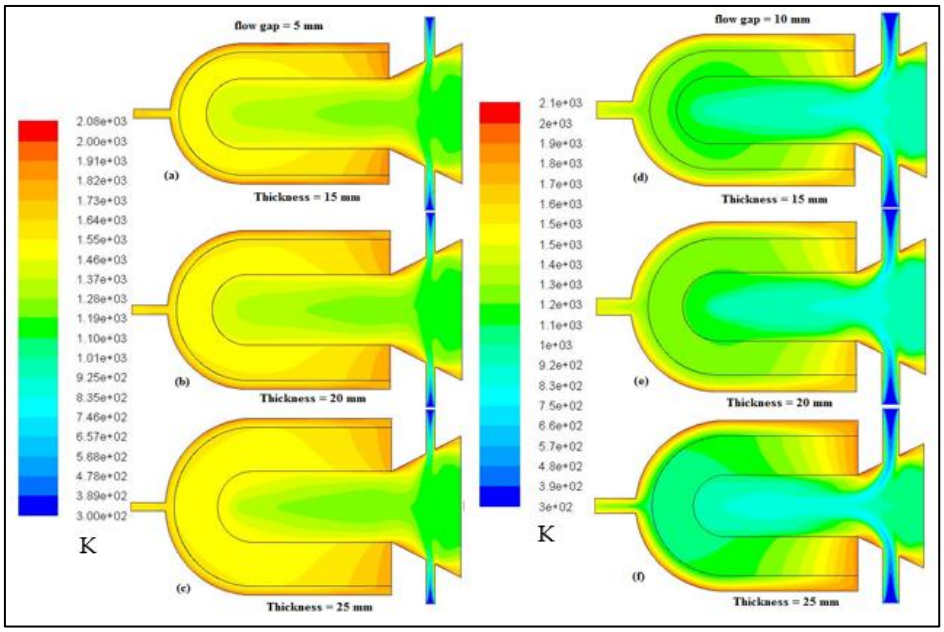

Fig. 31: Fluid phase temperature (K) contours of 15 mm, 20 and 25 RPC thickness with 5 mm and 10 mm inert gas (N_2) flow gap

Similar temperature distribution can be seen for 20 mm and 25 mm RPC thickness. Fig. 31 shows the temperature contours for RPC thickness of 15, 20 and 25 mm with 10 mm gas flow gap. It can be seen that when the gas flow gap is increases, the fluid velocity decreases and fluid spend rather more time in the cavity before it exits through the outlet as compared to the 5 mm gas flow gap.

4.5.1.1 Temperature distribution in the radial direction

The non-uniform radiation heat flux profile was applied at the front transparent quartz glass window. As the flux enters the reactor cavity, it heats the cavity and generates the temperature distribution in the radial as well as in the axial direction in the porous RPC region. The analysis of temperature distribution in the radial direction in porous media having different thickness (15 mm, 20 mm & 25 mm) are studied which allows better understanding of the optimum required thickness of the porous region in the solar thermochemical cavity. Fig. 32 (a) show the radial temperature distribution in porous media for 25 mm RPC thickness with5 mm and 10 mm gas flow gap, respectively.

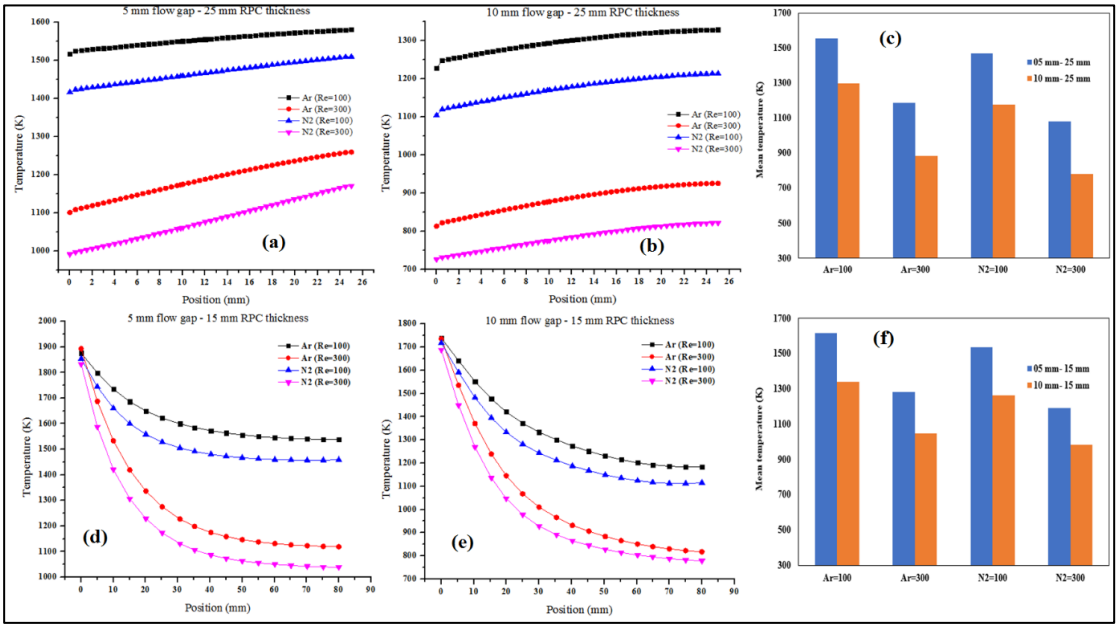

Fig. 32: Temperature plot for (a) 25 mm RPC thickness – 5 mm flow gap; (b) 25 mm RPC thickness – 10 mm flow gap in radial direction; (c) Bar graph showing the mean temperatures in radial direction of porous media; & (d) 15 mm RPC thickness – 5 mm flow gap; (e) 15 mm RPC thickness – 10 mm flow gap in axial direction; (f) Bar graph showing the mean temperatures in axial direction of porous media

The temperature in the RPC region with *5 mm* flow gap is uniformly distributed for both flowing fluids. However, the increasing value of the Reynolds number affects the temperature distribution. The upper layer temperature of porous media goes up to *1580.91 K* and *1509.94 K* for argon and nitrogen, respectively. The avg. temperature of porous media for argon and nitrogen is recorded to be *1549.08 K* and *1463.38 K*, respectively. The increasing thickness of the gas flow gap from *5 mm* to *10 mm* substantially decreases the porous media temperature in the radial direction as shown

in the Fig. 32 (b).The avg. temperature of the porous media drops by *270.3* K and *304.35* K and it suggests that in any case argon is better choice as inert gas in STCR cavity to maintain higher temperature.

4.5.1.2 Temperature distribution in the axial direction

The analysis of temperature distribution in the axial direction in porous media is necessary to have a better understanding of the optimum required length of the RPC region in the solar thermochemical cavity.

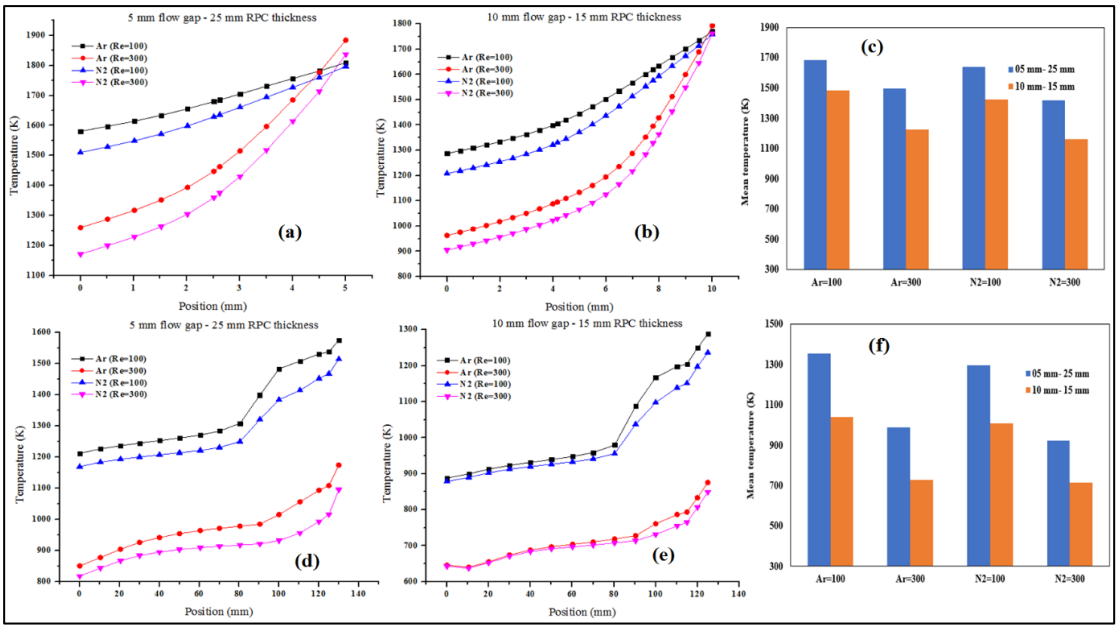

Fig. 33: Temperature plot for (a) 5 mm flow gap; (b) 10 mm flow gap; (c) Bar graph showing the mean temperature for 5 mm and 10 mm gas flow gap; & (d) Reactor temperatures for 15 mm RPC thickness –5 mm flow gap; (e) 15 mm RPC thickness –10 mm flow gap along the centerline; (f) Bar graph showing the mean temperatures for 5 mm and 10 mm gas flow gap with 25 mm and 15 mm RPC thickness, respectively

The temperature distribution in the axial direction in the porous media for 15 mm RPC thickness with5 mm and 10 mm gas flow gap for two flowing fluids, nitrogen and argon has been shown in Fig. 32 (c) & (d). The radiative flux generates the uniform temperature distribution over the porous media length of 80 mm. The combination of 5 mm flow gap and Ar gas makes the perfect combination to achieve the required high temperature in the porous media to initiate the redox reactions. The average temperature of porous media is decreased by 50.98 K for nitrogen as compared to argon at Re=100.

4.5.2 Effect of gas flow gap

The gas flow gap prolongs the gas and reactant (RPC) contact time and path in the preheating stage. Thus, it becomes crucial to analyze the influences of gas flow gap in the STCR cavity. The radial temperature distribution in the gas flow gap of 5 mm and 10 mm has been plotted in the Fig. 33 (a) & (b), respectively. In the gas flow region, argon and nitrogen both achieve almost same temperature and also it has been seen that the 5 mm gas flow gap is more suitable option as it offers low temperature gradient in the radial direction as compared to 10 mm flow gap. As fluid comes down through the inlet and moves through the porous media, it creates a vortex along the porous media and gas flow gap contact region. As the gas flow gas is increased from 5 mm to 10 mm, the effect of vortex gets subdued. Increasing velocity in the gas flow gap and the RPC region leads to vortex formation. Narrow gas flow gap increases the velocity and since the RPC thickness remains content, the fluid hits the insulation walls and alters the velocity vector direction. It is clearly evident that as the gas flow gap increases with constant RPC thickness, the average temperature decreases.

4.5.3 Temperature distribution along the STCR centerline

The analysis of temperature distribution in the solar thermochemical reactor cavity is necessary to have a better understanding of the optimum required length of the cavity receiver to carry out the solar thermochemical water splitting process efficiently. The temperature distribution in the STCR cavity along the centerline for 25 mm RPC thickness with 5 mm gas flow gap and 15 mm RPC thickness with 10 mm gas flow case have been shown in Fig. 33 (c) & (d), respectively. The temperature for both flowing fluids is uniformly distributed over the entire length of the cavity. However, as the velocity increases, the average temperature of the porous media decreases but the average temperature for argon for all cases remains higher compared to nitrogen due to strong cooling effect of nitrogen. The increasing thickness of RPC zone combined with content gas flow gap leads to decrease in the average fluid temperature in the STCR cavity along the centerline. From the temperature distribution in steady state and transient analysis in the STCR cavity, it is evident that argon achieves slightly higher temperature as compared to nitrogen in STCR cavity as well as in the porous region. However, when reduction cycle completes and oxidation cycle starts, temperature

needs to be reduced and nitrogen works as a controlling factor due to its cooling capacity. Thus, nitrogen gas proves itself a quite suitable candidate as sweep gas.

4.5.4 Distribution of solar flux

The solar flux profile is applied to the transparent front quartz window. The solar flux enters into the cavity and heats the entire reactor cavity including flowing fluid and cavity walls from inside. Solar flux distribution inside the solar thermochemical cavity for 15 mm, 20 mm and 25 mm RPC thickness has been shown Fig. 34.

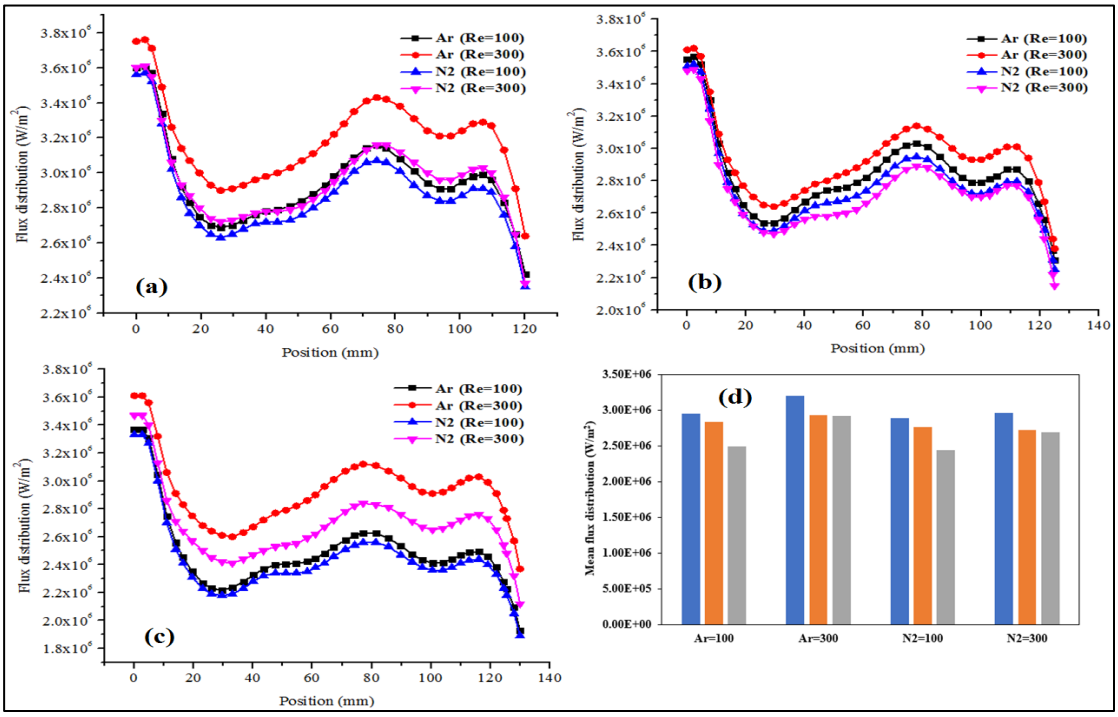

Fig. 34: Flux distribution in the solar thermochemical cavity; (a) RPC thickness 15 mm; (b) RPC thickness 20 mm; (c) RPC thickness 25 mm with 5 mm flow gap

The solar flux distribution is uniformly distributed in the STCR cavity and it shows higher magnitude at the front quartz window side and lowest at the outlet side. The flux distribution is highly affected by the cooling effect of the flowing fluid and fluid velocity. The highest magnitude is seen in the cavity with *15 mm* RPC thickness and lowest in the cavity with *25 mm* RPC thickness.

4.5.5 Transient analysis

Solar thermochemical water splitting is a time bound chemical process which occurs in two subsequent steps. To simulate the first *i.e.* reduction step of ceria based

solar thermochemical cycle for chemical reaction analysis, transient study was also carried out. This step was subsequently divided into two part were in the first part the STCR cavity was first preheated for the period of two minutes to evaluate the rise in temperature and in the second part, the ceria reduction reaction was initiated and carried out for *10* minutes while subjecting the RPC medium at the initial temperature of *1280* K.

4.5.5.1 Pre – heating stage

Since the reduction of ceria is high-temperature based reaction thus, preheating allows the cavity to reach at a temperature where the reduction takes without further delay. The radiative flux is uniformly distributed in the interface regions and in the porous domain. Since the volume of the STCR cavity remains constrained, there is a commutation between cavity and the reactive RPC region. There RPC thickness (15 mm, 20 mm, and 25 mm) has been studied and the velocity profiles has been shown in Fig. 35(1). The larger cavity space improves the velocity distribution and gas velocity reaches to a relative uniform value before entering the porous region. The vortex gets formed in the smaller RPC thickness (15 mm) cavity which forms a dead zone close to the porous region interface as seen from the velocity contours. The dead zone doesn't allow efficient heat transfer as well as the reaction mechanism in the reactive RPC region. However, these conditions seen to be improved significantly in the 25 mm RPC thickness cavity.

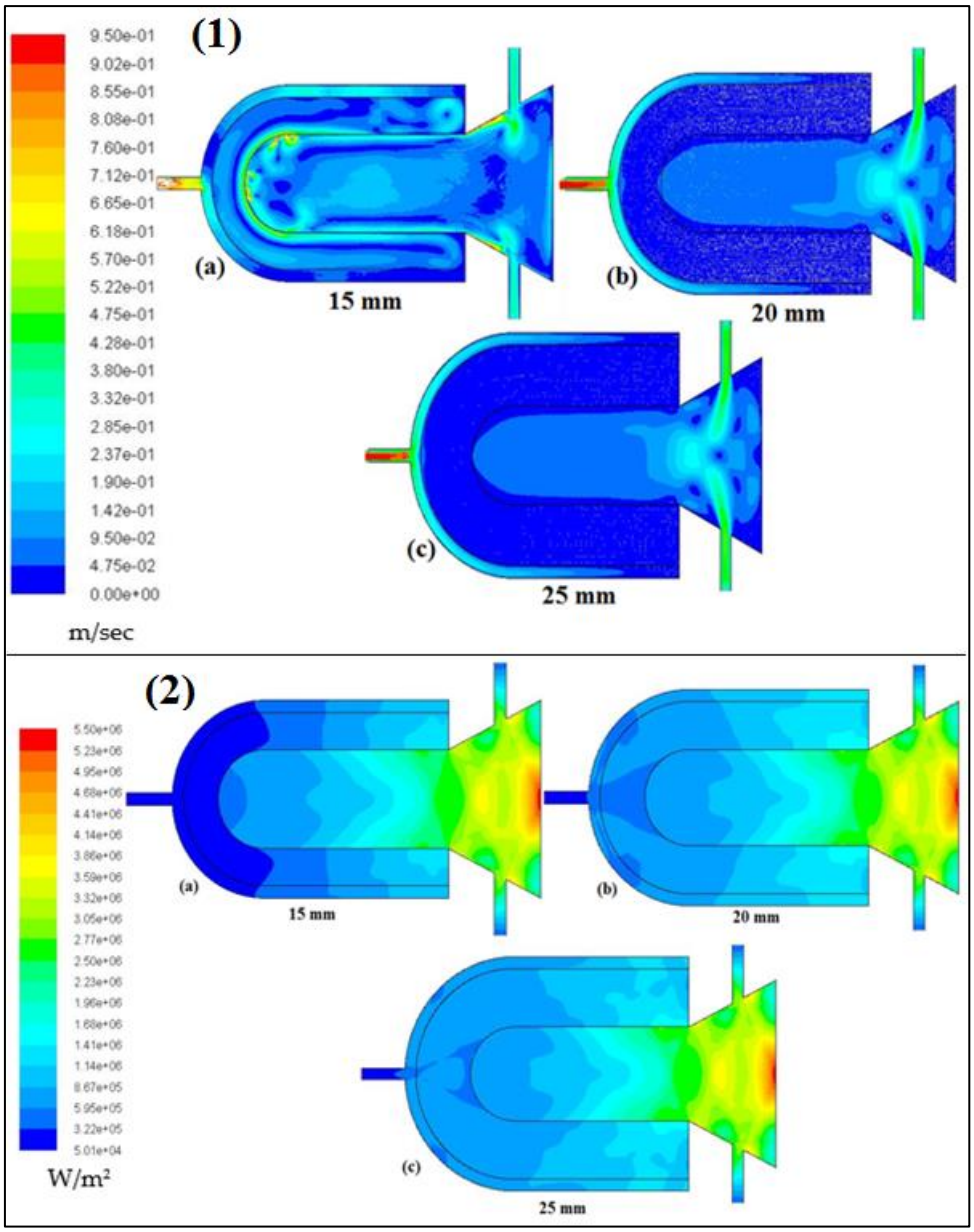

Fig. 35: (1) Time dependent velocity distribution & (2) Time dependent incident irradiation contours at 120 sec

The variation in RPC thickness plays a crucial role in achieving the uniform flux distribution in the STCR cavity. Moreover, thermofluidic characteristics are also influenced by the RPC thickness which allow to attain required operational temperature to carry out redox reactions. The contours for incident radiation for all three cases at 120 sec has been shown in Fig. 35(2). The STCR cavity with 15 mm RPC thickness attains the lowest radiant flux whereas 25 mm RPC thickness cavity attains the highest magnitude radiant flux at the same power. Given the operating CDF algorithm for DO

model, the incident radiation takes account of the receiving radiation for each cell which can be seen in the flux distribution contours. The aperture of all three cavities are same (40 mm) thus radial radiative transfer path for incident radiation becomes the strongest factor to influence the uniform flux distribution in the cavity porous region. The STCR cavity with 25 mm RPC thickness has the longest radial path which allows the development and uniform distribution of radiation flux as shown in Fig. 35 (2)-(c).

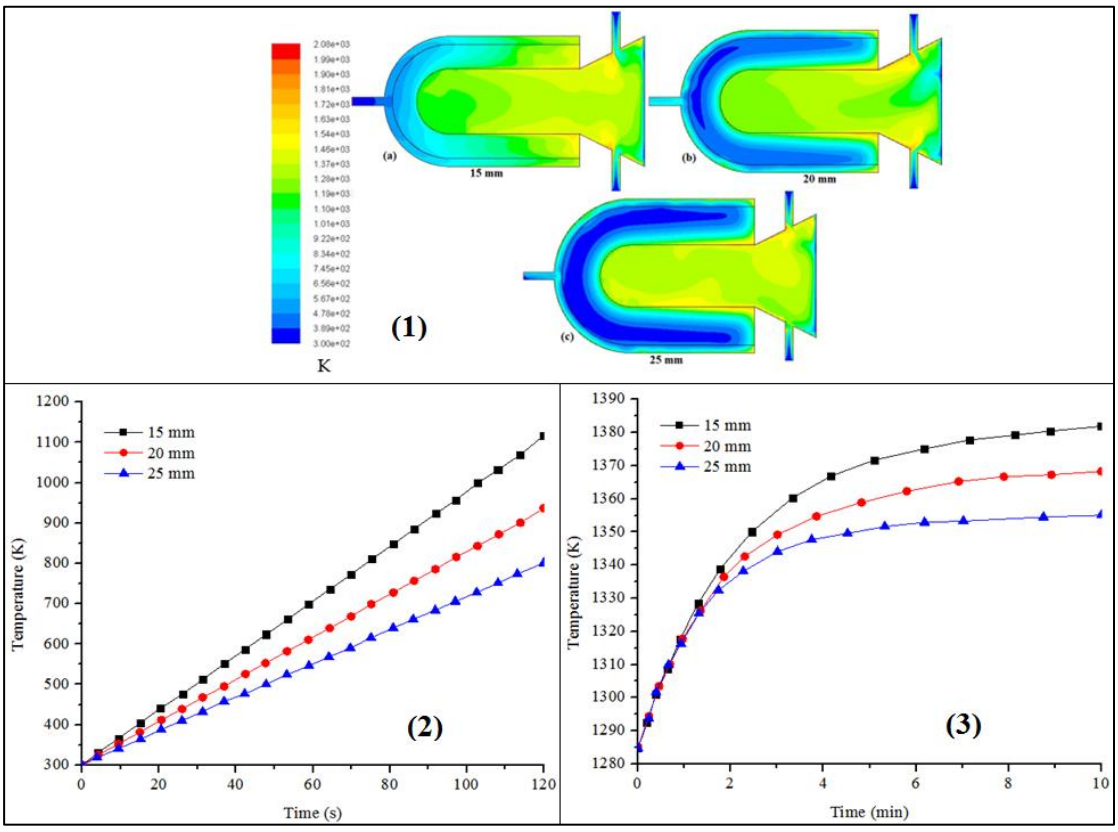

Fig. 36: (1) Time dependent temperature contours at 120 sec; (2) Time dependent temperature distribution for different RPC thickness at 120 sec & (3) Time dependent fluid phase temperature of porous media during reduction reaction at 10 mins

The temperature contours considering the conjugate heat transfer at 120 sec has been shown in Fig. 36 (1). The higher temperature in the STCR cavity with 15 mm RPC region is due to the higher incident irradiation distribution. Even though, the temperature is also higher in 20 mm and 25 mm thick RPC cavity but the incident irradiation distribution is not consistent which directly affects the temperature distribution in the whole cavity. This phenomenon can be explained as the opposite influences of radiation and convention heat transfer in porous region. The strong heat convection between the incoming cold fluid and porous interface leads to temperature

drop due to dominating heat convection where all the accumulated energy in the porous region is transferred to the cold fluid which results in low temperature in the RPC zone. Time dependent temperature profiles for all three RPC thickness has been shown in Fig. 36(2). The fluid phase temperatures of 15 mm and 25 mm RPC thickness attains the highest and the lowest temperature, respectively in 120 sec. However, it was seen that the 15 mm RPC zone shows comparatively more variation in fluid phase due to convection effects. In each case, the temperature profiles are consistent with incident radiation flux.

4.5.6 Solar-to-fuel conversion efficiency

The reduction reaction step was initiated for H_2O dissociation which gives the oxygen evolution. Firstly, the thermodynamic analysis was carried out using HSC chemistry software as shown in the Table 6. As results show in Fig. 37 (a) that ΔG (Gibbs free energy) increases with the increasing temperature in reduction reaction of ceria. For instance, in ceria reduction reaction ΔG increases from 140.70 kcal to 295.167 kcal at the temperature increase of 773 K to 1773 K. The vapor pressure in the thermal reduction reaction of ceria is plotted in the Fig. 37 (b). It was indicated that the reduction temperature has strong influence on the vapor pressure as it reduces at first with increasing temperature till 1273 K and reduces afterwards.

Table 7: Thermodynamic analysis of CeO_2 reduction step

T (^{0}C)	delta H (kcal)	delta S (cal/K)	delta G (kcal)	K	Log(K)
500	81.241	-76.907	140.702	1.67E-40	-39.776
600	65.372	-96.206	149.374	4.06E-38	-37.392
700	49.243	-113.693	159.883	1.23E-36	-35.909
800	32.869	-129.707	172.064	9.03E-36	-35.044
900	16.263	-144.5	185.784	2.44E-35	-34.613
1000	-0.569	-158.268	200.93	3.20E-35	-34.495
1100	-17.621	-171.161	217.408	2.48E-35	-34.605
1200	-34.891	-183.3	235.137	1.30E-35	-34.887
1300	-52.374	-194.781	254.046	5.06E-36	-35.296
1400	-70.069	-205.685	274.074	1.57E-36	-35.803
1500	-87.973	-216.078	295.166	4.13E-37	-36.384

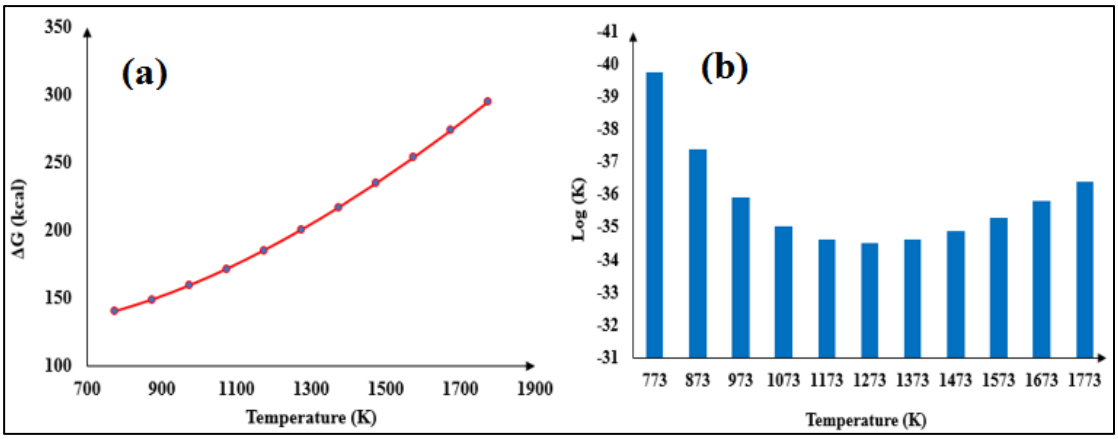

Fig. 37: (a) Change in Gibbs free energy as a function of reduction temperature& (b) oxygen partial pressure in the inert gas at reduction temperature

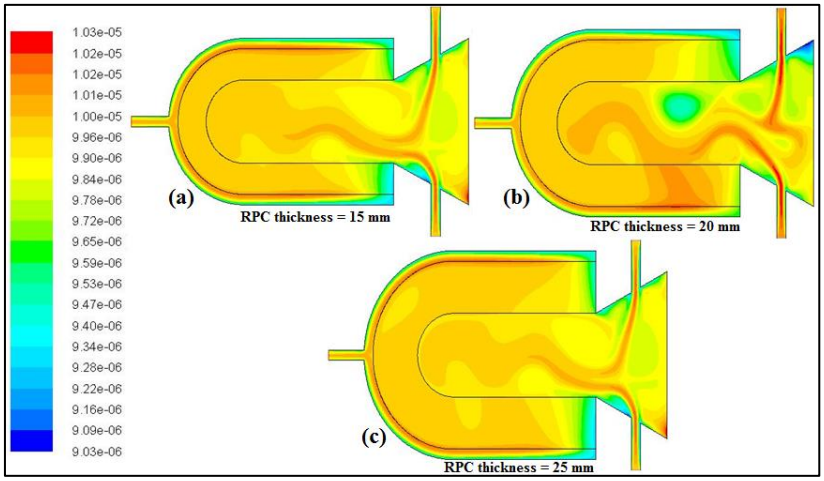

Fig. 38: Molar fraction contours of Oxygen

The CeO_2 reduction reaction is thermodynamically analyzed to be initiated at above 1200 K. Thus, the reduction reaction was carried out for 10 mins under SolTrace generated solar flux profile. Since, the rate of reaction is the function of temperature, the time dependent fluid phase temperature of porous media at 10 mins has been plotted in Fig. 36 (3). The temperature profiles of all three RPC thickness clearly indicate that the 15 mm RPC thickness achieve the highest temperature among all three porous media thicknesses, which is indistinctively consistent with the flux profiles and steady state heat transfer results. Time dependent oxygen concentration at peak oxygen evolution has been shown in Fig. 38 .It has been observed that the RPC zone exposed to higher temperature tends to reach peak value of oxygen concentration. The oxygen evolution rates for different RPC thicknesses for this study has been plotted in Fig. 39 and compared with the Zhang et al. [206].The study performed by Zhang et al. [206]

reported the oxygen evolution about 0.929 mL/gCeO_2 and 1.184 mL/gCeO_2 in 5 minutes for the 20mm and 30mmRPCs, respectively. However, when the ceria mass loading is considered, the oxygen evolution in 5 minutes goes up to 1179.8 mL and 1973.6 mL and the theoretical solar-to-fuel efficiency is 9.5% and 15.9% (without heat recovery) for 20 mm and 30 mm, respectively. while in this study, the RPC zone having 25 mm thickness yields the highest rate of oxygen evolution, about 0.34 mL/min/gCeO_2.

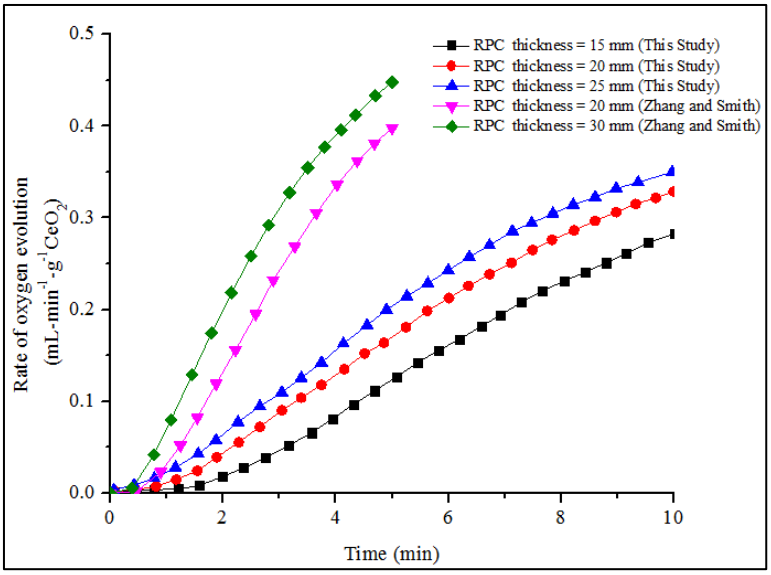

Fig. 39: Oxygen evolution rates plot in the CeO_2 reduction process

The total amount of oxygen generation for all three RPC thickness in 10 mins is about 1.422 mL/gCeO_2, 1.645 mL/gCeO_2 and 1.764 mL/gCeO_2 for 15mm, 20mm and 25 mm, respectively. However, the total amount of oxygen evolution for the period of 10 mins goes up to1578.42 mL, 2434.6 mL and 3263.4 mL for 15 mm, 20 mm and 25 mm, respectively, when the ceria mass loading is considered. Solar-to-fuel conversion efficiency is the function of Stoichiometric fuel production rate (r_{fuel}) which was assumed as $r_{CO} = 2r_{O_2}$, HHV of fuel (286 kJ/mole) and input solar power (Q). Solar-to-fuel efficiencies for the presented three cases are estimated to be 7.82%, 12.07% and 16.18% for 15 mm, 20 mm and 25 mm of RPC thickness, respectively without heat recovery.

4.6 Conclusion

We have presented a numerical model of high-temperature solar thermochemical reactor of hybrid cavity shape that couples the Monte Carlo Ray Tracing (MCRT) technique with computational fluid dynamics (CFD). The influences of RPC thickness on solar-to-fuel conversion efficiency in a solar thermochemical reactor cavity has been explored by means of steady state and transient CFD models. MCRT was applied using SolTrace software to generate the solar flux profile and it was coupled with CFD module to study the heat transfer and concentrated solar flux distribution in the STCR cavity. The conclusions have been drawn as follows;

1. The heat transfer inside the cavity and in the porous region (fluid-to-solid) is highly affected by the gas flow gap size which ultimately influences the inert gas flow pattern.
2. Among all three porous media thicknesses case considered, the 15 mm RPC thickness shows a very uniform distribution of solar heat flux as well as achieves the highest temperature.
3. Larger gas flow gap allows the fluid to flow slower at given velocity thus cooling the porous region rapidly which results in undesired distribution of temperature in the RPC zone.
4. The concentrated flux distribution is uniform in the STCR cavity for all three RPC thicknesses. Even though, the temperature profiles are barely different for varying RPC thicknesses, the thinner RPC zone attains the highest temperature could be considered as an advantage.
5. For the two-step H_2O splitting process, the RPC thickness with 25 mm attains the highest oxygen evolution rate as well as yields the highest solar-to-fuel conversion efficiency, among all three cases considered.
6. The RPC zone subjected to higher temperature attains the peak value of O_2 concentration. However, the ceria mass loading is a factor plays a significant role in rate of H_2 production rate. The RPC zone having 25 mm thickness yields the highest rate of 0.34 mL/min/gCeO_2 oxygen evolution.
7. For RPC thickness 15 mm, 20 mm and 25 mm yield about 1.422 mL/gCeO_2, 1.645 mL/gCeO_2 and 1.764 mL/gCeO_2 oxygen in 10 min cycle, respectively

and when the ceria mass load is considered the total oxygen evolution goes up to 1578.42 mL, 2434.6 mL and 3263.4 mL, respectively.

8. Solar-to-fuel efficiencies for 15 mm, 20 mm and 25 mm RPC thickness are estimated to be 7.82%, 12.07% and 16.18%, respectively without heat recovery.

Chapter – 5

5 Effect of inlet positioning and orientation on the thermal performance of Solar Thermochemical Reactor

5.1 Introduction

The solar thermochemical processes are the high-temperature based processes thus the advancement of solar concentrated systems has become a matter of great importance to the researchers throughout the world [35–38]. Most of the numerical studies have been performed on the volumetric porous media solar thermochemical reactor. A three-dimensional numerical study was performed by PitzPaal et al. [45] to understanding the solar incident radiation distribution and fluid flow effect. It was evident from the results that in a volumetric porous media reactor, the temperature distribution depends on the solar incident irradiation distribution inside the porous media. The investigation carried out by Alazmi and Vafai [46] indicated that the velocity field is rather strongly affected by the variances as compared to the temperature distribution.

In another numerical investigation carried out by Wu et al. studied the flow field and pressure drop in the ceramic porous media and proposed a model to predict the pressure drop [47]. Wu et al. also studied the effects of thermal conductivity on the temperature in a solid phase [48-49]. A numerical model to simulate the fluid flow, heat, and species transfer and to solve the chemical reactions in a volumetric porous media reactor was developed by Villafán-Vidales et al. [50]. Wang et al. [51] also developed a numerical model to generate the heat flux distribution on the porous surface by incorporating the ANSYS Fluent solver and Monte Carlo Ray Tracing (MCRT) [52], [53]. Researchers have also explored the axisymmetric numerical approach for the investigation of coupled heat transfer in porous media reactor [54-55]. Some other transport models have also been investigated to understand the thermal performance of the porous media reactor [56-57]. In the model developed by Chen et al. [58], solar

radiation was coupled with internal heat transfer to analyze the thermal performance of a porous media reactor.

To investigate the solar thermochemical reactor numerically, CFD (computational fluid dynamics) presents itself as a tool to simulate the operating conditions [59]. One dimensional heat transfer model (steady and unsteady) was developed to investigate the thermal decomposition of ZnO at the operating temperature range of 1950–2400 K [60]. They also developed a cylindrical solar thermochemical reactor and studied the effects of inert gas flow [61]. The radiative properties of an indirectly irradiated solar reactor having a quartz glass window was studied by Yong et al. by using the MCRT method [62]. The geometrical effect of solar thermochemical reactor on temperature distribution including the heat loss was studied by Costandy et al. [63]. A multi-chamber porous media reactor was developed by Thomey et al. [64] for the sulphuric acid (H_2SO_4) decomposition. Konstandopoulos and Agrofiotis [65] developed 'Conti-reactor' model to tackle the intermittent problem in hydrogen production.

Primarily, solar thermochemical cycles used metal oxides for the hydrogen production in two-steps metal oxide redox reactions. First step is reduction step (endothermic) in which metal oxide gets decomposed into metal and releases oxygen at high temperature. Second step is oxidation step (exothermic) in which metal oxide reacts with H_2O/CO_2 to produces H_2/CO as product. Further, hydrogen and syngas can be converted in to hydrocarbon fuels via. Fischer-Tropsch process. Since year 2006, Non-stoichiometric cerium oxide or ceria (CeO_2) has emerged as one of the best-suited redox material [66–69] for solar thermochemical cycle due to its high oxygen solid-state conductivity, fast redox kinetics [70] and crystallographic stability.

5.2 Problem statement and reactor configuration

This reactor-receiver cavity consists of a combination of cylindrical and hemisphere as a reactive zone and a transparent quartz window for incoming solar irradiation as shown in Fig. 40. The reactive zone is of 100 mm axial length and 20 mm in thickness, 5 mm gas flow gap, and composed of catalyst known as reticulated porous ceria (RPC). In this work, a steady-state numerical analysis has been performed on a hybrid cylindrical-hemispherical cavity shape to study the effects of inlet positioning

and orientation of cavity reactor-receiver. The inert gas enters the reactor-receiver cavity from the inlet and flows through the RPC and exits from the outlet. The combination of the cylindrical and hemispherical cavity increases the contact area and also the solar radiation gets uniformly distributed on the cavity surface.

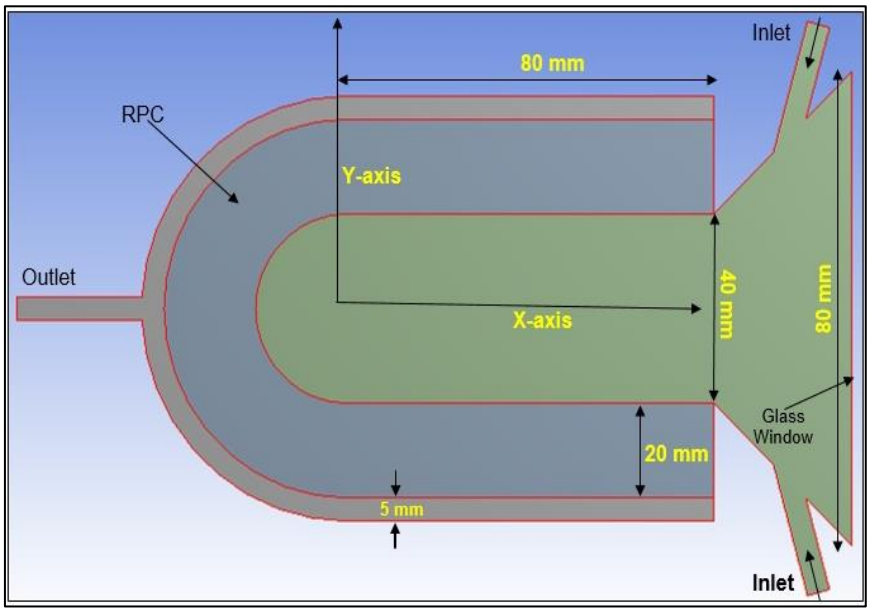

Fig. 40: Schematic displaying dimensions of the solar thermochemical reactor-receiver cavity

The concentrated solar radiation enters into the reactor-receiver cavity from the quartz glass window, heats the entire inner surface of the cavity, and gets transferred into the porous catalyst region (RPC). The outer surface of the cavity has been fully insulated to minimize the thermal loss. In this paper, the inlet position has been varied as 5 mm, 8 mm, 10 mm, 12 mm, and 15 mm from the front quartz glass window. The angular orientation of the inlet also has been varied as 90^0, $75^{0,}$ and 65^0 from the horizontal plane at each position to study the hydrodynamic and thermal effects of the inlet position and its angular orientation as shown in Fig. 41. The main focus is kept on the flow pattern effects and radial heat transfer through the catalyst region in the Reynolds number (Re) range of 100-700. In this study, a 2-Dimensional model of the reactor-receiver cavity was simulated using the ANSYS Fluent 16.2 version. Nitrogen gas (N_2) was used as the carrier gas for heat transfer. The concentrated radiation heat flux of 4 kW_{th} was applied to the quartz glass window using a UDF heat flux profile.

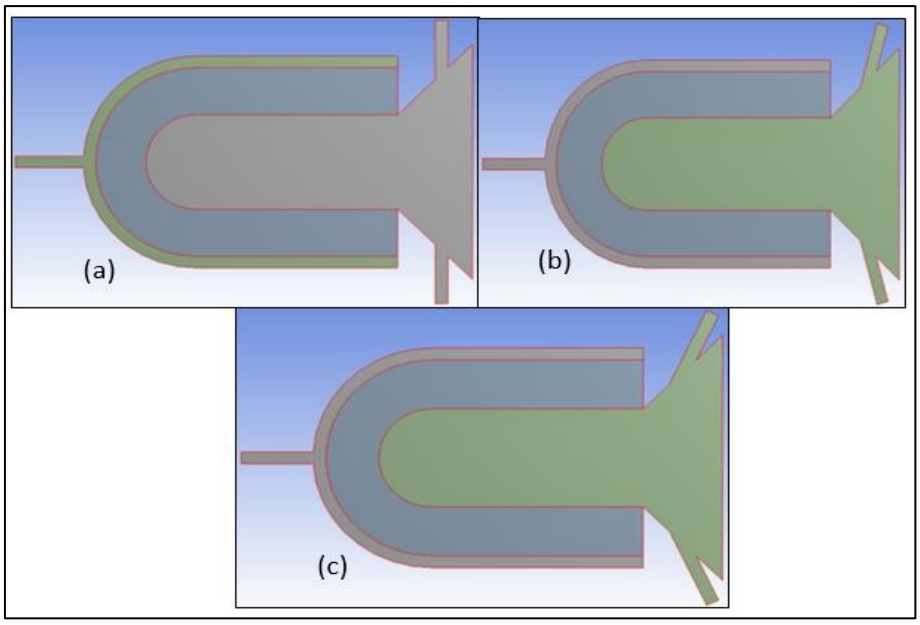

Fig. 41: Solar reactor-receiver cavity configurations, (a) 90°from horizontal, (b) 75°from horizontal and (c) 65°from horizontal

5.3 Numerical implementation and model validation

To carry out the numerical simulation, the solar collector was simulated using an open source software, SolTrace, which traces the solar ray path by MCRT technique. MCRT uniformly distributes solar power by dividing it into larger number of rays determined by the sun shape and slope error [204-205]. The interaction between the rays and the reactor cavity is influenced by the transmissivity, reflectivity and absorptivity. The solar flux profile obtained from the SolTrace shown in Fig. 9 (a) was validated against Lee's study and further used as radiative flux boundary condition on the quartz glass window. ANSYS Fluent v.16.2 solver was used to solve the conservation equations by the finite volume method with a tetragonal/hexagonal unstructured mesh having 0.5 mm element size. The DO radiation model was applied to calculate the radiative heat transfer (RTE equation) in the solar thermochemical reactor cavity. Steady-state simulation with SIMPLE first-order upwind for discrete ordinates and second order for energy calculation was implemented.

Table 8: Initial/ Boundary conditions

Surface	Boundary conditions
Inlets	$v_{inlet} = \frac{v^*}{Ac_{inlet}};\ T_{inlet} = T_{initial}$
Outlet	$P_{out} = P_{atm}$
Inner surface	$k_q \frac{\partial T}{\partial n} = S_{E,rad} + h_q \Delta T;\ \varepsilon = 0.08,\ \tau = 0.86$
Insulation wall	$k_s \frac{\partial T}{\partial n} = \Delta q_r + h_s \Delta T;\quad \varepsilon = 0.28,\ \tau = 0$
Quartz window	$T_{aperture} = T_{initial};\ \varepsilon = 0.08,\ \tau = 0.86$
Other surfaces	$\frac{\partial T}{\partial n} = 0$
Initial conditions	
$T_{initial}$	300 K
Pressure	1 atm
T_{outlet}	300 K

5.4 Results and discussion

5.4.1 Temperature distribution in the RPC zone

The porous media (RPC) is the catalyst region stabilized with CeO_2 on zirconia honeycomb structure where the redox reactions are initiated by the high-temperature to split H2O molecule to produce hydrogen. The carrier gas flows through the porous zone and raises its temperature. Thus, the distribution of temperature in the porous zone is highly influenced by the inlet positions and orientation. The carrier gas nitrogen flows through the porous media as the solar heat flux heats the catalyst region. In this study, the porous medium temperature has been explored radially as well as axially at different inlet positions. The contours of temperature for all 3 inlet orientations (65^0, 75^0 and 90^0) for the front quartz glass window have been shown in Fig. 42. It shows that placement of inlet at tilt orientation (65^0 and 75^0) allows the flowing fluid to be carried further into the cavity which allows uniform distribution of inert gas into the reactor cavity. However, the inlet orientation at 90^0 creates a swirl because the fluid coming in from the both inlets strikes and velocity gets reduced. As a result, the fluid doesn't get distributed uniformly inside the cavity.

5.4.1.1 In the radial direction

The temperature distribution in the radial direction demonstrating the inlet position and orientation effect in the porous media has been shown in Fig. 43. The temperature distribution plotted for the RPC thickness of 20 mm the temperature yield at different inlet positions at Re = 100. The data reported in Fig. 43 (a) for the inlet orientation of 65^0, 75^0 and 90^0 indicates that the 5 mm positioning yield the avg. temperature of 1544 K, 1570 K and 1526 K in the 20 mm RPC thickness. Which suggest that the 75^0 orientation of inlet achieves the highest temperature while 90^0 yields the lowest temperature for 5 mm inlet position.

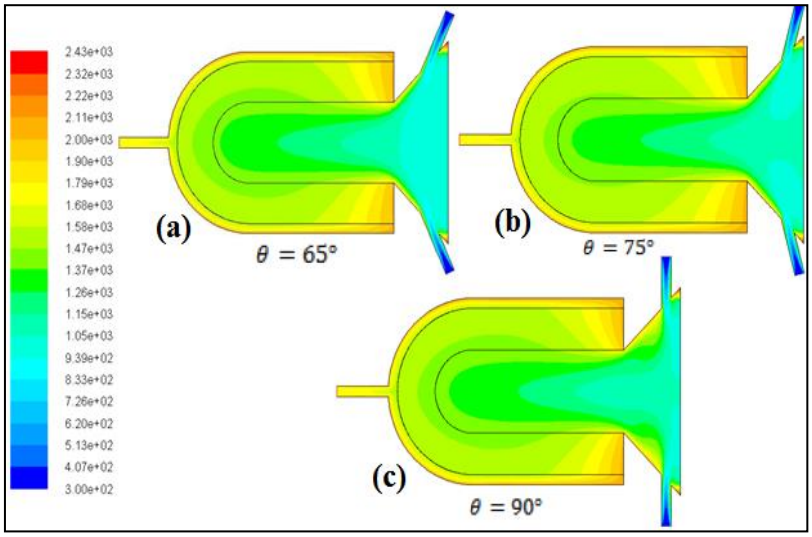

Fig. 42: Fluid-phase temperature contours at 5 mm from inlet position

In Fig. 43(b), the inlet position was at 8 mm and it shows that the avg. temperature was reported to be 1563 K, 1582 K and 1530 K. The temperature distribution seen to be followed the similar pattern as 5 mm position where highest and lowest temperature was reported for 75^0 and 90^0 orientation. Further, when the inlet position was at 10 mm, the highest avg. temperature of 1593 K was achieved for the 90^0 orientation and the lowest avg. temperature of 1570 K was recorded for 65^0 orientation as shown in Fig. 43(c). The similar pattern was seen for the rest of two inlet position at 12 mm and 15 mm from the front quartz glass window as shown in Fig. 43(d) and (e). However, the highest avg. temperature for the 12 mm and 15 mm position reported to be 1591 K and 1573 K, respectively for 90^0 orientation and the lowest avg. temperature of 1568 K and 1545 K, respectively was reported for 65^0 orientation. The

collective statistical analysis suggests that the 90^0 inlet orientation is the best suitable choice for 10 mm, 12 mm and 15 mm inlet positions to achieve higher temperature in the porous media in the radial direction. However, at 5 mm and 8 mm inlet position, 75^0 inlet orientation yields the highest temperature. Overall, it was seen that the highest avg. temperature (1593 K) was achieved by the 10 mm inlet position at 90^0 inlet orientation.

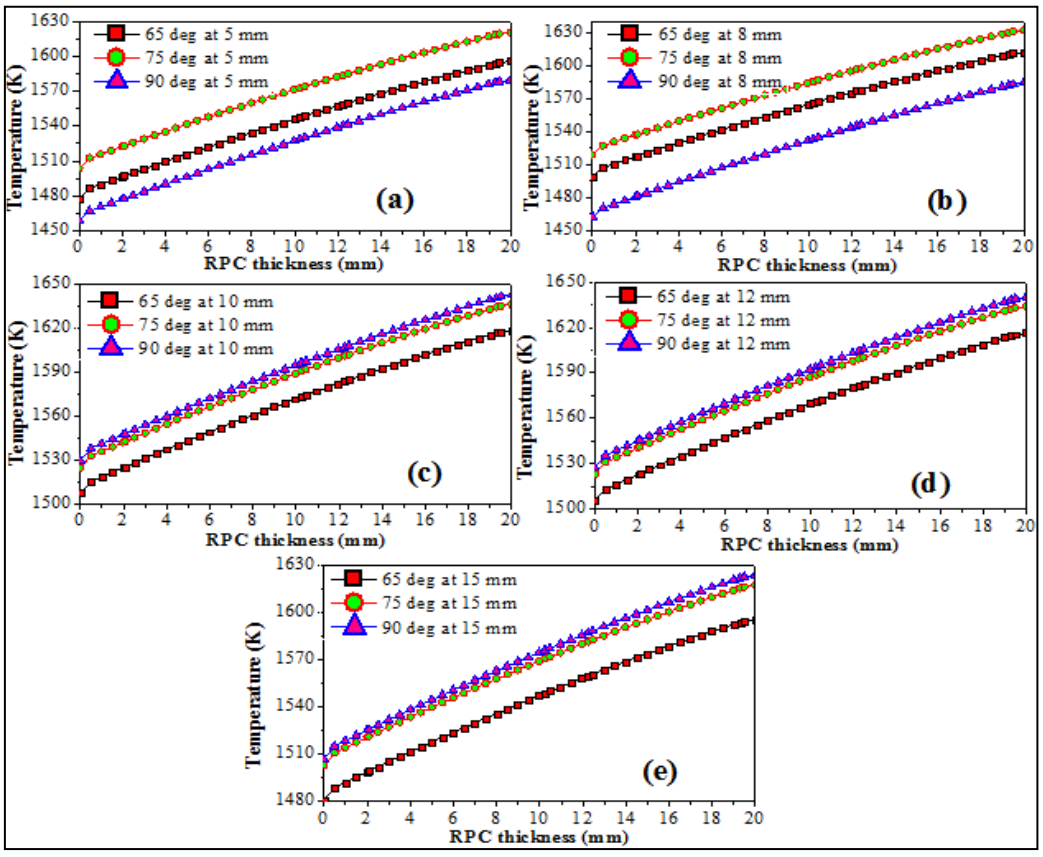

Fig. 43: Fluid-phase temperature distribution in the radial direction in the porous media

5.4.1.2 In the axial direction of RPC zone

The temperature distribution in the axial direction is evaluated to identify the necessary length of the ceria loading porous zone. The temperature distribution in the length of 80 mm RPC porous zone for the all five inlet position at 65^0, 75^0, and 90^0 has been shown in Fig. 44. Inlet position shows quite distinct effect on the temperature distribution in the axial direction. The assessment of Fig. 44 (a) shows that at 5 mm inlet position, the fluid temperature swings from 2025 K to 1490 K for 65^0, 2042 K to 1514 K for 75^0 and 2036 K to 1492 K for 90^0 inlet orientation from x = 0 to x = 80 mm. Evidently, the temperature drops from cavity aperture (x = 0) to x = 80 mm and

generates a temperature profile in the porous region. Thus, the highest avg. temperature of 1644 K in the porous media in axial direction was achieved for 75^0 and the lowest avg. temperature of 1606 K was reported for 90^0 orientation. In Fig. 44 (b), the highest and lowest avg. temperatures of 1656 K and 1614 K were reported for 75^0 and 90^0 orientation. Similar to the previous 5 mm position. Fig. 44 (c) shows the axial temperature distribution for 10 mm position and it was seen that the highest (1666 K) and the lowest avg. temperature (1645 K) was reported for 90^0 and 65^0 orientation, respectively. The inlet position at 12 mm as shown in Fig. 44 (d), reported the highest avg. temperature of 1665 K and the lowest avg. temperature of 1644 K for 90^0 and 65^0 orientation, respectively following the similar trend as the 10 mm inlet position. The temperature distribution for 15 mm inlet position also follow the similar pattern as the 10 and 12 mm position i.e. 90^0 exhibits the highest avg. temperature (1650 K) and the lowest avg. temperature (1625 K) was reported by the 65^0 orientation as shown in Fig. 44 (e).

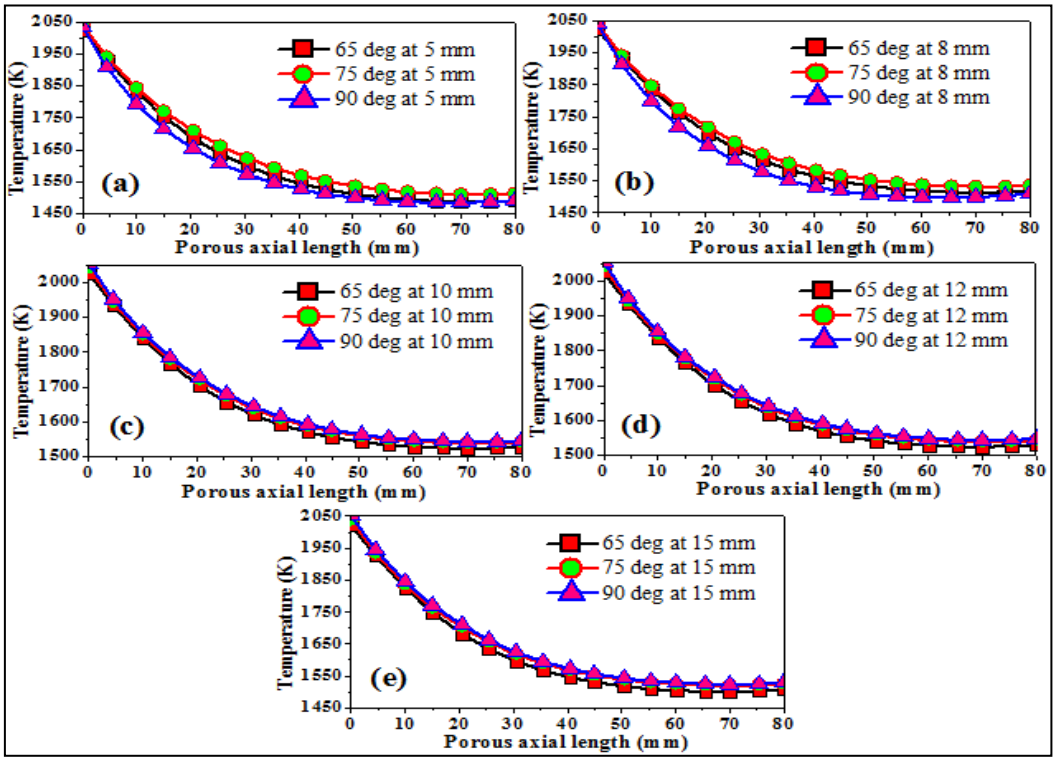

Fig. 44: Fluid-phase temperature distribution in the axial direction in the porous media

Statistically, it was identified that the best-case scenario for the axial temperature distribution in the porous media, among all cases investigated in the study,

was presented by the inlet position at 10 mm combined with 90^0 inlet orientation where the highest avg. temperature was reported to be 1666 K.

5.4.1.3 Reactor temperature

The fluid phase temperature in the STCR cavity along the centerline was evaluated and analyzed to understand temperature distribution in the reactor section where the conduction heat transfer does not play a role and the heat transfer occurs by means of convection and radiation. The temperature distribution along the centerline has been shown in Fig. 45. The fluid-phase reactor temperature for 5 mm inlet position for 65^0, 75^0 and 90^0 has been shown in Fig. 45 (a). It was seen that highest avg. temperature of 1298 K was reported by the 75^0 orientation and the lowest avg. temperature of 1272 K was registered by the 65^0 orientation.

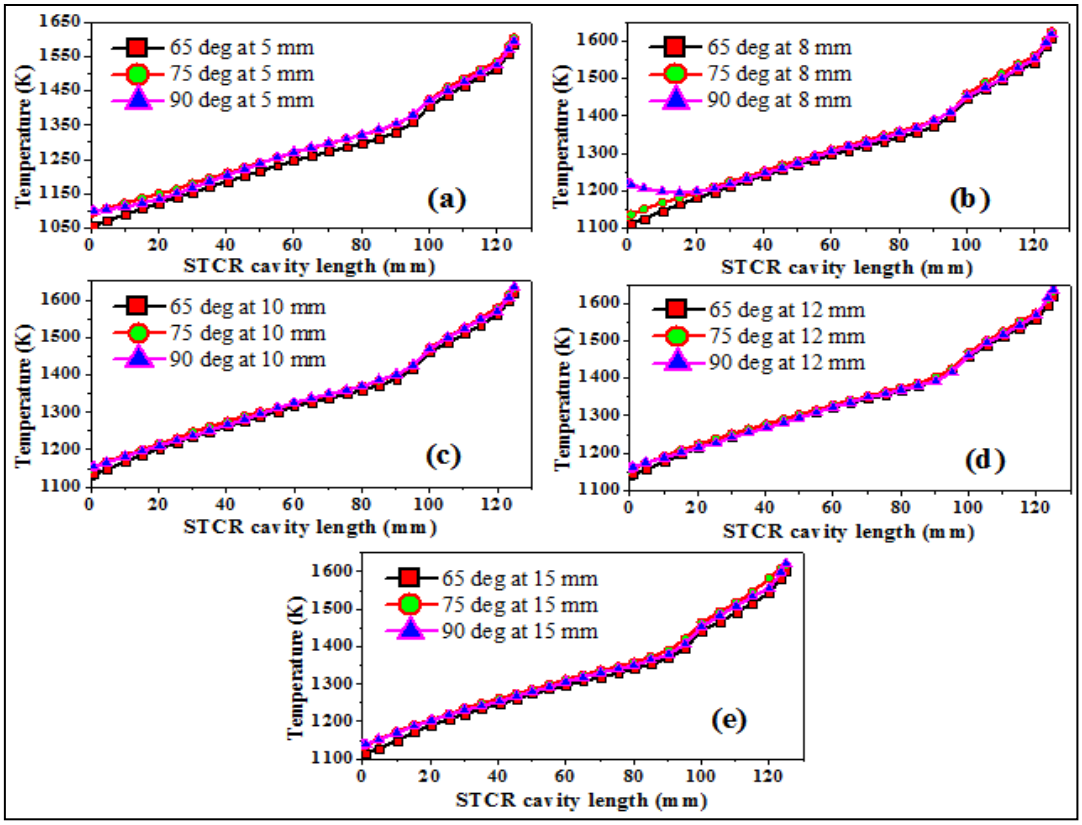

Fig. 45: Fluid-phase temperature distribution in the STCR cavity along the centerline

The 8 mm inlet position temperature distribution was shown in Fig. 45 (b) and it shows that the 90^0 yield the highest avg. temperature (1339 K) and the lowest avg. temperature (1318 K) was reported by 65^0 orientation. In Fig. 45 (c), the highest and lowest avg. temperatures of 1350 K and 1337 K were reported by the 75^0 and 65^0

orientation, respectively at 10 mm position. For 12 mm inlet position as shown in the Fig. 45 (d), it was seen that the highest avg. temperature of 1353 K was reported by the inlet orientation at 75^0 and the lowest avg. temperature of 1343 K was recorded at 65^0 orientation. For the 15 mm inlet position in Fig. 45 (e), the avg. temperature drops slightly and the highest and lowest avg. temperature were reported to be 1340 K and 1320 K, respectively. It is understandable that from x=0 to x=100 mm, the cavity region is open and the heat transfer is through convection and radiation. Thus, the increment in temperature occurs on linear curve. However, from x=100 mm to x=120 mm, the RPC zone is heated by convection, radiation as well as conduction. Therefore, the temperature increases rapidly and reaches to a sufficient value to carry out reduction reaction. Collective analysis of the figure 6 suggest that as 75^0 orientation at 12 mm position reaches to the highest avg. temperature which makes it an optimal and efficient choice.

5.5 Effect of Reynolds number

5.5.1 In radial direction

The influence of inert gas velocity is critical in the evaluation of temperature distribution in the STCR cavity. The inert gas is heated by solar radiation and carries the heat into the porous media where it gets dissipated and raises its temperature to carry out the redox reaction. Thus, its crucial to obtain a specific range of inert gas velocity for it to function as a temperature control mechanism to switch between the reduction (high-temperature) and oxidation (low-temperature) reaction. Therefore, the effect of inert gas velocity on temperature distribution in the radial direction in the porous region has been shown in Fig. 46. The effect of fluid velocity has been interpreted in terms of Reynolds number (Re) and the range of Reynolds number was set to be 100-700.

The avg. temperature for inlet position at 5 mm on the increasing value of Re has been shown in Fig. 46 (a). It was seen that the increasing value of Re significantly reduces the avg. temperature in the radial direction for all three inlet orientations of 65^0, 75^0 and 90^0. It's evident from the plot that the avg. temperature in the radial direction reaches up to 1544 K, 1570 K and 1526 K for 65^0, 75^0 and 90^0 orientation, respectively at Re = 100. Furthermore, a quite significant drop in avg. temperature of 422 K, 417 K

and 428 K was reported when the value of Re increased from 100 to 300 for the inlet orientation of 65^0, 75^0 and 90^0, respectively.

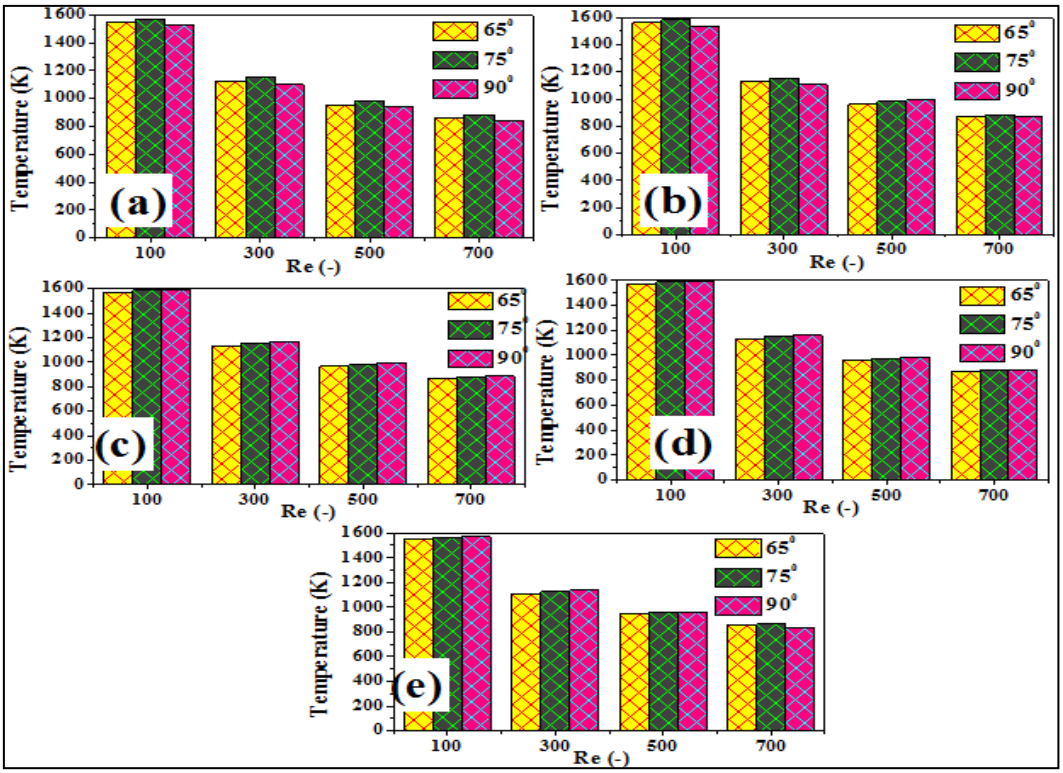

Fig. 46: Effect of fluid velocity on temperature distribution in the radial direction in the RPC zone

When the value of Re is increased from 300 to 500, it was seen that there was further decrease of 166 K, 172 K and 162 K for the inlet orientation of 65^0, 75^0 and 90^0, respectively. Additionally, increasing the Re from 500 to 700, the avg. temperature decreases by 94 K, 99 K and 93 K for 65^0, 75^0 and 90^0 inlet orientation, respectively. Statistically, it was observed that the avg. temperature drops heavily in radial direction for the Reynolds number increase from 100 to 300. The avg. temperature for the inlet position at 8 mm has been shown in Fig. 46 (b). Analysis of the graph shows that the highest avg. temperature at the inlet orientation of 65^0, 75^0 and 90^0 reached 1563 K, 1582 K and 1531 K, respectively for Re = 100. The avg. temperature decreases by 432 K, 429 K and 424 K with the Re increase from 100 to 300 and the avg. temperature further drops by 170 K, 173 K and 116 K for 65^0, 75^0 and 90^0 inlet orientation, respectively. Additionally, for further increase of Re from 500 to 700, decreases the avg. temperature by 96 K, 99 K and 124 K for the inlet orientation of 65^0, 75^0 and 90^0.

Fig. 46 (c) shows the avg. temperature for 10 mm inlet position. The highest avg. temperature for 65^0, 75^0 and 90^0 inlet orientation reported to be 1570 K, 1587 K and 1593 K for Re = 100. At this inlet position, when the Re increased from 100 to 300, the avg. temperature drops by 437 K, 435 K and 425 K at the inlet orientation of 65^0, 75^0 and 90^0, respectively. Moreover, the stepwise increase of Re from 300 to 500 and 500 to 700 results in the decrease of avg. temperature by 170 K, 173 K, & 178 K and 95 K, 99 K and 103 K for the inlet orientation of 65^0, 75^0 and 90^0, respectively. The avg. temperature for 12 mm inlet position has been shown in Fig. 46 (d). The reported data suggest that the avg. temperature was highest for Re = 100 and it was 1568 K, 1586 K and 1591 K for the inlet orientation of 65^0, 75^0 and 90^0, respectively. As expected, the similar trend was followed for the Re = 300, 500 and 700 for which the avg. temperature was decreased by 440 K, 438 K and 431 K at Re = 300, 168 K, 172 K & 176 K for Re = 500 and 95 K, 98 K & 100 K for Re = 700 for the inlet orientation of 65^0, 75^0 and 90^0, respectively. Fig. 46 (e) shows the avg. temperature for 15 mm inlet position. The inlet orientation of 65^0, 75^0 and 90^0 reported the avg. temperature of 1546 K, 1567K and 1573 K, respectively at Re = 100. When the value of Re was increased to 300, the avg. temperature values dropped to a significant magnitude of 440 K, 442 K & 436 K in the radial direction. Further, increasing the value of Re to 500 and 700 showed that the avg. temperature decreased by in the set of 161 K, 168 K & 174 K and 89 K, 96 K & 134 K for the inlet orientation of 65^0, 75^0 and 90^0, respectively.

5.5.2 In the axial direction

The temperature distribution on the entire length of the porous section is affected by the inert gas velocity. The inert gas gets distributed in the cylindrical as well as in the dome section of the STCR cavity and flows through the porous region carrying heat and raises the temperature of the cavity. Ultimately, it is well understood that the inert gas flowing at higher velocity will has less contact time with the porous section. Thus, the heat transfer will be affected significantly and to determine the magnitude of avg. temperature drop in the axial direction with increasing value of Re has been plotted in Fig. 47.

In Fig. 47 (a), the effect of Re on avg. temperature in the axial direction of the porous media for inlet position at 5 mm has been shown. The data indicated that at Re

= 100, the avg. temperature was reported to be 1622 K, 1644 K and 1606 K for 65^0, 75^0 and 90^0 inlet orientation, respectively. It was also seen that there was a drop in the avg. temperature by 387 K, 380 K & 402 K for increasing the Re from 100 to 300, 159 K, 164 K & 155 K for Re increment from 300 to 500 and 91 K, 95.4 K & 92 K for increasing Re from 500 to 700.

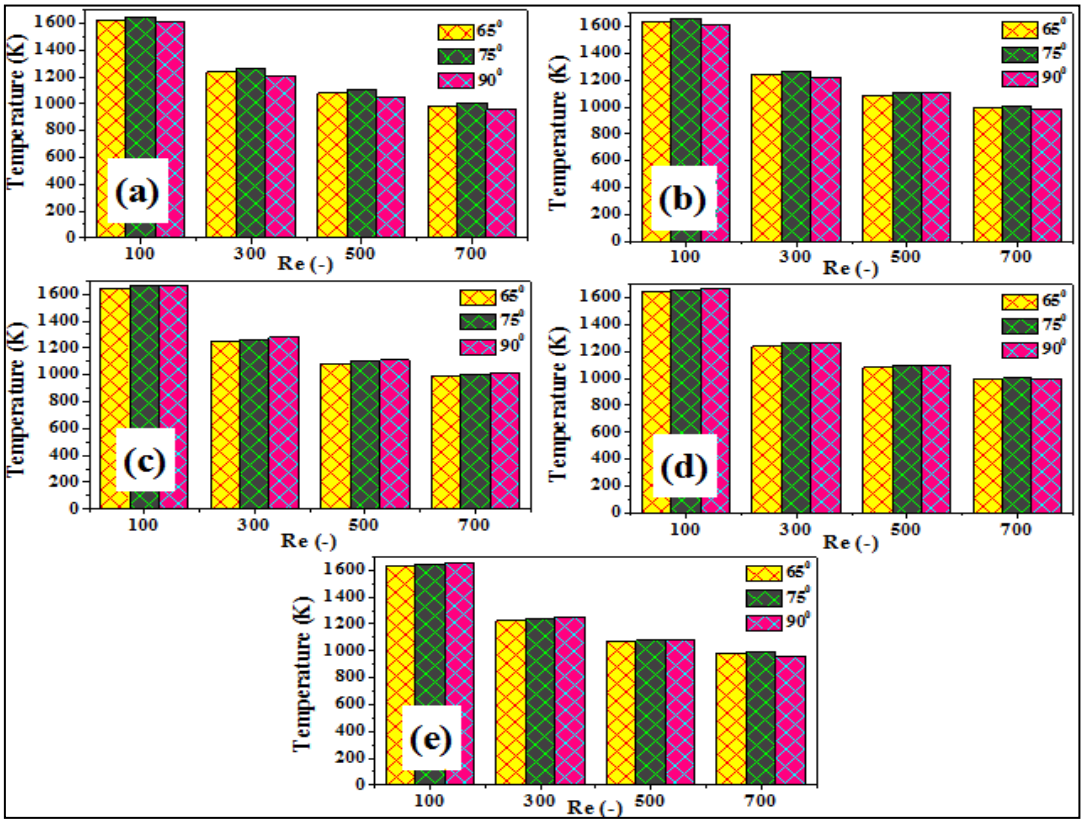

Fig. 47: Effect of fluid velocity on temperature distribution in the axial direction in the RPC zone

The Re effect on avg. temperature for 8 mm position has been shown in Fig. 47 (b). It has been shown that for the inlet orientations of 65^0, 75^0 and 90^0, the avg. temperature was reported to be 1638 K, 1656 K & 1614 K, respectively at Re value of 100. As the Re was increased from 100 to 300, 300 to 500 and 500 to 700 for the inlet orientations of 65^0, 75^0 and 90^0, the drop in the avg. temperature was observed to be 396 K, 391 K & 396 K and 162 K, 165 K & 111 K and 93 K, 95 K & 130 K, respectively. In Fig. 47 (c), the avg. temperature for inlet position at 10 mm on the increasing value of Re has been displayed. The reported data shows the highest avg temperature at Re = 100 for 65^0, 75^0 and 90^0 inlet orientations were 1645 K, 1660 K & 1666 K, respectively. further increasing the Re from 100 to (i) 300, (ii) 500 and (iii)

700 caused the avg. temperature to drop by (i) 400 K, 396 K & 388 K, (ii) 162 K, 165 K & 170 K, (iii) 91 K, 94 K & 99 K, respectively.

The effect of Re on the avg. temperature at 12 mm inlet position has been shown in Fig. 47 (d). It was seen that the avg. temperature of 1644 K, 1659 K & 1665 K was reported at Re = 100 for 65^0, 75^0 and 90^0 inlet orientations. Further, on increasing Re value to 300, 500 and 700, the avg. temperature drop was reported to be 402 K, 400 K & 395 K for Re increase from 100 to 300, 160 K, 164 K & 169 K for Re increase from 300 to 500 and 90 K, 94 K & 107 K for Re increase from 500 to 700 for inlet orientations of 65^0, 75^0 and 90^0, respectively. Fig. 47 (e) shows the effect of increase in Re on the avg. temperature for the inlet position at 15 mm. The avg. temperature for Re = 100 was observed to be 1625 K, 1643 K & 1650 K for the inlet orientation of 65^0, 75^0 and 90^0, respectively. additionally, increasing Re from 100 to 300, 500 and 700, gives the decrease in the avg. temperature of 403 K, 403 K & 399 K and 154 K, 160 K & 166 K and 85 K, 91 K & 131 K for inlet orientations of 65^0, 75^0 and 90^0, respectively.

5.5.3 On the STCR cavity

The statistical analysis showing the effect of increasing Reynolds number on the avg. temperature of STCR cavity along the centerline for all inlet positions has been shown in Fig. 48. It has been shown in Fig. 48 (a) that for the inlet position at 5 mm, the avg. temperature along the centerline reaches upto 1272 K, 1297 K, 1293 K for the inlet orientations of 65^0, 75^0 and 90^0, respectively at Re = 100. It was also seen that increasing the Reynolds number from 100 to 300, 500 and 700 leads to the drop in the avg. temperature by 395 K, 397 K, 408 K and 161 K, 158 K, 104 K and 83 K, 87 K, 81 K, respectively. It's been seen that similar to previous pattern, the drop in the avg. temperature is highest for when Re is increased from 100 to 300 and lowest for 500 to 700.

Consequently, it was seen in Fig. 48 (b) that by shifting the inlet position at 8 mm increases the avg. temperature at for Re = 100 as compared to 5 mm position which was reported to reach 1318 K, 1334 K, 1339 K for 65^0, 75^0 and 90^0, respectively. Further, the drop in the avg. temperature was seen with the increasing value of Re from 100 to 300, 500 and 700 by 422K, 422K, 392K and 168K, 164K, 191K and 88K, 90K, 51K with each set corresponding to the inlet orientation of 65^0, 75^0 and 90^0,

respectively. Similarly, in Fig. 48 (c) the avg. temperature for the inlet position at 10 mm goes up to 1336 K, 1350 K, 1347 K for Re value of 100. Additionally, the drop in the avg. temperature reported to be 429 K, 431 K, 423K for 100 to 300, 171 K, 165 K, 162 K for 300 to 500 and 88 K, 91 K, 89 K for 500 to 700 Re value increase at the inlet orientation of 65^0, 75^0 and 90^0, respectively for each set.

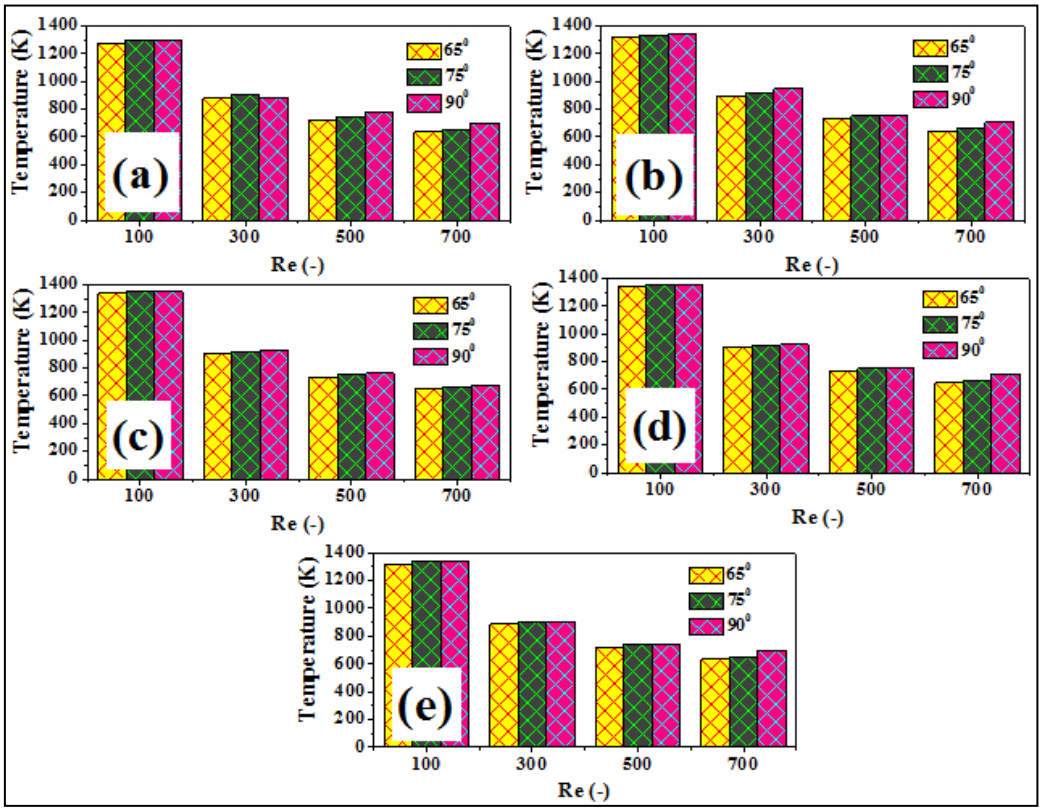

Fig. 48: Effect of fluid velocity on temperature distribution in STCR cavity along the centerline

In Fig. 48 (d) shows the inlet position of 12 mm and the avg. temperature for the Re value of 100 to which the avg. temperature reaches up to 1342 K, 1352 K, 1347 K. Further, the downswing in the avg. temperature was reported to be 434 K, 435 K, 422 K and 173 K, 165 K, 166 K and 88 K, 91 K, 47 K, when the value of Re increases from 100 to 300, 500 and 700, respectively for the inlet orientation of 65^0, 75^0 and 90^0. The avg. temperature for 15 mm inlet position has been shown in Fig. 48 (e). The analysis of the plot shows that the avg. temperature goes up to 1319 K, 1339 K, 1332 K for the inlet orientation of 65^0, 75^0 and 90^0, respectively at Re = 100. Moreover, increasing the Re from 100 to 300, 500 and 700 decreases the avg. temperature and the drop is reported as 435 K, 437 K, 428 K for 65^0, 169 K, 163 K, 160 K for 75^0 and 84 K,

89 K, 44 K for 90^0 inlet orientation, respectively. Collective analysis of the plots show that the highest avg. temperature was achieved by the 12 mm inlet position at 75^0 orientation for Re = 100.

5.5.4 Summary and conclusion

The results of the study have shown that the inlet position and orientation have quite significant impact on the temperature distribution in the porous as well as in the STCR cavity along the centerline. The main conclusive point drawn from this study have been listed below;

1. The inlet position at 10 mm combined with the orientation of 75^0 inclination from the horizontal plane was seen to achieve the highest avg. temperature of 1587 K in the radial direction in the porous media with the Re value of 100.
2. The avg. temperature in the axial direction in the porous media reached highest value of 1666 K for the inlet position of 10 mm with the orientation of 90^0 with the Re value of 100.
3. The highest avg. temperature of 1353 K was achieved by the inlet position of 12 mm at the orientation of 75^0 along the centerline of the STCR cavity for Re=100.

Chapter – 6

6 Effect of cerium oxide non-stoichiometry on the solar-to-fuel conversion efficiency of water splitting Solar Thermochemical Cycle

6.1 Introduction

Solar energy has been widely used in the production of solar fuels such as H_2 and syngas via thermochemical water-splitting cycles which use solar concentrated energy as energy input and water as material input to produce the solar fuels [81, 206–210]. Researchers have thoroughly explored several metal oxide-based solar thermochemical water splitting cycles such as zinc oxide [211-212], iron oxide [214-215], ferrites [215-217], tin oxide [150, 218], ceria and doped ceria [220–223], perovskites [224–226], and others [227]. Researchers have also been exploring similar cycles such as sulfur iodine plus the hybrid sulfur cycle [229] and the hybrid photo-thermal sulfur-ammonia water splitting cycle [231] to produce solar fuels. The combination of metal oxide-sulfate (MO-MS) based solar thermochemical cycle has been the center of attention. Mainly, iron oxide-iron sulfate [233], zinc oxide-zinc sulfate [158], and strontium oxide-strontium sulfate [234] water splitting cycles fall in this category.

The thermochemical reactions of MO-MS based water splitting cycle can be written as follows:

$$MSO_4 \rightarrow MO + SO_2(g) + \frac{1}{2}O_2(g) \tag{74}$$

$$MO + SO_2(g) + H_2O(g) \rightarrow MSO_4 + H_2(g) \tag{75}$$

The results of the MO-MS water splitting cycles such as Iron oxide-iron sulfate, zinc oxide-zinc sulfate, and strontium oxide-strontium sulfate showed that their solar-to-fuel conversion efficiency was higher than the rest of the solar thermochemical cycles explored earlier. The MO-MS water splitting cycles are the best-suited option

for hydrogen production but it is necessary to find a combination of MO-MS which will attain the highest solar-to-fuel conversion efficiency operating at low reduction temperature. This study investigates the thermodynamic equilibrium and solar-to-fuel efficiency analysis of CeO_2-$CeO_{1.72/1.83}$ thermochemical two-step water-splitting cycle as shown in Fig. 49.

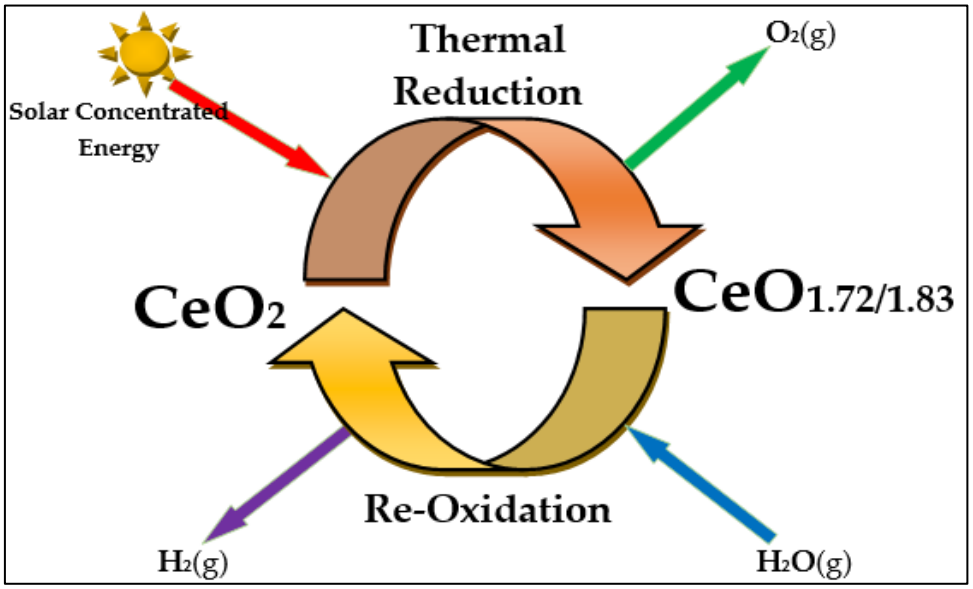

Fig. 49: Cerium oxide-based solar thermochemical cycle of H_2 production

6.2 Mathematical modelling

The primary step of the solar-to-fuel conversion efficiency ($\eta_{solar-to-fuel}$) is the calculation of solar absorption efficiencies of solar reactor ($\eta_{abs-solar-reactor-WS}$) and solar H_2O heater ($\eta_{abs-solar-H_2O-heater-WS}$) from the Eq. (76) and Eq. (77) given below;

$$\eta_{abs-solar-reactor-WS} = \left[1 - \left(\frac{\sigma T_L^4}{IC}\right)\right] \tag{76}$$

$$\eta_{abs-solar-H_2O-heater-WS} = \left[1 - \left(\frac{\sigma T_H^4}{IC}\right)\right] \tag{77}$$

In the above given equation, the values of I, C *and* σ are taken as 1000 W/m^2, 3000 suns and $5.67 \times 10^{-8}\, W/m^2 \cdot K^4$, respectively.

The input solar energy required to operate the solar reactor ($Q_{solar-reactor-WS}$) and solar H_2O heater ($Q_{solar-H_2O-heater-WS}$) was estimated using the following given Eq. (78) and Eq. (79);

$$Q_{solar-reactor-WS} = \frac{Q_{CeO_2-partial-reduction-WS}}{\eta_{abs-solar-reactor-WS}} \quad (78)$$

$$Q_{solar-H_2O-heater-WS} = \frac{Q_{H_2O-heating-WS}}{\eta_{abs-solar-H_2O-heater-WS}} \quad (79)$$

Further, the solar heat required to facilitate the partial reduction of CeO_2 ($Q_{CeO_2-partial-reduction-WS}$)is estimated by the Eq. (80), while the Eq. (81) is used to calculate the solar heat required for the H_2O heating ($Q_{H_2O-heating-WS}$).

$$Q_{CeO_2-partial-reduction-WS} = \dot{m}\Delta H|_{CeO_2(s)\ at\ T_L \rightarrow aCeO_2(s) + bCeO_{1.72/1.83}(s) + cO_2(g)\ at\ T_H} \quad (80)$$

$$Q_{H_2O-heating-WS} = \dot{m}\Delta H|_{eH_2O(l)\ at\ 298\ K \rightarrow eH_2O(g)\ at\ T_L} \quad (81)$$

When the $Q_{CeO_2-partial-reduction-WS}$ and $Q_{H_2O-heating-WS}$ are added it gives net solar heat required to drive the cycle as given in the Eq. (82);

$$Q_{\text{cycle-net-}WS} = Q_{CeO_2-partial-reduction-WS} + Q_{H_2O-heating-WS} \quad (82)$$

Correspondingly, the addition of $Q_{solar-reactor-WS}$ from Eq. (78) and $Q_{solar-H_2O-heater-WS}$ from Eq. (79) results in the solar heat energy required to drive the whole solar cycle as shown in Eq. (83);

$$Q_{\text{solar-cycle-}WS} = Q_{solar-reactor-WS} + Q_{solar-H_2O-heater-WS} \quad (83)$$

Even though the conduction and convection losses from solar reactor and solar H_2O heater have been neglected but since solar reactor and H_2O heater operate at very high temperature thus, the re-radiation thermal losses are still accounted for and can be calculated using the Eq. (84) and Eq. (85) given below;

$$Q_{\text{re-rad-solar-reactor-}WS} = Q_{solar-reactor-WS} - Q_{CeO_2-partial-reduction-WS} \quad (84)$$

$$Q_{re-rad-solar-H_2O-heater-WS} = Q_{solar-H_2O-heater-WS} - Q_{H_2O-heating-WS} \quad (85)$$

Thus, re-radiation losses from the WS cycle ($Q_{re-rad-cycle-WS}$) can be estimated by the summation of Eq. (84) and Eq. (85) and it is expressed as Eq. (86) given below;

$$Q_{re-rad-cycle-WS} = Q_{\text{re-rad-solar-reactor-}WS} + Q_{re-rad-solar-H_2O-heater-WS} \quad (86)$$

To calculate the solar-to-fuel conversion efficiency ($\eta_{solar-to-fuel}$) without heat recuperation can be estimated using the following given Eq. (87);

$$\eta_{solar-to-fuel} = \frac{moles\ of\ H_2 \times HHV\ of\ H_2}{Q_{solar-cycle-WS}} \quad (87)$$

However, if the heat recuperation is taken into consideration, the role of coolers and WS reactor has to be accountable. Thus, the $Q_{\text{recuperation}-WS}$ can be calculated using the following given Eq. (88);

$$Q_{\text{recuperation}-WS} = Q_{\text{Cooler-A}-WS} + Q_{\text{Cooler-B}-WS} + Q_{\text{WS-splitting-reactor}-WS} + Q_{\text{Cooler-C}-WS} \quad (88)$$

The value of $Q_{\text{recuperation}-WS}$ can be calculated by the following given Eq. (89) to (92);

$$Q_{\text{Cooler-A}-WS} = -\dot{m}\Delta H|_{aCeO_2(s)+bCeO_{1.72/1.83}(s)+cO_2(g)\ at\ T_H \rightarrow aCeO_2(s)+bCeO_{1.72/1.83}(s)+cO_2(g)at\ T_L} \quad (89)$$

$$Q_{\text{Cooler-B}-WS} = -\dot{m}\Delta H|_{cO_2(g)\ at\ T_L \rightarrow cO_2(g)\ at\ 298\ K} \quad (90)$$

$$Q_{\text{Cooler-C}-WS} = -\dot{m}\Delta H|_{dH_2O(g)\ at\ T_L \rightarrow dH_2O(l)\ at\ 298\ K} \quad (91)$$

$$Q_{H_2\text{O-splitting-reactor}-WS} = -\dot{m}\Delta H|_{aCeO_2(s)+bCeO_{1.72/1.83}(s)+eH_2(g)\ at\ T_L \rightarrow CeO_2(s)+dH_2O(g)\ at\ T_L} \quad (92)$$

The total amount of solar heat energy required to drive the CeO_2 WS solar cycle can be calculated by using the Eq. (93) given below;

$$Q_{\text{solar-cycle-HR}-WS} = Q_{\text{solar-cycle}-WS} - Q_{\text{recuperation-HR}-WS} \quad (93)$$

and $Q_{\text{recuperation-HR}-WS}$ can be calculated by the Eq. (94);

$$Q_{\text{recuperation-HR}-WS} = (\%HR) \times Q_{\text{recuperable}-WS} \quad (94)$$

Thus, solar-to-fuel conversion efficiency ($\eta_{solar-to-fuel-HR}$) after taking the heat recuperation into taking account can be estimated by the Eq. (95) mentioned below;

$$\eta_{solar-to-fuel-HR} = \frac{moles\ of\ H_2 \times HHV\ of\ H_2}{Q_{solar-cycle-HR-WS}} \tag{95}$$

The study is validated using the work output from the fuel cell ($W_{FC-ideal-WS}$) by the following Eq. (96) and (98);

$$W_{FC-ideal-WS} = -\dot{m}\Delta G|_{dH_2O(l)+cO_2\ at\ 298\ K \rightarrow eH_2(g)\ at\ 298\ K} \tag{96}$$

$$W_{FC-ideal-WS} = Q_{solar-cycle-WS} - \left(Q_{re-rad-cycle-WS} + Q_{Cooler-A-WS} + Q_{Cooler-B-WS} + Q_{Cooler-C-WS} + Q_{H_2O-splitting-reactor-WS} + Q_{FC-ideal-WS}\right) \tag{97}$$

Where,

$$Q_{FC-ideal-WS} = -(298) \times \dot{m}\Delta S|_{dH_2O(l)+cO_2\ at\ 298\ K \rightarrow eH_2(g)\ at\ 298\ K} \tag{98}$$

6.3 System configuration and equilibrium analysis

The thermodynamic analysis on the solar driven non-stoichiometric cerium oxide ($CeO_2 - CeO_{1.72/1.83}$) WS thermochemical cycles was performed using HSC Chemistry 9.9 software. HSC chemistry allows to numerically investigate the chemical processes and the effects of various variables such as change in enthalpy (ΔH), entropy (ΔS), Gibbs free energy (ΔG) and heat capacity (ΔCp). HSC chemistry software database is inbuilt with 28,000 chemical species thus enabling the user to validate the feasibility of the chemical process.

In the thermodynamic analysis of a solar thermochemical cycle, first step is the evaluation of equilibrium composition and thermal reduction temperature (T_H) for the thermal reduction (TR) of *CeO_2* and water splitting (WS) of the redox reactions and in the second step, solar-to-fuel conversion efficiency ($\eta_{solar-to-fuel}$) analysis is performed. Consequently, primarily, equilibrium analysis was carried out as first step of the thermodynamic analysis of solar–assisted ($CeO_2 - CeO_{1.72/1.83}$) cycle. The equilibrium composition associated with thermal reduction temperature (T_H) has been shown in the Fig. 50. The reduction of *CeO_2* was carried out at oxygen partial pressure (P_{O_2}) of 1 bar. The thermal reduction (TR) of *CeO_2* was plotted as a function of thermal

reduction temperature (T_H). The equilibrium composition of CeO_2, $CeO_{1.72/1.83}$, and O_2 reported in Fig. 50 shows that the thermal reduction (TR) of CeO_2 started at 1400 K and the full extent of thermal reduction (100% TR) was achieved at 2734 K.

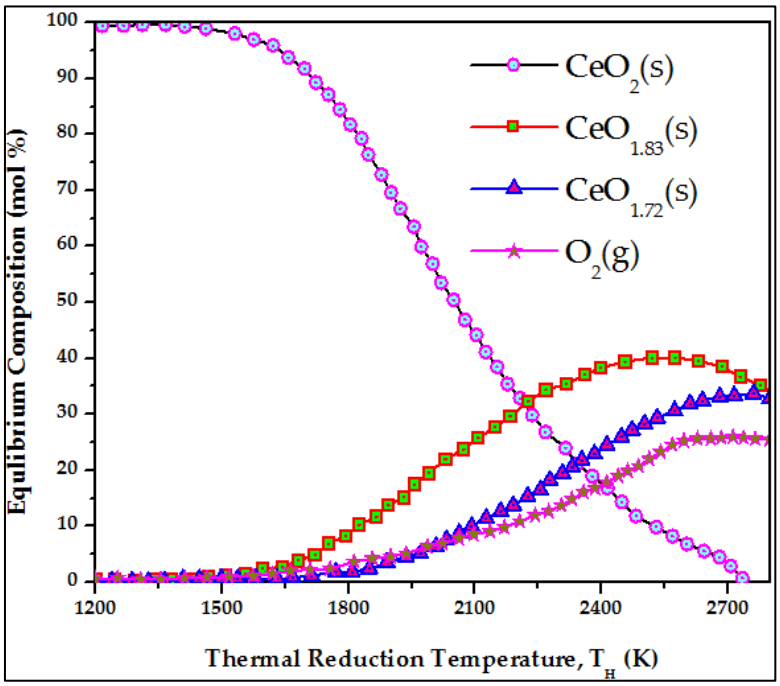

Fig. 50: Equilibrium composition as function of thermal reduction temperature (T_H)

Cerium oxide (CeO_2) is a non-volatile compound therefore, this study was concentrated on comprehending the effect of thermal reduction of CeO_2 on the overall solar-to-fuel conversion efficiency$(\eta_{solar-to-fuel})$. The identification of the thermal reduction temperature (T_H) is essential at which the thermal reduction (TR) of CeO_2 goes from 0.98% to 100%. The results reported in the Fig. 51 show that from 1412 K to 1622 K, the thermal reduction (TR) of CeO_2 occurs slowly (0.69% to 4.08%). However, as the thermal reduction temperature (T_H) further upsurge from 1622 K to 2315 K, the thermal reduction of CeO_2 increases slight rapidly on a linear curve and goes from 4.08% to 76.03%. The increase in thermal reduction of CeO_2 occurs ever faster and goes from 76.03% to 100%, when the thermal reduction temperature increases from 2315 K to 2734 K. Thus, establishing that 2734 K is the ultimate thermal

reduction temperature (T_H) at which full 100% thermal reduction (TR) of CeO_2 is achieved.

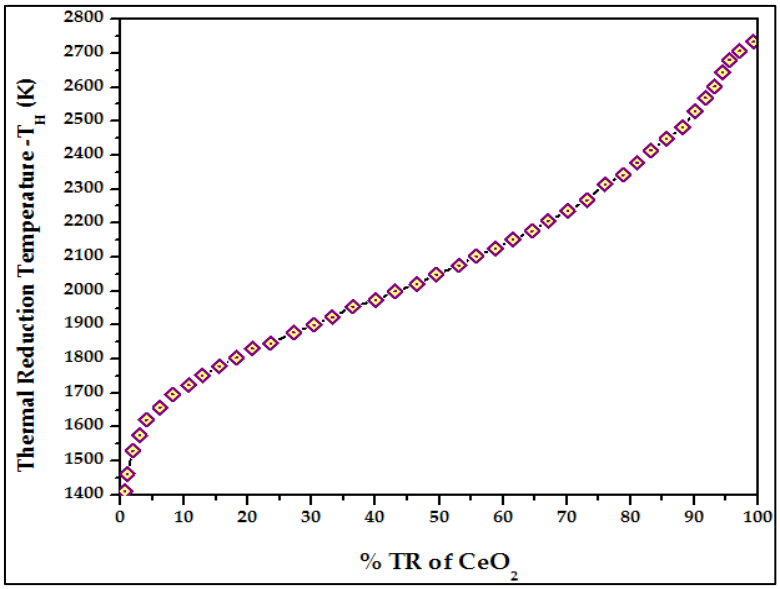

Fig. 51: Influence of TH on %TR of CeO_2

The equilibrium analysis was proceeded further by the estimation of next crucial step which is re-oxidation temperature (T_L) of the redox reaction. The determination of re-oxidation temperature is accomplished by the analysis of change in Gibbs free energy (ΔG) as a function of operating temperature (T) as shown in ***Fig. 52***. The change in Gibbs free energy (ΔG) being the function of temperature is used to justify the practicable reduction temperature (T_H) as well as re-oxidation temperature (T_L). Since, the reduction reaction is an exothermic reaction, thus ΔG is inversely bound with the temperature and eventually approaches zero value to sustain the chemical equilibrium. Subsequently, re-oxidation reaction is an endothermic reaction and ΔG value rises with the increasing temperature and approaches zero.

It can be seen from ***Fig. 52*** that during the reduction reaction$\left(CeO_2 \rightarrow CeO_{1.72/1.83} + O_2\right)$, the value of Gibbs free energy (G) decreases from 600 kJ to -103.87 kJ and 590 kJ to -177.05 kJ for $CeO_{1.72}$ and $CeO_{1.83}$, respectively. However, in the re-oxidation step$\left(CeO_{1.72/1.83} + H_2O \rightarrow CeO_2 + H_2\right)$ of the redox reaction, the Gibbs free energy (G) value increases from -71.35 kJ to 130.15 kJ and -66.04 kJ to 166.72 kJ for

$CeO_{1.72}$ and $CeO_{1.83}$, respectively when the operating temperature increases from 300 K to 3000 K both reduction step and re-oxidation step.

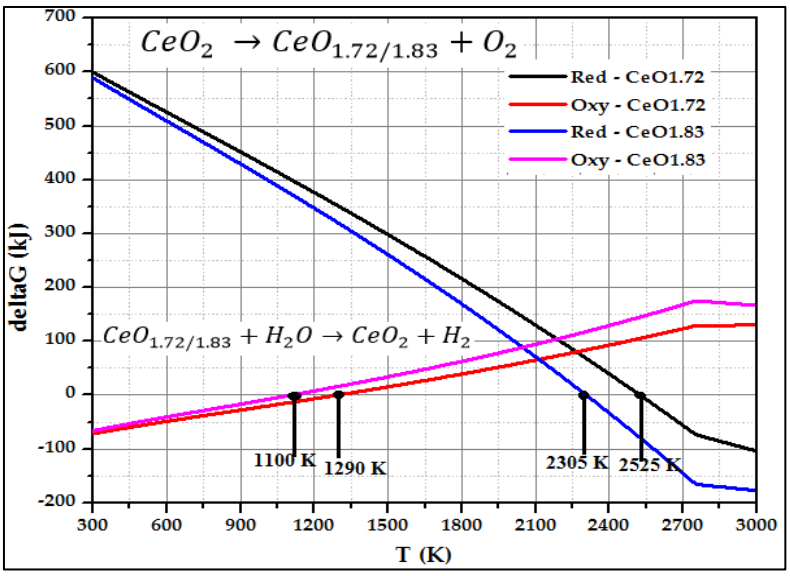

Fig. 52: The influence of thermal reduction (T_H) and re-oxidation temperature (T_L) on change in Gibbs free energy (ΔG)

It was also seen in ***Fig. 52*** that for re-oxidation reaction, Gibbs free enery (G) approaches the zero value where the chemical equilibrium in the reaction is achieved at the re-oxidation temperature (T_L) of 1100 K and 1290 K for $CeO_{1.83}$ and $CeO_{1.72}$, respectively. Which suggests that the re-oxidation is practicable at temperature below 1100 K for $CeO_{1.83}$ and 1290 K for$CeO_{1.72}$. Hence, to carry out the analysis, the re-oxidation temperature (T_L) was opted to be 1050 K and 1200 K for $CeO_{1.83}$ and $CeO_{1.72}$, respectively.

Another significant part of the study was the development of process flow configuration of the system and its essential parts such as solar reactor, solar H_2O heater, cooler-A, cooler-B, cooler-C and WS reactor as shown in Fig. 53.

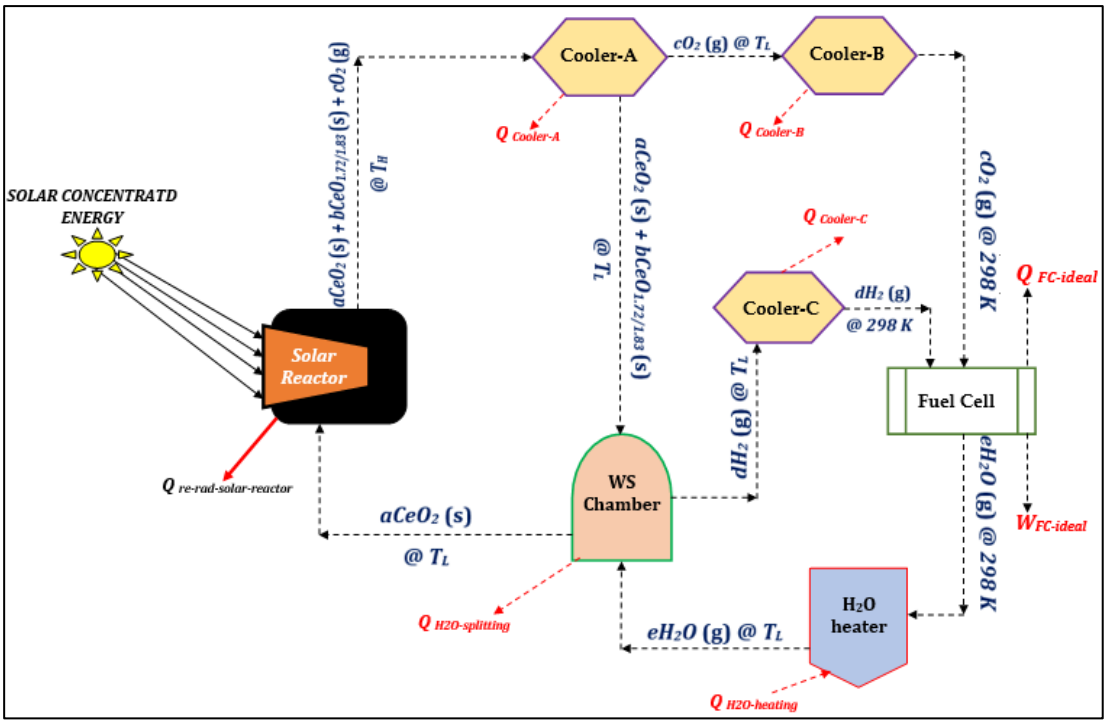

Fig. 53: Process flow arrangement of the CeO_2 thermochemical cycle

The thermal reduction (TR) and water splitting (WS) reactions of CeO_2-*WS* cycle were carried out in solar reactor and WS reactor, respectively. The thermal reduction of CeO_2 into $CeO_{1.72/1.83}$ takes place at high temperature in a solar-driven solar reactor and CeO_2 *(s)*, $CeO_{1.72/1.83}$ *(s)* and O_2 *(g)* at T_H go into cooler-A for temperature control to carry out the re-oxidation reaction. Cooler-A reduces the temperature of all three species from thermal reduction temperature (T_H) to re-oxidation temperature (T_L) and forwards the oxygen gas (O_2) to Cooler-B and CeO_2 *(s)*, $CeO_{1.72/1.83}$ *(s)* to WS reactor chamber. The temperature of O_2 *(g)* was further reduced from T_L to 298 K and then it is transferred into fuel cell (operating at assumed 100% efficiency). The water splitting reaction takes place in the WS reactor chamber and produced hydrogen gas *(H_2)* at T_L and hydrogen gas is then redirected into Cooler-C where it I cooled from T_L to 298 K. Further, the hydrogen was fed into fuel cell at 298 K where it reacts with already present O_2 *(g)* at 298 K and produces H_2O *(l)* molecules at 298 K and passes through H_2O heater and raises the water temperature to T_L and convers into steam and then this steam is fed into WS reactor chamber and makes it a closed loop cycle. WS reactor chamber also produces the CeO_2 *(s)* at T_L which further moves into solar reactor and achieves the thermal reduction temperature (T_H) and a closed loop cycle of the

CeO_2 *(s)* is completed. The numerical thermodynamic calculation was carried out by considering following assumptions;

(i) Solar reactor is operated at the molar flow rate ($\dot{m}$) of 1 mol/sec of CeO_2 *(s)*

(ii) All the thermal losses by means of conduction and convection mode are not accounted for

(iii) The full extent of thermal reduction of CeO_2 *(s)* is assumed

(iv) The changes in the kinetic and potential energies are negligible

(v) HEX calculations are not accounted for in the overall analysis

6.4 Results and discussion

6.4.1 Solar reactor and heaters

The thermodynamic efficiency analysis for the CeO_2–WS cycle was carried out by using the data obtained from the HSC chemistry software. The calculation of the related parameters was performed systematically using the thermodynamic empirical correlations mentioned in the mathematical modelling section.

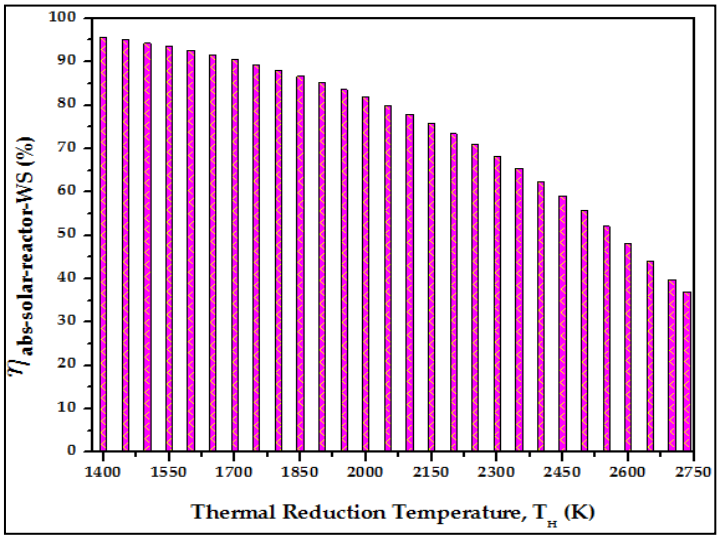

Fig. 54: Effect of T_H on absorption efficiency of solar reactor

First, it is critical to estimate the absorption efficiencies of solar reactor ($\eta_{abs-solar-reactor-WS}$) and solar H_2O heater ($\eta_{abs-solar-H2O-heater-WS}$) using the Eqs. (3) and (4), respectively. Since, the water-splitting reactor was operating at a steady re-oxidation temperature (T_L). It is to be noted that the re-oxidation temperature (T_L) is kept steady because the incoming superheated steam will further fluctuate the

WS reactor temperature and if the temperature of WS reactor is constant, it becomes easier to control the unilateral temperature deviations in the system. Thus, the re-oxidation temperature was kept constant at 1050 K and 1200 K for $CeO_{1.83}$ and $CeO_{1.72}$, respectively and value of concentration ratio (C) considered as 4000 suns. The absorption efficiency of the solar H_2O heater ($\eta_{abs-solar-H2O-heater-WS}$) was stabilized at 98.3% and 97.06% for $CeO_{1.83}$ and $CeO_{1.72}$, respectively.

Conversely, the thermal reduction temperature (T_H) swings in the range of 1400 K to 2734 K and $\eta_{abs-solar-reactor-WS}$ being the function of T_H, decreases with the increasing reduction temperature (T_H). The absorption efficiency of the solar reactor ($\eta_{abs-solar-reactor-WS}$) falls from 95.6% to 37%, when the T_H increases from 1400 K to 2734 K as shown in the Fig. 54. Statistical analysis of the absorption efficiency plot shows that drop in the absorption efficiency of solar reactor was 3.08%, 4.47%, 6.24%, 8.42%, 11.06%, 14.20% and 11.17% for thermal reduction temperature (T_H) increase from 1400 K–1600 K, 1600 K–1800 K, 1800 K–2000 K, 2000 K–2200 K, 2200 K–2400 K, 2400 K–2600 K, and 2600 K–2734 K.

The thermal reduction of CeO_2 is a directly proportional function of T_H which suggest that the increment in the thermal reduction temperature (T_H) results in the rapid reduction rate of CeO_2. Similarly, the increase in T_H shows its effect on the required solar heat energy to reduce the CeO_2 and also to raise the temperature of steam from 298 K to T_L has been shown in Fig. 55. The reported trends show that the increase in thermal reduction temperature (T_H), increases the heat required for the partial reduction of CeO_2 ($Q_{CeO_2-partial-reduction-WS}$) and for the conversion of water (H_2O) into superheated steam ($Q_{H_2O-heating-WS}$). As the reduction of CeO_2 proceeds from 0 to 100% at two different re-oxidation temperatures 1050 K (for formation of $CeO_{1.83}$) and 1200 K (for formation of $CeO_{1.72}$), the solar heat energy required for the partial reduction of CeO_2 ($Q_{CeO_2-partial-reduction-WS}$) increases from 108.19 kW to 2938.78 kW for $CeO_{1.72}$ and from 115.96 kW to 3055.12 kW for $CeO_{1.83}$.

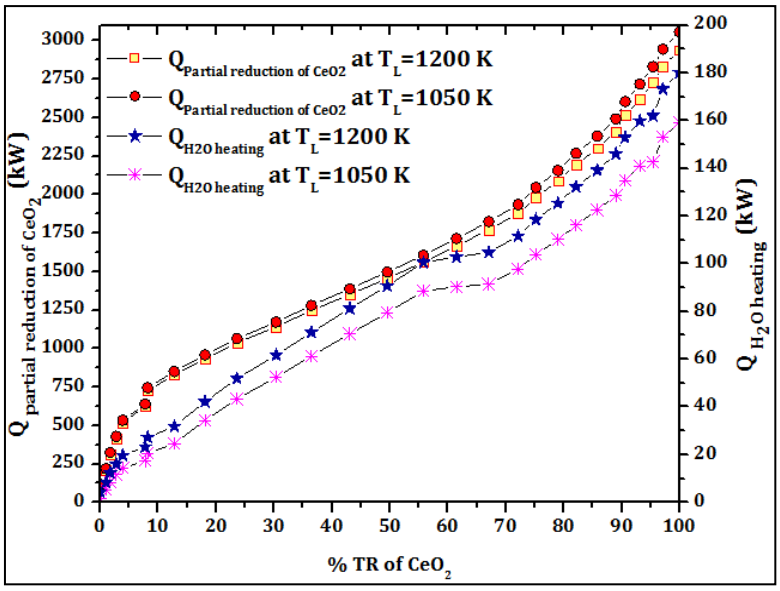

Fig. 55: Effect of %TR of CeO_2 on $Q_{partial\ reduction\ of\ CeO_2}$ and $Q_{H_2O\ heating}$ with increasing T_H

Apparently, for %TR of CeO_2 from 0 to 10.62%, the $Q_{CeO_2-partial-reduction-WS}$ increases quite rapidly and goes from 108.19 kW to 780.6 kW for $CeO_{1.72}$ (T_L = 1200 K) and 115.96 kW to 792.97 kW for $CeO_{1.83}$ (TL = 1050 K). Subsequently, as the %TR of CeO_2 upturns from 10.62% to 76.65%, a slow rise in $Q_{CeO_2-partial-reduction-WS}$ from 780.6 kW to 2021.98 kW for $CeO_{1.72}$ and 792.97 kW to 2103.18 kW for $CeO_{1.83}$ was seen on a liner curve. However, for the further %TR of CeO_2 from 76.65% to 100%, the rise in $Q_{CeO_2-partial-reduction-WS}$ for CeO_2 at T_L = 1200 K ($CeO_{1.72}$) and at T_L = 1050 K ($CeO_{1.83}$) was reported to be from 2021.98 kW to 2938.78 kW and 2103.18 kW to 3055.13 kW, respectively. Statistically, the difference for input solar heat energy required for %TR of CeO_2 at the intervals of 0, 12.8%, 36.44%, 61.5%, and 89.01% to 100% was reported to be 7.78 kW, 20.96 kW, 33.2 kW, 48.85 kW, 84.48kW and 116.34 kW for T_L of 1050 K ($CeO_{1.83}$) and 1200 K ($CeO_{1.72}$).

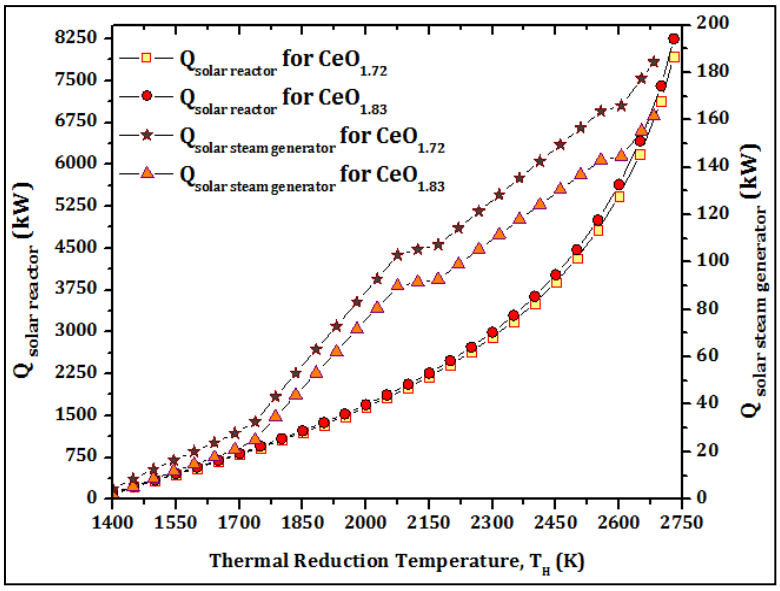

Fig. 56: Influence of T_H on $Q_{solar\ reactor}$ *and* $Q_{solar\ steam\ generator}$

The heat required to drive the solar cycle ($Q_{cycle-net}$) is essentially is a function of heat required to partially reduce the CeO_2 ($Q_{partial\ reduction\ of\ CeO2}$) and to heat up the water ($Q_{H2O\ heating}$) to convert it into the steam to feed into the WS chamber to carry out the re-oxidation reaction and it can be mathematically expressed as Eq. (9). Therefore, it is interpreted that as the $Q_{partial\ reduction\ of\ CeO2}$ and $Q_{H2O\ heating}$ increased, the $Q_{cycle-net}$ also increased with the increasing T_H. Further, the analysis shows that as the reduction temperature (TH) increased from 1400 K to 2750 K, the partial reduction of CeO_2 goes from 0 to 100%. According to the reported data, the upswing in $Q_{cycle-net}$ for $CeO_{1.83}$ (T_L= 1050 K) and $CeO_{1.72}$ (T_L=1200 K) was resulted with the increase in the thermal reduction of CeO_2 from 0 to 100% with the increment in T_H. As the reduction of CeO_2 increases from 0 to 7.74%, the increase in $Q_{cycle-net}$ was reported to be from 112.41 to 645.76 kW for $CeO_{1.83}$ and from 117.74 to 656.06 kW for $CeO_{1.72}$. Furthermore, when the CeO_2 goes up from 7.74% to 23.6%, 43.08%, 61.5%, 75.22%, 93.17% and 100%, the upsurge in $Q_{cycle-net}$ was reported as 1089.27 kW, 1431.74 kW, 1768.26 kW, 2100.46 kW, 2779.99 kW, and 3118.84 kW for $CeO_{1.83}$ and 1107.37 kW, 1457.95 kW, 1804.50 kW, 2148.64 kW, 2857.85 kW, and 3214.42 kW for $CeO_{1.72}$.

The required heat input in the solar reactor ($Q_{solar\ reactor}$) and solar steam generator ($Q_{solar\ H2O\ heater}$) presented in Fig. 56 was estimated using the mathematical

expression given in the Eq. (5) & (6), respectively. It can be observed from the Eq. (5) that the $Q_{solar\ reactor}$ is function of $Q_{partial\ reduction\ of\ CeO2}$ and $\eta_{abs-solar-reactor-WS}$. As stated earlier, the upsurge in the thermal reduction temperature (T_H) directly corresponds to the increase in %TR of CeO_2 which in turn increases the $Q_{partial\ reduction\ of\ CeO2}$ but decreases the $\eta_{abs-solar-reactor-WS}$. Consequently, $Q_{solar\ reactor}$ being a function of %TR of CeO_2 increases with the increase of %TR of CeO_2. In terms of values, it was reported that as %TR of CeO_2 upturns from 0 to 20%, 40%, 60%, 80%, 90% and 100%, the value of $Q_{solar\ reactor}$ upsurged from 121.25 kW to 1174.32 kW, 1642.10 kW, 2226.99 kW, 3455.78 kW, 4801.77 kW, 8254.60 kW for $CeO_{1.83}$ and from 113.12 kW to 1126.55 kW, 1576.70 kW, 2139.55 kW, 3322.07 kW, 4617.39 kW, 7940.25 kW for $CeO_{1.72}$, respectively.

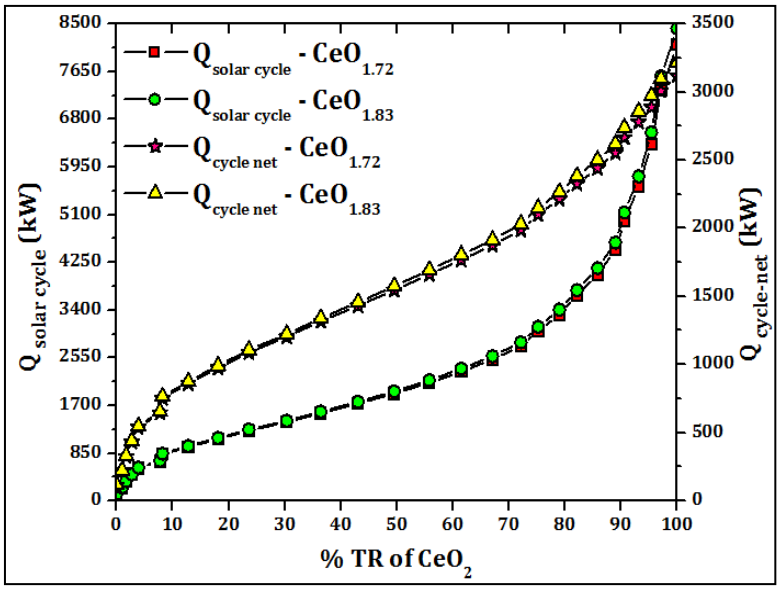

Fig. 57: Effect of %TR of CeO2 on $Q_{solar\ cycle}$ and $Q_{cycle\ net}$

Furthermore, the energy required to superheat the water (H2O) by raising its temperature from 300 K to T_L and convert it into superheated steam in the H2O heater is mathematically estimated by the expression given in the Eq. (6). It was seen that the upsurge in $Q_{solar\ H2O\ heater}$ was reported to be significantly less as compared to the $Q_{solar\ reactor}$. It is indicated in the expression that the $Q_{solar\ H2O\ heater}$ is the function of $Q_{H_2O-heating-WS}$ and $\eta_{abs-solar-H_2O-heater-WS}$. It was seen from the results that the absorption efficiency of the solar water heater ($\eta_{abs-solar-H_2O-heater-WS}$) remains

constant with the increasing %TR of CeO_2. However, $Q_{H_2O-heating-WS}$ is also a function of %TR of CeO_2 and it is directly proportional to the %TR of CeO_2 which allows the $Q_{H_2O-heating-WS}$ to increase with the increasing %TR of CeO_2. It was seen that the $Q_{solar\ H2O\ heater}$ was increased by the factor of 12.94, 18.10, 24.77, 38.13, 50.86 and 89.65 for $CeO_{1.83}$ and 6.73, 9.05, 12.16, 18.37, 24.43 and 42.64 for $CeO_{1.72}$, as the %TR of CeO_2 upturns 20%, 40%, 60%, 80% 90% and 100%, respectively.

The solar energy required in $Q_{\text{cycle-net}-WS}$ and $Q_{\text{solar-cycle}-WS}$ is mathematically expressed in the Eq. (9) and (10). According to the Eq. (9), the addition of $Q_{CeO_2-partial-reduction-WS}$ and $Q_{H_2O-heating-WS}$ gives the $Q_{\text{cycle-net}-WS}$. Thus, the analysis of Fig. 57 reveals that as the %TR of CeO_2 upturns from 0 to 10%, the $Q_{\text{cycle-net}-WS}$ goes up from 112.41 kW to 804.89 kW for $CeO_{1.72}$ and from 117.74 kW to 1095.18 kW for $CeO_{1.83}$. Further, as the %TR of CeO_2 increased to 20%, 40%, 60%, 80% and 100%, the $Q_{\text{cycle-net}-WS}$ also upsurges to 1021.11 kW, 1388.50 kW, 1734.28 kW, 2253.32 kW, 2621.13 kW, and 3118.84 kW, respectively for $CeO_{1.72}$ and 1221.38 kW, 1446.74 kW, 1658.68 kW, 2011.23 kW, 2425.54 kW and 3214.43 kW, respectively for $CeO_{1.83}$. Moreover, the addition of $Q_{solar-reactor-WS}$ and $Q_{solar-H_2O-heater-WS}$ results in $Q_{\text{solar-cycle}-WS}$ as shown in Eq. (10). Therefore, the increase in $Q_{\text{solar-cycle}-WS}$ also has been plotted in the Fig. 57 and it was seen that $Q_{\text{solar-cycle}-WS}$ upsurges with the increase in the %TR of CeO_2. According to the reported data, the %TR of CeO_2 increases to 10%, 20%, 40%, 60%, 80% and 100% resulted in upsurge in $Q_{\text{solar-cycle}-WS}$ by the factor of 10.51, 11.92, 14.62, 17.44, 23.13, 32.15 and 69.18, respectively for $CeO_{1.72}$ and 10.20, 11.58, 14.22, 17.04, 22.61, 31.64, and 68.40, respectively for $CeO_{1.83}$. It was observed that absorption efficiency of the solar reactor ($\eta_{abs-solar-reactor-WS}$) decreases with increasing the oxidation temperature (TL) and it is also a function of the %TR of CeO_2 which leads to $Q_{\text{solar-cycle}-WS}$ reach higher values as compared to $Q_{\text{cycle-net}-WS}$.

6.4.2 Estimation of radiative losses

Given the pre-established assumptions, the thermal losses in the form of conduction and convection from the solar heater and solar reactor had been chosen as negligible as compared to the re-radiation losses. The decreases in solar reactor

absorption efficiency ($\eta_{abs-solar-reactor-WS}$) with the increasing thermal reduction temperature (TH) was the prime reason behind the re-radiation losses from the solar reactor as established in the expression given in the Eq. (11). As the thermal reduction temperature (TH) increased from 1400 K to 1600 K, 1800 K, 2000 K, 2200 K, 2400 K, 2600 K, 2700 K and 2730 K, the re-radiation losses from solar reactor ($Q_{\mathrm{re-rad-solar-reactor-}WS}$) upsurged from 4.93 kW to 40.23 kW, 133.47 kW, 318.57 kW, 661.68 kW, 1344.29 kW, 2832.15 kW, 4290.85 kW and 5001.47 kW, respectively for $CeO_{1.83}$ and from 5.28 kW to 42.82 kW, 129.33 kW, 307.51 kW, 659.82 kW, 1367.47 kW, 2922.17 kW, 4465.2 kW and 5199.48 kW, respectively for $CeO_{1.72}$ as shown in the Fig. 58.

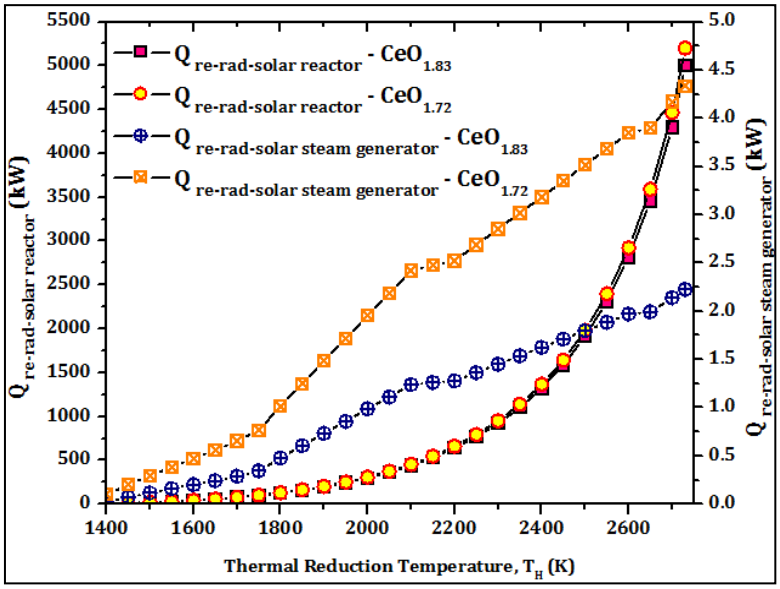

Fig. 58: Effect of Thermal reduction temperature (T_H) on re-radiation losses from solar heater and solar reactor

The solar heater operates at the steady re-oxidation temperature (TL) of 1050 K for $CeO_{1.83}$ and 1200 K for $CeO_{1.72}$ therefore, the absorption efficiency of the solar heater ($\eta_{abs-solar-H_2O-heater-WS}$) remained stabilized at 98.3% and 97.06% for $CeO_{1.83}$ and $CeO_{1.72}$, respectively. Consequently, the re-radiative losses from the solar heater occurred due to the temperature difference between re-oxidation temperature (TL) and ambient temperature. In numeric terms, with the upsurge in the thermal reduction temperature (TH) to 1600 K, 1800 K, 2000 K, 2200 K, 2400 K, 2600 K, 2700 K and 2730 K, the $Q_{re-rad-solar-H_2O-heater-WS}$ increased to 0.20 kW, 0.48 kW, 0.98

kW, 1.28 kW, 1.62 kW, 1.97 kW, 2.14 kW and 2.23 kW, respectively for $CeO_{1.83}$ and 0.47 kW, 1.02 kW, 1.96 kW, 2.52 kW, 3.18 kW, 3.85 kW, 4.17 kW and 4.34 kW, respectively for $CeO_{1.72}$ as shown in the Fig. 58.

The thermal re-radiation losses from the solar cycle were calculated using the expression given in the Eq. (13). It was established from the expression that the re-radiative losses from the solar cycle ($Q_{re-rad-cycle-WS}$) are the combination of $Q_{\text{re-rad-solar-reactor}-WS}$ and $Q_{re-rad-solar-H_2O-heater-WS}$. The re-radiative losses from the solar cycle ($Q_{re-rad-cycle-WS}$) as a function of the %TR of CeO_2 for both $CeO_{1.72}$ and $CeO_{1.83}$ are reported in the Fig. 59.

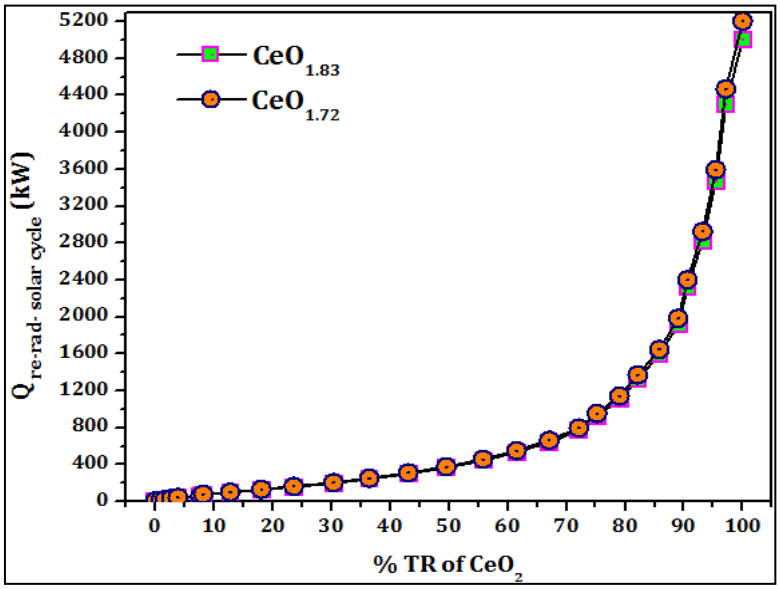

Fig. 59: Effect of %TR of CeO_2 on re-radiative losses from the solar cycle

It was observed as the %TR of CeO_2 increased, the re-radiative losses from the solar cycle ($Q_{re-rad-cycle-WS}$) for both $CeO_{1.72}$ and $CeO_{1.83}$ also increased. According to the data reported in the Fig. (11), the rise in ($Q_{re-rad-cycle-WS}$) was significantly low and occurs linearly for %TR of CeO_2 till 80%. However, after the 80% reduction of CeO_2, the re-radiative losses increased exponentially. In numeric terms, as the %TR of CeO_2 goes up from 0 to 20%, 40%, 60% and 80%, the rise in $Q_{re-rad-cycle-WS}$ occurs from 4.95 kW to 146.99 kW, 298.51 kW, 540.64 kW, 1188.25 kW, respectively for $CeO_{1.83}$ and 5.38 kW, 153.19 kW, 301.50 kW, 562.72 kW, 1236.18 kW, respectively for $CeO_{1.72}$. Conversely, as the reduction of CeO_2 goes to 92%, 95%, 98% and 100%,

the upturn in $Q_{re-rad-cycle-WS}$ was reported to be 2592.05 kW, 3347.91 kW, 455.76 kW and 5003.72 kW, respectively for $CeO_{1.83}$ and 2694.94 kW, 3481.98 kW, 4717.21 kW and 5203.81 kW, respectively for $CeO_{1.72}$.

6.4.3 Coolers and WS reactor

The heat recuperation is the technique applied to reuse the dissipated heat in the solar thermochemical cycle and coolers and WS reactor are the equipments that were used for the purpose of heat energy recuperation. The recuperated heat energy from cooler A, cooler B, cooler C and WS reactor was estimated using the expression given in the Eq. (16), (17), (18) and (19), respectively.

The cooler A was installed to reduce the temperature of entities coming from the solar reactor (CeO_2, $CeO_{1.72/1.83}$ and O_2) from thermal reduction temperature (TH) to re-oxidation temperature (TL). According to the previously established relation, the %TR of CeO_2 directly correlates with the thermal reduction temperature (TH) *i.e.* higher the TH, faster the %TR of CeO_2. Therefore, as the TH increases from 1400 K to 2730 K but the TL remains constant at 1050 K ($CeO_{1.83}$) and 1200 K ($CeO_{1.72}$), the difference between TH and TL also increases. Consequently, a larger gap between the TH and TL results in a greater amount of heat dissipation by the cooler-A and the results have been presented in Fig. 60. The data reported in Fig. 60 suggest that the heat energy dissipated from cooler-A ($Q_{Cooler-A}$) rises from 83.51 kW to 110.83 kW, 345.63 kW, 500.57 kW, 929.14 kW, 1262.78 kW, 1646.62 kW and 1908.71 kW for $CeO_{1.83}$ and 72.25 kW to 73.69 kW, 282.27 kW, 410.96 kW, 813.34 kW, 1120.72 kW, 1478.40 kW and 1720.82 kW for $CeO_{1.72}$, with the thermal reduction temperature (TH) increase from 1400 K to 1600 K, 1800 K, 2000 K, 2200 K, 2400 K, 2600 K and 2734 K, respectively.

Correspondingly, the heat energy dissipated from the cooler-B ($Q_{Cooler-B}$) and the cooler-C ($Q_{Cooler-C}$) also increases with the increase in thermal reduction temperature (TH). The reasons for the increase in heat dissipation were exposed to be the production of high amount of O_2 and H_2 during thermal reduction and re-oxidation step of the thermochemical cycle. Statistically, for the thermal reduction temperature (TH) rise from 1400 K to 1800 K, 2200 K, 2600 K and 2734 K, the $Q_{Cooler-B}$ upturns

from 0.22 kW to 3.99 kW, 14.97 kW, 27.89 kW and 32.44 kW, respectively for $CeO_{1.83}$ and 0.11 kW, 3.04 kW, 13.17 kW, 25.24 kW and 29.46 kW, respectively for $CeO_{1.72}$. While, the $Q_{Cooler-C}$ rises from 0.47 kW, 7.79 kW, 22.53 kW, 39.19 kW and 45.15 kW, respectively for $CeO_{1.83}$ and 0.28 kW, 7.22 kW, 21.46 kW, 37.64 kW and 43.41 kW, respectively for $CeO_{1.72}$.

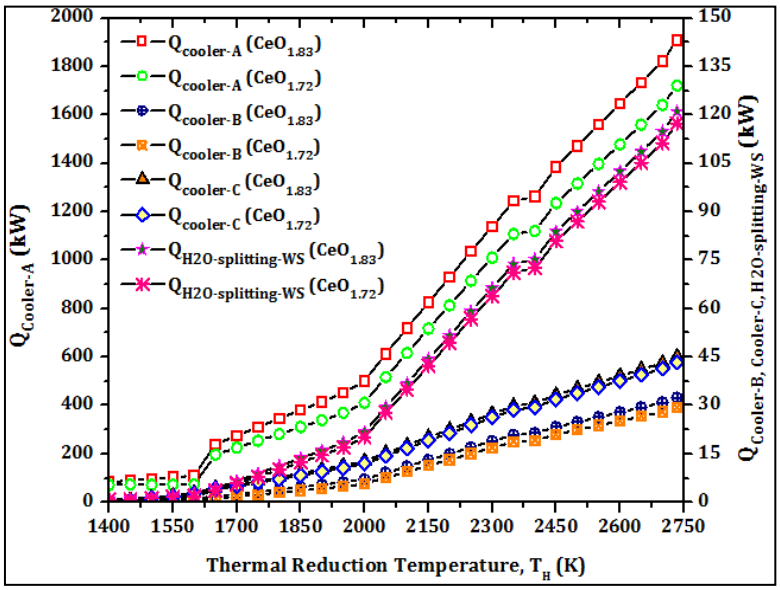

Fig. 60: Effect of TH on $Q_{Cooler-A}$, $Q_{Cooler-B}$, $Q_{Cooler-C}$ and $Q_{H2O\ splitting\ WS}$

Furthermore, the re-oxidation is an exothermic reactor that's why the WS reactor also emits a significant amount of heat energy. Therefore, the release of heat energy from the WS reactor is a function of thermal reduction temperature (TH). The increase of thermal reduction temperature (TH) increases the %TR of CeO_2 which is directly associated with the improved generation of O_2 during the TR step and H_2 production during the WS step. In terms of numbers, the $Q_{H_2O-splitting-reactor-WS}$ rises from 0.75 kW to 11.28 kW, 51.64 kW, 102.45 and 121.05 kW for $CeO_{1.83}$ and 0.84 kW to 10.17 kW, 49.42 kW, 99.13 kW and 117.32 kW for $CeO_{1.72}$, for the thermal reduction temperature (TH) increase from 1400 K to 1800 K, 2200 K, 2600 K and 2734 K, respectively.

6.4.4 Solar-to-fuel conversion efficiency analysis

The solar-to-fuel energy conversion efficiency analysis was the most crucial and the final step of the study. First, all the essential parameters required in the efficiency

analysis were calculated systematically and then the solar-to-fuel energy conversion efficiency was estimated. According to the Eq. (14), the $\eta_{solar-to-fuel}$ directly depends upon the higher heating value (HHV) of H_2 produced and it inversely relates to the solar energy required to drive the solar thermochemical cycle ($Q_{solar-cycle-WS}$). The variations in the solar-to-fuel conversion efficiency ($\eta_{solar-to-fuel}$) associated with the increase in %TR of CeO_2 for both $CeO_{1.72}$ and $CeO_{1.83}$ have been shown in Fig. 61. According to the reported data, the $\eta_{solar-to-fuel}$ rises quite rapidly from 0 to 2.41% ($CeO_{1.83}$) and 2.32% ($CeO_{1.72}$) for the %TR of CeO_2 from 0 to 5%. Further, as the %TR of CeO_2 increased to 10%, 20%, 30%, 40%, 50%, 60%, the $\eta_{solar-to-fuel}$ gradually upturned to 3.53%, 5.00%, 6.19%, 6.99%, 7.48%, 7.67%, respectively and the maximum solar-to-fuel energy conversion efficiency of 7.69% was attained at the %TR of CeO_2 of 61.72% for $CeO_{1.83}$.

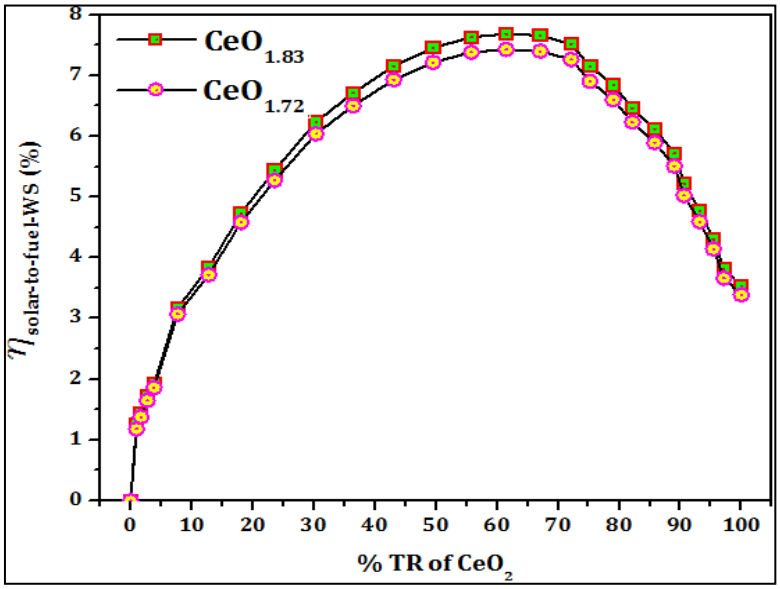

Fig. 61: Effect of %TR of CeO_2 on $\eta_{solar-to-fuel}$

Similarly, for the $CeO_{1.72}$, the $\eta_{solar-to-fuel}$ rises to 3.43%, 4.85%, 5.99%, 6.77%, 7.24%, 7.42%, respectively and it attains the maximum value of $\eta_{solar-to-fuel}$ of 7.45% at the %TR of CeO_2 of 61.72%. It was observed from the reported data that once the cycle reached it maximum efficiency, it preceded to decline with the increase in %TR of CeO_2. At the %TR of CeO_2 of 70%, 80%, 90%, 94%, 97% and 100%, the $\eta_{solar-to-fuel}$ gradually decreased to the value of 7.57%, 6.64%, 5.30%, 4.43%, 3.85%

and 3.53%, respectively for $CeO_{1.83}$ and 7.31%, 6.41%, 5.10%, 4.26%, 3.70% and 3.38%, respectively for $CeO_{1.72}$.

It has been stated that the $\eta_{solar-to-fuel}$ can be improved with the utilization of the heat recovery technique where the heat released from the cooler-A, cooler-B, cooler-C and WS reactor is re-used in the solar thermochemical cycle. The heat recuperation solar-to-fuel energy conversion efficiency ($\eta_{solar-to-fuel-HR}$) can only be estimated after the calculation of the $Q_{\text{recuperation}-WS}$ using the expression given in the Eq. (15). According to the obtained data, the $Q_{\text{recuperation}-WS}$ increased with the increased thermal reduction temperature (TH). Statistically, as the TH increased to 1600 K, 1800 K, 2000 K, 2200 K, 2400 K, 2600 K and 2734 K, the $Q_{\text{recuperation}-WS}$ increased to 39.42 kW, 151.35 kW, 224.39 kW, 448.70 kW, 621.00 kW, 820.20 kW and 955.51 kW, respectively for $CeO_{1.72}$ and 58.71 kW, 184.35 kW, 271.12 kW, 509.14 kW, 695.15 kW, 908.09 kW and 1053.68 kW, respectively for $CeO_{1.83}$ as shown in Fig. 62.

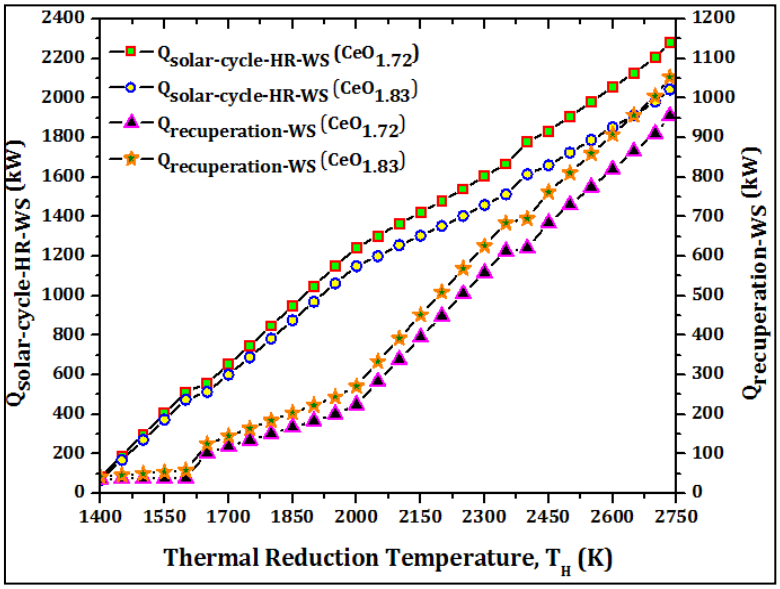

Fig. 62: Effect of thermal reduction temperature (TH) on $Q_{solar-cycle-HR-WS}$ and $Q_{recuperation-WS}$

After the estimation of $Q_{\text{recuperation}-WS}$, the calculation of $Q_{\text{solar-cycle-HR}-WS}$ was required which was done using the Eq. (20). It was observed that the $Q_{\text{solar-cycle-HR}-WS}$ is a function of %HR and the thermal reduction temperature (TH). Further, it was seen that the $Q_{\text{solar-cycle-HR}-WS}$ dropped to a significant value as

compared to the $Q_{\text{solar}-\text{cycle}-WS}$. The reported data suggest that as the TH increased to 1600 K, 1800 K, 2000 K, 2200 K, 2400 K, 2600 K and 2734 K, the $Q_{\text{solar}-\text{cycle}-\text{HR}-WS}$ increased to 513.50 kW, 847.90 kW, 1244.13 kW, 1480.08 kW, 1778.44 kW, 2056.36 kW and 2279.67 kW, respectively for $CeO_{1.72}$ and 475.05 kW, 783.34 kW, 1150.05 kW, 1353. 12 kW, 1615. 15 kW, 1853.18 kW and 2044.41 kW, respectively for $CeO_{1.83}$.

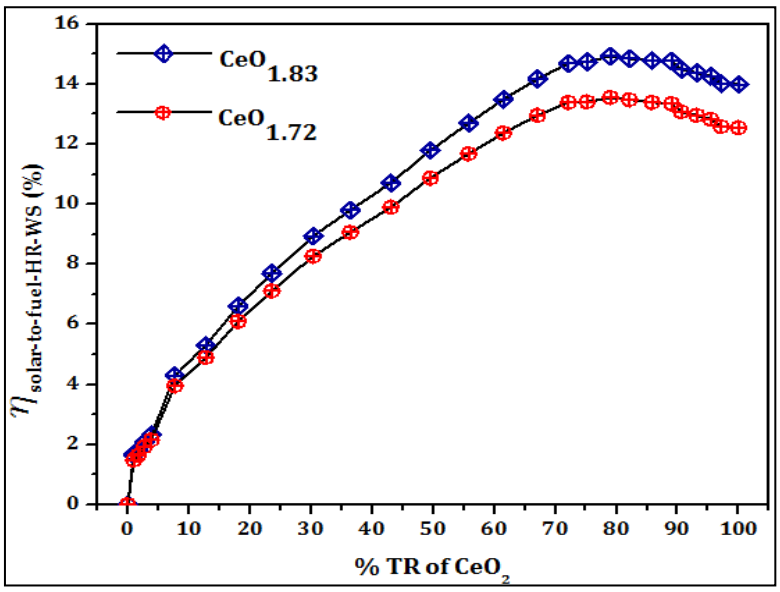

Fig. 63: Effect of %TR of CeO_2 on $\eta_{solar-to-fuel-HR}$

The reduction in the $Q_{\text{solar}-\text{cycle}-\text{HR}-WS}$ improved the solar-to-fuel conversion efficiency $\eta_{solar-to-fuel-HR}$ as shown in Fig. 63 by employment of 50% heat recovery. The reported data suggest that the increase in %TR of CeO_2 to 5%, 10%, 20%, 40%, 60%, 70%, 80% 90% and 100%, the upsurge in the $\eta_{solar-to-fuel-HR}$ to 2.88%, 4.89%, 6.91%, 10.29%, 13.34%, 14.49%, 14.92%, 14.58% and 13.99%, respectively for $CeO_{1.83}$ and 2.73%, 4.54%, 6.42%, 9.53%, 12.25%, 12.24%, 13.54%, 12.16% and 12.55%, respectively for $CeO_{1.72}$. Therefore, it was seen that the maximum efficiency with the 50% heat recovery was 14.92% and 13.54% for $CeO_{1.83}$ and $CeO_{1.72}$, respectively at the %TR of CeO_2 of 80%.

6.5 Summary and conclusion

This study thermodynamically investigated the conversion of H_2O into H_2 via solar thermochemical water splitting cycle and analyzed the effect of two different non-stoichiometric configuration as $CeO_{1.72}$ and $CeO_{1.83}$. HSC chemistry v6.0 software was

used for the parametric analysis and Engineering Equation Solver (EES) was used to solve the thermodynamic equations. The equilibrium analysis suggested that the %TR of CeO_2 increased from 0 to 8.2%, 55.8%, 82.2%, 93.3% and 100% with the increase in thermal reduction temperature (TH) from 1400 K to 1700 K, 2100 K, 2400 K, 2600 K and 2734 K, respectively. Further, it was seen that the $Q_{\text{partial reduction of } CeO_2}$, $Q_{H_2O-heating-WS}$, $Q_{solar-H_2O-heater-WS}$and $Q_{solar-reactor-WS}$ was upturned up to 2834.48 kW ($CeO_{1.83}$) & 2944.03 kW ($CeO_{1.72}$), 153.12 kW($CeO_{1.83}$) & 173.21 kW($CeO_{1.72}$), 155.27 kW($CeO_{1.83}$) & 177.38 kW($CeO_{1.72}$) and 7133.54 kW($CeO_{1.83}$) & 7409.23 kW($CeO_{1.72}$), respectively when the thermal reduction temperature (TH) increased to 2700 K. Furthermore, The increase in $Q_{solar-reactor-WS}$ and $Q_{solar-H_2O-heater-WS}$ caused an increase in $Q_{solar-\text{cycle}-WS}$ and $Q_{re-rad-solar-cycle-WS}$ from 7310.92 kW ($CeO_{1.72}$) & 7564.50 kW ($CeO_{1.83}$) and 4301.20 kW & 4469.37 kW with the increase in reduction temperature (TH) up to 2700 K. Therefore, the solar-to-fuel conversion efficiency ($\eta_{solar-to-fuel}$) reached the maximum value of 7.45% ($CeO_{1.72}$) and 7.69% ($CeO_{1.83}$) at the %TR of CeO_2 of 61.72% without heat recuperation and it attained the maximum value of 14.92% and 13.54% for $CeO_{1.83}$ and $CeO_{1.72}$, respectively at the %TR of CeO_2 of 80% with the 50% heat recuperation.

Chapter – 7

7 Thermodynamic evaluation of Cerium Sulfate – Cerium Oxide water-splitting Solar Thermochemical Cycle

7.1 Introduction

The rapid depletion of fossil fuels has given a wakeup call to the research community and it has been abundantly clear that solar fuels such as hydrogen and syngas are the future source of energy [235]. Research on renewable energy sources has been focused on finding a viable solar thermochemical cycle to produce hydrogen or syngas at pilot scale. Thus, researchers have investigated solar thermochemical water and/or CO_2 splitting cycles. Years of extensive research have revealed that the metal oxide based thermochemical cycles are one of the best options for hydrogen production. Many metal oxide based solar thermochemical cycles such as iron oxide [235–238], doped iron oxides (ferrites) [207, 217-218, 240-241], tin oxide [219, 242–244], zinc oxide [245–247], ceria and doped ceria [220, 247–252], perovskites material [224], [252–255] and some other materials [155, 210, 257, 258] were investigated for hydrogen production. It should be noted that the ceria based thermochemical cycles are capable of yielding significant amount of hydrogen. However, Cerium oxide is a non-volatile compound thus it requires extremely high temperatures to thermally dissociate. When metal oxide is combined with sulfur-based compounds, it provides a possible solution of thermal dissociation of cerium oxide at lower temperature.

Bhosale et al. perfomed thermodynamic analysis on iron oxide – ferrous sulfate (FeSO4/FeO) [233] and zinc oxide – zinc sulfate (ZnSO4/ZnO) [158] water splitting cycle and proved that solar-to-fuel conversion efficiency was higher than the other metal oxide based solar thermochemical cycles. The metal oxide – metal sulfate (MO – MS) based WS cycles provides the means to reduce the operating temperature of the cycle and the operating cost of the rare earth-based metal can be reduced by the combination of less expansive sulfate compound.

Among all the WS cycles explored, Ceria (cerium oxide – CeO_2) based cycle proved to be one of the most promising thermochemical cycle for hydrogen production. In the study, $Ce_2(SO_4)_3/CeO_2$ WS cycle was thermodynamically investigated for hydrogen production due to its ability to operate at relatively low reduction temperature. The redox reactions for the cerium sulfate – cerium oxide thermochemical cycle have been given in the Eq. (99) and (100);

$$Ce_2(SO_4)_3 \rightarrow 2CeO_2 + 3SO_2(g) + O_2(g) \quad (99)$$

$$2CeO_2 + 3SO_2(g) + 2H_2O(g) \rightarrow Ce_2(SO_4)_3 + 2H_2(g) \quad (100)$$

The first step of the cycle is endothermic reduction reaction as mentioned in the Eq. (99) where $Ce_2(SO_4)_3$ reduced into $2CeO_2$, $3SO_2(g)$ and $O_2(g)$ in a solar reactor operating at high temperature. The second step of the cycle is exothermic re-oxidation reaction which takes place in the WS reactor at lower temperature than the reduction reaction. In this step, $2CeO_2$, $3SO_2(g)$ and $2H_2O(g)$ combine to produce $2H_2(g)$ and $Ce_2(SO_4)_3$ which is moved into solar reactor to continue the thermochemical cycle.

7.2 Theory and system design

The solar driven cerium (III) sulfate ($Ce_2(SO_4)_3$)-cerium (IV) oxide (CeO_2) water splitting cycle operates in two-step redox cycle to produce hydrogen as shown in Fig. 64. In the first step, the reduction reaction of $Ce_2(SO_4)_3$ takes place in the solar reactor at high temperature and cerium oxide (CeO_2), Oxygen (O_2) and Sulphur di-oxide (SO_2) is released. In the second step, re-oxidation of CeO_2 occurs at lower temperature in the presence of SO_2 gas and H_2O to produce $Ce_2(SO_4)_3$ and hydrogen (H_2) gas.

The process flow arrangement of $Ce_2(SO_4)_3$ solar thermochemical water splitting cycle has been shown in Fig. 65. The concentrated solar energy raises the temperature of the solar reactor to its operational temperature (TH) to carry out the thermal reduction of $Ce_2(SO_4)_3$. The cerium sulfate ($Ce_2(SO_4)_3$) is thermally reduced into cerium oxide (CeO_2), Sulphur di-oxide (SO_2) and oxygen (O_2) in the presence of nitrogen (N_2) gas which acts as a reducing agent. CeO_2 is directed towards the WS reactor to carry out the re-oxidation reaction. Other species coming from the solar reactor such as SO_2, O_2 and N_2 pass through the cooler-A which reduces their

temperature from T_H to 300 K. Further, these species at 300 K pass through the gas separator where all three gaseous species are separated.

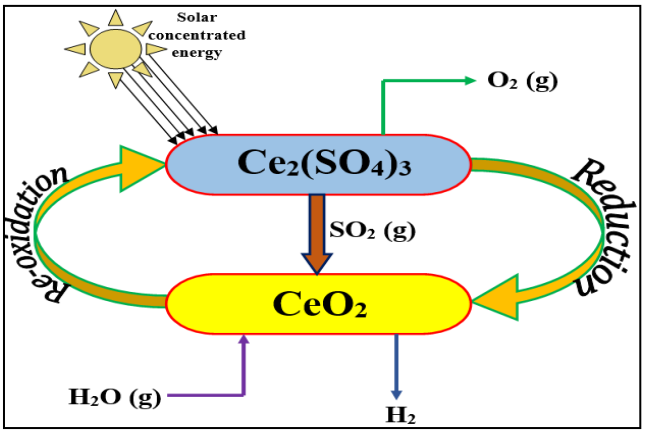

Fig. 64: Cerium (III) sulfate – cerium (IV) oxide water splitting cycle solar driven thermochemical cycle

The N_2 gas then flows through the N_2 heater and goes back into the solar reactor while the SO_2 passes through the SO_2 heater which raises its temperature to TL and feeds int the WS reactor to participate into re-oxidation reaction. The O_2 gas from the gas separator goes into fuel cell and converts into water after combining with already present H_2 at 300 K.

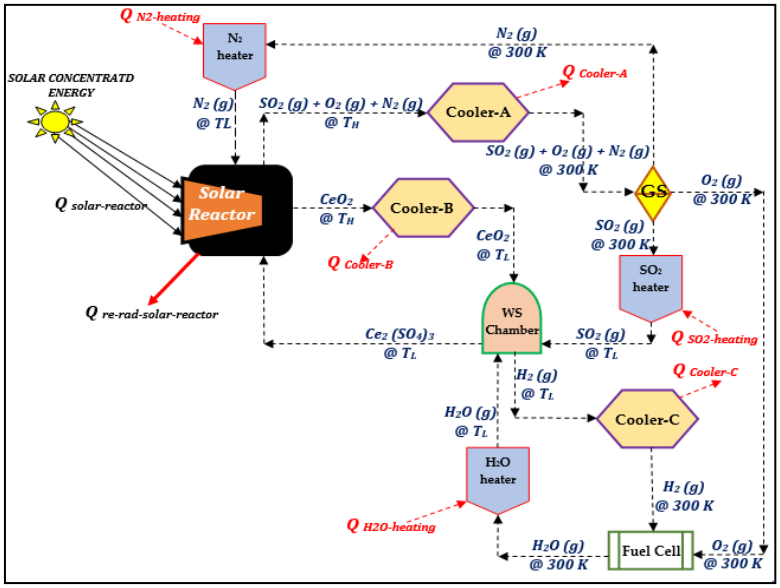

Fig. 65: Process flow system arrangement for cerium (III) sulfate – cerium (IV) oxide WS cycle

This water then passes through the H2O heater which raises with temperature to TL and feeds it into the WS reactor. All the species present in the WS reactor take part in

the re-oxidation reaction at TL and produce $Ce_2(SO_4)_3$ which goes back into the solar reactor and the whole process occurs in a cycle.

The thermodynamic analysis of solar driven cerium (III) sulfate – cerium (IV) oxide WS thermochemical cycle is based on following mentioned assumptions;

(i) The molar flow rate ($\dot{m}$) of $Ce_2(SO_4)_3$ was kept steady at 1 mol/sec
(ii) The thermal losses via heat transfer mode of conduction and convection are not included in the calculation
(iii) The overall analysis doesn't include the HEXs
(iv) The full extent of thermal reduction of $Ce_2(SO_4)_3$ had been achieved
(v) The changes in the kinetic as well as potential energies are rendered as negligible

7.3 Mathematical modelling

7.3.1.1 Absorption efficiency

The absorption efficiency of solar reactor ($\eta_{abs-solar-reactor-WS}$) and H_2O heater ($\eta_{abs-solar-H_2O-heater-WS}$) is calculated using the Stefan-Boltzmann law for a black body subjected to perfectly insulation and only thermal losses are through re-radiation. The absorption efficiencies have to be estimated first in order to calculate the solar-to-fuel ($\eta_{solar-to-fuel}$) conversion efficiency. Therefore, the expressions to calculate absorption efficiencies of solar reactor and H_2O heater (N_2 heater and SO_2 heater as well) are mentioned in the Eq. (101) and (102), respectively.

$$\eta_{abs-solar-reactor-WS} = \left[1 - \left(\frac{\sigma T_H^4}{IC}\right)\right] \tag{101}$$

$$\eta_{abs-solar-H_2O-heater-WS} = \left[1 - \left(\frac{\sigma T_L^4}{IC}\right)\right] \tag{102}$$

In the aforementioned expressions, I, σ and C are the constant and their values are taken as 1000 W/m^2, 6.67×10^{-8} and 2000 suns. However, the value of concentration ratio (C) function of the normal direct solar irradiation (I), aperture area of solar reactor (A_{ap}) and q_{solar} as mentioned in the Eq. (103),

$$C = \frac{q_{solar}}{I \times A_{ap}} \tag{103}$$

Therefore, in case of limited power supply to the solar reactor, the value of concentration ratio (C) can be estimated using the Eq. (103). The units of q_{solar} and A_{ap} are taken as Watt and m^2, respectively.

7.3.1.2 Heaters and $Ce_2(SO_4)_3$ reduction

In a thermochemical cycle, the solar heat energy required to drive the reduction reaction of $Ce_2(SO_4)_3$ and other species involved in the redox reaction cycle such as N_2, SO_2 and H_2O is based on the change in enthalpy and flow rate of the species. At the beginning of the cycle reactants are at NTP. Thus, heaters are used to raise the temperature of species from 300 K to re-oxidation temperature (T_L). The solar heat energy required to achieve the re-oxidation temperature (T_L) for N_2, SO_2 and H_2O is given in the Eq. (104), (105) and (106), respectively.

$$Q_{N_2-heating} = \left(\dot{m}_{N_2}\right)\Delta H|_{N_2(g)\ at\ 300\ K \rightarrow N_2(g)\ at\ T_L} \quad (104)$$

$$Q_{SO_2-heating} = \left(\dot{m}_{SO_2}\right)\Delta H|_{SO_2(g)\ at\ 300\ K \rightarrow SO_2(g)\ at\ T_L} \quad (105)$$

$$Q_{H_2O-heating} = \left(\dot{m}_{H_2O}\right)\Delta H|_{H_2O(l)\ at\ 300\ K \rightarrow H_2O(g)\ at\ T_L} \quad (106)$$

The Eq. (107) is given to estimate the solar heat energy required for the reduction of $Ce_2(SO_4)_3$ where the change in enthalpy (ΔH) with the increase in temperature from T_L to T_H.

$$Q_{Ce_2(SO_4)_3-reduction} = \left(\dot{m}_{Ce_2(SO_4)_3}\right)\Delta H|_{Ce_2(SO_4)_3(s) + (\dot{m}_{N_2})N_2(g)\ at\ T_L \rightarrow CeO_2(s) + SO_2(g) + O_2(g) + (\dot{m}_{N_2})N_2(g)\ at\ T_H} \quad (107)$$

The above given Eq. (108) also incorporates the effect of enthalpy change of inert gas (N_2) due to the reason that N_2 acts as a reducing agent and assists in rapid reduction of $Ce_2(SO_4)_3$ with the increasing reduction temperature (TH).

$$Q_{net-cycle} = Q_{N_2-heating} + Q_{SO_2-heating} + Q_{H_2O-heating} + Q_{Ce_2(SO_4)_3-reduction} \quad (108)$$

The addition of Eq. (104), (105), (106) and (107) results in the net solar heat energy require to drive the thermal reduction cycle ($Q_{net-cycle}$).

Furthermore, the solar heat energy required to operate the $N_2 - heater$ is a function of solar heat energy required to heat nitrogen gas from 300 K to T_L ($Q_{N_2-heating}$) and the absorption efficiency of the $N_2 - heater$ ($\eta_{abs-N_2-heater}$) as mentioned in the Eq. (109). Congruently, the solar heat energy required for $SO_2 - heater$ and $H_2O - heater$ has been given in the Eq. (110) and Eq. (111), respectively.

$$Q_{N_2-heater} = \left[\frac{Q_{N_2-heating}}{\eta_{abs-N_2-heater}}\right] \quad (109)$$

$$Q_{SO_2-heater} = \left[\frac{Q_{SO_2-heating}}{\eta_{abs-SO_2-heater}}\right] \quad (110)$$

$$Q_{H_2O-heater} = \left[\frac{Q_{H_2O-heating}}{\eta_{abs-H_2O-heater}}\right] \quad (111)$$

The reduction reaction of $Ce_2(SO_4)_3$ takes place in the solar reactor. Therefore, the solar heat energy required to efficiently operate the solar reactor is the function of the thermal reduction of $Ce_2(SO_4)_3$ ($Q_{Ce_2(SO_4)_3-reduction}$) and the absorption efficiency of the solar reactor ($\eta_{abs-solar-reactor}$) as mentioned in the Eq. (112). Examination of the given expression suggest that the $\eta_{abs-solar-reactor}$ has to be significantly low for the efficient operation of the solar reactor.

$$Q_{solar-reactor} = \left[\frac{Q_{Ce_2(SO_4)_3-reduction}}{\eta_{abs-solar-reactor}}\right] \quad (112)$$

Meanwhile, the thermal reduction of $Ce_2(SO_4)_3$ gradually increases with the increasing thermal reduction temperature (T_H) which in turn leads to increase in the $Q_{Ce_2(SO_4)_3-reduction}$.

$$Q_{solar-cycle} = Q_{N_2-heater} + Q_{SO_2-heater} + Q_{H_2O-heater} + Q_{solar-reactor} \quad (113)$$

7.3.1.3 Re-radiative thermal losses

While operating a thermochemical water splitting cycle for hydrogen production, thermal losses from the solar reactor and heaters are inevitable. However, thermal losses by means of conduction and convection mode of heat transfer have been rendered negligible and re-radiative losses are taken into consideration because the conductive and convective losses are insignificant as compared to the re-radiative losses. This cycle is operational with use of three heaters *i.e.* N_2-heater, SO_2-heater,

H_2O-heater. The mathematical expression to estimate the re-radiative losses from the N2-heater has been given in the Eq. (114).

$$Q_{re-rad-N_2-heater} = \left(Q_{N_2-heater}\right) - \left(Q_{N_2-heating}\right) \quad (114)$$

The expression mentioned above suggest that the re-radiative heat loss from the N_2-heater depends upon the solar heat energy required to operate the N_2-heater $\left(Q_{N_2-heater}\right)$ from the Eq. (109) and heat energy required to heat up the N_2 gas to raise its temperature from 300 K to T_L $\left(Q_{N_2-heating}\right)$ from the Eq. (104). Therefore, subtraction of the Eq. (104) from the Eq. (109) provides with the re-radiative heat loss from the N_2-heater.

$$Q_{re-rad-SO_2-heater} = \left(Q_{SO_2-heater}\right) - \left(Q_{SO_2-heating}\right) \quad (115)$$

$$Q_{re-rad-H_2O-heater} = \left(Q_{H_2O-heater}\right) - \left(Q_{H_2O-heating}\right) \quad (116)$$

Similarly, the re-radiative heat loss from SO_2 and H_2O heaters can be calculated from the Eq. (115) and (116), respectively. As stated above, the re-radiative heat loss from SO_2-heater is the result of the Eq. (105) being subtracted from the Eq. (110) and re-radiative heat loss from H_2O-heater is estimated by subtracting the Eq. (111) from the Eq. (106).

Given the fact that the solar reactor operates at higher temperature therefore, the re-radiative heat loss from the solar reactor are significantly higher as compared to all three heaters. Hence, the re-radiative heat loss from the solar reactor is calculated using the Eq. (117). Assessment of the Eq. (117) implies that $Q_{re-rad-solar-reactor}$ is obtained by subtracting the Eq. (112) from the Eq. (107) where the Eq. (112) estimates the solar heat energy required to operate the solar reactor and Eq. (107) deals with the solar heat energy needed for the full extent (100%) reduction of $Ce_2(SO_4)_3$.

$$Q_{re-rad-solar-reactor} = \left(Q_{solar-reactor}\right) - \left(Q_{Ce_2(SO_4)_3-reduction}\right) \quad (117)$$

Once the re-radiative heat losses from all three heaters and solar reactor have been calculated, the re-radiative heat loss from the cycle can be estimated by merely adding all the entities as shown in the Eq. (118).

$$Q_{re-rad-solar-cycle} = Q_{re-rad-N_2-heater} + Q_{re-rad-SO_2-heater} + Q_{re-rad-H_2O-heater} + Q_{re-rad-solar-reactor} \quad (118)$$

7.3.1.4 Coolers and WS reactor

Temperature control between two successive steps of water splitting redox reaction cycle *i.e.* high-temperature reduction reaction and low-temperature re-oxidation reaction is accomplished by the use of coolers. Solar reactor operates at high temperature to carry out the thermal reduction of $Ce_2(SO_4)_3$ and WS reactor operates at low temperature to carry out the re-oxidation of CeO_2 in the presence of superheated steam. Therefore, installment of cooler-A between the solar reactor and gas separator (GS) reduces the temperature of species coming from the solar reactor such as SO_2, O_2 and N_2 from T_H to 300 K which in turn decreases the enthalpy of the species.

$$Q_{cooler-A} = -\left(\dot{m}_{Ce_2(SO_4)_3}\right)\Delta H|_{SO_2(g) + O_2(g) + (\dot{m}_{N_2})N_2(g)\ at\ T_H \rightarrow SO_2(g) + O_2(g) + (\dot{m}_{N_2})N_2(g)\ at\ 300\ K} \quad (119)$$

The heat energy extracted from the cooler-A has been shown in Eq. (119). It's seen that $Q_{cooler-A}$ is the function of molar flow rate of $Ce_2(SO_4)_3$ ($\dot{m}_{Ce_2(SO_4)_3}$) and the change in enthalpy with decrease in temperature from TH to 300 K.

$$Q_{cooler-B} = -\left(\dot{m}_{Ce_2(SO_4)_3}\right)\Delta H|_{CeO_2(s)\ at\ T_H \rightarrow CeO_2(s)\ at\ T_L} \quad (120)$$

Meanwhile, the cooler-B was mounted between the solar reactor and WS reactor to reduce the temperature of the CeO_2 coming from the solar reactor. According to the Eq. (120), cooler-B extracts the heat energy from the CeO_2 at T_H and brings it down to T_L. The enthalpy difference between T_H and T_L combine with the molar flow rate of $Ce_2(SO_4)_3$, which determines the amount of CeO_2 released, estimates the amount of heat energy extracted by the cooler-B.

$$Q_{cooler-C} = -\left(\dot{m}_{Ce_2(SO_4)_3}\right)\Delta H|_{H_2(g)\ at\ T_L \rightarrow H_2(g)\ at\ 300\ K} \quad (121)$$

Correspondingly, the cooler-C was equipped to moderate the temperature of produced H_2 gas. Since, H_2 gas is produced in the WS reactor and exits the WS reactor

at TL where the cooler-B extracts the heat energy and brings its temperature down to 300 K as shown in the Eq. (121).

$$Q_{WS-reactor} = -\left(\dot{m}_{Ce_2(SO_4)_3}\right)\Delta H|_{CeO_2(s)+H_2O(g)+SO_2(g)\ at\ T_L \rightarrow Ce_2(SO_4)_3(s)+H_2(g)\ at\ T_L} \quad (122)$$

The re-oxidation reaction takes place in the WS reactor where CeO_2, H_2O and SO_2 react and produce $Ce_2(SO_4)_3$ and H_2 gas while the WS reactor temperature remains unchanged at T_L for reactants as well as the product as shown in the Eq. (122). Furthermore, the solar heat energy required to operate the WS reactor depends upon the molar flow rate of $Ce_2(SO_4)_3$ and the change in enthalpy of the reactants and the product species.

The solar-to-fuel conversion efficiency of the $Ce_2(SO_4)_3$ solar thermochemical cycle was estimated using the Eq. (123) where the $Q_{solar-cycle}$ was calculated using the Eq. (113).

$$\eta_{solar-to-fuel} = \left\{\frac{HHV_{H_2} \times moles\ of\ H_2}{Q_{solar-cycle}}\right\} \quad (123)$$

7.3.1.5 Heat recuperation

The solar-to-fuel conversion efficiency of the $Ce_2(SO_4)_3$ solar thermochemical cycle can be improved by applying the heat recuperation concept. The heat rejected from the solar reactor and all three heaters was recovered using three coolers.

$$Q_{recuperable} = Q_{cooler-A} + Q_{cooler-B} + Q_{cooler-C} + Q_{WS-reactor} \quad (124)$$

The recuperable solar heat energy ($Q_{recuperable}$) was estimated using the Eq. (124) where the heat recovered by all three coolers (cooler-A, B and C) as well as WS reactor was added. Further, the $Q_{recuperation}$ was calculated using the Eq. (125) by taking account of percentage of heat recovery (%HR).

$$Q_{recuperation} = (\%HR) \times Q_{recuperable} \quad (125)$$

Once the $Q_{recuperation}$ has been calculated, the solar heat energy required to operate the solar cycle after taking account of heat recovery ($Q_{solar-cycle-HR}$) was

estimated by subtracting the $Q_{recuperation}$ from the $Q_{solar-cycle}$ as mentioned in the Eq. (126).

$$Q_{solar-cycle-HR} = Q_{solar-cycle} - Q_{recuperation} \quad (126)$$

$$\eta_{solar-to-fuel-HR} = \left\{\frac{HHV_{H_2} \times moles\ of\ H_2}{Q_{solar-cycle-HR}}\right\} \quad (127)$$

After the estimation of $Q_{solar-cycle-HR}$, the solar-to-fuel conversion efficiency with heat recuperation ($\eta_{solar-to-fuel-HR}$) was calculated using the Eq. (127) where the $Q_{solar-cycle}$ from Eq. (113) was substituted with $Q_{solar-cycle-HR}$ as calculated from the Eq. (126).

7.3.1.6 Study validation

$$W_{Fuel-cell-ideal} = -\left(\dot{m}_{Ce_2(SO_4)_3}\right)\Delta G|_{2H_2(g) + O_2(g)\ at\ 300\ K \rightarrow 2H_2O(l)\ at\ 300\ K} \quad (128)$$

$$Q_{Fuel-cell-ideal} = -(298) \times \left(\dot{m}_{Ce_2(SO_4)_3}\right)\Delta S|_{2H_2(g) + O_2(g)\ at\ 300\ K \rightarrow 2H_2O(l)\ at\ 300\ K} \quad (129)$$

7.4 Thermodynamic modelling

The thermodynamic analysis on solar assisted $Ce_2(SO_4)_3$ thermochemical water splitting cycle was carried out by applying the second law of thermodynamics and HSC chemistry software. The numerical study of the various chemical processes and the effects of crucial variables such as change in enthalpy (ΔH), entropy (ΔS), Gibbs free energy (ΔG) and heat capacity (ΔCp) can be performed with the help of HSC chemistry software because it provides access to 28,000 chemical species.

The primary step of the thermodynamic analysis is to evaluate the equilibrium composition and stipulate the thermal reduction temperature (T_H) as well as the re-oxidation temperature (T_L) of the $Ce_2(SO_4)_3$ thermochemical water splitting cycle. In the second step, the solar-to-fuel conversion efficiency ($\eta_{solar-to-fuel}$) of the thermochemical cycle is estimated with and without heat recuperation. Therefore, the equilibrium analysis on the solar assisted $Ce_2(SO_4)_3$ thermochemical water splitting cycle was performed using HSC database to explore the effect of operating temperature on the change in the Gibbs free energy (ΔG) as shown in Fig. 66. Given the fact that the change in gibs free energy (ΔG) is the function of operating temperature of the

thermochemical cycle thus it allows to justify the reduction temperature (TH) and re-oxidation temperature (TL).

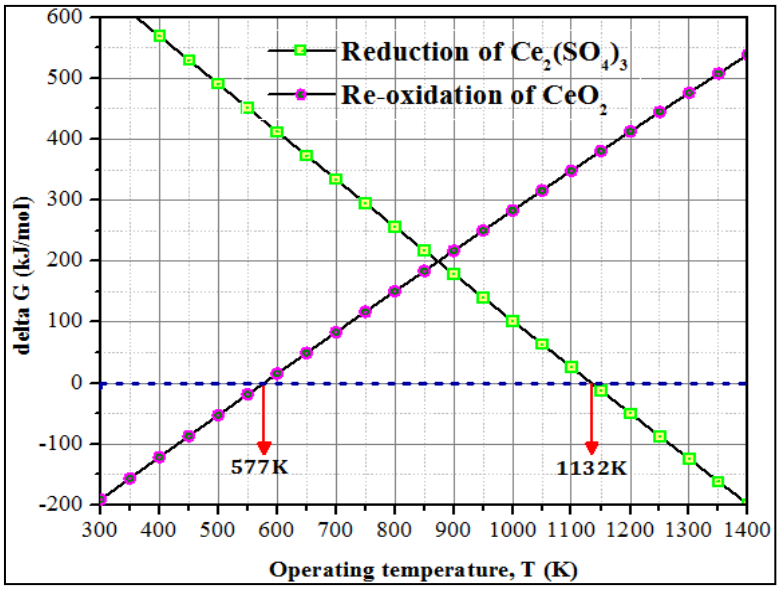

Fig. 66: Effect of operating temperature (T) on delta G

The re-oxidation reaction is an endothermic reaction which implies that ΔG is directly related to the temperature. However, the reduction reaction is exothermic reaction therefore ΔG is inversely related to temperature. According to the Gibbs free energy (ΔG) relation, eventually ΔG will approach zero value at some temperature for both re-oxidation and reduction. The change in Gibbs free energy (ΔG) for $Ce_2(SO_4)_3$ thermochemical water splitting cycle reaches to the zero value at the temperature of 577 K for re-oxidation reaction and 1132 K for reduction reaction. Consequently, for $Ce_2(SO_4)_3$ thermochemical cycle, the re-oxidation is practicable below 577 K and the reduction of $Ce_2(SO_4)_3$ will be feasible over 1132 K.

The evaluation and stipulation of re-oxidation temperature (TL) and thermal reduction temperature (TH) range facilitates the equilibrium analysis for the estimation of CeO_2, SO_2 and O_2 production from the reduction of the single mole of $Ce_2(SO_4)_3$ as shown in Fig. 67. The oxygen partial pressure (P_{O_2}) was set to be 1 bar for the reduction of $Ce_2(SO_4)_3$. The thermal reduction (of $Ce_2(SO_4)_3$) being the function of temperature starts at 900 K and show moderate reduction up to 1050 K. However, as the thermal reduction temperature (TH) increased beyond 1050 K, the reduction of $Ce_2(SO_4)_3$ increased rapidly and the 100% reduction of single mole of $Ce_2(SO_4)_3$ was achieved at

1200 K. Therefore, the reduction of $Ce_2(SO_4)_3$ results in the evolution of SO_2, CeO_2 and O_2 and increases continuously with the increase of T_H.

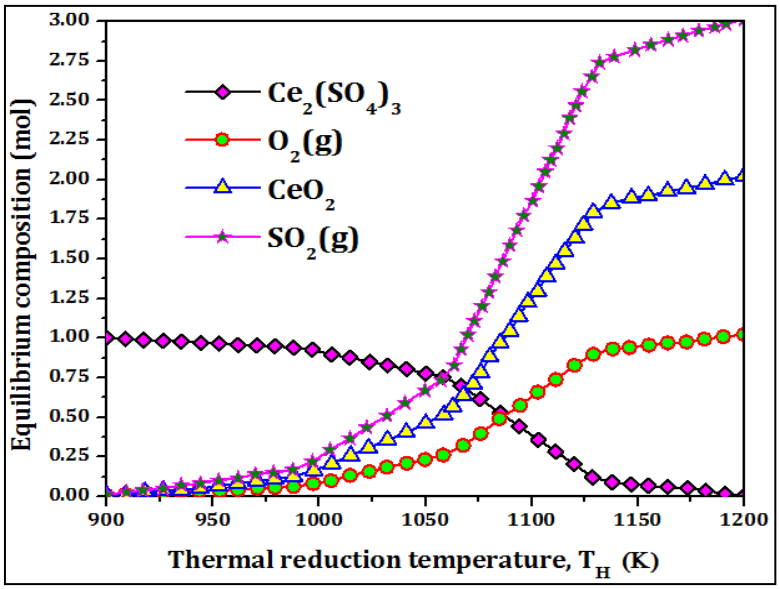

Fig. 67: Effect of thermal reduction temperature (T_H) on the equilibrium composition of $Ce_2(SO_4)_3$

As stated earlier, the thermal reduction of Cerium sulfate ($Ce_2(SO_4)_3$) is a function of thermal reduction temperature (T_H). Hence, continuous increase in TH results in the increase of thermal reduction of $Ce_2(SO_4)_3$.

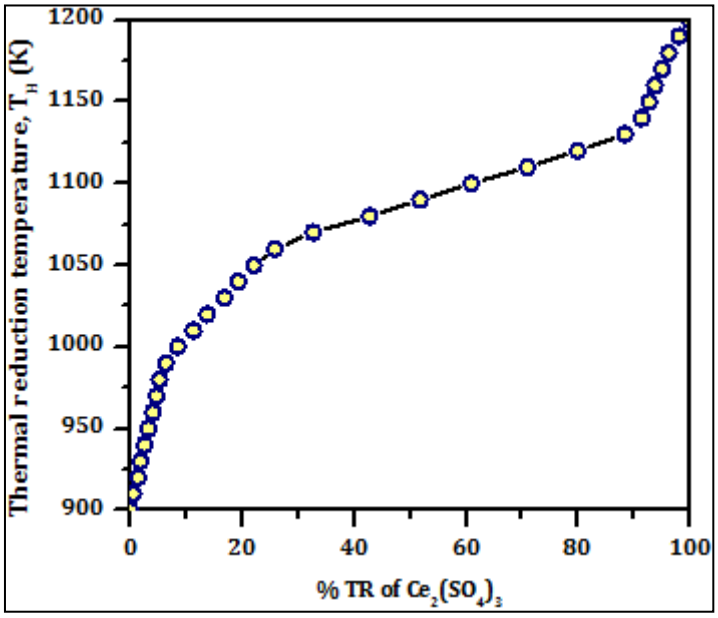

Fig. 68: Effect of thermal reduction temperature (T_H) on %TR of $Ce_2(SO_4)_3$

The %TR of $Ce_2(SO_4)_3$ against the thermal reduction temperature (T_H) has been shown in Fig. 68. It was seen that the TR of $Ce_2(SO_4)_3$ starts at 900 K and 100% thermal reduction was achieved at 1200 K. The data reported in plot show that the TR of $Ce_2(SO_4)_3$ increased rapidly at the start from 0 to 10% with the increase in TH from 900 K to 1005 K. Further, as the TH upswings to 1042 K, the %TR of $Ce_2(SO_4)_3$ reached 20% and continue to rise rapidly to 40% with the TH increasing to 1076 K. However, in the mid-section from 40% to 80%, the TR of $Ce_2(SO_4)_3$ rises gradually when TH increased from 1076 K to 1120 K. it was seen further that the TH upturn from 1120 K to 1200 K, reduced the rest 20% of $Ce_2(SO_4)_3$ significantly quickly.

7.5 Results and discussion

The thermodynamic analysis of the $Ce_2(SO_4)_3$ thermochemical WS cycle was carried out using the HSC chemistry software to evaluate the solar-to-fuel efficiency. The parameters and the empirical correlation used in the analysis have been mentioned in the mathematical modelling section. The effect of the parameter variation on the system performance have been plotted and discussed in detail.

7.5.1 Solar reactor and heaters

The absorption efficiencies of the solar reactor as well as the installed heaters such as N_2 heater, H_2O heater and SO_2 heater as mentioned in the Eq. (3) and Eq. (4) are extremely significant as they direct effect on the solar reactor and heaters performance.

As postulated earlier, the $Ce_2(SO_4)_3$ thermochemical WS cycle operates in the thermal reduction temperature (TH) range from 900 K to 1200 K while the re-oxidation temperature of the cycle was kept steady at 550 K. Therefore, the operating temperature for the N2, H2O and SO2 heater becomes the TL as 550 K. Since, the heaters operate at constant temperature of TL thus the absorption efficiency ($\eta_{abs-solar-N2/H2O/SO2-heater-WS}$) of the heaters remains constant at 99.7%. The re-oxidation temperature (TL) was taken as constant to avoid the further temperature fluctuations in the WS reactor due to the superheated steam. The value of the concentration ratio (C) was taken as 2000 suns.

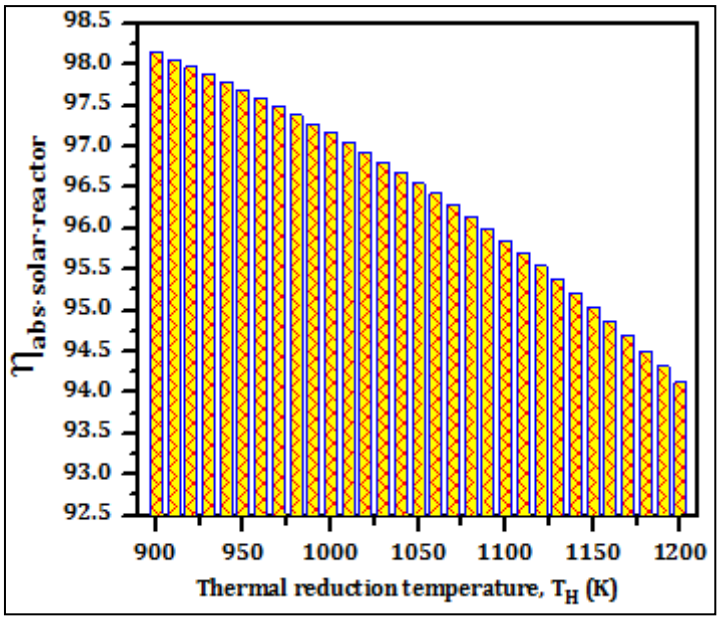

Fig. 69: Effect of thermal reduction temperature (T_H) on $\eta_{abs-solar-reactor}$

On the contrary, the operating temperature for solar reactor *i.e.* the thermal reduction temperature (TH) goes from 900 K to 1200 so the absorption efficiency for the solar reactor ($\eta_{abs-solar-reactor-WS}$) being the function of TH decreases with respect to the increasing thermal reduction temperature (TH) as shown in Fig. 69. The reported data in the plot suggest that at 900 K, the absorption efficiency of the solar reactor was at 98.1% which went down to 97.7%, 97.2%, 96.6%, 95.8%, 95% and 94.1% with the TH increase to 950 K, 1000 K, 1050 K, 1100 K, 1150 K and 1200 K, respectively.

The thermal reduction of $Ce_2(SO_4)_3$ is a function of thermal reduction temperature (T_H) *i.e.* the reduction rate of $Ce_2(SO_4)_3$ is directly proportionate to TH. Subsequently, the effect of increasing thermal reduction temperature (TH) on solar heat energy required for the 100% reduction of $Ce_2(SO_4)_3$ ($Q_{Ce_2(SO_4)_3-reduction}$) as well as to raise the temperature of H2O in H2O heater ($Q_{H_2O-heating}$) and SO2 in SO2 heater ($Q_{SO_2-heating}$) from 300 K to T_L has been shown in Fig. 70.

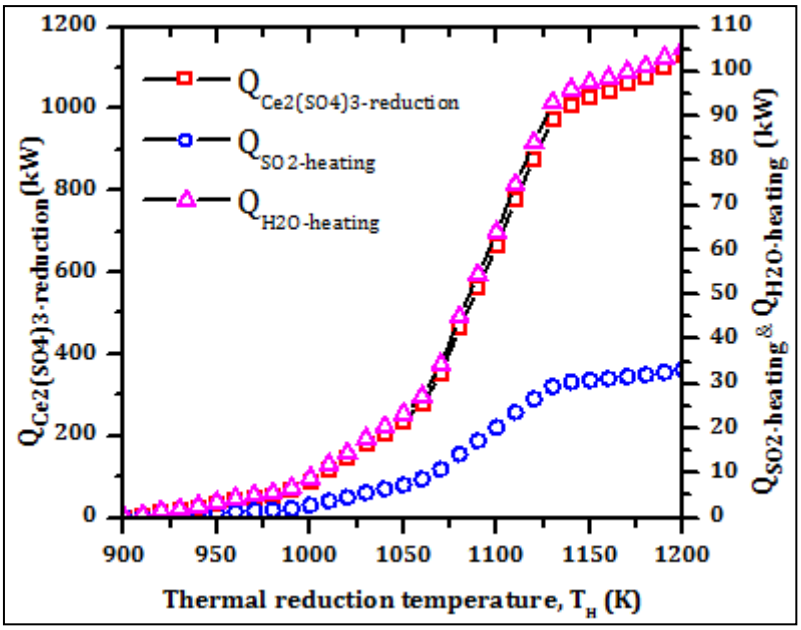

Fig. 70: Effect of TH on $Q_{Ce_2(SO_4)_3-reduction}$, $Q_{SO_2\ heating}$ and $Q_{H_2O\ heating}$

Analysis of the reported data indicated that solar heat energy required to thermally reduce the $Ce_2(SO_4)_3$ *i.e.* ($Q_{Ce_2(SO_4)_3-reduction}$) increased with the increase in thermal reduction temperature (TH). Quantitatively, as the thermal reduction temperature (TH) rises from 900 K to 920 K, 940 K, 960 K, 980 K and 1000 K, a sluggish upsurge in $Q_{Ce_2(SO_4)_3-reduction}$ from 1.41 kW to 14.27 kW, 26.09 kW, 41.62 kW, 54.66 kW and 88.91 kW, respectively was reported. However, further increase of reduction temperature (TH) to 1050 K, 1100 K and 1150 K resulted in the rapid increase of $Q_{Ce_2(SO_4)_3-reduction}$ to 236.60 kW, 664.05 kW and 1029.47 kW, respectively and for the last 50 K from 1150 K to 1200 K, the $Q_{Ce_2(SO_4)_3-reduction}$ increased a little amount and reached up to 1130.34 kW.

In the case of H2O heating, the upsurge in the $Q_{H_2O-heating}$ with the increase in the thermal reduction temperature (TH) follows a similar progress curve as the $Q_{Ce_2(SO_4)_3-reduction}$ due to high absorption efficiency (99.7%) of the H2O heater ($\eta_{abs-H2O-heater}$). Thus, the $Q_{H_2O-heating}$ was 0.15 kW at 900 K and increased by the factor of 23.07, 60.42, 157.84, 434.95, 662.21 and 714.21 as the TH upturned to 950 K, 1000 K, 1050 K, 1100 K, 1150 K and 1200 K, respectively. The SO2 heating signifies the solar heat energy required to raise the temperature of SO2 gas from 300 K to TL = 550 K. Given the fact that the difference between initial temperature to the re-

oxidation temperature is mere 250 K thus, the amount of $Q_{SO_2-heating}$ upsurge with respect to the increase in the thermal reduction temperature (TH) is significantly low as compared to the $Q_{Ce_2(SO_4)_3-reduction}$ as well as the $Q_{H_2O-heating}$. Analysis of the plot show that the $Q_{SO_2-heating}$ upsurged from 0.05 kW to 1.07 kW, 2.82 kW, 7.35 kW, 20.26 kW, 30.85 kW and 33.28 kW for the thermal reduction temperature (TH) increase from 900 K to 950 K, 1000 K, 1050 K, 1100 K, 1150 K and 1200 K respectively.

These above discussed three quantities $Q_{Ce_2(SO_4)_3-reduction}$, $Q_{H_2O-heating}$ and $Q_{SO_2-heating}$ radially affect the amount of solar heat energy needed to operate the solar reactor ($Q_{solar-reactor}$), H_2O heater ($Q_{H2O-heater}$) and SO_2 heater ($Q_{SO2-heater}$). The thermal reduction of the $Ce_2(SO_4)_3$ upturns with increasing T_H and the solar heat energy required for the functioning of solar reactor ($Q_{solar-reactor}$) and both the heaters ($Q_{H2O-heater}$ & $Q_{SO2-heater}$) increases as well as shown in Fig. 71. As expectedly, $Q_{solar-reactor}$ reached the highest value where the $Q_{SO2-heater}$ required the lowest amount of solar heat energy to operate.

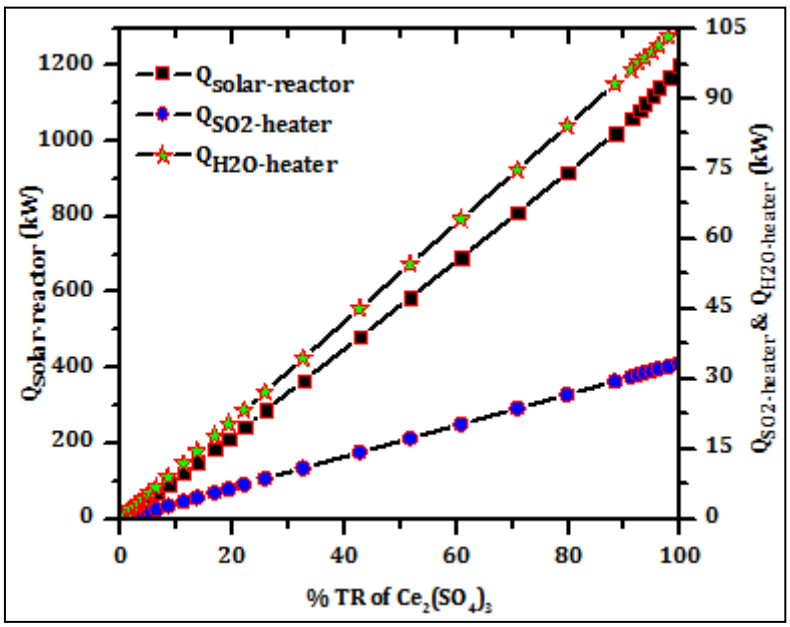

Fig. 71: Effect of % TR of $Ce_2(SO_4)_3$ on $Q_{solar-reactor}$, $Q_{H2O-heater}$ and $Q_{SO2-heater}$

In terms of statistics, the $Q_{SO2-heater}$ was 0.05 kW for the 0.15% of TR of $Ce_2(SO_4)_3$ and as the %TR of $Ce_2(SO_4)_3$ kept increasing to 5%, 10%, 20%, 40%, 60%, 80% and 100%, the $Q_{SO2-heater}$ increased on a linearly curve to 1.7 kW, 3.4 kW, 6.7

kW, 13.2 kW, 20.0 kW, 26.7 kW and 33.4 kW, respectively. Similarly, the $Q_{H2O-heater}$ increased as 5.4 kW, 16.1 kW, 31.4 kW, 63.1 kW, 94.8 kW and 105.5 kW for the % TR of $Ce_2(SO_4)_3$ of 5%, 15%, 30%, 60%, 90% and 100%. The $Q_{solar-reactor}$ was an important factor which reported to be increased from 55.6 kW to 164.1 kW, 338.8 kW, 567.8 kW, 802.9 kW, 1044.1 kW and 1201.0 kW at the % TR of $Ce_2(SO_4)_3$ from 5% to 15%, 30%, 50%, 70% 90% and 100%, respectively.

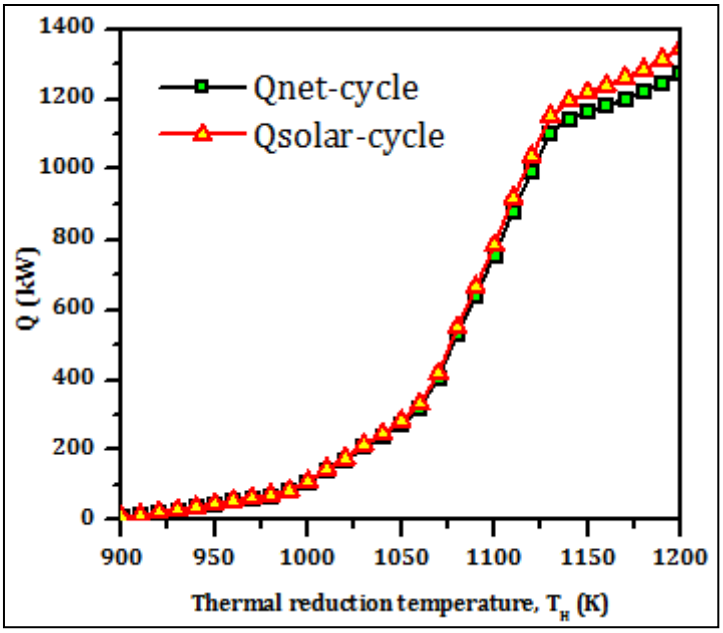

Fig. 72: Effect of thermal reduction temperature (TH) on $Q_{net-cycle}$ and $Q_{solar-cycle}$

The solar heat energy required for the heating *i.e.* raising the temperature of N_2, SO_2 and H_2O from 300 K to T_L=550 K in the heater and heat energy needed to thermally reduce the $Ce_2(SO_4)_3$ is mentioned in the Eq. (10) sums up to the $Q_{cycle-net}$ while, the solar heat energy required for efficient operation of solar reactor and all three heaters such as N_2 heater, SO_2 heater and H_2O heater is given in the Eq. (14) gives the $Q_{solar-cycle}$. According to the reported data in Fig. 72, the minimal difference between the $Q_{cycle-net}$ and the $Q_{solar-cycle}$ was resulted due to the very high absorption efficiency of the solar reactor ($\eta_{abs-solar-reactor}$). In the terms of numbers, the $Q_{cycle-net}$ and the $Q_{solar-cycle}$ was 8.95 kW and 8.99 kW at the thermal reduction temperature (TH) of 900 K, respectively. As the reduction temperature (TH) upturned to 920 K, 940 K, 960 K, 980 K & 1000 K, the $Q_{cycle-net}$ increased to 23.55 kW, 36.95

kW, 54.53 kW, 69.25 kW & 107.96 kW, respectively and the $Q_{solar-cycle}$ risen to 23.88 kW, 37.58 kW, 55.57 kW, 70.76 kW & 110.60 kW, respectively. It was observed that the rise in the $Q_{cycle-net}$ and $Q_{solar-cycle}$ was quite slow for the thermal reduction temperature (TH) range of 900 K to 1000 K. However, the further upsurge in TH to 1020 K, 1050 K, 1070 K & 1100 K leads to a slightly rapid increase in the $Q_{cycle-net}$ to 171.47 kW, 274.53 kW, 404.66 kW & 755.68 kW, respectively and the $Q_{solar-cycle}$ increased to 176.14 kW, 283.07 kW, 418.38 kW & 784.67 kW, respectively. The $Q_{cycle-net}$ and $Q_{solar-cycle}$ upturned massively to 1144.39 kW, 1220.40 kW & 1276.08 kW and 1195.56 kW, 1283.58 kW & 1347.07 kW as the TH risen to 1140 K, 1180 K and 1200 K, respectively.

7.5.1.1 Estimation of thermal losses

The thermal losses via conduction and convection mode of heat transfer had been rendered negligible. However, the re-radiation thermal losses from the solar reactor and all three heaters are quite necessary to evaluate for the energy balance in the thermochemical cycle.

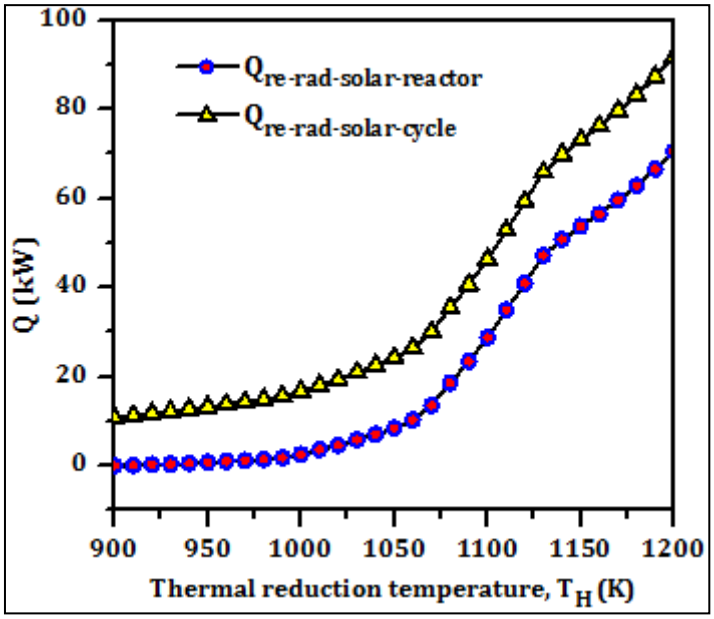

Fig. 73: Effect of thermal reduction temperature (TH) on $Q_{re-rad-solar-reactor}$ and $Q_{re-rad-solar-cycle}$

According to the Eq. (19), the thermal losses from the solar reactor are the function of the absorption efficiency of the solar reactor ($\eta_{abs-solar-reactor}$). Therefore, a solar reactor operating with high absorption efficiency will result in low re-radiative thermal losses. The increase in the solar heat energy lost from solar reactor and solar cycle via re-radiation has been shown in Fig. 73. In the reduction temperature (TH) range of 900 K to 1200 K, the $Q_{re-rad-solar-reactor}$ and the $Q_{re-rad-solar-cycle}$ increase sluggishly from 900 K to 1050 K and it increased rather quickly with the further rise in TH from 1050 K to 1200 K. Statistically, the re-radiative solar heat loss from the solar reactor ($Q_{re-rad-solar-reactor}$) were seen to be tremendously low about 0.03 kW at the thermal reduction temperature (TH) of 900 K.

However, the re-radiative heat loss from the solar cycle ($Q_{re-rad-solar-cycle}$) were rather high as compared to solar reactor about 10.85 kW at the same TH. This difference in the re-radiative heat loss between solar reactor and solar cycle was due to the functioning of the three installed heaters (N2 heater, SO2 heater, H2O heater). Further, as the TH increased to 950 K, 1000 K & 1050 K, the $Q_{re-rad-solar-reactor}$ upturned to 0.79 kW, 2.60 kW & 8.44 kW and the $Q_{re-rad-solar-cycle}$ increased to 13.23 kW, 16.70 kW & 24.23 kW, respectively. After the TH increased further from 1050 K to 1100 K, 1150 K and 1200 K, the $Q_{re-rad-solar-reactor}$ and the $Q_{re-rad-solar-cycle}$ increased rapidly and reached to 28.75 kW, 53.70 kW & 70.59 kW and 46.34 kW, 73.07 kW & 91.67 kW, respectively.

7.5.1.2 Efficiency analysis without heat recuperation

The most crucial part of the thermodynamic analysis was the estimation of solar-to-fuel conversion efficiency ($\eta_{solar-to-fuel}$). The solar-to-fuel conversion efficiency if the function of H2 moles produced during the reaction and the $Q_{solar-cycle}$ required to drive the cerium sulfate – cerium oxide thermochemical cycle as mentioned in the Eq. (25). The H2 moles production and $Q_{solar-cycle}$ is directly related function of thermal reduction temperature (TH), therefore, increasing TH results in higher H2 moles production and increased amount of the $Q_{solar-cycle}$. However, according to the Eq. (25), H2 moles production directly relates to the $\eta_{solar-to-fuel}$ and the $Q_{solar-cycle}$ inversely relates to the $\eta_{solar-to-fuel}$.

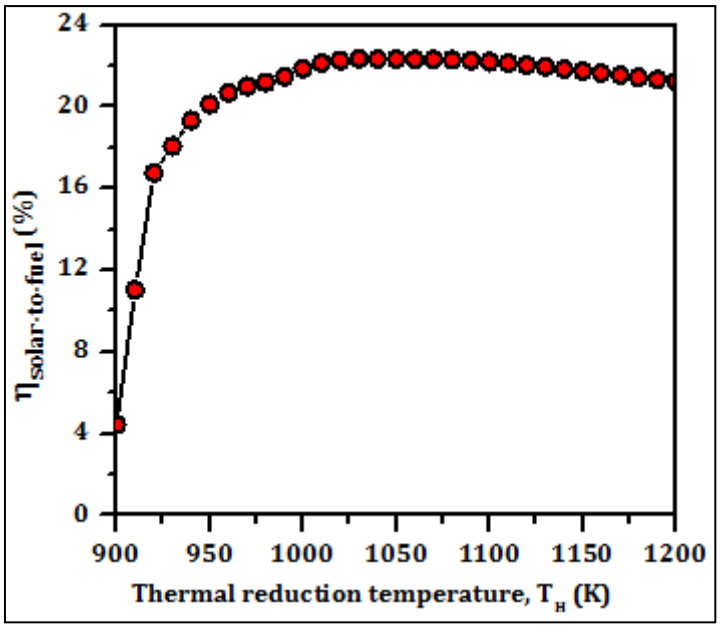

Fig. 74: Solar-to-fuel conversion efficiency of cerium sulfate – cerium oxide thermochemical cycle

The solar-to-fuel conversion efficiency ($\eta_{solar-to-fuel}$) as a function of thermal reduction temperature (TH) has been plotted in Fig. 74. According to the reported data, at the reduction temperature (TH) of 900 K, the $\eta_{solar-to-fuel}$ was 4.45%. A sudden rise in the solar-to-fuel conversion efficiency was seen when the TH increased from 900 K to 910 K and reached to 11.04% and a further upturn in TH to 920 K, increased the $\eta_{solar-to-fuel}$ to 16.77%. A further upsurge in TH from 920 K to 950 K, 1000 K, 1020 K and 1040 K brought the $\eta_{solar-to-fuel}$ up to 20.11%, 21.87%, 22.26% and 22.35%, respectively. It was observed that the highest value of solar-to-fuel conversion efficiency (22.35%) was achieved at the TH of 1040 K. Beyond this point, the additional increase in the TH resulted in a minor drop in the $\eta_{solar-to-fuel}$. Such as for the thermal reduction temperature (TH) of 1050 K, 1100 K, 1150 K and 1200 K, the $\eta_{solar-to-fuel}$ value dropped down to 22.32%, 22.19%, 21.75% and 21.23%.

7.5.1.3 Coolers and WS reactor

The coolers are installed in the flow arrangement of the cerium sulfate – cerium oxide based solar thermochemical water splitting cycle to reuse the solar heat energy to maximize the $\eta_{solar-to-fuel}$ of the cycle. In this WS cycle, three coolers (cooler-A,

cooler-B and cooler-C) were installed and the heat recovered by these coolers and WS reactor has been plotted in Fig. 75.

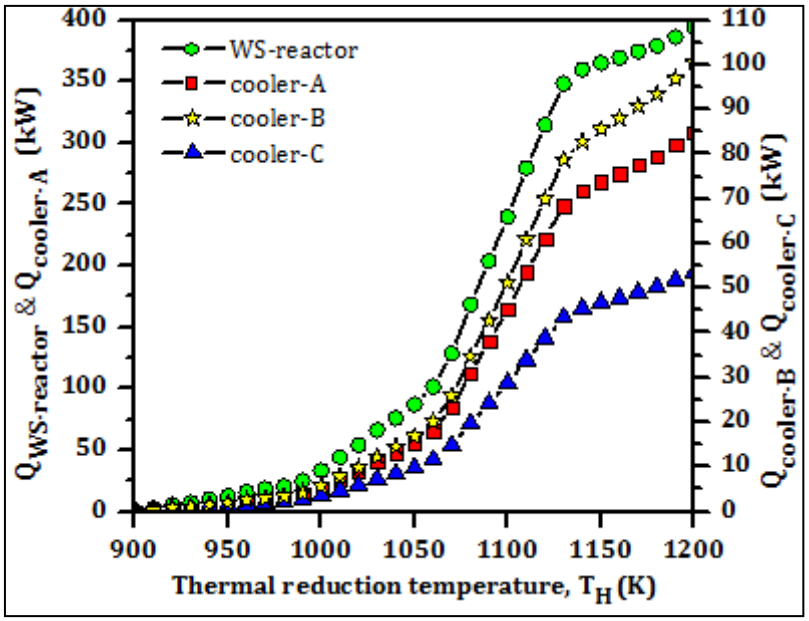

Fig. 75: Effect of TH on the heat recovery by cooler-A, cooler-B, cooler-C and WS reactor

The data reported in Fig. 75 show that the increasing thermal reduction temperature allows the increasing heat recovery by the coolers and the WS reactor. The solar heat energy extracted from the WS reactor ($Q_{WS-reactor}$), cooler-A ($Q_{cooler-A}$), cooler-B ($Q_{cooler-B}$) and cooler-C ($Q_{cooler-\mathrm{C}}$) was sluggish for the TH range of 900 K to 1000 K and beyond this point, further increase of TH led to the rather quicker and higher amount of heat energy extraction. In terms of numbers, as the TH increased from 900 K to 950 K, 970 K and 1000 K, the $Q_{WS-reactor}$ increased from 0.55 kW to 12.72 kW, 18.47 kW and 33.32 kW, the $Q_{cooler-A}$ increased from 0.27 kW to 6.98 kW, 10.47 kW and 19.81 kW, the $Q_{cooler-B}$ upturned from 0.07 kW to 1.95 kW, 2.98 kW and 5.78 kW and the $Q_{cooler-\mathrm{C}}$ upsurged from 0.05 kW to 1.23 kW, 1.84 kW and 3.48 kW, respectively. As the TH was upturned from 1000 K to 1050 K, 1100 K, 1150 K and 1200 K, the rise in the $Q_{WS-reactor}$ was reported to be 87.04 kW, 239.87 kW, 365.19 kW and 393.87 kW, respectively. At the same reduction temperature (TH) intervals, the upsurge in the $Q_{cooler-A}$ was seen to be 55.79 kW, 164.97 kW, 268.36 kW and 308.11 kW, respectively. The increase in the $Q_{cooler-B}$ and the $Q_{cooler-\mathrm{C}}$ was observed

to be 16.85 kW & 9.76 kW at 1050 K, 51.32 kW & 28.76 kW at 1100 K, 85.56 kW & 46.66 kW at 1150 K and at the peak TH it was recorded to be 100.39 kW & 53.44 kW.

7.5.1.4 Efficiency analysis with heat recuperation

As it was mentioned above that the solar-to-fuel conversion efficiency ($\eta_{solar-to-fuel}$) of cerium sulfate – cerium oxide thermochemical WS cycle can be improved by employing the technique of heat recuperation. The concept of heat recuperation is to re-utilize the heat recovered from the cooler-A, cooler-B, cooler-C and WS reactor in WS solar thermochemical cycle. Therefore, the estimation of $Q_{recuperable}$ and $Q_{solar-cycle-HR}$was carried out using the Eq. (26) & (28) and the reported data has been presented in graphical form in ***Fig. 76***.

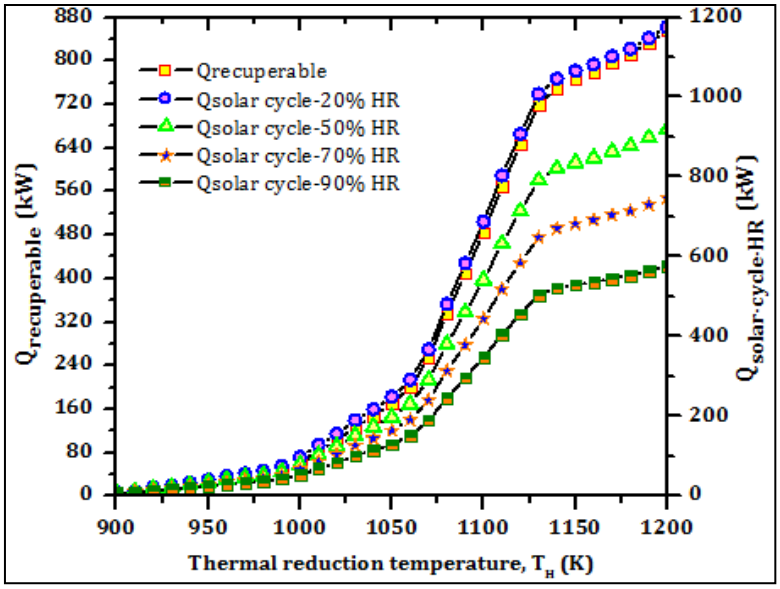

Fig. 76: Effect of thermal reduction temperature (TH) on $Q_{solar-cycle-HR}$ and $Q_{recuperable}$

According to the reported data in ***Fig. 76***, it was observed that the increment in the $Q_{recuperable}$ and the $Q_{solar-cycle-HR}$ was rather slow for the TH upsurge from 900 K to 1050 K. In this reduction temperature (TH) range, the $Q_{recuperable}$ starts from 0.95 kW at 900 K and goes to 22.88 kW, 62.39 kW and 169.45 kW at the TH of 950 K, 1000 K and 1050 K, respectively. However, the $Q_{recuperable}$ increased significant faster after 1050 K and reached to 484.91 kW, 765.80 kW & 885.80 kW at the TH of 1100 K, 1150 K & 1200 K, respectively. The $Q_{recuperable}$ is used to calculate the $Q_{recuperation}$ by taking 20%, 50%, 70% and 90% heat recovery into account as suggested in the Eq (27).

Consequently, the $Q_{solar-cycle-HR}$ also increased with the increasing TH. However, it is to be noted that the higher amount of heat recuperation resulted in the lower $Q_{solar-cycle-HR}$ and vise versa. In terms of numbers, as the thermal reduction temperature upswings from 900 K to 1000 K, 1100 K and 1200 K, the $Q_{solar-cycle-HR}$ with 20% HR goes from 8.81 kW to 98.13 kW, 687.69 kW & 1175.90 kW, with 50% HR it increases from 8.52 kW to 79.41 kW, 542.21 kW & 919.17 kW, with 70% HR it upswings from 8.33 kW to 66.93 kW, 445.23 kW & 748.01 kW and with 90% HR it increased from 8.14 kW to 54.45 kW, 348.25 kW & 576.84 kW, respectively.

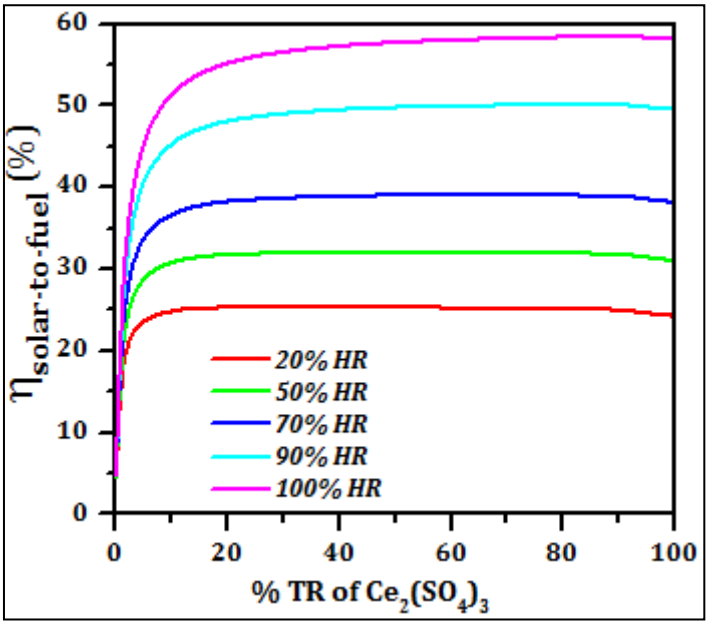

Fig. 77: Effect of %TR of Ce2(SO4)3 on the solar-to-fuel conversion efficiency with heat recuperation

The solar-to-fuel conversion efficiency was improved by employing the 20%, 50%, 70%, 90% and 100% heat recuperation and the obtained results have been plotted in Fig. 77. The effect of %TR of Ce2(SO4)3 on the solar-to-fuel conversion efficiency with heat recuperation ($\eta_{solar-to-fuel-HR}$) has been shown in the Fig. (14). The analysis of the plot show that the $\eta_{solar-to-fuel-HR}$ increased rapidly within 10% TR of Ce2(SO4)3 and then hold steady for the rest of the TR of Ce2(SO4)3. Statistically, the $\eta_{solar-to-fuel-HR}$ for 20% HR increased from 4.55% to 11.66%, 18.25%, 21.36% and 23.73% for the %TR of Ce2(SO4)3 from 0.14% to 0.52%, 1.4%, 2.54% and 5.24%. The $\eta_{solar-to-fuel-HR}$ for 20% HR reached the peak value of 25.42% at the %TR of

Ce2(SO4)3 of 42.79% at the TH of 1080 K. Consequently, the $\eta_{solar-to-fuel-HR}$ for 50%, 70%, 90% and 100% HR started at the initial value of 4.70%, 4.81%, 4.92% and 4.98%, respectively at the TH of 900 K and the %TR of Ce2(SO4)3 of 0.14%. The highest value of the $\eta_{solar-to-fuel-HR}$ for 50% HR was reported to be 32.15% at the same TH and %TR of Ce2(SO4)3, for 70% HR the maximum value of solar-to-fuel conversion efficiency was reported to be 39.12% at the TH of 1100 K and the %TR of Ce2(SO4)3 of 60.9% and the highest value of $\eta_{solar-to-fuel-HR}$ for 90% and 100% HR was seen to be 50.16% and 58.51%, respectively at the same TH of 1130 K and the %TR of Ce2(SO4)3 of 88.40%.

7.6 Summary and conclusion

In this study, solar assisted cerium sulfate – cerium oxide thermochemical water splitting cycle has been thermodynamically investigated to analyze its solar-to-fuel conversion efficiency with and without heat recuperation taken into consideration. The parametric analysis was carried out using the HSC chemistry (thermodynamic Equilibrium analysis) and EES (Engineering Equation Solver) software. The thermodynamic equilibrium analysis suggested that the thermal reduction of cerium sulfate (Ce2(SO4)3) was initiated at 900 K and it upturned to 8.46% at 1000 K, 22.1%% at 1050 K, 60.9% at 1100 K, 92.72% at 1150 K and the 100% TR of Ce2(SO4)3 was achieved at the TH of 1200 K. Further, the $Q_{Ce_2(SO_4)_3-reduction}$ being the function of TH increased with the increasing TH and it was reported to be 1.42kW at 900 K, 33.32 kW at 950 K, 88.91 kW at 1000 K, 664.04 kW at 1100 K and reached 1130.34 kW at 1200 K. The $Q_{solar-reactor}$ is a function of $Q_{Ce_2(SO_4)_3-reduction}$ and the absorption efficiency of the solar reactor. Given the fact that the solar reactor was operating at high absorption efficiency therefore, the $Q_{solar-reactor}$ was essentially depended on the $Q_{Ce_2(SO_4)_3-reduction}$. The initial value of $Q_{solar-reactor}$ was 1.44 kW at 900 K and it increased to 91.50 kW, 692.80 kW and 1200.94 kW at the TH of 1000 K, 1100 K and 1200 K, respectively. Furthermore, the solar-to-fuel conversion efficiency ($\eta_{solar-to-fuel}$) without heat recovery was reported to be 4.45% at 900 K and it increased to 20.11% at 950 K, 21.88% at 1000 K, 22.20% at 1100 K and 21.23% at 1200 K. The highest value of $\eta_{solar-to-fuel}$ without heat recovery was observed to be 22.35% at the TH of 1040 K. The cooler-A, cooler-B and cooler-C were used re-use

the lost solar heat in the WS cycle and it was seen that the heat extraction was quite significant from the cooler-A and WS reactor. Such that the cooler-A was responsible for extracting 0.28 kW and WS reactor for 0.55 kW at 900 K which further increased to 19.81 kW and 33.32 kW at 1000 K, 164.97 kW and 168.54 kW at 1100 K and the peak values were seen to be 308.11 kW and 393.87 kW at 1200 K. The heat recuperation increased the solar-to-fuel conversion efficiency ($\eta_{solar-to-fuel-HR}$) significantly. It was observed that the peak values of $\eta_{solar-to-fuel-HR}$ were 25.42% at 1080 K, 32.15% at 1080 K, 39.12% at 1100 K, 50.16% at 1130 K and 58.51% at 1140 K with 20%, 50%, 70%, 90% and 100% heat recuperation, respectively.

Chapter – 8

8 Morphological characterization of CeO_2/SZ ceramic foam material

8.1 Introduction

The reticulated porous ceramic (RPC) foam structure are subjected to physical processes in order to increase its thermal transport properties and the rate of reaction [258-259]**.** Solar assisted water/CO_2 splitting thermochemical redox cycles are the main area of application of RPC foam structure [261]-261]. In solar thermochemical cycle, RPC foam structure first undergoes high-temperature thermal reduction reaction to produce oxygen and then relatively low-temperature re-oxidation reaction to produce hydrogen. Metal oxides (mainly ceria based) are the high-performance redox material for oxygen evolution [263].

There have been many researches around the world to explore the porous structures of ceramic foams which have submicron sized pores to avoid the sintering process sintering the reduction reaction [264]. In solar thermochemical reactors, the optimization process follows the volume averaging technique where the heat and mass transfer properties of RCP are effectively optimized to calculate the mass, momentum and energy transport in the numerical modeling [265]. In this work, SEM method is used to investigate the RPC foam structures with dual scale porosity.

8.2 Preparation of CSZ

The ceria stabilized zirconia honeycomb structured foam (10 ppi) was tested for the material analysis which included the porosity of foam through a calcination process. Fig. 78 shows picture of a zirconia foam matrix with the cerium oxide coating. The foam matrix was loaded with the cerium oxide and subjected to high temperature for the calcination process as shown in the Fig. 79(a) and (b).

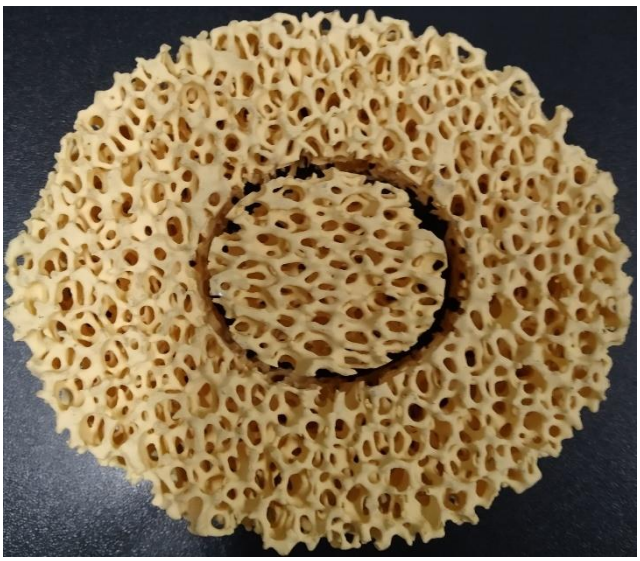

Fig. 78: 10 PPI zirconia foam matrix before the ceria coat

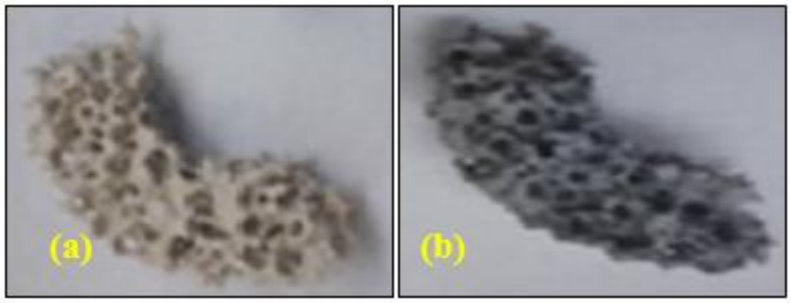

Fig. 79: CSZ (a) before and (b) after subjected to high-temperature

The preparation process of the CSZ have been mentioned below;

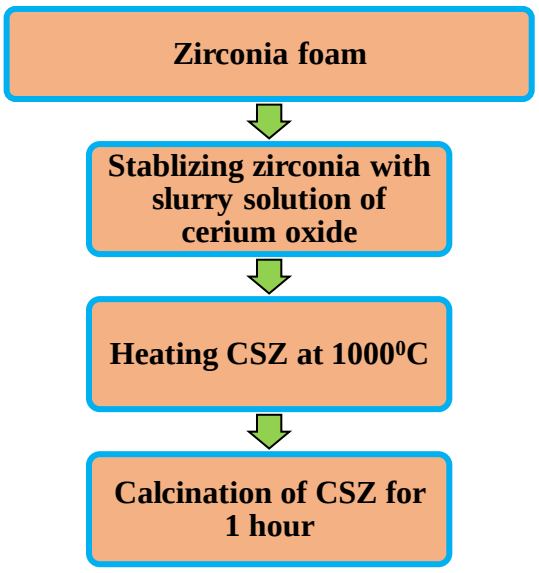

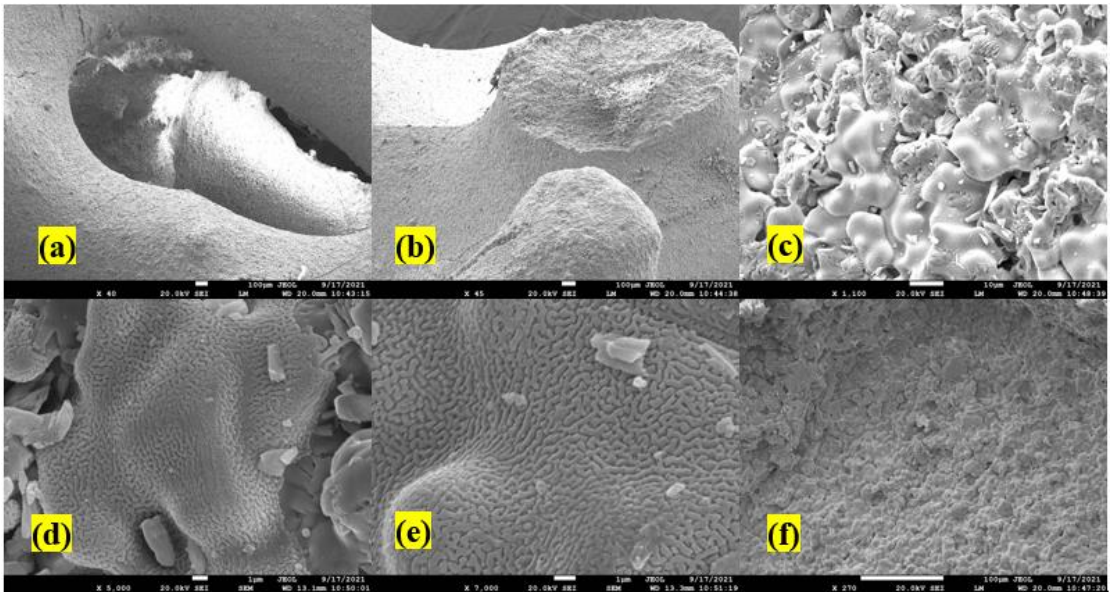

Fig. 80: SEM images of RCP foam structure at different magnifications

8.3 Morphological characterization

The dual scale porosity of the RPC structures was calculated with the help of following given equation;

$$\varepsilon_{dual} = \varepsilon_{RPC} + (1+\varepsilon_{RPC}).\varepsilon_{strut} \tag{130}$$

The pore distribution (ϕ) in RPC structure is linearly fitted with the ε_{strut} . Therefore, 10% pore distribution with 0.12 sized ε_{strut} gives the mean diameter of 9.2 μm. Where the mean pore diameter is calculated as given follows;

$$d_{m,RPC} = \left[5.3\times\varepsilon_{RPC-\sin gle} + 2.2\right]\times\frac{3.57}{n_{ppi}}\times10^{-3} \tag{131}$$

and the surface area for the thermal transport has been calculated as;

$$A_{s_f} = \frac{n_{ppi}}{3.57\left[5.65\times\varepsilon^{2}{}_{RPC-\sin gle} - 6.08\times\varepsilon_{RPC-\sin gle} + 4.5\right]} \tag{132}$$

8.4 Results and discussion

Fig. 80 shows the scanning electron microscopy image view of RPC ceria before and after being subjected to the thermal treatment. The size of the grain, the porosity and the pore and strut size of doped ceria were measured with the help of imaging analysis technique. The size of the grain was reported to be in the range of 4-10 μm in

the undoped sample of the RPC. Meanwhile, the grain size was increased by 28% after the ceria doping. The strut porosity was sampled as 13% and the size of the pore was reported to be 1-5 μm according to the Fig. 80(a). The calcination step introduced the cracks in the surface of the structure which evidently increases the surface area required for the re-oxidation step to increase the hydrogen yield. The calcination process also introduces the white region as shown in Fig. 80(b) and (c) which prevents the sintering phenomenon therefore, the solar reactor can operate in several cycles without switching the porous structure. The densification in the microstructure due to high-temperature leads to the increase in the grain size and strut size.

The thermal conductivity of the porous structure could also be dependent on the densification of the porous microstructure. Since, the high temperature leads to the increase in the pore size which indicates that the structure has the low thermal conductivity. The most important part of analysis was the observation that the high temperature leads to the surface cracks which suggest that the re-oxidation reaction is favorable in the reactive doped porous zone with access to the hydrogen gas.

8.5 Conclusion

The thermal and structural characteristic of the ceria doped RCP used in numerical analysis was analyzed with the help of SEM testing and one-dimensional analysis. A 10 ppi porous open foam structure was thermally treated and structure was analyzed with SEM. The results of the study revealed that the strut size and porosity of the structure was seen to be a function of high-temperature which suggest the favorable re-oxidation reaction.

Chapter – 9

9 Summary and conclusion

Solar energy is one of the most efficient sources of renewable energy which can be easily converted into electrical or thermal energy for various purposes. The concentrated solar power is used to split the water or the carbon di-oxide molecule to produce hydrogen or syngas. The thermochemical cycles are the most promising pathway to produce the solar fuels for the future. Therefore, the development of an efficient solar thermochemical reactor is primarily a crucial task.

In this research work, computational designs of 4 kWth solar thermochemical reactors with various optical as well as geometrical aspects have been proposed. In this work, the thermodynamic analysis on cerium oxide non-stoichiometry and cerium sulfate-cerium oxide have been performed for the advancement of the existing knowledge in the field.

9.1 Design and performance assessment of solar thermochemical reactor

A steady-state as well as transient analysis was carried out on the axisymmetric models of solar thermochemical coupled with the conjugate heat transfer numerical models. SolTrace software was used to generate the solar flux profile used in the computational fluid dynamics study. The solar thermochemical reactor was assessed as the single cylindrical – hemispherical hybrid shape for the optical parameters and the influence of focal point displacement. It was found that the distribution of solar flux inside the solar thermochemical reactor was uniform for case-1 with slope error 4 mrad and in case-2 for both slope errors (2 and 4 mrad). It was also observed that the high value of flux doesn't necessarily yield high temperature unless the heat flux gets uniformly distributed inside the cavity. Case-1 with slope error 2 mrad yields 33% higher solar flux value as compared to the 4 mard slope error and yet 4 mrad slope error yield the higher temperature inside the reactor cavity. The location of focal point was seen to have quite significant influence magnitude and the distribution of solar flux.

While, in the second part, the effects of STCR cavity shape integrated with optical parameters was analyzed. It was seen that the incident solar flux gets uniformly

distributed on the cavity walls for case-1 and case-2 and yields the highest temperature in the catalyst region. However, the flux distribution losses its uniformity for case-3 and its magnitude also reduces significantly, thus it doesn't attain the high temperature in the reactor cavity as compared to case-1. It was also seen that the model-2 yields the better uniformity and higher magnitude of temperature in the catalyst region in radial direction as compared to model-1 in case-1 and case-2. However, in case-3, model-1 and model-2 both yield the same radial temperature in the porous catalyst region.

9.2 Species transport and chemical kinetics in solar thermochemical reactor

A numerical model of high-temperature solar thermochemical reactor of hybrid cavity shape that couples the Monte Carlo Ray Tracing (MCRT) technique with computational fluid dynamics (CFD). The influences of RPC thickness on solar-to-fuel conversion efficiency in a solar thermochemical reactor cavity has been explored by means of steady state and transient CFD models. MCRT was applied using SolTrace software to generate the solar flux profile and it was coupled with CFD module to study the heat transfer and concentrated solar flux distribution in the STCR cavity. The analysis of the results suggested that the Among all three porous media thicknesses case considered, the 15 mm RPC thickness shows a very uniform distribution of solar heat flux as well as achieves the highest temperature.

For the two-step H2O splitting process, the RPC thickness with 25 mm attains the highest oxygen evolution rate as well as yields the highest solar-to-fuel conversion efficiency, among all three cases considered. The RPC zone subjected to higher temperature attains the peak value of O2 concentration. However, the ceria mass loading is a factor plays a significant role in rate of H2 production rate. The RPC zone having 25 mm thickness yields the highest rate of 0.34 mL/min/gCeO2 oxygen evolution. For RPC thickness 15 mm, 20 mm and 25 mm yield about 1.422 mL/gCeO2, 1.645 mL/gCeO2 and 1.764 mL/gCeO2 oxygen in 10 min cycle, respectively and when the ceria mass load is considered the total oxygen evolution goes up to 1578.42 mL, 2434.6 mL and 3263.4 mL, respectively. Solar-to-fuel efficiencies for 15 mm, 20 mm and 25 mm RPC thickness are estimated to be 7.82%, 12.07% and 16.18%, respectively without heat recovery.

The study carried out to the geometrical optimization of the solar thermochemical reactor by considering the 5 inlet positions and 3 inlet orientations showed that the inlet position at 10 mm combined with the orientation of 750 inclination from the horizontal plane was seen to achieve the highest avg. temperature of 1587 K in the radial direction in the porous media with the Re value of 100. The avg. temperature in the axial direction in the porous media reached highest value of 1666 K for the inlet position of 10 mm with the orientation of 900 with the Re value of 100. The highest avg. temperature of 1353 K was achieved by the inlet position of 12 mm at the orientation of 750 along the centerline of the STCR cavity for Re=100.

9.3 Thermodynamic analysis

The thermodynamic studied were carried out to investigate the effect of non-stoichiometry (δ = 1.72 and 1.83) of cerium oxide and to test the feasibility of cerium sulfate – cerium oxide thermochemical cycle. The conversion of H_2O into H_2 via solar thermochemical water splitting cycle and analyzed the effect of two different non-stoichiometric configuration as $CeO_{1.72}$ and $CeO_{1.83}$. The solar-to-fuel conversion efficiency ($\eta_{solar-to-fuel}$) reached the maximum value of 7.45% ($CeO_{1.72}$) and 7.69% ($CeO_{1.83}$) at the %TR of CeO_2 of 61.72% without heat recuperation and it attained the maximum value of 14.92% and 13.54% for $CeO_{1.83}$ and $CeO_{1.72}$, respectively at the %TR of CeO_2 of 80% with the 50% heat recuperation. Meanwhile, in the solar assisted cerium sulfate – cerium oxide thermochemical water splitting cycle, it was observed that the peak values of $\eta_{solar-to-fuel-HR}$ were 25.42% at 1080 K, 32.15% at 1080 K, 39.12% at 1100 K, 50.16% at 1130 K and 58.51% at 1140 K with 20%, 50%, 70%, 90% and 100% heat recuperation, respectively.

As stated above, the solar fuels are the prime solution to the growing energy demand and it can solve the fossil fuel dependency problem. The hydrogen energy can be directly converted into fossil fuel and also it can be directly used to drive the transportation systems. Therefore, this thesis aimed at the following parts from the practicality point of view,

1. The geometrical design of the solar thermochemical reactor was investigated to allow the insights into the preferred or the optimal design of

the reactor to achieve the uniform/higher solar flux and temperature distribution to carry out the redox reactions.

2. The thermodynamic analysis of chemical species part of the thesis was planned to further the insights into better operating thermochemical cycles. It was also aimed at the evaluation of optimal operating parameter to achieve the higher solar-to-fuel conversion efficiency.

9.4 Future work recommendation

The solar energy is available in abundance but the fossil fuel sources are about to be emptied due to over use. Therefore, the researchers around the world have been focused on the development of alternative or renewable energy technologies. The hydrogen or syngas production via solar driven thermochemical cycles have been foreseen as the best possible alternative to replace the fossil fuel. One further step might be taken towards the production of production of fossil fuels synthesized from the hydrogen using the Fischer–Tropsch process.

To improve the solar-to-fuel conversion efficiency of two-step H_2O/CO_2 splitting cycle, optical-thermal analysis and cavity shape optimization plays an important role. It's crucial to choose the perfect cavity shape to achieve the uniform distribution of solar flux inside the cavity to achieve the optimum temperature to carry out the redox reactions efficiently. Thus, future/upcoming research papers are/will be based on optical-thermal analysis and STCR cavity shape optimization in combination with varying geometrical parameters.

The present 2-D model of the reactor does not adequately describe convective flow within the cavity. The produced model might be enlarged to include the full reactor with all six reactive elements to estimate the temperature dependency of the convective heat energy loss. To the best of the researcher's knowledge, heat transport coefficients for calculating convective losses in a cylindrical cavity with an ensemble of radially oriented cylinders are not present in the literature. The computational models established in this research work are expedient for researching various solar thermal and thermochemical processes, as well as novel redox materials for sustainable fuel generation. The numerical framework would be incredibly beneficial for physical processes involving more interdependence of transport and chemical processes in the

catalytically active material. An appropriate example is the isothermal ceria redox cycle, which uses methane to reduce ceria.

According to thermodynamic studies, the variation in non-stoichiometry should be at least an order of magnitude higher than the differences in ceria non-stoichiometry observed with inert swept reduction. This means that chemical energy sinks/sources have a greater influence on transitory fluctuations in reacting material temperature. The model created in this work is well-suited to assessing the combined effects of heat and mass transfer mechanisms on the overall performance of such a physical system.

Appendices

Nomenclature

Symbols		***Subscripts***	
A	area (m^2)	b	body
d	collector aperture diameter (m)	conv	convection
f	focal length (m)	E	energy
F	force (N)	f	Fluid
Fs	particle surface force (N)	f_p	fluid-particle interphase
g	gravitational acceleration (m/s^2)	fs	fluid-solid interphase
G	Incident radiative heat flux (W/m^2)	fuel	chemical fuel
h	collector height (m)	m	mass
I	radiative intensity (W/m^2)	p	particles
k	thermal conductivity (W/m-K)	p_b	particle black body
k_a	absorption coefficient (1/m)	q	quartz glass
k_{pa}	particle absorption coefficient (1/m)	rad	radiation
k_{ps}	particle scattering coefficient (1/m)	reac	reaction
k_{red}	reduction rate coefficient	rim	Rim
k_s	scattering coefficient (1/m)	s	solid
p	pressure (Pa)	solar	solar energy
q_r	re-radiation (W/m^2)	t	total
Q	heat amount (J)	th	thermal
$Q_{a,p}$	absorption efficiency of particle	abs	Absorption
r	reaction rate (mol/s)	***Abbreviation***	
rπ	parcel position	CFD	computational fluid dynamics
s	distance in Ω direction	DEM	discrete element method
S	source term	DNI	direct normal irradiance
T	temperature (K)	DOM	discrete ordinate method
v	velocity (m/s)	HHV	higher heating value
V	volume (m^3)	STCR	Solar thermochemical reactor
T_H	Reduction temperature	RPC	Reticulated porous ceria
T_L	Re-oxidation temperature		

G	Gibbs free energy
Greek Symbols	
β	extinction coefficient
η	Efficiency
δ	non-stoichiometric coefficient
δ_p	Dirac delta function
η	efficiency
μ	dynamic viscosity (Pa s)
ρ	density (kgm−3)
σ	Stefan-Boltzmann constant
ψ	angle (rad)
Ω	solid angle

List of publications

Sno.	**Title of paper with author names**	**Name of journal / conference**	**Published date**	**Issn no/ vol no, issue no**	**Indexing in Scopus/ Web of Science/UGC-CARE list**
1.	A numerical investigation on thermal analysis of RPC based solar thermochemical reactor for two-step H2O splitting cycle for hydrogen production	Journal of thermal engineering	Article in press	NA	Scopus
2.	Numerical Thermal Analysis on the Effects of Focal Point Displacement on Temperature and Flux Distribution in the Solar Thermochemical Reactor for	International journal of heat and technology	Article accepted	NA	Scopus

	Hydrogen Production				
3.	Evaluating Solar Flux-Temperature Distribution in the STCR Cavity- A SolTrace-CFD approach	International Conference (Virtual Mode) on Simulation, Automation & Smart Manufacturing- GLA MATHURA - 2021	Article accepted	NA	Scopus
4.	Optical and Thermal analysis of STCR Cavity subjected under flow and no flow conditions	ICAST – 2020 & Lecture notes in mechanical engineering	5- Aug.-2021	DOI: https://doi.org/10.1007/978-981-16-3132-0_22	Scopus
5.	Numerical investigation on the effects of inlet positioning and orientation on pressure and velocity distribution in the STCR cavity	ICAST - 2020	Article accepted	NA	Scopus

References

[1] T. Kodama and N. Gokon, 'Thermochemical cycles for high-temperature solar hydrogen production', *Chemical Reviews*, vol. 107, no. 10, pp. 4048–4077, Oct. 2007.

[2] A. Steinfeld, 'Solar thermochemical production of hydrogen - A review', *Solar Energy*, vol. 78, no. 5, pp. 603–615, May 2005.

[3] J. J. C. S. Santos, J. C. E. Palacio, A. M. M. Reyes, M. Carvalho, A. J. R. Freire, and M. A. Barone, 'Concentrating Solar Power', 2018.

[4] R. Bader, S. Haussener, and W. Lipinski, 'Optical Design of Multisource High-Flux Solar Simulators', *Journal of Solar Energy Engineering*, vol. 137, no. 2, p. 021012, 2014.

[5] J. A. Alarcón, J. E. Hortúa, and A. L. G, 'Design and construction of a solar collector parabolic dish for rural zones in Colombia Diseño y construcción de un colector solar parabólico tipo disco para zonas rurales', *Renuable Econmics*, vol. 7, no. 14, pp. 14–22, 2013.

[6] M. Günther, M. Joemann, and S. Csambor, 'Advanced CSP Teaching Materials Chapter 5 Parabolic Trough Technology Authors', *2011*, pp. 1–43, 2011.

[7] E. A. Fletcher and R. L. Moen, 'Hydrogen- and Oxygen from Water', *Science*, vol. 197, no. 4308, pp. 1050–1056, Sep. 1977.

[8] T. Nakamura, 'Hydrogen production from water utilizing solar heat at high temperatures', *Solar Energy*, vol. 19, no. 5, pp. 467–475, 1977.

[9] A. KOGAN, 'Direct solar thermal splitting of water and on-site separation of the products?II. Experimental feasibility study', *International Journal of Hydrogen Energy*, vol. 23, no. 2, pp. 89–98, Feb. 1998.

[10] M. Kuhn, S. R. Bishop, J. L. M. Rupp, and H. L. Tuller, 'Structural characterization and oxygen nonstoichiometry of ceria-zirconia (Ce1−xZrxO2−δ) solid solutions', *Acta Materialia*, vol. 61, no. 11, pp. 4277–

4288, Jun. 2013.

[11] S. Abanades and G. Flamant, ‘Thermochemical hydrogen production from a two-step solar-driven water-splitting cycle based on cerium oxides’, *Solar Energy*, vol. 80, no. 12, pp. 1611–1623, 2006.

[12] T. Kodama, N. Gokon, and R. Yamamoto, ‘Thermochemical two-step water splitting by ZrO2-supported NixFe3−xO4 for solar hydrogen production’, *Solar Energy*, vol. 82, no. 1, pp. 73–79, Jan. 2008.

[13] R. Bader, L. J. Venstrom, J. H. Davidson, and W. Lipiński, ‘Thermodynamic analysis of isothermal redox cycling of ceria for solar fuel production’, *Energy and Fuels*, vol. 27, no. 9, pp. 5533–5544, 2013.

[14] H. Kaneko, H. Ishihara, S. Taku, Y. Naganuma, N. Hasegawa, and Y. Tamaura, ‘Cerium ion redox system in CeO2–xFe2O3 solid solution at high temperatures (1,273–1,673 K) in the two-step water-splitting reaction for solar H2 generation’, *Journal of Materials Science*, vol. 43, no. 9, pp. 3153–3161, May 2008.

[15] O. R. Sandoval, B. C. Caetano, M. U. Borges, J. J. García, and R. M. Valle, ‘Modelling, simulation and thermal analysis of a solar dish/Stirling system: A case study in Natal, Brazil’, *Energy Conversion and Management*, vol. 181, pp. 189–201, Feb. 2019.

[16] B. Widyolar *et al.*, ‘Theoretical and experimental performance of a two-stage (50X) hybrid spectrum splitting solar collector tested to 600 °C’, *Applied Energy*, vol. 239, pp. 514–525, 2019.

[17] J. Lilliestam, M. Labordena, A. Patt, and S. Pfenninger, ‘Empirically observed learning rates for concentrating solar power and their responses to regime change’, *Nature Energy*, vol. 2, no. 7, 2017.

[18] S. Y. Wu, L. Xiao, Y. Cao, and Y. R. Li, ‘Convection heat loss from cavity receiver in parabolic dish solar thermal power system: A review’, *Solar Energy*, vol. 84, no. 8, pp. 1342–1355, 2010.

[19] W. Fuqiang, C. Ziming, T. Jianyu, Y. Yuan, S. Yong, and L. Linhua, ‘Progress

in concentrated solar power technology with parabolic trough collector system: A comprehensive review', *Renewable and Sustainable Energy Reviews*, vol. 79, pp. 1314–1328, 2017.

[20] D. Jafrancesco *et al.*, 'Optical simulation of a central receiver system: Comparison of different software tools', *Renewable and Sustainable Energy Reviews*, vol. 94, pp. 792–803, 2018.

[21] A. Z. Hafez, A. Soliman, K. A. El-Metwally, and I. M. Ismail, 'Design analysis factors and specifications of solar dish technologies for different systems and applications', *Renewable and Sustainable Energy Reviews*, vol. 67, pp. 1019–1036, 2017.

[22] G. Gavagnin, D. Sánchez, G. S. Martínez, J. M. Rodríguez, and A. Muñoz, 'Cost analysis of solar thermal power generators based on parabolic dish and micro gas turbine: Manufacturing, transportation and installation', *Applied Energy*, vol. 194, pp. 108–122, 2017.

[23] M. Moradi and M. Mehrpooya, 'Optimal design and economic analysis of a hybrid solid oxide fuel cell and parabolic solar dish collector, combined cooling, heating and power (CCHP) system used for a large commercial tower', *Energy*, vol. 130, pp. 530–543, 2017.

[24] M. Mehrpooya, B. Ghorbani, and S. S. Hosseini, 'Thermodynamic and economic evaluation of a novel concentrated solar power system integrated with absorption refrigeration and desalination cycles', *Energy Conversion and Management*, vol. 175, pp. 337–356, 2018.

[25] T. jia, J. Huang, R. Li, P. He, and Y. Dai, 'Status and prospect of solar heat for industrial processes in China', *Renewable and Sustainable Energy Reviews*, vol. 90, pp. 475–489, 2018.

[26] F. Dähler *et al.*, 'Optical design and experimental characterization of a solar concentrating dish system for fuel production via thermochemical redox cycles', *Solar Energy*, vol. 170, pp. 568–575, 2018.

[27] W. Wang, B. Li, C. Gao, and C. Guo, 'The temporal dynamics of perceptual and

conceptual fluency on recognition memory', *Brain and Cognition*, vol. 127, pp. 1–12, 2018.

[28] M. R. Meas and T. Bello-Ochende, 'Thermodynamic design optimisation of an open air recuperative twin-shaft solar thermal Brayton cycle with combined or exclusive reheating and intercooling', *Energy Conversion and Management*, vol. 148, pp. 770–784, 2017.

[29] E. Bellos and C. Tzivanidis, 'A review of concentrating solar thermal collectors with and without nanofluids', *Journal of Thermal Analysis and Calorimetry*, vol. 135, no. 1, pp. 763–786, 2019.

[30] R. A. Rasih, N. A. C. Sidik, and S. Samion, 'Numerical Investigation of Direct Absorption Solar Collector using Nanofluids: A Review', *IOP Conference Series: Materials Science and Engineering*, vol. 469, no. 1, 2019.

[31] K. Hong, Y. Yang, S. Rashidi, Y. Guan, and Q. Xiong, 'Numerical simulations of a Cu–water nanofluid-based parabolic-trough solar collector', *Journal of Thermal Analysis and Calorimetry*, no. 0123456789, Feb. 2020.

[32] E. Bellos, C. Tzivanidis, and A. Papadopoulos, 'Enhancing the performance of a linear Fresnel reflector using nanofluids and internal finned absorber', *Journal of Thermal Analysis and Calorimetry*, vol. 135, no. 1, pp. 237–255, 2019.

[33] A. Steinfeld, 'Solar thermochemical production of hydrogen—a review', *Solar Energy*, vol. 78, no. 5, pp. 603–615, May 2005.

[34] C. Agrafiotis, H. Von Storch, M. Roeb, and C. Sattler, 'Solar thermal reforming of methane feedstocks for hydrogen and syngas production - A review', *Renewable and Sustainable Energy Reviews*, vol. 29, pp. 656–682, 2014.

[35] D. Yadav and R. Banerjee, 'A review of solar thermochemical processes', *Renewable and Sustainable Energy Reviews*, vol. 54, pp. 497–532, 2016.

[36] D. Marxer, P. Furler, M. Takacs, and A. Steinfeld, 'Solar thermochemical splitting of CO2 into separate streams of CO and O2 with high selectivity, stability, conversion, and efficiency', *Energy and Environmental Science*, vol.

10, no. 5, pp. 1142–1149, 2017.

[37] W. Villasmil and A. Steinfeld, ‘Hydrogen production by hydrogen sulfide splitting using concentrated solar energy - Thermodynamics and economic evaluation’, *Energy Conversion and Management*, vol. 51, no. 11, pp. 2353–2361, 2010.

[38] C. Agrafiotis, M. Roeb, and C. Sattler, ‘A review on solar thermal syngas production via redox pair-based water/carbon dioxide splitting thermochemical cycles’, *Renewable and Sustainable Energy Reviews*, vol. 42, pp. 254–285, Feb. 2015.

[39] Y. Mahmoudi and M. Maerefat, ‘Analytical investigation of heat transfer enhancement in a channel partially filled with a porous material under local thermal non-equilibrium condition’, *International Journal of Thermal Sciences*, vol. 50, no. 12, pp. 2386–2401, 2011.

[40] C. Y. Zhao, ‘Review on thermal transport in high porosity cellular metal foams with open cells’, *International Journal of Heat and Mass Transfer*, vol. 55, no. 13–14, pp. 3618–3632, 2012.

[41] M. Zhao and L. Cheng, ‘Finite element analysis of flow control using porous media’, *Ocean Engineering*, vol. 37, no. 14–15, pp. 1357–1366, 2010.

[42] M. Torabi, N. Karimi, G. P. Peterson, and S. Yee, ‘Challenges and progress on the modelling of entropy generation in porous media: A review’, *International Journal of Heat and Mass Transfer*, vol. 114, pp. 31–46, 2017.

[43] T. Montini, M. Melchionna, M. Monai, and P. Fornasiero, ‘Fundamentals and Catalytic Applications of CeO2-Based Materials’, *Chemical Reviews*, vol. 116, no. 10, pp. 5987–6041, 2016.

[44] T. Otake, H. Yugami, K. Yashiro, Y. Nigara, T. Kawada, and J. Mizusaki, ‘Nonstoichiometry of Ce1-XYXO 2-0.5X-δ (X=0.1, 0.2)’, *Solid State Ionics*, vol. 161, no. 1–2, pp. 181–186, 2003.

[45] R. Pitz-Paal, B. Hoffschmidt, M. Böhmer, and M. Becker, ‘Experimental and

numerical evaluation of the performance and flow stability of different types of open volumetric absorbers under non-homogeneous irradiation', *Solar Energy*, vol. 60, no. 3–4, pp. 135–150, Mar. 1997.

[46] B. Alazmi and K. Vafai, 'Analysis of variants within the porous media transport models', *Journal of Heat Transfer*, vol. 122, no. 2, pp. 303–326, 2000.

[47] Z. Wu *et al.*, 'Experimental and numerical studies of the pressure drop in ceramic foams for volumetric solar receiver applications', *Applied Energy*, vol. 87, no. 2, pp. 504–513, 2010.

[48] Z. Wu, C. Caliot, G. Flamant, and Z. Wang, 'Coupled radiation and flow modeling in ceramic foam volumetric solar air receivers', *Solar Energy*, vol. 85, no. 9, pp. 2374–2385, 2011.

[49] Z. Wu, C. Caliot, G. Flamant, and Z. Wang, 'Numerical simulation of convective heat transfer between air flow and ceramic foams to optimise volumetric solar air receiver performances', *International Journal of Heat and Mass Transfer*, vol. 54, no. 7–8, pp. 1527–1537, 2011.

[50] H. I. Villafán-Vidales, S. Abanades, C. Caliot, and H. Romero-Paredes, 'Heat transfer simulation in a thermochemical solar reactor based on a volumetric porous receiver', *Applied Thermal Engineering*, vol. 31, no. 16, pp. 3377–3386, 2011.

[51] F. Wang, Y. Shuai, H. Tan, and C. Yu, 'Thermal performance analysis of porous media receiver with concentrated solar irradiation', *International Journal of Heat and Mass Transfer*, vol. 62, no. 1, pp. 247–254, 2013.

[52] T. J. Li, J. Sun, Y. Yuan, C. L. Xu, Y. Shuai, and H. P. Tan, 'Simulation of calibration process in flame measurement by plenoptic camera', *Applied Thermal Engineering*, vol. 135, pp. 179–187, 2018.

[53] T. J. Li, S. N. Li, Y. Yuan, F. Q. Wang, and H. P. Tan, 'Light field imaging analysis of flame radiative properties based on Monte Carlo method', *International Journal of Heat and Mass Transfer*, vol. 119, pp. 303–311, 2018.

[54] X. Huang *et al.*, 'Heat transfer analysis of solar-thermal dissociation of NiFe2O4 by coupling MCRTM and FVM method', *Energy Conversion and Management*, vol. 106, pp. 676–686, 2015.

[55] Z. D. Cheng, Y. L. He, and F. Q. Cui, 'Numerical investigations on coupled heat transfer and synthetical performance of a pressurized volumetric receiver with MCRT-FVM method', *Applied Thermal Engineering*, vol. 50, no. 1, pp. 1044–1054, 2013.

[56] F. Wang, J. Tan, S. Yong, H. Tan, and S. Chu, 'Thermal performance analyses of porous media solar receiver with different irradiative transfer models', *International Journal of Heat and Mass Transfer*, vol. 78, pp. 7–16, 2014.

[57] F. Wang, J. Tan, and Z. Wang, 'Heat transfer analysis of porous media receiver with different transport and thermophysical models using mixture as feeding gas', *Energy Conversion and Management*, vol. 83, pp. 159–166, Jul. 2014.

[58] X. Chen, X. L. Xia, H. Liu, Y. Li, and B. Liu, 'Heat transfer analysis of a volumetric solar receiver by coupling the solar radiation transport and internal heat transfer', *Energy Conversion and Management*, vol. 114, pp. 20–27, 2016.

[59] A. Meier, J. Ganz, and A. Steinfeld, 'Modeling of a novel high-temperature solar chemical reactor', *Chemical Engineering Science*, vol. 51, no. 11, pp. 3181–3186, 1996.

[60] S. Möller and R. Palumbo, 'Solar thermal decomposition kinetics of ZnO in the temperature range 1950-2400 K', *Chemical Engineering Science*, vol. 56, no. 15, pp. 4505–4515, 2001.

[61] S. Möller and R. Palumbo, 'The development of a solar chemical reactor for the direct thermal dissociation of zinc oxide', *Journal of Solar Energy Engineering, Transactions of the ASME*, vol. 123, no. 2, pp. 83–90, 2001.

[62] Y. Shuai, F. Q. Wang, X. L. Xia, H. P. Tan, and Y. C. Liang, 'Radiative properties of a solar cavity receiver/reactor with quartz window', *International Journal of Hydrogen Energy*, vol. 36, no. 19, pp. 12148–12158, 2011.

[63] J. Costandy, N. El Ghazal, M. T. Mohamed, A. Menon, V. Shilapuram, and N. Ozalp, 'Effect of reactor geometry on the temperature distribution of hydrogen producing solar reactors', *International Journal of Hydrogen Energy*, vol. 37, no. 21, pp. 16581–16590, 2012.

[64] D. Thomey, L. de Oliveira, J.-P. Säck, M. Roeb, and C. Sattler, 'Development and test of a solar reactor for decomposition of sulphuric acid in thermochemical hydrogen production', *International Journal of Hydrogen Energy*, vol. 37, no. 21, pp. 16615–16622, Nov. 2012.

[65] A. G. Konstandopoulos and C. Agrofiotis, 'Hydrosol : Advanced monolithic reactors for hydrogen generation from solar water splitting', 2006.

[66] J. E. Miller, A. H. McDaniel, and M. D. Allendorf, 'Considerations in the design of materials for solar-driven fuel production using metal-oxide thermochemical cycles', *Advanced Energy Materials*, vol. 4, no. 2, 2014.

[67] G. P. Smestad and A. Steinfeld, 'Review: Photochemical and thermochemical production of solar fuels from H 2O and CO 2 using metal oxide catalysts', *Industrial and Engineering Chemistry Research*, vol. 51, no. 37, pp. 11828–11840, 2012.

[68] C. Perkins and A. W. Weimer, 'Likely near-term solar-thermal water splitting technologies', *International Journal of Hydrogen Energy*, vol. 29, no. 15, pp. 1587–1599, 2004.

[69] A. Steinfeld, 'Solar thermochemical production of hydrogen - A review', *Solar Energy*, vol. 78, no. 5, pp. 603–615, 2005.

[70] W. C. Chueh *et al.*, 'Highly Enhanced Concentration and Stability of Reactive Ce 3+ on Doped CeO 2 Surface Revealed In Operando', *Chemistry of Materials*, vol. 24, no. 10, pp. 1876–1882, May 2012.

[71] F. A. Costa Oliveira *et al.*, 'High performance cork-templated ceria for solar thermochemical hydrogen productionviatwo-step water-splitting cycles', *Sustainable Energy and Fuels*, vol. 4, no. 6, pp. 3077–3089, 2020.

[72] J. Zeng, X. Yu, Y. Xuan, Q. Li, and D. Liu, 'Direct solar thermochemical conversion of methanol into syngas: Via nanocatalysts at lower temperatures', *Sustainable Energy and Fuels*, vol. 4, no. 4, pp. 1693–1703, 2020.

[73] M. Ezbiri *et al.*, 'High redox performance of Y0.5Ba0.5CoO3-: δ for thermochemical oxygen production and separation', *Reaction Chemistry and Engineering*, vol. 5, no. 4, pp. 685–695, 2020.

[74] M. Tou, J. Jin, Y. Hao, A. Steinfeld, and R. Michalsky, 'Solar-driven co-thermolysis of CO2 and H2O promoted by: In situ oxygen removal across a non-stoichiometric ceria membrane', *Reaction Chemistry and Engineering*, vol. 4, no. 8, pp. 1431–1438, 2019.

[75] B. Dou *et al.*, 'Hydrogen production from the thermochemical conversion of biomass: Issues and challenges', *Sustainable Energy and Fuels*, vol. 3, no. 2, pp. 314–342, 2019.

[76] S. Ardo *et al.*, 'Pathways to electrochemical solar-hydrogen technologies', *Energy and Environmental Science*, vol. 11, no. 10, pp. 2768–2783, 2018.

[77] Q. Zhu and Y. Xuan, 'Pore scale numerical simulation of heat transfer and flow in porous volumetric solar receivers', *Applied Thermal Engineering*, vol. 120, pp. 150–159, 2017.

[78] M. R. Shaner, H. A. Atwater, N. S. Lewis, and E. W. McFarland, 'A comparative technoeconomic analysis of renewable hydrogen production using solar energy', *Energy and Environmental Science*, vol. 9, no. 7, pp. 2354–2371, 2016.

[79] J. A. Herron, J. Kim, A. A. Upadhye, G. W. Huber, and C. T. Maravelias, 'A general framework for the assessment of solar fuel technologies', *Energy and Environmental Science*, vol. 8, no. 1, pp. 126–157, 2015.

[80] A. H. Bork, M. Kubicek, M. Struzik, and J. L. M. Rupp, 'Perovskite La0.6Sr0.4Cr1-xCoxO3-δ solid solutions for solar-thermochemical fuel production: Strategies to lower the operation temperature', *Journal of Materials Chemistry A*, vol. 3, no. 30, pp. 15546–15557, 2015.

[81] J. R. Scheffe, A. H. McDaniel, M. D. Allendorf, and A. W. Weimer, ‘Kinetics and mechanism of solar-thermochemical H2 production by oxidation of a cobalt ferrite-zirconia composite’, *Energy and Environmental Science*, vol. 6, no. 3, pp. 963–973, 2013.

[82] P. Furler, J. R. Scheffe, and A. Steinfeld, ‘Syngas production by simultaneous splitting of H 2O and CO 2via ceria redox reactions in a high-temperature solar reactor’, *Energy and Environmental Science*, vol. 5, no. 3, pp. 6098–6103, 2012.

[83] M. Roeb, M. Neises, N. Monnerie, C. Sattler, and R. Pitz-Paal, ‘Technologies and trends in solar power and fuels’, *Energy and Environmental Science*, vol. 4, no. 7, pp. 2503–2511, 2011.

[84] R. D. Jilte, S. B. Kedare, and J. K. Nayak, ‘Investigation on convective heat losses from solar cavities under wind conditions’, in *Energy Procedia*, 2014, vol. 57.

[85] R. D. Jilte, J. K. Nayak, and S. B. Kedare, ‘Experimental Investigation on Heat Losses From Differentially Heated Cylindrical Cavity Receiver Used in Paraboloid Concentrator’, *Journal of Solar Energy Engineering*, vol. 139, no. 3, p. 031013, 2017.

[86] R. D. Jilte, S. B. Kedare, and J. K. Nayak, ‘Natural Convection and Radiation Heat Loss from Open Cavities of Different Shapes and Sizes Used with Dish Concentrator’, *Mechanical Engineering Research*, vol. 3, no. 1, p. 25, 2013.

[87] J. A. Harris and T. G. Lenz, ‘Thermal performance of solar concentrator/cavity receiver systems’, *Solar Energy*, vol. 34, no. 2, pp. 135–142, 1985.

[88] J. Delatorre *et al.*, ‘Monte Carlo advances and concentrated solar applications’, *Solar Energy*, vol. 103, pp. 653–681, May 2014.

[89] H. Li, W. Huang, F. Huang, P. Hu, and Z. Chen, ‘Optical analysis and optimization of parabolic dish solar concentrator with a cavity receiver’, *Solar Energy*, vol. 92, pp. 288–297, Jun. 2013.

[90] A. M. Daabo, S. Mahmoud, and R. K. Al-Dadah, ‘The effect of receiver

geometry on the optical performance of a small-scale solar cavity receiver for parabolic dish applications', *Energy*, vol. 114, pp. 513–525, Nov. 2016.

[91] A. M. Daabo, S. Mahmoud, and R. K. Al-Dadah, 'The optical efficiency of three different geometries of a small scale cavity receiver for concentrated solar applications', *Applied Energy*, vol. 179, pp. 1081–1096, Oct. 2016.

[92] A. M. Daabo, Y. S. Al-Mola, A. Y. Al-Rawy, and T. Lattimore, 'State of the art single-objective optimization of small scale cylindrical cavity receiver', *Sustainable Energy Technologies and Assessments*, vol. 35, no. June, pp. 278–290, 2019.

[93] A. M. Daabo, S. Mahmoud, R. K. Al-Dadah, and A. Ahmad, 'Numerical investigation of pitch value on thermal performance of solar receiver for solar powered Brayton cycle application', *Energy*, vol. 119, pp. 523–539, Jan. 2017.

[94] S. Pavlovic, A. M. Daabo, E. Bellos, V. Stefanovic, S. Mahmoud, and R. K. Al-dadah, 'Experimental and numerical investigation on the optical and thermal performance of solar parabolic dish and corrugated spiral cavity receiver', *Journal of Cleaner Production*, vol. 150, pp. 75–92, 2017.

[95] F. Cui, Y. He, Z. Cheng, and Y. Li, 'Study on combined heat loss of a dish receiver with quartz glass cover', *Applied Energy*, vol. 112, pp. 690–696, Dec. 2013.

[96] S. Li, G. Xu, X. Luo, Y. Quan, and Y. Ge, 'Optical performance of a solar dish concentrator/receiver system: Influence of geometrical and surface properties of cavity receiver', *Energy*, vol. 113, pp. 95–107, Oct. 2016.

[97] G. Barreto, P. Canhoto, and M. Collares-Pereira, 'Three-dimensional modelling and analysis of solar radiation absorption in porous volumetric receivers', *Applied Energy*, vol. 215, pp. 602–614, Apr. 2018.

[98] Q. Mao, Y. Shuai, and Y. Yuan, 'Study on radiation flux of the receiver with a parabolic solar concentrator system', *Energy Conversion and Management*, vol. 84, pp. 1–6, 2014.

[99] W. Huang, F. Huang, P. Hu, and Z. Chen, ‘Prediction and optimization of the performance of parabolic solar dish concentrator with sphere receiver using analytical function’, *Renewable Energy*, vol. 53, pp. 18–26, May 2013.

[100] G. Xiao, T. Yang, D. Ni, K. Cen, and M. Ni, ‘A model-based approach for optical performance assessment and optimization of a solar dish’, *Renewable Energy*, vol. 100, pp. 103–113, Jan. 2017.

[101] J. Garrido, L. Aichmayer, A. Abou-Taouk, and B. Laumert, ‘Experimental and numerical performance analyses of a Dish-Stirling cavity receiver: Geometry and operating temperature studies’, *Solar Energy*, vol. 170, pp. 913–923, Aug. 2018.

[102] T. Mancini *et al.*, ‘Dish-Stirling Systems: An Overview of Development and Status’, *Journal of Solar Energy Engineering*, vol. 125, no. 2, pp. 135–151, May 2003.

[103] D. Mills, ‘Advances in solar thermal electricity technology’, *Solar Energy*, vol. 76, no. 1–3, pp. 19–31, 2004.

[104] L. D. Jaffe, ‘Dish Concentrators for Solar Thermal Energy’, *Journal of Energy*, vol. 7, no. 4, pp. 304–312, Jul. 1983.

[105] R. Loni, A. B. Kasaeian, E. Askari Asli-Ardeh, and B. Ghobadian, ‘Optimizing the efficiency of a solar receiver with tubular cylindrical cavity for a solar-powered organic Rankine cycle’, *Energy*, vol. 112, pp. 1259–1272, 2016.

[106] L. Reich, R. Bader, T. Simon, and W. Lipiński, ‘Thermal transport model of a packed-bed reactor for solar thermochemical CO2 capture’, *Special Topics and Reviews in Porous Media*, vol. 6, no. 2, pp. 197–209, 2015.

[107] S. Haussener, D. Hirsch, C. Perkins, A. Weimer, A. Lewandowski, and A. Steinfeld, ‘Modeling of a multitube high-temperature solar thermochemical reactor for hydrogen production’, *Journal of Solar Energy Engineering, Transactions of the ASME*, vol. 131, no. 2, pp. 0245031–0245035, May 2009.

[108] Q. Wu, *Handbook of Porous Media*. CRC Press, 2015.

[109] M. M. Keshtkar and S. A. Gandjalikhan Nassab, ‘Theoretical analysis of porous radiant burners under 2-D radiation field using discrete ordinates method’, *Journal of Quantitative Spectroscopy and Radiative Transfer*, vol. 110, no. 17, pp. 1894–1907, 2009.

[110] H. Lee, ‘The geometric-optics relation between surface slope error and reflected ray error in solar concentrators’, *Solar Energy*, vol. 101. pp. 299–307, 2014.

[111] H. Zhang *et al.*, ‘Analysis of thermal transport and fluid flow in high-temperature porous media solar thermochemical reactor’, *Solar Energy*, vol. 173, pp. 814–824, 2018.

[112] T. Cooper and A. Steinfeld, ‘Derivation of the Angular Dispersion Error Distribution of Mirror Surfaces for Monte Carlo Ray-Tracing Applications’, *Journal of Solar Energy Engineering*, vol. 133, no. 4, Nov. 2011.

[113] W. Huang and Z. Han, ‘Theoretical analysis of error transfer from the surface slope to the reflected ray and their application in the solar concentrated collector’, *Solar Energy*, vol. 86, no. 9, pp. 2592–2599, 2012.

[114] Y. Luo, X. Z. Du, L. J. Yang, and Y. P. Yang, ‘Numerical simulation on the performance of a combination of external and cavity absorber for solar power plant’, *Energy Procedia*, vol. 49, pp. 428–437, 2014.

[115] C. P. Zhang *et al.*, ‘Investigations of thermal and flow behavior of bifurcations and bends in fractal-like microchannel networks: Secondary flow and recirculation flow’, *International Journal of Heat and Mass Transfer*, vol. 85, pp. 723–731, 2015.

[116] R. J. Xu, X. H. Zhang, R. X. Wang, S. H. Xu, and H. S. Wang, ‘Experimental investigation of a solar collector integrated with a pulsating heat pipe and a compound parabolic concentrator’, *Energy Conversion and Management*, vol. 148, pp. 68–77, 2017.

[117] M. T. Jamal-Abad, S. Saedodin, and M. Aminy, ‘Experimental investigation on a solar parabolic trough collector for absorber tube filled with porous media’, *Renewable Energy*, vol. 107, pp. 156–163, 2017.

[118] R. Michalsky, B. J. Parman, V. Amanor-Boadu, and P. H. Pfromm, ‘Solar thermochemical production of ammonia from water, air and sunlight: Thermodynamic and economic analyses’, *Energy*, vol. 42, no. 1, pp. 251–260, 2012.

[119] S. Z. Baykara, ‘Hydrogen production by direct solar thermal decomposition of water, possibilities for improvement of process efficiency’, *International Journal of Hydrogen Energy*, vol. 29, no. 14, pp. 1451–1458, 2004.

[120] P. G. Loutzenhiser, A. Meier, and A. Steinfeld, ‘Review of the Two-Step H2O/CO2-Splitting solar thermochemical cycle based on Zn/ZnO redox reactions’, *Materials*, vol. 3, no. 11, pp. 4922–4938, 2010.

[121] J. E. Miller, A. H. McDaniel, and M. D. Allendorf, ‘Considerations in the design of materials for solar-driven fuel production using metal-oxide thermochemical cycles’, *Advanced Energy Materials*, vol. 4, no. 2, pp. 1–19, 2014.

[122] J. Lapp, J. H. Davidson, and W. Lipiński, ‘Heat Transfer Analysis of a Solid-Solid Heat Recuperation System for Solar-Driven Nonstoichiometric Redox Cycles’, *Journal of Solar Energy Engineering*, vol. 135, no. 3, p. 031004, 2013.

[123] R. B. Diver, J. E. Miller, M. D. Allendorf, N. P. Siegel, and R. E. Hogan, ‘Solar Thermochemical Water-Splitting Ferrite-Cycle Heat Engines’, *Journal of Solar Energy Engineering*, vol. 130, no. 4, p. 041001, 2008.

[124] H. Kaneko *et al.*, ‘Rotary-type solar reactor for solar hydrogen production with two-step water splitting process’, *Energy and Fuels*, vol. 21, no. 4, pp. 2287–2293, 2007.

[125] J. R. Scheffe, M. Welte, and A. Steinfeld, ‘Thermal reduction of ceria within an aerosol reactor for H2O and CO2 splitting’, *Industrial and Engineering Chemistry Research*, vol. 53, no. 6, pp. 2175–2182, 2014.

[126] S. Abanades and G. Flamant, ‘Thermochemical hydrogen production from a two-step solar-driven water-splitting cycle based on cerium oxides’, *Solar Energy*, vol. 80, no. 12, pp. 1611–1623, 2006.

[127] I. Ermanoski, N. P. Siegel, and E. B. Stechel, 'A New Reactor Concept for Efficient Solar-Thermochemical Fuel Production', *Journal of Solar Energy Engineering*, vol. 135, no. 3, p. 031002, 2013.

[128] T. Kodama, S. Enomoto, T. Hatamachi, and N. Gokon, 'Application of an Internally Circulating Fluidized Bed for Windowed Solar Chemical Reactor with Direct Irradiation of Reacting Particles', *Journal of Solar Energy Engineering*, vol. 130, no. 1, p. 014504, 2008.

[129] S. Brendelberger, A. Rosenstiel, A. Lopez-Roman, C. Prieto, and C. Sattler, 'Performance analysis of operational strategies for monolithic receiver-reactor arrays in solar thermochemical hydrogen production plants', *International Journal of Hydrogen Energy*, vol. 45, no. 49, pp. 26104–26116, Oct. 2020.

[130] S. Zoller, E. Koepf, P. Roos, and A. Steinfeld, 'Heat Transfer Model of a 50 kW Solar Receiver-Reactor for Thermochemical Redox Cycling Using Cerium Dioxide', *Journal of Solar Energy Engineering, Transactions of the ASME*, vol. 141, no. 2, Apr. 2019.

[131] J. E. Garnier, R. N. Blumenthal, R. J. Panlener, and R. K. Sharma, 'A thermodynamic study on CaO-doped nonstoichiometric cerium dioxide', *Journal of Physics and Chemistry of Solids*, vol. 37, no. 4, pp. 368–378, 1976.

[132] M. Zinkevich, D. Djurovic, and F. Aldinger, 'Thermodynamic modelling of the cerium-oxygen system', *Solid State Ionics*, vol. 177, no. 11–12, pp. 989–1001, Apr. 2006.

[133] J. Lapp, J. H. Davidson, and W. Lipiński, 'Efficiency of two-step solar thermochemical non-stoichiometric redox cycles withheat recovery', *Energy*, vol. 37, no. 1, pp. 591–600, 2012.

[134] J. R. Scheffe and A. Steinfeld, 'Oxygen exchange materials for solar thermochemical splitting of H2O and CO2: A review', *Materials Today*, vol. 17, no. 7, pp. 341–348, 2014.

[135] B. Bulfin *et al.*, 'Analytical model of CeO2 oxidation and reduction', *Journal of Physical Chemistry C*, vol. 117, no. 46, pp. 24129–24137, Nov. 2013.

[136] A. Farooqui, A. Bose, D. Ferrero, J. Llorca, and M. Santarelli, 'Simulation of two-step redox recycling of non-stoichiometric ceria with thermochemical dissociation of CO 2 /H 2 O in moving bed reactors – Part I: Model development with redox kinetics and sensitivity analysis', *Chemical Engineering Science*, 2019.

[137] S. Li, P. B. Kreider, V. M. Wheeler, and W. Lipinski, 'Thermodynamic Analyses of Fuel Production Via Solar-Driven Ceria-Based Nonstoichiometric Redox Cycling: A Case Study of the Isothermal Membrane Reactor System', *Journal of Solar Energy Engineering, Transactions of the ASME*, vol. 141, no. 2, 2019.

[138] V. I. Anikeev and V. A. Kirillov, 'Basic design principles and some methods of investigation of catalytic reactors-receivers of solar radiation', *Solar Energy Materials*, vol. 24, no. 1–4, pp. 633–646, 1991.

[139] N. Gokon, S. Kumaki, Y. Miyaguchi, S. Bellan, T. Kodama, and H. Cho, 'Development of a 5kW th internally circulating fluidized bed reactor containing quartz sand for continuously-fed coal-coke gasification and a beam-down solar concentrating system', *Energy*, vol. 166, pp. 1–16, 2019.

[140] T. Yu, Q. Yuan, J. Lu, J. Ding, and Y. Lu, 'Thermochemical storage performances of methane reforming with carbon dioxide in tubular and semi-cavity reactors heated by a solar dish system', *Applied Energy*, vol. 185, pp. 1994–2004, 2017.

[141] R. Bader *et al.*, 'Design of a solar reactor to split CO2 via isothermal redox cycling of ceria', *Journal of Solar Energy Engineering, Transactions of the ASME*, vol. 137, no. 3, 2015.

[142] P. Lichty, X. Liang, C. Muhich, B. Evanko, C. Bingham, and A. W. Weimer, 'Atomic layer deposited thin film metal oxides for fuel production in a solar cavity reactor', *International Journal of Hydrogen Energy*, vol. 37, no. 22, pp. 16888–16894, 2012.

[143] M. Chambon, S. Abanades, and G. Flamant, 'Thermal dissociation of compressed ZnO and SnO2 powders in a moving-front solar thermochemical

reactor', *AIChE Journal*, vol. 57, no. 8, pp. 2264–2273, Aug. 2011.

[144] L. O. Schunk, P. Haeberling, S. Wept, D. Wuillemin, A. Meier, and A. Steinfeld, 'A receiver-reactor for the solar thermal dissociation of zinc oxide', *Journal of Solar Energy Engineering, Transactions of the ASME*, vol. 130, no. 2, pp. 0210091–0210096, 2008.

[145] W. C. Chueh *et al.*, 'Highly enhanced concentration and stability of reactive Ce 3+ on doped CeO 2 surface revealed in operando', *Chemistry of Materials*, vol. 24, no. 10, pp. 1876–1882, May 2012.

[146] J. Lapp, J. Davidson, and W. Lipiński, 'Heat transfer analysis of a solid-solid heat recuperation system for solar-driven non-stoichiometric redox cycles', *ASME 2012 6th International Conference on Energy Sustainability, ES 2012, Collocated with the ASME 2012 10th International Conference on Fuel Cell Science, Engineering and Technology*, no. PARTS A AND B, pp. 1081–1092, 2012.

[147] J. E. Miller *et al.*, 'Final Report Reimagining Liquid Transportation Fuels : Sunshine to Petrol; Sandia National Laboratories, Albuquerque, NM, Report No. SAND2012-0307', 2012.

[148] B. Guene Lougou *et al.*, 'Numerical and experimental analysis of reactor optimum design and solar thermal-chemical energy conversion for multidisciplinary applications', *Energy Conversion and Management*, vol. 213, p. 112870, Jun. 2020.

[149] F. Safari and I. Dincer, 'A review and comparative evaluation of thermochemical water splitting cycles for hydrogen production', *Energy Conversion and Management*, vol. 205, 2020.

[150] R. R. Bhosale, A. Kumar, and P. Sutar, 'Thermodynamic analysis of solar driven SnO2/SnO based thermochemical water splitting cycle', *Energy Conversion and Management*, vol. 135, pp. 226–235, 2017.

[151] X. Chen, F. Wang, Y. Han, R. Yu, and Z. Cheng, 'Thermochemical storage analysis of the dry reforming of methane in foam solar reactor', *Energy*

Conversion and Management, vol. 158, pp. 489–498, 2018.

[152] F. Wang, J. Tan, L. Ma, and Y. Leng, 'Effects of key factors on solar aided methane steam reforming in porous medium thermochemical reactor', *Energy Conversion and Management*, vol. 103, pp. 419–430, 2015.

[153] F. Wang, J. Tan, Y. Shuai, L. Gong, and H. Tan, 'Numerical analysis of hydrogen production via methane steam reforming in porous media solar thermochemical reactor using concentrated solar irradiation as heat source', *Energy Conversion and Management*, vol. 87, pp. 956–964, 2014.

[154] P. Charvin, A. Stéphane, L. Florent, and F. Gilles, 'Analysis of solar chemical processes for hydrogen production from water splitting thermochemical cycles', *Energy Conversion and Management*, vol. 49, no. 6, pp. 1547–1556, 2008.

[155] R. Bhosale *et al.*, 'Solar hydrogen production via a samarium oxide-based thermochemical water splitting cycle', *Energies*, vol. 9, no. 5, p. 316, Apr. 2016.

[156] R. R. Bhosale *et al.*, 'Solar hydrogen production via erbium oxide based thermochemical water splitting cycle', *Journal of Renewable and Sustainable Energy*, vol. 8, no. 3, p. 034702, May 2016.

[157] R. Bhosale, A. Kumar, and F. AlMomani, 'Solar Thermochemical Hydrogen Production via Terbium Oxide Based Redox Reactions', *International Journal of Photoenergy*, vol. 2016, pp. 1–9, 2016.

[158] R. Bhosale, A. Kumar, F. AlMomani, and R. B. Gupta, 'Solar thermochemical ZnO/ZnSO4 water splitting cycle for hydrogen production', *International Journal of Hydrogen Energy*, vol. 42, no. 37, pp. 23474–23483, Sep. 2017.

[159] R. Bhosale, F. AlMomani, and G. Takalkar, 'Thermodynamic analysis of solar-driven chemical looping steam methane reforming over Cr2O3/Cr redox pair', *International Journal of Hydrogen Energy*, vol. 45, no. 17, pp. 10370–10380, Mar. 2020.

[160] R. R. Bhosale, F. AlMomani, and S. Rashid, 'Solar thermochemical H2 production via MnSO4/MnO water splitting cycle: Thermodynamic equilibrium

and efficiency analysis', *International Journal of Hydrogen Energy*, vol. 45, no. 17, pp. 10324–10333, Mar. 2020.

[161] G. D. Takalkar *et al.*, 'Transition metal doped ceria for solar thermochemical fuel production', *Solar Energy*, vol. 172, no. November 2017, pp. 204–211, 2018.

[162] J. Sarwar, G. Georgakis, K. Kouloulias, and K. E. Kakosimos, 'Experimental and numerical investigation of the aperture size effect on the efficient solar energy harvesting for solar thermochemical applications', *Energy Conversion and Management*, vol. 92, pp. 331–341, 2015.

[163] O. Siddiqui, H. Ishaq, and I. Dincer, 'A novel solar and geothermal-based trigeneration system for electricity generation, hydrogen production and cooling', *Energy Conversion and Management*, vol. 198, 2019.

[164] Q. Jiang, H. Zhang, Y. Cao, H. Hong, and H. Jin, 'Solar hydrogen production via perovskite-based chemical-looping steam methane reforming', *Energy Conversion and Management*, vol. 187, pp. 523–536, 2019.

[165] M. Sedighi, R. V. Padilla, R. A. Taylor, M. Lake, I. Izadgoshasb, and A. Rose, 'High-temperature, point-focus, pressurised gas-phase solar receivers: A comprehensive review', *Energy Conversion and Management*, vol. 185, no. February, pp. 678–717, 2019.

[166] H. Lee, A. Kim, B. Lee, and H. Lim, 'Comparative numerical analysis for an efficient hydrogen production via a steam methane reforming with a packed-bed reactor, a membrane reactor, and a sorption-enhanced membrane reactor', *Energy Conversion and Management*, vol. 213, 2020.

[167] Y. Wang, Q. Liu, J. Sun, J. Lei, Y. Ju, and H. Jin, 'A new solar receiver/reactor structure for hydrogen production', *Energy Conversion and Management*, vol. 133, pp. 118–126, 2017.

[168] L. Zhu, Y. Lu, and F. Li, 'Reactivity of Ni, Cr and Zr doped ceria in CO2 splitting for CO production via two-step thermochemical cycle', *International Journal of Hydrogen Energy*, vol. 43, no. 30, pp. 13754–13763, 2018.

[169] I. Teknetzi, P. Nessi, V. Zaspalis, and L. Nalbandian, ‘Ni-ferrite with structural stability for solar thermochemical H2O/CO2 splitting’, *International Journal of Hydrogen Energy*, vol. 42, no. 42, pp. 26231–26242, 2017.

[170] B. Guene Lougou, J. Hong, Y. Shuai, X. Huang, Y. Yuan, and H. Tan, ‘Production mechanism analysis of H2 and CO via solar thermochemical cycles based on iron oxide (Fe3O4) at high temperature’, *Solar Energy*, vol. 148, pp. 117–127, 2017.

[171] C. L. Muhich, S. Blaser, M. C. Hoes, and A. Steinfeld, ‘Comparing the solar-to-fuel energy conversion efficiency of ceria and perovskite based thermochemical redox cycles for splitting H2O and CO2’, *International Journal of Hydrogen Energy*, vol. 43, no. 41, pp. 18814–18831, 2018.

[172] S. Wu, C. Zhou, E. Doroodchi, R. Nellore, and B. Moghtaderi, ‘A review on high-temperature thermochemical energy storage based on metal oxides redox cycle’, *Energy Conversion and Management*, vol. 168, pp. 421–453, 2018.

[173] A. Alovisio, R. Chacartegui, C. Ortiz, J. M. Valverde, and V. Verda, ‘Optimizing the CSP-Calcium Looping integration for Thermochemical Energy Storage’, *Energy Conversion and Management*, vol. 136, pp. 85–98, 2017.

[174] Z. H. Pan and C. Y. Zhao, ‘Gas–solid thermochemical heat storage reactors for high-temperature applications’, *Energy*, vol. 130, pp. 155–173, 2017.

[175] T. Liu, Q. Liu, J. Lei, J. Sui, and H. Jin, ‘Solar-clean fuel distributed energy system with solar thermochemistry and chemical recuperation’, *Applied Energy*, vol. 225, pp. 380–391, 2018.

[176] A. de la Calle and A. Bayon, ‘Annual performance of a thermochemical solar syngas production plant based on non-stoichiometric CeO 2’, *International Journal of Hydrogen Energy*, vol. 44, no. 3, pp. 1409–1424, 2019.

[177] I. Dincer and C. Acar, ‘Innovation in hydrogen production’, *International Journal of Hydrogen Energy*, vol. 42, no. 22, pp. 14843–14864, 2017.

[178] A. Banerjee, R. B. Chandran, and J. H. Davidson, ‘Experimental investigation

of a reticulated porous alumina heat exchanger for high temperature gas heat recovery', *Applied Thermal Engineering*, vol. 75, pp. 889–895, 2015.

[179] R. Bala Chandran, R. M. De Smith, and J. H. Davidson, 'Model of an integrated solar thermochemical reactor/reticulated ceramic foam heat exchanger for gas-phase heat recovery', *International Journal of Heat and Mass Transfer*, vol. 81, pp. 404–414, Feb. 2015.

[180] R. B. Chandran, R. Bader, and W. Lipiński, 'Transient heat and mass transfer analysis in a porous ceria structure of a novel solar redox reactor', *International Journal of Thermal Sciences*, vol. 92, pp. 138–149, 2015.

[181] X. Chen, F. Wang, X. Yan, Z. Cheng, Y. Han, and Z. Jie, 'Thermal and chemical analysis of methane dry reforming in a volumetric reactor under highly concentrated solar radiation', *Solar Energy*, vol. 162, pp. 187–195, Mar. 2018.

[182] X. Chen, F. Wang, X. Yan, Y. Han, Z. Cheng, and Z. Jie, 'Thermochemical performance of solar driven CO 2 reforming of methane in volumetric reactor with gradual foam structure', *Energy*, vol. 151, pp. 545–555, 2018.

[183] P. Furler and A. Steinfeld, 'Heat transfer and fluid flow analysis of a 4kW solar thermochemical reactor for ceria redox cycling', *Chemical Engineering Science*, vol. 137, pp. 373–383, 2015.

[184] H. Kong, Y. Hao, and H. Jin, 'Isothermal versus two-temperature solar thermochemical fuel synthesis: A comparative study', *Applied Energy*, vol. 228, pp. 301–308, 2018.

[185] C. Agrafiotis, A. Becker, M. Roeb, and C. Sattler, 'Exploitation of thermochemical cycles based on solid oxide redox systems for thermochemical storage of solar heat. Part 5: Testing of porous ceramic honeycomb and foam cascades based on cobalt and manganese oxides for hybrid sensible/thermochemical heat s', *Solar Energy*, vol. 139, pp. 676–694, 2016.

[186] B. Guene Lougou *et al.*, 'Radiative heat transfer and thermal characteristics of Fe-based oxides coated SiC and Alumina RPC structures as integrated solar thermochemical reactor', *Science China Technological Sciences*, vol. 61, no. 12,

pp. 1788–1801, 2018.

[187] M. A. A. Mendes, P. Talukdar, S. Ray, and D. Trimis, ‘Detailed and simplified models for evaluation of effective thermal conductivity of open-cell porous foams at high temperatures in presence of thermal radiation’, *International Journal of Heat and Mass Transfer*, vol. 68, pp. 612–624, 2014.

[188] S. Du, M. J. Li, Q. Ren, Q. Liang, and Y. L. He, ‘Pore-scale numerical simulation of fully coupled heat transfer process in porous volumetric solar receiver’, *Energy*, vol. 140, pp. 1267–1275, 2017.

[189] T. Kogawa, L. Chen, J. Okajima, A. Sakurai, A. Komiya, and S. Maruyama, ‘Effects of concentration of participating media on turbulent natural convection in cubic cavity’, *Applied Thermal Engineering*, vol. 131, pp. 141–149, 2018.

[190] M. E. Nimvari, N. F. Jouybari, and Q. Esmaili, ‘A new approach to mitigate intense temperature gradients in ceramic foam solar receivers’, *Renewable Energy*, vol. 122, pp. 206–215, 2018.

[191] P. J. Valadés-Pelayo and C. A. Arancibia-Bulnes, ‘Transient behavior of a multi-tubular cavity solar thermochemical reactor’, *Applied Thermal Engineering*, vol. 123, pp. 1255–1262, 2017.

[192] X. Chen, X. L. Xia, X. W. Yan, and C. Sun, ‘Heat transfer analysis of a volumetric solar receiver with composite porous structure’, *Energy Conversion and Management*, vol. 136, pp. 262–269, 2017.

[193] B. Guene Lougou, Y. Shuai, Z. Guohua, G. Chaffa, C. Ahouannou, and H. Tan, ‘Analysis of H2 and CO production via solar thermochemical reacting system of NiFe2O4 redox cycles combined with CH4 partial oxidation’, *International Journal of Hydrogen Energy*, vol. 43, no. 12, pp. 5996–6010, 2018.

[194] N. Bayat, M. Rezaei, and F. Meshkani, ‘Methane decomposition over Ni-Fe/Al2O3 catalysts for production of COx-free hydrogen and carbon nanofiber’, *International Journal of Hydrogen Energy*, vol. 41, no. 3, pp. 1574–1584, 2016.

[195] C. L. Muhich *et al.*, ‘Predicting the solar thermochemical water splitting ability

and reaction mechanism of metal oxides: A case study of the hercynite family of water splitting cycles', *Energy and Environmental Science*, vol. 8, no. 12, pp. 3687–3699, 2015.

[196] N. Gokon, T. Suda, and T. Kodama, 'Oxygen and hydrogen productivities and repeatable reactivity of 30-mol%-Fe-, Co-, Ni-, Mn-doped CeO2-δ for thermochemical two-step water-splitting cycle', *Energy*, vol. 90, pp. 1280–1289, 2015.

[197] S. J. Roberts, N. G. Carr, J. McLaughlin, and H. E. Hagelin-Weaver, 'Iron precipitated onto ceria-zirconia nanoparticle mixtures for the production of hydrogen via two-step thermochemical water splitting', *International Journal of Hydrogen Energy*, vol. 43, no. 29, pp. 12970–12984, 2018.

[198] S. Haussener, D. Hirsch, C. Perkins, A. Weimer, A. Lewandowski, and A. Steinfeld, 'Modeling of a Multitube High-Temperature Solar Thermochemical Reactor for Hydrogen Production', *Journal of Solar Energy Engineering*, vol. 131, no. 2, p. 024503, 2009.

[199] T. Ishida, N. Gokon, T. Hatamachi, and T. Kodama, 'Kinetics of thermal reduction step of thermochemical two-step water splitting using CeO2 particles: Master-plot method for analyzing non-isothermal experiments', *Energy Procedia*, vol. 49, pp. 1970–1979, 2014.

[200] B. Bulfin *et al.*, 'Analytical Model of CeO 2 Oxidation and Reduction', *The Journal of Physical Chemistry C*, vol. 117, no. 46, pp. 24129–24137, Nov. 2013.

[201] M. F. Modest, *Radiative heat transfer*. 2013.

[202] P. Hsu and J. R. Howell, 'MEASUREMENTS OF THERMAL CONDUCTIVITY AND OPTICAL PROPERTIES OF POROUS PARTIALLY STABILIZED ZIRCONIA', *Experimental Heat Transfer*, vol. 5, no. 4, pp. 293–313, Oct. 1992.

[203] B. Bulfin *et al.*, 'Analytical model of CeO2 oxidation and reduction', *Journal of Physical Chemistry C*, vol. 117, no. 46, pp. 24129–24137, Nov. 2013.

[204] R. Jilte, M. H. Ahmadi, V. Kalamkar, and R. Kumar, 'Solar flux distribution study in heat pipe cavity receiver integrated with biomass gasifier', *International Journal of Energy Research*, vol. 44, no. 9, pp. 7698–7712, Jul. 2020.

[205] Y. Shuai, X.-L. Xia, and H.-P. Tan, 'Radiation performance of dish solar concentrator/cavity receiver systems', *Solar Energy*, vol. 82, no. 1, pp. 13–21, Jan. 2008.

[206] H. Zhang and J. D. Smith, 'Investigating influences of geometric factors on a solar thermochemical reactor for two-step carbon dioxide splitting via CFD models', *Solar Energy*, vol. 188, no. January, pp. 935–950, 2019.

[207] C. C. Agrafiotis, C. Pagkoura, A. Zygogianni, G. Karagiannakis, M. Kostoglou, and A. G. Konstandopoulos, 'Hydrogen production via solar-aided water splitting thermochemical cycles: Combustion synthesis and preliminary evaluation of spinel redox-pair materials', *International Journal of Hydrogen Energy*, vol. 37, no. 11, pp. 8964–8980, Jun. 2012.

[208] R. R. Bhosale *et al.*, 'Effectiveness of Ni incorporation in iron oxide crystal structure towards thermochemical CO2 splitting reaction', *Ceramics International*, vol. 43, no. 6, pp. 5150–5155, Apr. 2017.

[209] R. Bader, L. J. Venstrom, J. H. Davidson, and W. Lipiński, 'Thermodynamic analysis of isothermal redox cycling of ceria for solar fuel production', *Energy and Fuels*, vol. 27, no. 9, pp. 5533–5544, 2013.

[210] R. R. Bhosale *et al.*, 'Solar co-production of samarium and syngas via methanothermal reduction of samarium sesquioxide', *Energy Conversion and Management*, vol. 112, pp. 413–422, 2016.

[211] A. E. Kalyva *et al.*, 'Particle model investigation for the thermochemical steps of the sulfur–ammonia water splitting cycle', *International Journal of Hydrogen Energy*, vol. 42, no. 6, pp. 3621–3629, Feb. 2017.

[212] R. R. Bhosale, 'Thermodynamic efficiency analysis of zinc oxide based solar driven thermochemical H2O splitting cycle: Effect of partial pressure of O2, thermal reduction and H2O splitting temperatures', *International Journal of*

Hydrogen Energy, vol. 43, no. 32, pp. 14915–14924, 2018.

[213] P. G. Loutzenhiser and A. Steinfeld, 'Solar syngas production from CO2 and H2O in a two-step thermochemical cycle via Zn/ZnO redox reactions: Thermodynamic cycle analysis', *International Journal of Hydrogen Energy*, vol. 36, no. 19, pp. 12141–12147, Sep. 2011.

[214] P. Charvin, S. Abanades, G. Flamant, and F. Lemort, 'Two-step water splitting thermochemical cycle based on iron oxide redox pair for solar hydrogen production', *Energy*, vol. 32, no. 7, pp. 1124–1133, Jul. 2007.

[215] T. Kodama, N. Gokon, and R. Yamamoto, 'Thermochemical two-step water splitting by ZrO2-supported NixFe3-xO4 for solar hydrogen production', *Solar Energy*, vol. 82, no. 1, pp. 73–79, Jan. 2008.

[216] R. R. Bhosale, R. V. Shende, and J. A. Puszynski, 'Sol-gel derived NiFe2O4 modified with ZrO2 for hydrogen generation from solar thermochemical water-splitting reaction', *Materials Research Society Symposium Proceedings*, vol. 1387, pp. 34–39, 2011.

[217] J. R. Scheffe, J. Li, and A. W. Weimer, 'A spinel ferrite/hercynite water-splitting redox cycle', *International Journal of Hydrogen Energy*, vol. 35, no. 8, pp. 3333–3340, Apr. 2010.

[218] S. Lorentzou, C. C. Agrafiotis, and A. G. Konstandopoulos, 'Aerosol spray pyrolysis synthesis of water-splitting ferrites for solar hydrogen production', *Granular Matter*, vol. 10, no. 2, pp. 113–122, 2008.

[219] S. Abanades, P. Charvin, F. Lemont, and G. Flamant, 'Novel two-step SnO2/SnO water-splitting cycle for solar thermochemical production of hydrogen', *International Journal of Hydrogen Energy*, vol. 33, no. 21, pp. 6021–6030, Nov. 2008.

[220] R. R. Bhosale, G. Takalkar, P. Sutar, A. Kumar, F. AlMomani, and M. Khraisheh, 'A decade of ceria based solar thermochemical H2O/CO2 splitting cycle', *International Journal of Hydrogen Energy*, pp. 34–60, 2019.

[221] A. Le Gal, S. Abanades, and G. Flamant, ‘CO2 and H2O splitting for thermochemical production of solar fuels using nonstoichiometric ceria and ceria/zirconia solid solutions’, *Energy and Fuels*, vol. 25, no. 10, pp. 4836–4845, Oct. 2011.

[222] P. Furler, J. R. Scheffe, and A. Steinfeld, ‘Syngas production by simultaneous splitting of H 2O and CO 2via ceria redox reactions in a high-temperature solar reactor’, *Energy and Environmental Science*, vol. 5, no. 3, pp. 6098–6103, 2012.

[223] R. R. Bhosale *et al.*, ‘Assessment of CexZryHfzO2 based oxides as potential solar thermochemical CO2 splitting materials’, *Ceramics International*, vol. 42, no. 8, pp. 9354–9362, 2016.

[224] A. H. McDaniel *et al.*, ‘Sr- and Mn-doped LaAlO3-δ for solar thermochemical H 2 and CO production’, *Energy and Environmental Science*, vol. 6, no. 8, pp. 2424–2428, 2013.

[225] J. R. Scheffe, D. Weibel, and A. Steinfeld, ‘Lanthanum-strontium-manganese perovskites as redox materials for solar thermochemical splitting of H2O and CO2’, *Energy and Fuels*, vol. 27, no. 8, pp. 4250–4257, Aug. 2013.

[226] A. Demont, S. Abanades, and E. Beche, ‘Investigation of perovskite structures as oxygen-exchange redox materials for hydrogen production from thermochemical two-step water-splitting cycles’, *Journal of Physical Chemistry C*, vol. 118, no. 24, pp. 12682–12692, Jun. 2014.

[227] R. Bhosale, A. Kumar, and F. Almomani, ‘Solar Thermochemical Hydrogen Production via Terbium Oxide Based Redox Reactions’, *International Journal of Photoenergy*, vol. 2016, 2016.

[228] R. Bhosale *et al.*, ‘Solar hydrogen production via a samarium oxide-based thermochemical water splitting cycle’, *Energies*, vol. 9, no. 5, 2016.

[229] K. Onuki, S. Kubo, A. Terada, N. Sakaba, and R. Hino, ‘Thermochemical water-splitting cycle using iodine and sulfur’, *Energy and Environmental Science*, vol. 2, no. 5, pp. 491–497, 2009.

[230] X. Vitart, A. Le Duigou, and P. Carles, ‘Hydrogen production using the sulfur-iodine cycle coupled to a VHTR: An overview’, *Energy Conversion and Management*, vol. 47, no. 17, pp. 2740–2747, 2006.

[231] A. E. Kalyva *et al.*, ‘Investigation of the solar hybrid photo-thermochemical sulfur-ammonia water splitting cycle for hydrogen production’, *Chemical Engineering Transactions*, vol. 45, pp. 361–366, 2015.

[232] A. E. Kalyva *et al.*, ‘Hybrid photo-thermal sulfur-ammonia water splitting cycle: Thermodynamic analysis of the thermochemical steps’, *International Journal of Hydrogen Energy*, vol. 42, no. 15, pp. 9533–9544, Apr. 2017.

[233] R. R. Bhosale *et al.*, ‘Solar hydrogen production via thermochemical iron oxide-iron sulfate water splitting cycle’, *International Journal of Hydrogen Energy*, vol. 40, no. 4, pp. 1639–1650, Jan. 2015.

[234] R. R. Bhosale, ‘Thermochemical H 2 production via solar driven hybrid SrO/SrSO 4 water splitting cycle’, *International Journal of Hydrogen Energy*, pp. 118–127, 2019.

[235] J. R. Scheffe and A. Steinfeld, ‘Oxygen exchange materials for solar thermochemical splitting of H2O and CO2: A review’, *Materials Today*, vol. 17, no. 7, pp. 341–348, Sep. 2014.

[236] A. Statnatiou, P. G. Loutzenhiser, and A. Steinfeld, ‘Solar syngas production via H2O/CO2-splitting thermochemical cycles with Zn/ZnO and FeO/Fe3O4 redox reactions’, *Chemistry of Materials*, vol. 22, no. 3, pp. 851–859, Feb. 2010.

[237] T. Kodama, Y. Nakamuro, and T. Mizuno, ‘A two-step thermochemical water splitting by iron-oxide on stabilized zirconia’, *Journal of Solar Energy Engineering, Transactions of the ASME*, vol. 128, no. 1, pp. 3–7, Feb. 2006.

[238] P. Charvin, S. Abanades, G. Flamant, and F. Lemort, ‘Two-step water splitting thermochemical cycle based on iron oxide redox pair for solar hydrogen production’, *Energy*, vol. 32, no. 7, pp. 1124–1133, 2007.

[239] N. Gokon, T. Hasegawa, S. Takahashi, and T. Kodama, ‘Thermochemical two-

step water-splitting for hydrogen production using Fe-YSZ particles and a ceramic foam device', *Energy*, vol. 33, no. 9, pp. 1407–1416, Sep. 2008.

[240] R. R. Bhosale, R. V. Shende, and J. A. Puszynski, 'Sol-gel derived NiFe2O4 modified with ZrO2 for hydrogen generation from solar thermochemical water-splitting reaction', *Materials Research Society Symposium Proceedings*, vol. 1387, pp. 34–39, Apr. 2011.

[241] R. R. Bhosale *et al.*, 'Effectiveness of Ni incorporation in iron oxide crystal structure towards thermochemical CO2 splitting reaction', *Ceramics International*, vol. 43, no. 6, pp. 5150–5155, 2017.

[242] M. Chambon, S. Abanades, and G. Flamant, 'Thermal dissociation of compressed ZnO and SnO2 powders in a moving-front solar thermochemical reactor', *AIChE Journal*, vol. 57, no. 8, pp. 2264–2273, Aug. 2011.

[243] S. Abanades and M. Chambon, 'CO2 dissociation and upgrading from two-step solar thermochemical processes based on ZnO/Zn and SnO2/SnO redox pairs', *Energy and Fuels*, vol. 24, no. 12, pp. 6667–6674, Dec. 2010.

[244] R. R. Bhosale, A. Kumar, and P. Sutar, 'Thermodynamic analysis of solar driven SnO2/SnO based thermochemical water splitting cycle', *Energy Conversion and Management*, vol. 135, pp. 226–235, Mar. 2017.

[245] R. R. Bhosale, 'Thermodynamic efficiency analysis of zinc oxide based solar driven thermochemical H2O splitting cycle: Effect of partial pressure of O2, thermal reduction and H2O splitting temperatures', *International Journal of Hydrogen Energy*, vol. 43, no. 32, pp. 14915–14924, Aug. 2018.

[246] P. G. Loutzenhiser, A. Meier, and A. Steinfeld, 'Review of the Two-Step H2O/CO2-Splitting solar thermochemical cycle based on Zn/ZnO redox reactions', *Materials*, vol. 3, no. 11, pp. 4922–4938, 2010.

[247] J. R. Scheffe and A. Steinfeld, 'Thermodynamic analysis of cerium-based oxides for solar thermochemical fuel production', *Energy and Fuels*, vol. 26, no. 3, pp. 1928–1936, Mar. 2012.

[248] G. D. Takalkar *et al.*, 'Transition metal doped ceria for solar thermochemical fuel production', *Solar Energy*, vol. 172, pp. 204–211, 2018.

[249] R. R. Bhosale *et al.*, 'Assessment of CexZryHfzO2 based oxides as potential solar thermochemical CO2 splitting materials', *Ceramics International*, vol. 42, no. 8, pp. 9354–9362, Jun. 2016.

[250] S. Ackermann, J. R. Scheffe, and A. Steinfeld, 'Diffusion of oxygen in ceria at elevated temperatures and its application to H2O/CO2 splitting thermochemical redox cycles', *Journal of Physical Chemistry C*, vol. 118, no. 10, pp. 5216–5225, Mar. 2014.

[251] W. C. Chueh *et al.*, 'High-flux solar-driven thermochemical dissociation of CO2 and H2O using nonstoichiometric ceria', *Science*, vol. 330, no. 6012, pp. 1797–1801, Dec. 2010.

[252] P. Furler, J. R. Scheffe, and A. Steinfeld, 'Syngas production by simultaneous splitting of H 2O and CO 2via ceria redox reactions in a high-temperature solar reactor', *Energy and Environmental Science*, vol. 5, no. 3, pp. 6098–6103, 2012.

[253] R. R. Bhosale *et al.*, 'La-Based Perovskites as Oxygen-Exchange Redox Materials for Solar Syngas Production', *MRS Advances*, vol. 2, no. 55, pp. 3365–3370, 2017.

[254] M. Takacs, M. Hoes, M. Caduff, T. Cooper, J. R. Scheffe, and A. Steinfeld, 'Oxygen nonstoichiometry, defect equilibria, and thermodynamic characterization of LaMnO3 perovskites with Ca/Sr A-site and Al B-site doping', *Acta Materialia*, vol. 103, pp. 700–710, 2016.

[255] M. Kubicek, A. H. Bork, and J. L. M. Rupp, 'Perovskite oxides-a review on a versatile material class for solar-to-fuel conversion processes', *Journal of Materials Chemistry A*, vol. 5, no. 24, pp. 11983–12000, 2017.

[256] A. H. McDaniel *et al.*, 'Nonstoichiometric perovskite oxides for solar thermochemical H2 and CO production', *Energy Procedia*, vol. 49, pp. 2009–2018, 2014.

[257] R. R. Bhosale, A. Kumar, F. AlMomani, U. Ghosh, and M. Khraisheh, ‘A comparative thermodynamic analysis of samarium and erbium oxide based solar thermochemical water splitting cycles’, *International Journal of Hydrogen Energy*, vol. 42, no. 37, pp. 23416–23426, Sep. 2017.

[258] R. Bhosale, A. Kumar, and F. Almomani, ‘Solar Thermochemical Hydrogen Production via Terbium Oxide Based Redox Reactions’, *International Journal of Photoenergy*, vol. 2016, pp. 1–9, 2016.

[259] J. Bear and J. M. Buchlin, *Modelling and applications of transport phenomena in porous media*, vol. 5. Dordrecht: Springer Netherlands, 1991.

[260] C. K. Ho and S. W. Webb, Eds., *Gas Transport in Porous Media*, vol. 20. Springer Netherlands, 2006.

[261] M. Romero and A. Steinfeld, ‘Concentrating solar thermal power and thermochemical fuels’, *Energy & Environmental Science*, vol. 5, no. 11, p. 9234, 2012.

[262] J. E. Miller, A. H. McDaniel, and M. D. Allendorf, ‘Considerations in the Design of Materials for Solar-Driven Fuel Production Using Metal-Oxide Thermochemical Cycles’, *Advanced Energy Materials*, vol. 4, no. 2, p. 1300469, Jan. 2014.

[263] S. Ackermann, J. R. Scheffe, and A. Steinfeld, ‘Diffusion of Oxygen in Ceria at Elevated Temperatures and Its Application to H 2 O/CO 2 Splitting Thermochemical Redox Cycles’, *The Journal of Physical Chemistry C*, vol. 118, no. 10, pp. 5216–5225, Mar. 2014.

[264] W. T. Gibbons, L. J. Venstrom, R. M. De Smith, J. H. Davidson, and G. S. Jackson, ‘Ceria-based electrospun fibers for renewable fuel production via two-step thermal redox cycles for carbon dioxide splitting’, *Phys. Chem. Chem. Phys.*, vol. 16, no. 27, pp. 14271–14280, 2014.

[265] K. K. Bodla, J. A. Weibel, and S. V. Garimella, ‘Advances in Fluid and Thermal Transport Property Analysis and Design of Sintered Porous Wick Microstructures’, *Journal of Heat Transfer*, vol. 135, no. 6, Jun. 2013.